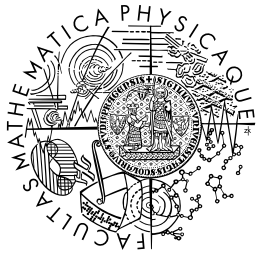

FACULTY
OF MATHEMATICS
AND PHYSICS
Charles University

DOCTORAL THESIS

Filip Kostka

Dynamic models of the earthquake source

Department of Geophysics

Supervisor of the doctoral thesis: doc. RNDr. František Gallovič, Ph.D.

Study programme: Physics

Study branch: Physics of the Earth and Planets

Prague 2022

I declare that I carried out this doctoral thesis independently, and only with the cited sources, literature and other professional sources. It has not been used to obtain another or the same degree.

I understand that my work relates to the rights and obligations under the Act No. 121/2000 Sb., the Copyright Act, as amended, in particular the fact that the Charles University has the right to conclude a license agreement on the use of this work as a school work pursuant to Section 60 subsection 1 of the Copyright Act.

In Prague, January 1, 2022 Filip Kostka

Poděkování

Ze všeho nejvíc bych rád poděkoval docentu Františku Gallovičovi za jeho inspirativní ochotu, pečlivost, erudovanost a trpělivost, se kterými mě provázel nejen při psaní této práce.

Všem pracovníkům a studentům na Katedře geofyziky jsem vděčný za vřelé a nápomocné prostředí, které tam díky nim panuje. Liborovi, Mírovi, Frantovi a Honzovi děkuji za všechny podnětné i nepodnětné diskuze. Zvláštní poděkování patří profesoru Jiřímu Zahradníkovi za odbornou pomoc i za laskavost, jež mi byla oporou v horších časech.

Členům své milé rodiny děkuji za jejich lásku i materiální výpomoc. Obzvláště mamince jsem vděčný za její empatii a stálou psychickou podporu.

Univerzita Karlova mi poskytla finanční prostředky skrze projekty GA UK 1698218 a SVV 115–09/260581, 115-09/260447. Ministerstvo školství, mládeže a tělovýchovy mě podpořilo poskytnutím výpočetních prostředků v národním superpočítačovém centru IT4Innovations (projekt e-INFRA CZ, ID:90140).

Název práce: Dynamické modely zemětřesného zdroje

Autor: Filip Kostka

Katedra: Katedra geofyziky

Vedoucí disertační práce: doc. RNDr. František Gallovič, Ph.D., Katedra geofyziky

Abstrakt: Dynamické modely zemětřesného zdroje umožňují simulovat vývoj napětí a skluzu na tektonických zlomech spojením pohybových rovnic v objemu obklopujícím zlom s konstitutivním zákonem, který představujíce plošné síly působící na zlomu. V první části práce shrnujeme důležité vlastnosti smykových trhlin pro ideálně křehké trhliny a konstitutivní zákony typu linear slip-weakening a rate-and-state. Ve druhé části práce představujeme dvě studie využívající 3-D dynamické modelování zlomů na dlouhém (stovky let) i krátkém (sekundy) časovém měřítku. V první ze studií modelujeme seismické cykly pomocí rate-and-state zákona tření a provádíme parametrický průzkum účinků náhlých perturbací smykového napětí během cyklu na uspíšení nebo zpoždění následujícího zemětřesení. Zjišťujeme, že pokud je perturbace aplikována během speciálních malých časových intervalů, zemětřesení následující po perturbaci jsou malá a neuvolní zcela napětí na celém zlomu. Doba trvání mezi velkými zemětřeseními se pak může prodloužit až o 80 % ve srovnání s neperturbovanými cykly. Toto chování reprodukujeme na numerickém heterogenním modelu parkfieldského segmentu zlomu San Andreas a demonstrujeme, že tento mechanismus mohl být zodpovědný za velké zpoždění zemětřesení na tomto segmentu v roce 2004 o magnitudu Mw 6. Ve druhé studii využíváme linear slip-weakening zákona tření a 12parametrický eliptický model, abychom provedli bayesovskou dynamickou inverzi zemětřesení na ostrově Lesbos o magnitudu Mw 6,3 z roku 2017. Vypočítáváme nejpravděpodobnější hodnoty a nejistoty jednotlivých parametrů, spolu s jejich vzájemnými korelacemi. Navrhujeme také metodu jak ocenit, do jaké míry jsou modelové parametry a další veličiny rozlišeny různými omezeními. Konkrétně zkoumáme vliv apriorních předpokladů, minimální podmínky na šíření trhliny, informace o momentovém magnitudu a seismických vlnových obrazů na konečný tvar hustot pravděpodobnosti různých veličin.

Klíčová slova: Dynamické modely zemětřesného zdroje, Rate-and-state model tření, Slip-weakening model tření, Bayesovská inverze

Title: Dynamic models of the earthquake source

Author: Filip Kostka

Department: Department of Geophysics

Supervisor: doc. RNDr. František Gallovič, Ph.D., Department of Geophysics

Abstract: Dynamic models of the earthquake source allow simulating the evolution of stress and slip at tectonic faults by coupling the equations of motion in a volume surrounding the fault with a constitutive law that represents the surface forces acting on the fault. In the first part of the thesis, we review important properties of shear rupture for brittle, linear slip-weakening, and rate-and-state constitutive laws. In the second part of the thesis, we present two studies utilizing 3-D dynamic modeling at both long (hundreds of years) and short (seconds) time scales. In the first study, we model seismic cycles using the rate-and-state laws of friction and perform a parametric exploration of the effects of sudden intra-cycle shear stress perturbations on the clock advance or delay of the subsequent large event. We find that when the perturbation is applied during specific time intervals, the earthquakes following the perturbation are only small ruptures that do not completely release stress on the whole fault. The time interval between large earthquakes may thus be prolonged up to 80% when compared to the unperturbed cycles. We reproduce this behavior on a numerical heterogeneous model of the Parkfield segment of the San Andreas fault and demonstrate that the mechanism could have been responsible for the observed large delay of the 2004 Mw 6 Parkfield earthquake. In the second study, we use the linear slip-weakening law with a 12-parametric elliptic model to carry out a Bayesian dynamic inversion of the 2017 Mw 6.3 Lesvos Earthquake. We calculate the most probable values and uncertainties of individual parameters, along with their mutual trade-offs. We also propose a method of assessing the degree to which model parameters and other quantities are resolved by different constraints. In particular, we examine the effect of prior assumptions, a minimum rupture expansion condition, the information about the moment magnitude, and seismic waveforms on the final shape of probability density functions for different quantities.

Keywords: Dynamic earthquake source models, Rate-and-state friction, Slip-weakening friction, Bayesian inversion

Contents

Introduction

An earthquake is the shaking of ground due to elastic waves, typically emitted by a source in the Earth's lithosphere. The consensus today is that the overwhelming majority of large earthquakes arise from two processes in the Earth's lithosphere: fracture of originally intact rock and frictional sliding along preexisting tectonic faults. In the most dramatic cases, large potential energy (up to millions of terajoules) that has been stored in the rocks for up to hundreds of years is released within a few seconds, in a fast, unstable process that generates destructive seismic waves, which then propagate to the surface. But the speed and vigor of the process are not the meaning of the word "dynamic" in the title of this thesis: *Dynamic models of the earthquake source.*

Rather, it refers to the branch of physics concerned with forces and their effect on the motion of matter. In the dynamic approach to earthquake modeling, the earthquake sources are described by the forces that govern their movement. As such, dynamic models are to be contrasted with kinematic (dislocation) models, which ignore the causative forces and directly prescribe the relative motion (slip) between tectonic fault surfaces. A great advantage of kinematic models is that they allow fast calculation of displacement outside of the fault. With suitable parametrization, they lead to linear problems and provide a more direct and transparent connection between slip and synthetic seismograms than dynamic models, which are non-linear and take more time to solve. But even though any kinematic model in an elastic medium has an associated surface force distribution, these distributions are often not realistic and violate reasonable assumptions such as continuity and causality.

The most common dynamic earthquake source models are those rooted in the field of fracture mechanics. Early studies modeled earthquakes as propagating ideally brittle cracks, assuming sudden release of stress behind the crack front. Even though such models can provide valid insights and approximate more realistic models in certain situations, they lead to infinite stresses and slip rates. They are also not consistent with laboratory and seismologic studies which show that the stress on the fault has a complicated dependence on slip, slip rate, and

other field quantities.

These problems can be solved in the framework of cohesive fracture. Here, the spatial distribution of stress and slip rate on the fault is made finite and continuous by means of a suitably chosen constitutive law. This is a rule relating traction to other physical quantities, most notably the slip, the slip rate, the normal stress and position, but possibly also time, temperature, porosity, or certain abstractly defined state variables. The constitutive law represents the forces acting during the rupture process and it is mathematically posed as a boundary condition on the fault. As such, it allows describing fracture and friction in a unified manner. Coupling the constitutive law with continuum equations of motion in a volume surrounding the fault allows calculating the displacement everywhere in the volume, including the slip.

The problem of determining the correct constitutive law is crucial for earthquake physics and has been the subject of theoretical, laboratory, and field studies. The most prominent constitutive law used in dynamic modeling of fast rupture is the *linear slip-weakening law*. It is mainly used for simplicity and efficiency but captures the most dominant feature of fast rupture, the rapid decrease of traction with slip.

An important piece of the puzzle is the values of parameters of this constitutive law on seismic faults. Their extrapolation from laboratory experiments, typically conducted on scales much smaller than seismic faults and at low values of slip rate, is not straightforward. One method in which they can be uncovered is dynamic source inversion. Unlike the forward problem described in the previous paragraph, in which initial conditions and the constitutive law are used to obtain displacement on the ground, this is an inverse problem, which uses ground motion measurements (seismograms and/or GPS data) to infer the parameters of the constitutive law and the initial conditions on the fault.

However, the interpretation of the inversion results is not straightforward. The first issue is that neither the ground motion measurements nor the solutions of the forward problem are exact, due to, for example, seismogram errors, inaccuracies in the rheological model of the crust, imprecise geometry of the fault, numerical errors, etc. This leads to inaccuracy in the obtained model parameters. Another source of uncertainty is that a large (possibly infinite) number of models can fit seismic data equally well, which may lead to non-uniqueness of the inverse problem. A natural way to understand and quantify these uncertainties is to frame the inversion as a problem of Bayesian inference on the model parameters. In this approach, the result of the inversion is not a single model, but rather a joint probability density function on the space of model parameters. This function, called the *posterior probability density function*,

quantitatively describes the plausibility of every model.

The second issue, inherent to every inverse method, is that the results are strongly affected by the starting assumptions, be they implicit or explicit. An important part of these is the prior assumptions about the model parameters. A key feature of Bayesian inverse methods is that these initial assumptions can, indeed must, be clearly formulated, in the form of the *prior probability density function*. However, another set of assumptions is that on the forward problem itself. What if inversions that assume a particular class of dynamic models tend to be biased toward certain values of the initial stress or frictional parameters, regardless of the seismic data? For example, the condition that a fracture propagates at all will cause the inversion to select or prefer a certain subset of the model space, depending on the assumed constitutive law, fault geometry, etc. Bias may also appear when we constrain the models in a way that is independent of the seismogram time series observed at the stations, e.g., by requiring that they produce a given moment magnitude. In this thesis, we present a Bayesian dynamic inversion method in which we try to separate the effects of different constraints on the resulting posterior probability density function. We do this by calculating and quantitatively comparing multiple intermediate probability density functions, each of which corresponds to adding progressively more information to the inversion. We apply the method to the 2017 M_w 6.3 Lesvos, Greece earthquake.

The fast rupture process that generates seismic waves – the co-seismic phase of rupture - is but one portion of dynamic earthquake source modeling. Another important component is the slow and often complicated evolution of slip and stress between the earthquakes, the so-called inter-seismic phase. Unlike the first process, which is over in seconds to tens of seconds, the latter process may occur on the time scale of hundreds of years. Because of the vastly different time scales, it has been difficult to study the inter-seismic and the co-seismic phases in a unified manner. The most common constitutive law used to study the inter-seismic phase is the so-called *rate-and-state friction law*, a phenomenological frictional law derived from laboratory experiments conducted at low slip rates. The rate-and-state friction laws predict that under certain ideal conditions, faults undergo simply periodic seismic cycles, hosting large characteristic earthquakes separated by regular inter-seismic periods. However, when shear or normal stress on the fault is suddenly increased or decreased, the cycle is disturbed and the arrival of the next earthquake in the cycle is either hastened or delayed. In this thesis, we thoroughly examine the dependence of the earthquake occurrence time on the properties of the perturbation, in particular its timing during the cycle, and show that in some cases,

a very large delay can be induced, even for a positive stress perturbation. We numerically demonstrate that this mechanism could have been the cause of the significant delay of the M_w 6 2004 earthquake observed on the Parkfield segment of the San Andreas fault

The structure of the thesis

Chapters 1, 2, 3, and 4 comprise the theoretical background of the thesis. Original research is presented in chapters 5 and 6.

In chapter 1, we present the mathematical formulation of dynamic earthquake modeling, posing it as a problem in fracture mechanics. We also explain key terms and classifications.

In chapter 2, we review solutions to simple problems in brittle fracture mechanics. We discuss the results and features which generalize to constitutive problems.

In chapter 3, we review and discuss important properties of the earthquake models that use the slip-weakening constitutive law.

In chapter 4, we discuss the rate-and-state law, and in particular its application to modeling seismic cycles.

In chapter 5, published as Kostka & Gallovič (2016), we examine the effect of a sudden change of fault traction on the long-term behavior of seismic cycles. In some cases, these changes may significantly delay the arrival of the following large earthquake. We numerically demonstrate that such a mechanism could have contributed to the extreme delay of the 2004 Mw 6 Parkfield earthquake.

In chapter 6, an overwhelming part of which was published as Kostka et al. (2022), we use the slip-weakening law to perform a detailed Bayesian dynamic inversion of the 2017 Mw 6.3 Lesvos earthquake. We also present a method for distinguishing the importance of various constraints for the resolution of quantities characterizing the rupture.

Theoretical background

1 Formulation of the dynamic source problem and basic definitions

1.1 Introduction

In this chapter, we formulate a framework suitable for dynamic earthquake source modeling and review basic notions and classifications.

Let $\Omega \subset \mathbb{R}^3$ represent a referential configuration of a linearly elastic body at time $t = 0$. Points in this referential body are labeled by $\boldsymbol{x}$. The configuration of the body at time t is specified by a smooth, invertible mapping $\boldsymbol{\chi}_t : \Omega \to \mathbb{R}^3$, $\boldsymbol{x} \mapsto \tilde{\boldsymbol{x}} = \boldsymbol{\chi}_t(\boldsymbol{x})$. The vector field $\boldsymbol{u}(t, \boldsymbol{x}) = \boldsymbol{\chi}_t(\boldsymbol{x}) - \boldsymbol{x}$ is called *displacement*.

Let S be an oriented surface in Ω and let $\boldsymbol{\nu}_t$ denote a field of unit vectors normal to its image $\boldsymbol{\chi}_t(S)$ at time t. According to Cauchy's stress theorem, there exists, under mild conditions (Gurtin et al., 1968; Šilhavý, 1991), a second-order tensor field $\sigma(t, \boldsymbol{x})$ such that the *traction* (surface force density) $\boldsymbol{T}(t, \boldsymbol{x})$ on the $\boldsymbol{\nu}_t$ side of $\boldsymbol{\chi}_t(S)$ is given by

$$\boldsymbol{T}(t, \boldsymbol{\xi}) = \sigma(t, \boldsymbol{\xi}) \cdot \boldsymbol{\nu}_t(\boldsymbol{\chi}_t(\boldsymbol{\xi})) \; \forall \boldsymbol{\xi} \in S. \tag{1.1}$$

The tensor $\sigma(t, \boldsymbol{x})$ is called the Cauchy stress tensor.

We assume that the body is initially in static equilibrium and denote the initial stress tensor by $\sigma^0(\boldsymbol{x})$. The incremental stress tensor $\tau(t, \boldsymbol{x})$ is defined as

$$\tau(t, \boldsymbol{x}) = \sigma(t, \boldsymbol{x}) - \sigma^0(\boldsymbol{x}). \tag{1.2}$$

In the absence of body forces and when the spatial derivatives of the deviatoric part of σ^0 are negligible, the equation of motion in the body, correct to first order in the gradient of $\boldsymbol{u}$, can be written as (Martinec, 2019, ch. 9.6):

$$\rho(\boldsymbol{x})\partial_{tt}u_i(t,\boldsymbol{x}) = \tau_{ij,j}(t,\boldsymbol{x})\ \forall \boldsymbol{x} \in \Omega. \tag{1.3}$$

Under the approximation of linear elasticity, the stress increment is linearly related to the gradient of $\boldsymbol{u}$ through the fourth-order stiffness tensor c:

$$\tau_{ij}(t,\boldsymbol{x}) = c_{ijkl}(\boldsymbol{x})u_{k,l}(t,\boldsymbol{x}). \tag{1.4}$$

The tensor c has the symmetry $c_{ijkl} = c_{jikl}$. In general, it depends on the deviatoric part of σ^0. When the dependence on the deviatoric part of σ^0 is neglected, c has the additional symmetries $c_{ijkl} = c_{klij} = c_{ijlk}$ (Dahlen, 1972). As is common in classical seismology, we assume the infinitesimal strain theory, in which the undeformed and deformed configurations are not distinguished, and $\boldsymbol{x} \approx \tilde{\boldsymbol{x}}$, $\boldsymbol{\nu}_t(\boldsymbol{\chi}_t(\boldsymbol{\xi})) \approx \boldsymbol{\nu}(\boldsymbol{\xi})$, $\boldsymbol{\chi}_t(S) \approx S$.

The classical elastodynamic problem consists of finding a displacement field $\boldsymbol{u}(t,\boldsymbol{x})$ that i) solves Eqs. (1.3)-(1.4), ii) satisfies the initial conditions $\boldsymbol{u}(0,\boldsymbol{x}) = \boldsymbol{u}_0(\boldsymbol{x})$ and $\partial_t\boldsymbol{u}(0,\boldsymbol{x}) = \boldsymbol{v}_0(\boldsymbol{x})$ for $\forall \boldsymbol{x} \in \Omega$, and iii) satisfies specified boundary conditions on $\partial\Omega$. According to the classical linear-elastic uniqueness theorem (Knops & Payne, 1971; Aki & Richards, 2002), when the boundary $\partial\Omega$ is partitioned into two disjoints subsets on which either $\boldsymbol{u}$ or $\boldsymbol{T}$ is specified, and c is a positive-definite tensor (i.e. $A_{ij}c_{ijkl}A_{kl} > 0$ for all non-zero second-order tensors A), then the problem admits at most one solution. For isotropic elasticity, the latter requirement is equivalent to the conditions $\mu > 0$ and $-1 < \nu < 1/2$, where μ is the elastic shear modulus and ν is the Poisson's ratio (Knops & Payne, 1971).

To allow modeling tectonic earthquake sources, the above problem is modified by introducing a fixed two-dimensional simple oriented surface $\Gamma \subset \Omega$, the *fault*, across which $\boldsymbol{u}$ (but not $\boldsymbol{T}$) is allowed to be discontinuous. The discontinuity $\boldsymbol{s}$ of $\boldsymbol{u}$ across Γ is called *slip:*

$$\boldsymbol{s}(t,\boldsymbol{\xi}) = \lim_{\epsilon\to 0}[\boldsymbol{u}(t,\boldsymbol{\xi} + \epsilon\boldsymbol{n}(\boldsymbol{\xi})) - \boldsymbol{u}(t,\boldsymbol{\xi} - \epsilon\boldsymbol{n}(\boldsymbol{\xi}))],\ \boldsymbol{\xi} \in \Gamma, \tag{1.5}$$

where $\boldsymbol{n}$ is the field of unit vectors normal to Γ. Flipping the orientation of $\boldsymbol{n}$ corresponds to multiplying $\boldsymbol{s}$ by -1. Here, we adopt the convention that when we speak of traction and slip, we use the same orientation of $\boldsymbol{n}$.

Prescribing the slip $\boldsymbol{s}(t,\boldsymbol{\xi})$ at all times everywhere on the fault, we would obtain a *kinematic* (*dislocation*) *model* of rupture. In *dynamic models,* however, we leave the slip unspecified and instead postulate the existence of a (not necessarily connected) surface of fracture $\gamma(t) \subseteq \Gamma$

(Fig. 1.1). The set $\gamma(t)$ may be prescribed or it may dynamically evolve according to a specified crack-propagation criterion. We then prescribe mixed boundary conditions on Γ which require that:

1. No slip occurs outside of $\gamma(t)$:

$$\boldsymbol{s}(t,\boldsymbol{\xi}) = \mathbf{0} \ \forall \boldsymbol{\xi} \in \Gamma \backslash \gamma(t). \tag{1.6}$$

2. The traction within $\gamma(t)$ is constrained by a constitutive law of the form:

$$\boldsymbol{T}(t,\boldsymbol{\xi}) \in \mathcal{T}\left(t,\boldsymbol{\xi}, p_1(t,\boldsymbol{\xi}), p_2(t,\boldsymbol{\xi})..., p_n(t,\boldsymbol{\xi})\right) \ \forall \boldsymbol{\xi} \in \gamma(t). \tag{1.7}$$

   Here, $\mathcal{T}$ is the set of admissible tractions on the crack and p_i are scalar or vector fields. The most important examples of p_i include the slip $\boldsymbol{s}$, slip rate $\dot{\boldsymbol{s}}$, normal stress

$$\sigma_n := \boldsymbol{T} \cdot \boldsymbol{n} = \boldsymbol{n} \cdot \sigma \cdot \boldsymbol{n}, \tag{1.8}$$

   temperature, porosity, or abstract scalar variables that characterize the state of the sliding interface. Note that the constraint is imposed on the total traction, not only on the traction increment.

For simplicity, it is often assumed that the fault Γ is straight and very long or infinite along one direction (which we take here, without loss of generality, to be the y-axis) and the displacement depends on only two spatial coordinates that span the plane perpendicular to this direction (which we take to be x and z). When $\boldsymbol{u}(t,x,z) = (u_x(t,x,z), 0, u_z(t,x,z))$ we speak of plane strain. When $\boldsymbol{u}(t,x,z) = (0, u_y(t,x,z), 0)$ we speak of anti-plane strain. Alternatively, the traction on the planes perpendicular to the y-axis can be assumed zero, which is appropriate for thin plates with free surfaces, this state is called plane stress. In all these cases, the problem can be studied on a cross-section C perpendicular to the y-axis (e.g., the $x-z$ plane), so it effectively reduces to a 2-D problem. As is common in literature, we refer to these cases simply as 2-D problems, although, strictly speaking, they still take place in a 3-D body (and the definition of anti-plane strain even requires 3 spatial dimensions).

The above framework is used in many studies concerning dynamic earthquake source physics. However, modeling of fracture and friction is a vast field of mechanics, and we only barely scratch the surface. The limitations and assumptions behind the above formulation include:

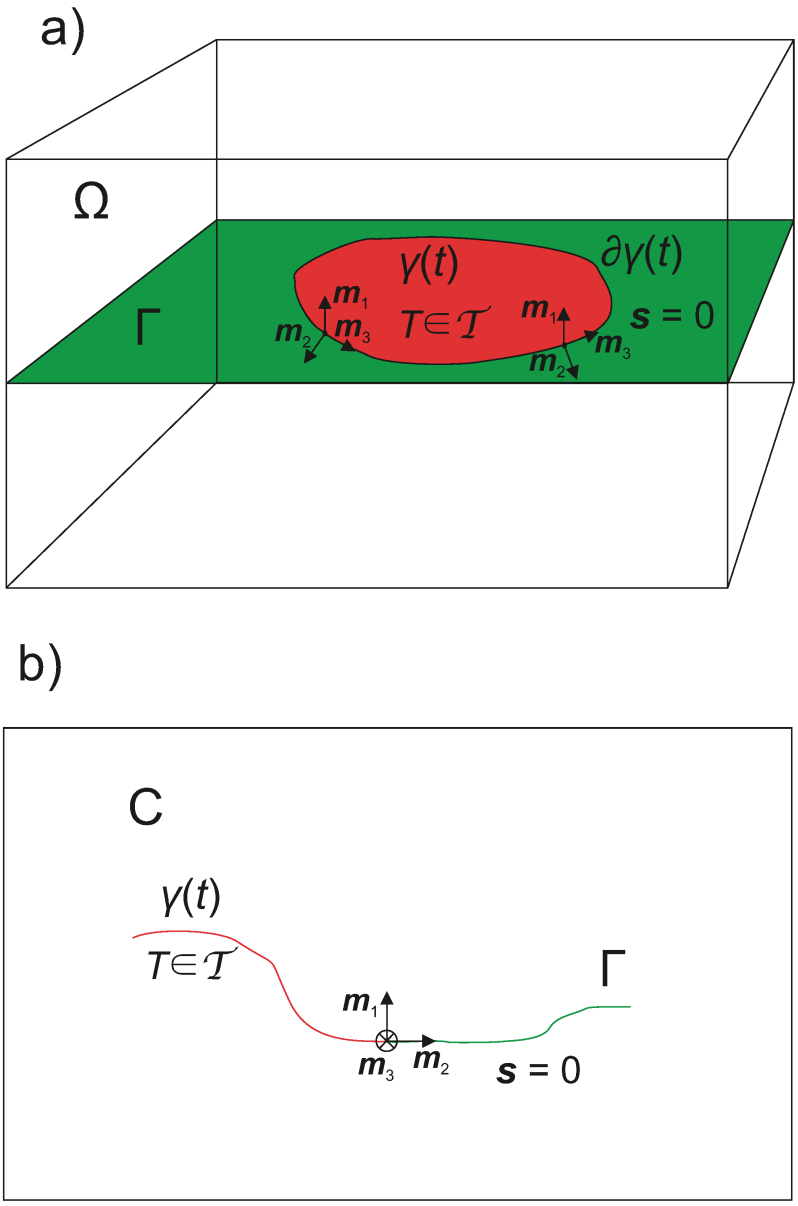

Figure 1.1: a) Crack $\gamma(t)$ at time t on fault Γ contained in a three-dimensional elastic body Ω. Slip $\boldsymbol{s}$ outside of $\gamma(t)$ is zero. The traction $\boldsymbol{T}$ within $\gamma(t)$ is constrained by the constitutive law $\boldsymbol{T} \in \mathcal{T}$. The boundary $\partial\gamma(t)$ between $\gamma(t)$ and $\Gamma/\gamma(t)$ is called the crack edge or the crack front. The fracture propagation modes I, II, and III correspond to the slip being proportional to the vectors $\boldsymbol{m}_1$, $\boldsymbol{m}_2$, and $\boldsymbol{m}_3$, respectively. b) The cross-section C of a three-dimensional body Ω for the effectively two-dimensional case, in which both the fault Γ and the crack $\gamma(t)$ (unrelated to Fig. a) are assumed to extend straight in a direction perpendicular to the picture and field variables depend only on time and two spatial coordinates that span C. The projection of the crack edge on C is called the crack tip.

1. The whole fracture is confined to the prescribed surface Γ. For 2-D problems, this implies that the crack $\gamma(t)$ proceeds along a predetermined path. For 3-D problems, this corresponds to fracture on a predefined fault, without the generation of new faulting surfaces. Constraining the problem this way makes it easier to solve, as it reduces the dimensionality of the crack (in the sense that $\gamma(t)$ may be described by a predefined set of $n-1$ coordinates for all t), and allows using less complex criteria for the crack growth. It is justified when we are modeling a fracture problem on a (retrospectively) known surface, on faults confined by large lithostatic stress, on surfaces with weak (relative to their surroundings) fracture resistance, or when modeling friction during sliding of pre-cut surfaces. As recent alternatives, we mention the models of Preuss et al. (2019, 2020), and Okubo et al. (2020) that include a predefined main fault and allow its spontaneous growth or creation of secondary branches in its vicinity.

2. The fracture may accurately be modeled using continuum mechanics. Alternatives include molecular dynamics models (Rountree et al., 2002; Brochard et al., 2016), lattice models (Pan et al., 2017), discrete element methods (Scholtès & Donzé, 2012; van den Ende, 2018), cellular automata models (Burridge & Knopoff, 1967; Gobron & Chiba, 2001; Castellaro & Mulargia, 2001), and large-scale models such as RSQSim (Dieterich & Richards-Dinger, 2010; Richards-Dinger & Dieterich, 2012) in which time evolution is realized by transitions between discrete states of large blocks ($\sim$km), allowing to efficiently model whole fault systems.

3. The medium outside of the crack surface is linearly elastic. We do not consider off-fault damage (Xu et al., 2014; Thomas et al., 2017; Okubo et al., 2020), non-local elasticity (Polizzotto, 2002), viscosity (Allison & Dunham, 2018; Miyake & Noda, 2019), plasticity (Templeton & Rice, 2008; Dunham et al., 2011; Erickson et al., 2017) or porosity (Viesca et al., 2008).

4. The fracture is modeled as a discontinuity in displacement, sharply localized to a surface of zero volume measure. In the seismological context, this may be justified by geological observations indicating that most slip is accommodated along *principle fracture zones* which are relatively thin (on the order of mm-cm, Sibson, 2003) compared to the observational scale and resolution available in numerical models. Among alternatives to this is the approach of *continuum damage mechanics*, which is concerned with modeling defects

such as pores, voids, and microcracks (Lyakhovsky & Ben-Zion, 2014; Altenbach & Öchsner, 2020). These are represented by damage variables that affect macroscopic material properties of the medium (e.g., decrease its effective shear modulus and induce nonlinear elasticity). Another alternative to the discontinuous model is diffuse models such as the *phase-field fracture* model, in which the displacement is continuous everywhere and fracture is instead characterized by an additional scalar field localized in a small band of finite thickness. This *phase-field* can take continuous values between 0 and 1, representing intact and completely broken material, respectively (Wu et al., 2019). Both the displacement and the phase-field jointly evolve according to equations of motion which can be naturally obtained in variational formulations by including their energetic contribution to the action functional (or to the potential energy for quasi-static problems) and using the continuum version of Hamilton's principle (Bedford, 1985; Bourdin et al., 2008). This contribution depends, among others, on the gradient of the phase-field, which gives rise to second-order spatial derivatives of the phase-field in the governing equations. A different example of a diffuse model is that of Gabriel et al. (2021), which also includes scalar phase fields but is instead governed by a complicated system of first-order partial differential equations.

5. The model is *deterministic*, as opposed to *stochastic* models in which some aspects of the material failure are described probabilistically. One of the simplest models in this class is *fiber-bundle* models in which discrete cells (fibers) are arranged on a lattice and are assigned random failure thresholds, along with post-failure redistribution rules for stress (Moreno et al., 2001; Monterrubio-Velasco et al., 2019). For example, the stress may be transferred only to the nearest neighbors of the failed fiber or shared equally among all remaining fibers. In *random fuse networks* (De Arcangelis et al., 1985; Zapperi et al., 2005), suitable for anti-plane strain, an analogy is made between the displacement and voltage, stress and current, and Hooke's law and Ohm's law. In the simplest form, fracture is modeled as an electrical system composed of fuses with linear $I - V$ curves which burn out when the current density in them surpasses a threshold, sampled from a random distribution. When a fuse fails, the current (stress) is redistributed according to Kirchhoff's circuit laws. For an extensive treatment of the statistical approach to fracture, we refer the reader to Alava et al. (2006) or Biswas et al. (2015).

In the rest of this section, we build on the presented formulation to explain important classi-

fications and notions in earthquake and fracture mechanics.

1.2 Fracture propagation modes

Following G. R. Irwin (1958), the direction of slip $\boldsymbol{s}(t, \boldsymbol{\xi})$ at a given time t and point $\boldsymbol{\xi}$ on the crack front $\partial\gamma(t)$ is often decomposed into three special *crack propagation modes*. These correspond to the following mutually orthogonal unit vectors (Fig. 1.1): 1) the normal $\boldsymbol{m_1}(\boldsymbol{\xi}) = \boldsymbol{n}(\boldsymbol{\xi})$ to the fault Γ at $\boldsymbol{\xi}$, 2) the vector $\boldsymbol{m_2}(\boldsymbol{\xi})$ orthogonal to both $\boldsymbol{m_1}(\boldsymbol{\xi})$ and the crack front and pointing away from the crack and 3) the vector $\boldsymbol{m_3}(\xi) = \boldsymbol{m_1}(\boldsymbol{\xi}) \times \boldsymbol{m_2}(\boldsymbol{\xi})$ tangent to the crack front:

1. $\boldsymbol{s} \parallel \boldsymbol{m_1}$: Mode I, also called the *opening* or *tensile* mode. It causes separation between the two faces of the crack. It is by far the most common mode in engineering structures (Broberg, 1999; Stephens et al., 2000) and the easiest to produce in laboratory settings. In homogeneous solids, crack naturally tend to turn into this mode (Rosakis, 2002). For these reasons, it is the most thoroughly studied propagation mode in fracture mechanics. This is rather unfortunate for earthquake physics because the importance of this mode is limited in the Earth's crust due to high lithostatic pressure, which prevents crack opening and favors fracture propagation in the other two modes (Melin, 1986; Udias et al., 2013). However, mode I fracture may occur in places with large fluid pore pressure (Vavryčuk, 2002; Saraò et al., 2010), which acts against the lithostatic pressure. They don't seem to play a crucial role for tectonic earthquakes and are usually not considered in dynamic earthquake modeling. Consequently, we mostly avoid discussing this mode in the thesis.

2. $\boldsymbol{s} \parallel \boldsymbol{m_2}$: Mode II, also called the *in-plane* shear mode, or the *sliding* mode. For a moving crack, this mode corresponds to slip in the direction of the crack velocity. For 2-D fracture in isotropic elastic media, this mode generates displacement with pure P-SV polarization (Aki & Richards, 2002).

3. $\boldsymbol{s} \parallel \boldsymbol{m_3}$: Mode III, also called *anti-plane* shear mode, or the *tearing* mode. For 2-D fracture in isotropic elastic media, this mode generates pure SH polarized displacement. Since this displacement is described by a single component, this mode is often the simplest to analyze.

Some authors (e.g., Broberg, 1999) require additional symmetries for displacement and stress, but for our purposes, this classification suffices. Note that the definitions require a preexisting crack. However, they do not require that the crack front be moving.

Examples of mode I fracture include splitting wood with an ax, pulling apart a thin pre-cut piece of paper or advancing open scissors through it. Using the scissors to cut into the paper in the usual way is an example of mode III. Puncturing the paper with a hole-puncher produces mode II fracture (Davies et al., 1994). Good examples of shear modes are provided by earthquake faulting - for pure strike-slip, a horizontally spreading fracture is in mode II and a vertically spreading fracture is in mode III. For pure dip-slip, the situation is reversed. For the case of a self-similarly expanding circular crack with slip oriented in the direction of 0° everywhere along the perimeter of the crack, the fracture is locally in mode II at 0°and 180° and in mode III at 90° and 270°. In all other directions, the rupture mode is mixed.

1.3 Constitutive laws

In this section, we discuss important special forms of the constitutive law (1.7): ideal brittle and cohesive models of fracture.

1.3.1 Ideally brittle fracture

When the traction right behind the crack edge sharply drops, so that the body is perfectly elastic until fracture, we speak of *ideal elastic brittle fracture* (also referred to as *brittle fracture* in the following text for the sake of brevity). In the simplest case,

$$\mathcal{T} = \{\mathbf{0}\}, \tag{1.9}$$

which corresponds to a sudden and total loss of cohesion on the crack. This is appropriate for mode I fracture, in which the faces of the crack get spatially separated. For the shear modes II and III, the cracks remain in frictional contact, so that the stress instead drops to *dynamic friction* $\boldsymbol{T}_d$:

$$\mathcal{T} = \{\boldsymbol{T}_d\}. \tag{1.10}$$

The field of mechanics developed to study brittle fracture in ambient linearly elastic media is called *Linear Elastic Fracture Mechanics* (LEFM). Prior to the 1960s, most concepts and problems in fracture mechanics were developed in the framework of LEFM (Anderson, 2017). An essential result due to Wieghardt (1907), rediscovered by Irwin (1957) (see Yarema, 1996; Gross, 2014), is that for each propagation mode, the stress field at the tip of static brittle cracks in 2-D is inverse square root singular, having the form

$$\begin{aligned} \tau_{ij}(r,\theta) &= \tau_{ij}^{S}(r,\theta) + \mathcal{O}(1) \\ &= \frac{K}{\sqrt{2\pi r}} q_{ij}(\theta) + \mathcal{O}(1), \end{aligned} \tag{1.11}$$

where r is the distance from the crack tip and q_{ij} are universal functions of the polar angle θ, independent of the geometrical configuration, applied loads, or elastic constants. The last three are instead encoded in the factor of proportionality K, the *stress-intensity factor*. Because the singular field is dominant at short distances from the crack tip, the stress-intensity factor is a very important quantity in fracture mechanics. Eq. (1.11) is also valid for dynamic cracks propagating below the shear velocity, but the stress-intensity factor is then additionally a function of time and the speed of the crack (Freund, 1990).

For mixed-mode fracture in 3-D, the singular part of the stress tensor at a point $\boldsymbol{\eta}$ near a point $\boldsymbol{\xi} \in \partial\gamma(t)$ can be written as (Hartranft & Sih, 1977):

$$\tau_{ij}^{S}(r,\theta,\phi) = \sum_{m\in\{I,II,III\}} \frac{K_m(\boldsymbol{\xi})}{\sqrt{2\pi r}} q_{ij}^{m}(\theta,\phi), \tag{1.12}$$

where K_m and q_{ij}^m are the stress-intensity factors and angular functions, respectively, for mode m, and (r,θ,ϕ) are spherical coordinates of the vector $\boldsymbol{\eta} - \boldsymbol{\xi}$, with origin at $\boldsymbol{\xi}$. The stress-intensity factors may vary along $\partial\gamma(t)$. They can be explicitly defined as:

$$K_m(\boldsymbol{\xi}) = \lim_{r\to 0^+} \sqrt{2\pi r}\boldsymbol{T}(\boldsymbol{\xi} + r\boldsymbol{m_2}) \cdot \boldsymbol{m}_m(\boldsymbol{\xi}). \tag{1.13}$$

Since unbounded stress is unphysical, some inelastic processes are necessarily present in real rupture. In LEFM, the domain of this inelasticity, *the cohesive zone*, is considered negligible in comparison to the modeling scale - a condition called *small-scale yielding*. When the problem is examined at smaller scales at which the inelastic behavior is important, the results of LEFM may still be used as a condition on the far field behavior of the solution (Freund, 1990). The

elastic uniqueness theorem may be extended to dynamic plane brittle crack problems, provided that the total mechanical energy of the body-crack system is finite (Freund & Clifton, 1974). Simple brittle problems are reviewed in chapter 2.

1.3.2 Cohesive models of fracture

When the traction on the crack front does not drop to the residual value instantly, but instead over a cohesive zone of finite length, we speak of *cohesive models*. The concept of the cohesive zone was introduced by Barenblatt (1959) and Dugdale (1960) for mode I fracture. Its inclusion allows regularizing the singular solutions found in ideally brittle fracture mechanics.

Cohesive models are applicable for both the tensile and the shear modes of fracture, but the physical mechanisms are different. Specifically, the cohesive zone in mode I fracture is due to bonding forces between atoms. As the surfaces lose contact with each other, the force quickly vanishes and the size of the cohesive zone is very small. In contrast, in the shear modes of fracture, the surfaces remain in frictional contact and strongly interact with each other, which means that the cohesive zone tends to be larger and geometric irregularities of the sliding surfaces play a greater role (Ohnaka, 2013).

Fractional and frictional processes may coexist in the cohesive zone. Sometimes, the physical distinction between friction and cohesive fracture may not even be meaningfully defined. For example, one proposed mechanism of friction in brittle materials is fracturing of contact asperities (Byerlee, 1967; Aghababaei & Budzik, 2020; Malekan et al., 2021). Since both phenomena can be described with the constitutive law formalism, the language of friction and fracture tends to be used interchangeably in studies on dynamic simulations. For example, the linear slip-weakening law reviewed below in subsection 1.3.2.1 may describe an originally intact material that starts fracturing when local stress reaches the yield stress and then progressively loses all cohesion except for friction between the two newly created surfaces, or it may describe a frictional process on two already precut surfaces in which friction continuously drops from static to dynamic values. One important difference is that for fracture, the fault plane Γ may evolve spontaneously, while in frictional models, it is determined from the outset. However, we exclude the former case by assumption, so the two cases are equivalent here.

Two classes of the constitutive law (1.7) are particularly common in earthquake physics models: the slip-dependent laws used primarily for modeling fast rupture and the rate-and-

state laws used mainly for modeling long-term (hundreds and thousands of years) behavior of faults. In both cases, it is often assumed (e.g., Andrews, 1976b,a; Madariaga et al., 1998; Day et al., 2005; Daub & Carlson, 2008; Premus et al., 2020) that the shear stress

$$\boldsymbol{T}_s := \boldsymbol{T} - \sigma_n \boldsymbol{n} = \boldsymbol{T} - (\boldsymbol{n} \cdot \boldsymbol{T})\boldsymbol{n} \tag{1.14}$$

acts against the shear slip rate

$$\boldsymbol{s}_s := \boldsymbol{s} - (\boldsymbol{n} \cdot \boldsymbol{s})\boldsymbol{n} \tag{1.15}$$

during sliding, so that:

$$\mathcal{T}(t, \boldsymbol{\xi}, ...) = \left\{ \boldsymbol{T} : \boldsymbol{T}_s = -F(t, \boldsymbol{\xi}, ...) \frac{\dot{\boldsymbol{s}}_s(t, \boldsymbol{\xi})}{\|\dot{\boldsymbol{s}}_s(t, \boldsymbol{\xi})\|} \right\} \quad \forall \boldsymbol{\xi} \in \gamma(t) : \dot{\boldsymbol{s}}_s(t, \boldsymbol{\xi}) \neq \boldsymbol{0}, \tag{1.16}$$

where the function F is called *shear strength*, and the ellipses represent the dependence on the fields $p_1(t, \boldsymbol{\xi}), ..., p_n(t, \boldsymbol{\xi})$. When $\dot{\boldsymbol{s}}_s = \boldsymbol{0}$, only the condition that the magnitude of $\boldsymbol{T}_s$ is bounded by the shear strength is imposed:

$$\mathcal{T}(t, \boldsymbol{\xi}, ...) = \{ \boldsymbol{T} : \|\boldsymbol{T}_{\boldsymbol{s}}(t, \boldsymbol{\xi})\| \leq F(t, \boldsymbol{\xi}, ...) \} \quad \forall \boldsymbol{\xi} \in \gamma(t) : \dot{\boldsymbol{s}}_s(t, \boldsymbol{\xi}) = \boldsymbol{0}. \tag{1.17}$$

We discuss the slip-dependent and rate-and-state laws below. For simplicity, we assume that the normal component of slip is zero, so that $\boldsymbol{s} = \boldsymbol{s}_s$. For an extensive discussion of various constitutive laws, we refer the reader to Bizzarri (2011).

1.3.2.1 Slip-dependent laws

The slip-dependent cohesive laws were first introduced by Barenblatt (1959, 1962) for tensile (mode I) cracks, where they model the dependence of cohesive forces on the separation of the broken surfaces. They were mathematically introduced to the shear crack problems by Ida (1972). A strong dependence of traction on slip was later corroborated by laboratory experiments (Okubo & Dieterich, 1984; Ohnaka & Yamashita, 1989; Hirose, 2005) and studies based on kinematic earthquake source inversions (e.g., Ide & Takeo, 1997; Tinti et al., 2005; Abercrombie & Rice, 2005; Burjánek & Zahradník, 2007)

The simplest slip-dependent law is probably the step slip-weakening law, to which Dunham

(2007) refers to as the Dugdale model:

$$F(\|\boldsymbol{s}\|) \coloneqq \begin{cases} T_u & \text{for } 0 \leq \|\boldsymbol{s}\| \leq D_c \\ T_d & \text{for } \|\boldsymbol{s}\| > D_c \end{cases}. \tag{1.18}$$

Here, T_u is the *yield strength*, T_d is dynamic friction and D_c is the *characteristic slip-weakening distance*. The difference $\Delta\sigma_{br}$ between the yield strength T_u and dynamic friction T_d is called the *breakdown stress drop*. This model is mostly used for simplicity as it facilitates certain analytic calculations (Ida & Aki 1972; Fialko 2007; Dunham 2007).

The simplest model with a gradual decrease from T_u to T_d is the piecewise *linear slip-weakening* (linear softening) law, introduced formally by Ida (1972) and first utilized for rupture modeling by Andrews (1976a,b). It has the form

$$F(\|\boldsymbol{s}\|) \coloneqq \begin{cases} (T_u - T_d)(1 - \|\boldsymbol{s}\|/D_c) + T_d & \text{for } 0 \leq \|\boldsymbol{s}\| \leq D_c \\ T_d & \text{for } \|\boldsymbol{s}\| > D_c \end{cases}. \tag{1.19}$$

It is the most common law employed in earthquake modeling, even though it has no proper empirical support in laboratory experiments. Moreover, for a 2-D infinite anti-plane crack with prescribed velocity, this law, just as Eq. (1.18) and many other piecewise polynomial laws, leads to infinite slip acceleration (Ida, 1973). Nevertheless, it is simple to use and captures the observed decrease of traction at larger values of slip (Ohnaka & Yamashita, 1989; Hirose, 2005; Sone & Shimamoto, 2009; Ohnaka, 2013). We are also not aware that the issue of infinite slip acceleration persists in spontaneous 3-D problems.

The linear slip-weakening law was originally formulated under the assumption of fixed direction of slip, so that slip only had one degree of freedom. The dependence on the magnitude of slip $\|\boldsymbol{s}\|$ presented above is just one way to generalize that situation to 3-D. Another possibility (Day, 1982; Day et al., 2005; Bizzarri, 2014) is to replace $\|\boldsymbol{s}\|$ with the *slip-path length* $\mathfrak{s}$:

$$\mathfrak{s}(t, \boldsymbol{\xi}) = \int_0^t |\dot{\boldsymbol{s}}(t', \boldsymbol{\xi})| dt'. \tag{1.20}$$

In this version, if the slip vector makes a round trip along a closed curve, the resulting shear strength is weaker than the initial strength. In the version that depends only on the magnitude, the shear strengths would be identical.

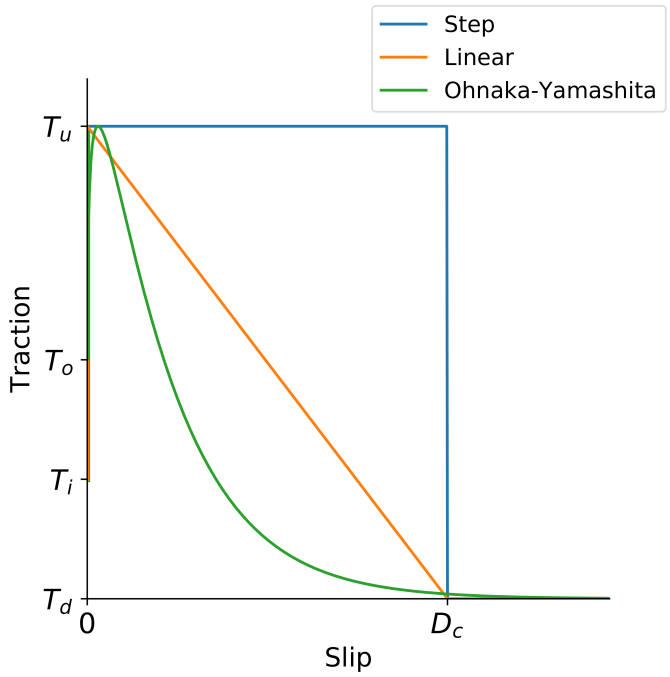

Figure 1.2: Examples of slip-dependent constitutive laws. T_u, T_i, and T_d are the yield strength, initial magnitude of traction, and dynamic friction, respectively. T_o is the value of traction at the onset of slip for the Ohnaka-Yamashita law. D_c is the characteristic slip-weakening distance. The area between each slip-dependent curve and the line $y = T_d$ is the corresponding fracture energy surface density G_c.

As an example of a law based on laboratory rock observations, we mention the one proposed by Ohnaka & Yamashita (1989) that reads:

$$F(\|\boldsymbol{s}\|) = (T_o - T_d)\,[1 + \alpha \ln(1 + \beta\|\boldsymbol{s}\|)] \exp(-\|\boldsymbol{s}\|/d) + T_d. \tag{1.21}$$

Here, α and β are positive constants and the term in the brackets corresponds to an initial slip-strengthening phase in which traction increases with slip from the value of T_o at the onset of slip to a peak value which is attained some distance behind the crack front. This strengthening phase usually ends at a very small value of slip as the exponential weakening term starts to dominate. The traction finally decreases to the dynamic value of T_d. The linear slip-weakening model (1.19) may be understood as an approximation of (1.21) when the short strengthening phase is neglected and the exponential decrease is replaced by a linear one.

Explicit dependence on the spatial coordinate, i.e. $F = F(\boldsymbol{\xi}, \boldsymbol{s}(t, \boldsymbol{\xi}))$, may be introduced in

the above laws by allowing heterogeneous distributions of parameters. For example, local areas of large T_u may act as barriers to rupture (Madariaga & Olsen, 2000; Page et al., 2005) and heterogeneous distribution of D_c may be used to model the roughness of the sliding surfaces (Ide & Aochi, 2005).

Another possible extension, common when modeling friction, is to make F explicitly depend on the normal stress σ_n:

$$F(\boldsymbol{\xi}, \boldsymbol{s}(t,\boldsymbol{\xi}), \sigma_n(t,\boldsymbol{\xi})) = \sigma_n(t,\boldsymbol{\xi}) f(\boldsymbol{\xi}, \boldsymbol{s}(t,\boldsymbol{\xi})). \tag{1.22}$$

The quantity f in this factorization is called the *coefficient of friction*.

A potential disadvantage of slip-dependent laws is that they do not allow for fault restrengthening and modeling long-term evolution of faults (e.g., seismic cycles). This can be fixed by enriching the laws with a suitable explicit dependence on time (Aochi & Matsu'ura, 2002; Bizzarri, 2012).

1.3.2.2 Rate-and-state dependent friction laws

The rate-and-state (RS) friction laws were postulated to explain the behavior of friction acting on precut rock surfaces mutually sliding at low values of slip rate ($\lessapprox 1$ mm/s) (e.g. Scholz et al., 1972; Dieterich, 1972, 1979; Scholz & Engelder, 1976; Johnson, 1981). Two types of experiments were particularly important for their establishment. In the *velocity stepping* tests (Dieterich, 1979; Marone et al., 1990; Bhattacharya et al., 2015; Bohloli et al., 2020) a rock specimen is sheared under externally imposed constant normal stress and slip rate. After some time, the shear stress reaches a steady-state value. When the imposed slip rate is abruptly changed, the coefficient of friction jumps in proportion to the difference in logarithms of the new and the old slip rate. After the jump, it is observed that the shear stress starts evolving towards a new steady-state value that depends on the new slip rate. The second type of founding experiments are the *slide-hold-slide* tests (e.g., Dieterich, 1972; Johnson, 1981; Beeler et al., 1994; Marone, 1998b; Renard et al., 2012; Marone & Saffer, 2015), in which a steadily sliding block is (almost) stopped for some time Δt and then forced to slide again. For a wide variety of materials, it was observed that the "static" coefficient of friction (the traction at the onset of sliding) increases approximately in proportion to the logarithm of Δt. This is probably caused by an increase in the area of contact between the two surfaces (Dieterich & Kilgore, 1994)

and adhesive effects (Renard et al., 2012). To model the described behavior, it was proposed (Dieterich 1979; Ruina 1983; in a somewhat different but equivalent form) to use the following constitutive law (denoting $V := \|\dot{\boldsymbol{s}}\|$):

$$F(\sigma_n, V, \theta) = \sigma_n f(V, \theta), \tag{1.23}$$

with the coefficient of friction $f(V, \theta)$ given by:

$$f(V, \theta) = f^* + a \ln \frac{V}{V^*} + b \ln \frac{V^* \theta}{L}, \tag{1.24}$$

where f^*, V^*, a, b and L are positive (and possibly position dependent) parameters. The first term of Eq. (1.24), f^*, is simply a referential value of the coefficient of friction such that $\sigma_n f^*$ is the friction measured when two surfaces are steadily sliding over another at the constant referential slip rate V^*. The second term models the direct velocity (slip rate) effect observed in the velocity-stepping tests. The third term describes the evolutionary behavior - the gradual increase of static friction and the relaxation to the steady-state - which cannot be explained by a purely rate-dependent law. They are encoded in the *state variable* $\theta(t)$ which figures in the third term. The state variable evolves with time according to an evolution law which is a first-order ordinary differential equation for $\theta(t)$:

$$\frac{d\theta}{dt} = H(V, \theta), \tag{1.25}$$

where $H(V, \theta)$ is a differentiable function of V and θ.

The two most popular evolution laws are the *aging* law (Ruina, 1980, 1983):

$$H(V, \theta) = 1 - \frac{V\theta}{L} \tag{1.26}$$

and the *slip* law (Dieterich, 1979; Kosloff & Liu, 1980):

$$H(V, \theta) = -\frac{V\theta}{L} \ln \frac{V\theta}{L}. \tag{1.27}$$

Neither of these laws can perfectly explain all qualitative features of the experiments, see Marone (1998a) for a thorough review. The aging law better describes healing behavior at small velocities (as $V \to 0$, the state variable correctly grows with time, whereas the slip law

predicts zero evolution), but it doesn't reproduce symmetric relaxation of stress after positive and negative velocity jumps observed in experiments, which the slip law does perfectly. The slip law also generally better predicts behavior at the stepping tests (Bhattacharya et al., 2015). Many other laws have been proposed (e.g., Linker & Dieterich, 1992; Perrin et al., 1995; Kato & Tullis, 2001; Nagata et al., 2012; Molinari & Perfettini, 2017), but there does not yet seem to be consensus on the correct formulation.

A potentially startling feature of the law (1.24) is that the friction diverges to negative infinity as $V \to 0$ or $\theta \to 0$. This is not necessarily a problem in numerical simulations, since these quantities may be kept high enough everywhere on the fault by setting up suitable initial conditions. Nevertheless, regularized versions are sometimes used instead (e.g., Perrin et al., 1995; Rice & Ben-Zion, 1996; Daub & Carlson, 2008; Lapusta et al., 2000). One such regularization, based on a model of energetically activated forward and backward jumps at asperity contacts of the sliding rocks (Lapusta et al., 2000), reads

$$f(V,\theta) = a \sinh^{-1}\left(\frac{V}{2V^*}\exp\left(\frac{f^* + b\ln(V^*\theta/D_c)}{a}\right)\right). \tag{1.28}$$

The great advantage of the RS law is that it allows modeling many features of the fault behavior, such as nucleation, propagation, arrest, healing, triggering, aseismic creep, slow earthquakes, etc., in a unified manner (see chapter 4), which is very convenient for numerical modeling. The whole fault is usually considered to be slipping, i.e. $\gamma(t) = \Gamma \ \forall t$ (so only the sliding part of the constitutive law, Eq. (1.16), needs to be considered), but the slip rate at certain parts of the fault is so slow that they are effectively locked. The boundary between the effectively locked and slipping parts can be understood as the crack edge and its evolution can be modeled without supplying any explicit fracture criterion. On the other hand, the scope of validity of the RS friction laws is limited by the fact that the experiments that motivated them were performed under small slip rates, in the range of $\approx 10^{-8} - 10^{-3}$ m/s. This is several orders lower than co-seismic slip rates, which may be as large as $\approx 10^{1}$ m/s (McGarr, 2003). Experiments at slip rates larger than $\approx 10^{-3}$ m/s showed that steady-state friction rapidly decreases with slip rate as co-seismic slip rates are reached, an effect which has been attributed to heating due to the shearing motion (see e.g., Hirose, 2005; Beeler et al., 2008; Di Toro et al., 2011; Goldsby & Tullis, 2011; Aharonov & Scholz, 2018). In addition, at seismic speeds, the RS laws behave similarly to the linear slip-weakening law, which is simpler to use. Therefore, the RS laws are better suited to simulate quasi-static and long-term evolution of faults, although

modifications have been developed that take the fast velocity weakening effect into account (Ampuero & Ben-Zion, 2008; Dunham et al., 2011; Gabriel et al., 2012; Zelst et al., 2019; etc.).

1.4 Spontaneous and prescribed rupture propagation

In *spontaneous rupture* problems, the shape of $\gamma(t)$ is not prescribed in advance but instead evolves dynamically according to a pre-defined fracture propagation criterion. The evolution of $\gamma(t)$ is therefore obtained as a part of the complete solution of the fracture problem. We discuss some fracture criteria in the following section.

Only few analytic solutions for spontaneous problems are known. The evolution of infinite, straight (effectively 2-D) spontaneous brittle cracks is briefly discussed in chapter 3. No analytic solutions seem to exist for finite spontaneous 3-D rupture problems. This makes intuitive sense when we consider the complex pattern of elastic wave diffraction at the crack front. The waves are affected by the crack front shape and position and themselves influence it. Spontaneous cracks modeled with the slip-weakening friction are discussed in chapters 3 and 6.

The fracture problem is significantly simplified when the shape of $\gamma(t)$ is pre-assigned, so boundary conditions at each time are known a priori. Despite such simplification, only special types of prescribed propagation problems are typically amenable to analytic solutions:

When the inertial term $\rho\partial_{tt}\boldsymbol{u}$ in Eq. (1.3) is neglected and no time-dependence is present in the boundary conditions (including those on the fault, i.e. $\gamma(t) = \gamma(0)\ \forall t > 0$, $\partial_t F = 0$), so that

$$\boldsymbol{u}(t, x, y, z) = \boldsymbol{u}(x, y, z) \tag{1.29}$$

we speak of a *static* problem. When only the inertial term is neglected, but time dependence in boundary conditions is allowed, we speak of *quasi-static* problems.

If it is assumed that the displacement can be written, for some spatial coordinates $\{x, y, z\}$, as

$$\boldsymbol{u}(t, x, y, z) = \boldsymbol{u}(x - vt, y, z), \tag{1.30}$$

for a constant crack speed v, we speak of *steady-state* (or just steady) problems.

Finally, when the displacement is sought under the constraint that it is a homogeneous

function of degree n, i.e. it satisfies

$$\boldsymbol{u}(\zeta t, \zeta x, \zeta y, \zeta z) = \zeta^n \boldsymbol{u}(t, x, y, z), \ \forall \zeta > 0 \tag{1.31}$$

we speak of *self-similar problems* (Willis, 1973; Nielsen & Madariaga, 2003). Specifically, taking $\zeta = t_0/t$ for an arbitrary but fixed $t_0 > 0$, this condition can be written as:

$$\boldsymbol{u}(t_0, t_0 x/t, t_0 y/t, t_0 z/t) = (t_0/t)^n \boldsymbol{u}(t, x, y, z). \tag{1.32}$$

Therefore, the solution satisfies (suppressing the explicit dependence on t_0):

$$\boldsymbol{u}(t, x, y, z) \propto t^n \tilde{\boldsymbol{u}}(x/t, y/t, z/t), \tag{1.33}$$

where $\tilde{\boldsymbol{u}}(x/t, y/t, z/t)$ is a dimensionless function of the quantities x/t, y/t and z/t. The degree n can be constrained by regularity conditions. For example, requiring that the displacement or the velocity remains finite as $t \to 0$ and $t \to \infty$ fixes n to 0 or 1, respectively. Self-similar cracks have the form $\gamma(t) = \left\{ \frac{t}{t_{ref}} \boldsymbol{\xi}_{ref}; \boldsymbol{\xi}_{ref} \in \gamma(t_{ref}) \right\}$ for some $t_{ref} > 0$, i.e. they radially expand from the origin with spatially variable crack velocity $\boldsymbol{v}$ that depends on $\gamma(t_{ref})$ and is constant on rays extending from the origin. Specifically, $\boldsymbol{v}\left(\boldsymbol{\xi} = \frac{t}{t_{ref}} \boldsymbol{\xi}_{ref}\right) = \boldsymbol{\xi}_{ref}/t_{ref}$.

Solutions to some of these problems are discussed in chapter 2.

1.5 Fracture criteria

Before the 20th century, fracture criteria were based on the concept of critical stress or strain, and brittle fracture was not clearly differentiated from plastic deformation (Gross, 2014). Well-known in geophysics is the Mohr-Coulomb criterion, which states that failure occurs when the shear stress at any point and plane equals the prescribed (often linear or affine) function of the normal stress (Labuz & Zang, 2012). Such point criteria can be used to model the onset of fracture in an intact brittle material. However, as displayed in Eq. (1.12), the stress field at the tip of brittle cracks is infinite. Therefore, criteria based on point values of stress or strain are not feasible for problems with pre-existing brittle cracks, since any infinitesimal load would lead to crack growth. One solution is to consider some characterization of the spatial distribution of stress (strain), e.g., the integral of stress (strain) over a small area at

the crack edge (Wieghardt, 1907, trans. Rossmanith, 1995).

A famous energy-based criterion was put forward by A. A. Griffith (1921). He observed that the fracture strength of brittle specimens (metal, glass) decreases with increasing diameter (fracture size effect). Similar size effects were observed long before Griffith, dating back to Leonardo da Vinci, who noted that fracture strength of iron wires decreases with their length (see Gdoutos, 1990; and references therein). Therefore, the fracture strength is not an intrinsic material constant but depends on the macroscopic properties of the specimen. Griffith also noted that if the specimen is scratched, its fracture strength decreases in proportion to the size of the scratch. In addition, the strength is several orders smaller than would correspond to simple estimates based on strength of atomic bonds. This could be explained by the assumption that the scratches and other defects amplify the ambient stress. Indeed if the defects are modeled as elliptical voids in a linearly elastic material, it can be shown that they concentrate stress at the tips. However, the maximum amplification of stress depends only on the shape of the void, not on its size, so a criterion based on point values of stress cannot explain the size-dependent reduction of strength.

To resolve this paradox, Griffith proposed a fracture criterion based on global energy balance. He considered a pre-existing straight quasi-static crack of area A located in a homogeneous isotropic body, possibly loaded by external forces. He postulated that the surfaces of the crack are associated with *surface* (or *fracture*) energy $E_c(A)$. If the crack expands, the potential energy $W(A)$ of the body (composed of its internal elastic energy minus the work of external forces) is reduced. The body-crack system is in equilibrium if this decrease is balanced by an increase in the crack surface energy, so that:

$$\partial_A(W(A) + E_c(A)) = 0. \tag{1.34}$$

Griffith postulated that the surface of the crack does not decrease and that it may extend quasi-statically only if Eq. (1.34) holds. This is called the *Griffith criterion of rupture.* Using this criterion, Griffith calculated the critical loading stress required for the growth of a straight crack in an infinite elastic plate, finding that it decreases with the length of the crack. This explains the dependence of fracture strength on the scratch size. Further, the specimen size effect is explained by assuming that brittle materials contain small defects, and that the maximum size of these defects scales with the volume of the specimen (a statistical model explaining the size effect was developed in 1939 by W. Weibull in his so-called worst-flaw

theory, see Rossmanith, 1997).

Important work on brittle cracks was done by G. R. Irwin. He generalized the surface energy to effective surface energy, including in it the work of plastic forces (Irwin, 1948, according to Yarema, 1996). Irwin (1957) introduced the concept of the *energy release rate* G (also called the *crack-driving force*; the letter G is likely a reference to Griffith):

$$G := -\partial_A W(A). \tag{1.35}$$

Assuming that the fracture energy is equal to

$$E_c(A) = 2\gamma_c A, \tag{1.36}$$

where γ_c is specific effective surface energy and the factor of 2 corresponds to contributions from both sides of the surface, the Griffith criterion (1.34) reads:

$$G = 2\gamma_c. \tag{1.37}$$

Therefore, the crack advances when the energy release rate is equal to the critical value $G_c := 2\gamma_c$. When $G < G_c$, the crack cannot grow.

For quasi-static, straight-ahead extending cracks in isotropic elastic materials, Irwin (1957, 1958) related the energy release rate to the stress-intensity factors K_m (Eq. 1.12) as:

$$G = \sum_{m\in\{I,II,III\}} C_m(\mu,\nu)K_m^2, \tag{1.38}$$

where C_m depends on the fracture propagation mode $m \in \{I, II, III\}$, the shear modulus μ and the Poisson's ratio ν, see e.g., Scholz (2002) and chapter 2 of this thesis for particular expressions. For $m \in \{I, II\}$, the function C_m slightly differs for plane-stress and plane-strain conditions. When only a single mode m of fracture is present, Eq. (1.38) implies that the Griffith criterion (1.37) on the critical value of the energy release rate is equivalent, for static straight cracks, to the following condition on the criticality of the respective stress-intensity factor:

$$K_m = K_c. \tag{1.39}$$

Eq. (1.39) is called the *Irwin criterion of fracture*. The quantity K_c is called the *fracture*

toughness of the material. It may differ for each propagation mode. Shimada et al. (2015) demonstrated that the Griffith/Irwin criteria are applicable even at the nanoscale, breaking down at $2-3$ nm.

When $G > G_c$, the crack does not increase quasi-statically, but instead dynamically. In dynamic conditions, the kinetic energy is generally nonzero and the decrease in elastic energy no more needs to be balanced only by the surface energy as in the quasi-static case. The Griffith criterion then generalizes to

$$G^{dyn}(v) = G_c, \tag{1.40}$$

where v is the instantaneous speed of the crack front and $G^{dyn}(v)$ is the *dynamic energy release rate*.

In 2-D, G^{dyn} can be defined (Freund, 1990) by enclosing the crack tip in a small contour Π_ϵ of circumference ϵ, and considering the flux $\mathcal{F}(\Pi_\epsilon)$ per unit time and unit thickness of the total mechanical energy across Π_ϵ. Because the stresses around the crack tip are singular in ideally brittle materials, $\mathcal{F}(\Pi_\epsilon)$ is generally non-zero even as $\epsilon \to 0$. The dynamic energy release rate is the influx of the total mechanical energy to the crack tip per unit area increase of the crack:

$$G^{dyn}(v) := \lim_{\epsilon \to 0} \frac{\mathcal{F}(\Pi_\epsilon)}{v} \tag{1.41}$$

(Freund, 1990; see his Ch. 5 for an explicit formula for $\mathcal{F}$ and a demonstration that the limit is well defined). For a steadily growing crack ($v = const$), $\mathcal{F}(\Pi_\epsilon)$ is independent of the enclosing contour Π_ϵ (even for large ϵ) and it is proportional to the crack tip speed v. Then $\lim_{v\to 0} G^{dyn}(v) = \lim_{v\to 0} \frac{\mathcal{F}(\Pi_\epsilon)}{v}$ is finite, and it coincides with the static energy release rate G. Due to this correspondence, we omit the ^{dyn} superscript and simply write G for both the static and the dynamic energy release rates.

In 3-D, the crack tip is replaced by a point on the crack edge and the contour is replaced by a small tube of surface ϵ surrounding this point. The energy release rate then depends on the position along the crack edge.

In dynamic conditions, the Irwin relation (1.38) no longer holds. However, the additive structure of the formula remains, and it simply generalizes to:

$$G(v) = \sum_{m \in \{I,II,III\}} C_m(\mu,\nu) g_m(v,\mu,\nu,\beta) K_m^2(v), \tag{1.42}$$

where g_m are functions increasing in v such that $g_m(v \to 0, ...) \to 1$ and $\beta = \sqrt{\frac{\mu}{\rho}}$ is the phase speed of shear elastic (S) body waves. Therefore, the evolution of dynamic cracks under the Griffith ($G(v) = G_c$) and Irvin ($K_m(v) = K_c$) criteria differs even for pure modes of fracture, according to the functions $g_m(v, ...)$ (see Das & Aki, 1977). The functions g_m do not depend on the loading applied at the boundary or on the geometry of the problem (Freund, 1990, ch. 5).

A drawback of both criteria is that they cannot predict the direction of crack growth and that they require the existence of preexisting cracks. Among many extensions that address the former issue, we mention criteria such as the 2-D *maximum circumferential stress* criterion according to which the crack grows under the polar angle θ along which $\sigma_{\theta\theta}$ is maximum, or the *maximum energy release rate criterion* (Erdogan & Sih, 1963) according to which the crack grows in the direction that maximizes the energy release rate (see, e.g. Bouchard et al., 2003). Among approaches that can solve both issues simultaneously is the *strain energy density* criterion (Sih, 1973; Sih & Macdonald, 1974), in which the fracture is governed by a finite volumetric field quantity (see, e.g., chapter 6 of Gdoutos, 1990) and variational formulations, such as that of Francfort & Marigo (1998) for quasi-static growth, in which the crack $\gamma(t)$ is the surface that minimizes total potential energy among a certain constrained set of cracks.

In cohesive models with appropriate constitutive laws, the singularities at the crack edges are removed and criteria based on maximum local values of fields may be introduced. For example, in the maximum nominal strain criterion, fracture at a point occurs when any component of strain exceeds a critical value. In linear slip-weakening models, the crack extends when the magnitude of shear stress reaches the yield strength T_u.

A connection between brittle and slip-weakening constitutive models is made by equating the area below the cohesive curves in Fig. 1.2 and above T_d to the fracture energy surface density (critical energy release rate) G_c, so that (Palmer & Rice, 1973; Rice, 1980):

$$G_c = \int_0^{D_c} (F(s) - T_d) ds, \tag{1.43}$$

where D_c is the slip at which the magnitude of traction reaches the final value T_d ($D_c = \infty$ for the Ohnaka-Yamashita law 1.21). This expression is valid only for cases in which the cohesive zone is small in comparison to the total crack size.

2 Analytic solutions for simple ideally brittle shear cracks

In this chapter, we review solutions to selected problems of linear elastic fracture mechanics in infinite, homogeneous, isotropic elastic media. Analytical solutions for crack problems are typically very complicated and only a few solutions to fully 3-D problems are known. Therefore, we restrict ourselves to a small set of problems with simple geometries, which nevertheless illustrate important features of brittle rupture. For an extensive reference to various problems, we refer the reader to (Freund, 1990; Broberg, 1999) and Tada et al. (2000).

In isotropic elastic media, the stiffness tensor relating the stress tensor increment τ and the displacement $\boldsymbol{u}$ has the form:

$$c_{ijpq} = \lambda\delta_{ij}\delta_{pq} + \mu(\delta_{ip}\delta_{jq} + \delta_{iq}\delta_{jp}), \tag{2.1}$$

where $\lambda = \frac{2\mu\nu}{1-2\nu}$ is Lamé's first parameter (e.g., Stein & Wysession, 2003, ch. 2). In a homogeneous medium, combining the relation (2.1) with Eqs. (1.3) and (1.4) shows that the displacement $\boldsymbol{u}$ satisfies the equation:

$$\frac{\rho}{\mu}\partial_{tt}u_i(t,\boldsymbol{x}) = \frac{1}{1-2\nu}u_{j,ji}(t,\boldsymbol{x}) + u_{i,jj}(t,\boldsymbol{x}),\ \forall\boldsymbol{x}\in\Omega/\Gamma, \forall t\in\mathbb{R}, \tag{2.2}$$

which is to be solved along with initial conditions, boundary conditions at $\partial\Omega$, and mixed boundary conditions (1.6) and (1.7) with $\mathcal{T} \equiv \{\boldsymbol{T}^0(\boldsymbol{x}) - \Delta\boldsymbol{\sigma}(t,\boldsymbol{x})\}$ on the fault plane Γ. Here, $\boldsymbol{T}^0$ is the initial traction and $\Delta\boldsymbol{\sigma}$ is the shear *stress drop*. Except for subsection 2.1.3, we consider $\Delta\boldsymbol{\sigma}$ constant in space and time. We suppose that $\Omega = \mathbb{R}^3$ and that the fault Γ is the $x-y$ plane, $\Gamma = \{(x,y,z)\in\mathbb{R}^3; z=0\}$.

We only discuss solutions for slip and traction on Γ. Displacement (and hence also the stress increment) elsewhere can be calculated from slip $\boldsymbol{s}$ on Γ according to the elastic representation

theorem (Aki & Richards, 2002, ch. 3):

$$u_i(t, \boldsymbol{x}) = \int_\Gamma s_k(t, \boldsymbol{\xi}) * c_{klpq} \mathcal{G}_{ip,q}(t, \boldsymbol{x}, \boldsymbol{\xi}) n_l dS, \tag{2.3}$$

where the Green's function $\mathcal{G}_{ip}(t, \boldsymbol{x}, \boldsymbol{\xi})$ is the ith component of displacement induced in homogeneous space at $(t, \boldsymbol{x})$ by a unit impulse force oriented in the direction of the pth axis and applied at $(0, \boldsymbol{\xi})$, $\boldsymbol{s}$ is slip, $\boldsymbol{n}$ is the normal to the fault plane and $*$ is the temporal convolution operator.

It is worth pointing out that the form of the solutions can be restricted by dimensional arguments. For static problems, assume that the solution depends only on the stress drop $\Delta\sigma$, the shear modulus μ, the Poisson's ratio ν, a finite characteristic length L and k non-dimensional geometric parameters $p_1, p_2, p_3, ..., p_k$. Dimensional analysis, formalized by the Buckingham Π theorem (e.g., Barenblatt, 2003) then implies that the magnitude of slip s must depend on these parameters as:

$$s = Lh(\frac{\Delta\sigma}{\mu}, \nu, p_1, p_2, ..., p_k, x/L, y/L), \tag{2.4}$$

where h is a non-dimensional function of non-dimensional arguments. The particular form of h depends on boundary conditions, including the shape of the crack. Since the stress drop and slip are linearly related by the assumption of linear elasticity, the preceding relation simplifies to

$$s = L\frac{\Delta\sigma}{\mu} h(\nu, p_1, p_2, ..., p_k, x/L_1, y/L_1), \tag{2.5}$$

where we have reused the notation h for the new function of the remaining parameters. For example, s on cracks in 2-D of half-length a must have the form:

$$s = a\frac{\Delta\sigma}{\mu} h(\nu, x/a), \tag{2.6}$$

while on a static circular crack with radius $r = L_1$, it has the form

$$s = r\frac{\Delta\sigma}{\mu} h(\nu, x/r, y/r). \tag{2.7}$$

The slip magnitude on an elliptic crack with semi-axis b, aspect ratio b/a and inclination ψ

must have the form:

$$s = b\frac{\Delta\sigma}{\mu}h(\nu, b/a, \psi, x/b, y/b). \tag{2.8}$$

Steady-state problems are additionally characterized by the shear wave phase speed β and the rupture speed v. For steady-state cracks propagating along the x-axis, s has the form:

$$s = a\frac{\Delta\sigma}{\mu}h(\nu, v/\beta, \frac{x-vt}{a}), \tag{2.9}$$

where a is the half-length of the crack. If the problem is instead self-similar and the rupture growth can be fully characterized by two rupture speeds v and w, then:

$$s = vt\frac{\Delta\sigma}{\mu}h(\nu, \frac{v}{\beta}, \frac{w}{v}, \frac{x}{vt}, \frac{y}{vt}). \tag{2.10}$$

2.1 Straight shear cracks infinite in the anti-plane direction

In this section, we consider cracks that are infinite and straight along the y-axis, so that they can be described as $\gamma(t) = \{(x, y, z); L(t) \leq x \leq R(t); z = 0\}$ for some functions L and R ($L \leq R$). Both the displacement and the stress are assumed independent of the y-coordinate, so these are effectively 2-D problems. They may be understood as approximations to problems with more complicated geometries on small enough spatial scales, at which the curvature of the crack may be neglected.

For anti-plane cracks, the only non-zero component of displacement is $u_y(t, x, z)$ (SH polarization) and Eq. (2.2) reduces to a simple scalar wave-equation for u_y:

$$\frac{1}{\beta^2}\partial_{tt}u_y(t, x, z) = (\partial_{xx} + \partial_{zz})u_y(t, x, z), \tag{2.11}$$

where $\beta = \sqrt{\frac{\mu}{\rho}}$ is the shear wave phase velocity. Because of the symmetry of the problem, the u_y component is anti-symmetric with respect to the fault plane (Das & Aki, 1977), so that $s_y(t, x) = 2u_y(t, x, z = 0)$.

In the in-plane case, the slip points in the direction of the x-axis. Displacement with the P-SV polarization is induced (Aki & Richards, 2002), with two non-zero components $u_x(t, x, z)$ and

$u_z(t,x,z)$ which are coupled in the resulting equations of motion. In homogeneous conditions, two scalar potentials ϕ and ψ may be introduced such that $\boldsymbol{u} = \nabla\phi + \nabla \times (0,\psi,0)$, and the vector problem decomposes into two scalar wave equations of the form (2.11) for each potential (with phase velocities $\alpha = \beta\sqrt{2\frac{1-\nu}{1-2\nu}}$ and β, respectively). However, the potentials remain coupled through the boundary conditions on displacement and traction. Therefore, the in-plane problem remains more complicated than the anti-plane problem, despite the identical equations of motion in the bulk volume. The shear component of displacement u_x is anti-symmetric with respect to the fault plane (Das & Aki, 1977) and $s_x(t,x) = 2u_x(t,x,z=0)$. The u_z component is symmetric, so $s_z \equiv 0$.

2.1.1 Semi-infinite straight cracks

The simplest non-trivial solutions are obtained for the problem of a semi-infinite straight crack occupying a left half-plane of the fault ($L = -\infty$), with zero stress increment at infinity and zero stress drop, i.e. $\gamma(t) = \gamma = \{(x,y,z) \in \Gamma; x < R(t)\}$, $\lim_{x^2+z^2\to\infty} \tau_{ij}(x,z) = 0$, $\Delta\boldsymbol{\sigma} = \mathbf{0}$. In this subsection, we consider two special cases, $R(t) = 0$ (static crack) and $R(t) = vt$ (steadily propagating crack). The more general case of arbitrary increasing $R(t)$ is treated in subsection 2.1.3.

2.1.1.1 Static case

In static problems, the inertial terms in the equations of motion are zero. For the anti-plane case (2.11), this implies that the static displacement u_y^0 solves the Laplace equation:

$$(\partial_{xx} + \partial_{zz})u_y^0(x,z) = 0. \tag{2.12}$$

This crack problem was solved for all modes by Irwin (1958) by the Westergaard method, in which displacements and stresses are expressed through a single harmonic complex function. It was re-derived on the basis of the elastic representation theorem (2.3) by Ida & Aki (1972). For the anti-plane case, non-zero components of slip and traction increment on the fault plane are:

$$s_y^0(x) = A\sqrt{-x}H(-x);\ \tau_{yz}^0(x,0) = K_{III}(A)\frac{H(x)}{\sqrt{2\pi x}}, \tag{2.13}$$

where $A \in \mathbb{R}$ is any constant with the dimension of $\mathrm{m}^{1/2}$, H is the Heaviside step function and K_{III} is the anti-plane stress-intensity factor:

$$K_{III}(A) = \frac{\sqrt{2\pi}}{4} A\mu. \tag{2.14}$$

The stress is infinite at the crack front, decaying with the inverse square root of the distance. This is in accordance with the general form seen in Eq. (1.11). In this case, the solution is exceptionally simple, containing only the singular term. We note that $\partial_x s_y$ and τ_{xy} also have inverse square root singularities at the crack-tip, but their support coincides with the crack.

The in-plane problem (also solved by Irwin, 1958) has a similar solution:

$$s_x^0(t,x) = A\sqrt{-x}H(-x'); \tau_{xz}^0(t,x,0) = K_{II}(A)\frac{H(x)}{\sqrt{2\pi x}}, \tag{2.15}$$

but the stress-intensity factor is now given by:

$$K_{II}(A) = \frac{\sqrt{2\pi}}{4} A \frac{\mu}{1-\nu}. \tag{2.16}$$

Therefore, the two solutions are identical except for the factor $1/(1-\nu)$ that appears in Eq. (2.16). This factor seems to be ubiquitous in mode II (and also mode I) problems. Denoting

$$\mu^* = \begin{cases} \frac{\mu}{1-\nu} & \text{for mode II} \\ \mu & \text{for mode III} \end{cases}, \tag{2.17}$$

the stress-intensity factors for both modes can be written compactly as

$$K_{II,III}(A) = \frac{\sqrt{2\pi}}{4} A\mu^*. \tag{2.18}$$

A general shear crack solution would be obtained as a superposition of the anti-plane and in-plane cases.

2.1.1.2 Steady propagation

The preceding problem may be generalized to the case of a semi-infinite crack steadily propagating with rupture speed v, i.e. $\gamma(t) = \{(x,y,z) \in \mathbb{R}^3; x < vt, z = 0\}$. In the anti-plane case,

the steady solution $u_y^v(t,x,z)$ can be obtained from the solution $u_y^0(x,z)$ of the static problem by using the transformation (McClintock, 1960; Eshelby, 1969; Aki & Richards, 2002, ch. 11)

$$x \to \eta(t,x) = (x - vt)/\gamma_\beta(v), \tag{2.19}$$

where

$$\gamma_\beta(v) = \sqrt{1 - \frac{v^2}{\beta^2}}, \tag{2.20}$$

so η is a function analogical to the spatial part of the Lorentz transformation.

The transformed displacement

$$u_y^v(t,x,z) = u_y^0\left(\eta(t,x),z\right), \tag{2.21}$$

solves the body equation of motion (2.11), as can be confirmed by direct substitution of (2.21) into Eq. (2.11), applying the chain rule $\partial_x u_y^v(t,x,z) = \frac{1}{\gamma_\beta(v)}\partial_\eta u_y^0(\eta,z)$, $\partial_t u_y^v(t,x,z) = \frac{-v}{\gamma_\beta(v)}\partial_\eta u_y^0(\eta,z)$, $\partial_z u_y^v(t,x,z) = \partial_z u_y^0(\eta,z)$, and using the fact that u_y^0 solves the static equation (2.12).

For τ_{yz}^v, Eq. (2.21) implies

$$\tau_{yz}^v(t,x,z) = \mu\frac{\partial u_y^v(t,x,z)}{\partial z} = \mu\frac{\partial u_y^0\left(\eta(t,x),z\right)}{\partial z} = \tau_{yz}^0\left(\eta(t,x),z\right). \tag{2.22}$$

Evaluating formulas (2.21) and (2.22) at $z = 0$ shows that since u_y^0 fulfills the mixed boundary conditions for the static problem, the transformed solution u_y^v fulfills the mixed boundary conditions for the steady problem. Therefore, u_y^v is indeed the solution of the steady problem.

Applying Eqs. (2.21) and (2.22) to Eq. (2.13), we obtain:

$$s_y^v(t,x) = \frac{A}{\sqrt{\gamma_\beta(v)}}\sqrt{-x'}H(-x');\ \tau_{yz}^v(t,x,0) = K_{III}(A)\sqrt{\gamma_\beta(v)}\frac{H(x')}{\sqrt{2\pi x'}}, \tag{2.23}$$

where

$$x' = x - vt. \tag{2.24}$$

Since A is undetermined, we may replace it by another undetermined constant B through the substitution:

$$B = A\sqrt{\gamma_\beta(v)}. \tag{2.25}$$

Using Eqs. (2.14) and (2.25), we see that:

$$\begin{aligned} K_{III}(A)\sqrt{\gamma_\beta(v)} &= \frac{\sqrt{2\pi}}{4}\mu A\sqrt{\gamma_\beta(v)} \\ &= \frac{\sqrt{2\pi}}{4}\mu B \\ &= K_{III}(B). \end{aligned} \tag{2.26}$$

Therefore, Eq. (2.23) can be rewritten as (dropping the v superscript):

$$s_y(t,x) = \frac{1}{\gamma(v)}B\sqrt{-x'}H(-x');\ \tau_{yz}(t,x,0) = K_{III}(B)\frac{H(x')}{\sqrt{2\pi x'}}, \tag{2.27}$$

which differs from the static result (2.14) only by a speed dependent factor that modifies the slip.

For straight-extending cracks, the relation between the dynamic energy release rate $G(v)$ and the stress-intensity factor K_{III} is (Freund, 1990, ch. 5):

$$G(v, K_{III}) = \frac{K_{III}^2}{2\mu}\frac{1}{\gamma_\beta(v)}. \tag{2.28}$$

Comparing this relation with Eqs. (1.38) and (1.42) introduced in section 1.5 we can identify the anti-plane functions C_{III} and g_{III}:

$$C_{III}(\mu,\nu) = C_{III}(\mu) = \frac{1}{2\mu} \tag{2.29}$$

and

$$g_{III}(v,\mu,\nu,\beta) = g_{III}(v,\beta) = 1/\gamma_\beta(v). \tag{2.30}$$

Combining Eqs. (2.26) and (2.28) yields the explicit expression for $G(v)$:

$$G(v) = \frac{\pi}{16}\mu B^2/\gamma_\beta(v), \tag{2.31}$$

which diverges as $v \to \beta$. In fact, β is the limiting speed for all, even cohesive, purely anti-plane cracks (Broberg, 1996).

For the in-plane problem, even though the potentials ϕ and ψ satisfy scalar wave equations of the same form (2.11) as the anti-plane displacement u_y, applying the transformation (2.19) to the x argument of the static potentials does not suffice to obtain the steady solution. This is because boundary conditions for displacement and traction on the fault are not fulfilled by the transformed potentials.

Nevertheless, the solution for the subshear ($v < \beta$) steady in-plane problem has the same structure as the anti-plane solution, differing in the crack speed dependent factor modifying the slip (see Freund, 1979; Aki & Richards, 2002, ch. 11):

$$s_x(t,x) = \frac{\gamma_\beta(v)}{P(v)} B\sqrt{-x'}H(-x'); \tau_{xz}(t,x,0) = K_{II}(B)\frac{H(x')}{\sqrt{2\pi x'}}, \tag{2.32}$$

where

$$P(v) = \frac{4\beta^2(1-\nu)}{v^2}\left[\gamma_\alpha(v)\gamma_\beta(v) - \left(1 - \frac{v^2}{2\beta^2}\right)^2\right] \tag{2.33}$$

for $v > 0$ and

$$P(v=0) = \lim_{v\to 0} P(v) = 1 \tag{2.34}$$

for $v = 0$. Here, $\alpha = \beta\sqrt{2\frac{1-\nu}{1-2\nu}}$ is the phase speed of longitudinal elastic (P) body waves and

$$K_{II}(B) = \frac{\sqrt{2\pi}}{4} B\mu^* \tag{2.35}$$

as in the static case (Eq. 2.18).

The relationship between G and K_{II} for straight-extending cracks in plane-strain is (Freund, 1990, ch. 5):

$$G(v, K_{II}) = \frac{K_{II}^2}{2\mu^*}\frac{\gamma_\beta(v)}{P(v)}. \tag{2.36}$$

Comparing with Eqs. (1.38) and (1.42) and noting that the speed dependent factor equals 1 for $v = 0$, we identify the functions C_{II} and g_{II} for (plane-strain) mode II cracks:

$$C_{II}(\mu,\nu) = \frac{1}{2\mu^*} \tag{2.37}$$

and

$$g_{II}(v,\mu,\nu,\beta) = \frac{\gamma_\beta(v)}{P(v)}. \tag{2.38}$$

The dynamic energy release rate for mode II can be calculated by combining Eqs. (2.35) and (2.36):

$$G(v) = \frac{\pi}{16}\mu^* B^2 \frac{\gamma_\beta(v)}{P(v)}. \tag{2.39}$$

This expression provides a constraint on steady-state rupture speeds for ideally brittle cracks. This is because, for physically admissible solutions, the energy release rate must be real, finite, and non-negative (so that the crack is not a source of energy, which would correspond to negative fracture energy). Since the speed-independent factors all fulfill these conditions, the admissibility at different speeds v is determined by the function $\gamma_\beta(v)/P(v)$.

For $v < \beta$, $\gamma_\beta(v)/P(v)$ is real, finite, and non-negative on the interval $[0, c_R)$, where c_R is the speed of Rayleigh surface waves[1], and negative on the interval (c_R, β). Therefore, steady-state propagation at speeds $v \in [c_R, \beta)$ is not realistic for ideally brittle purely in-plane cracks and the interval has been labeled as "forbidden" (Burridge et al., 1979).

For $v > \beta$, $\gamma_\beta(v)/P(v)$ is complex-valued, except for the *Eshelby speed* $c_E = \sqrt{2}\beta$, for which it is real and positive. Solutions for the speed range $[\beta, \alpha]/\{c_E\}$ exist, but they differ from the subshear result (2.32) (Freund, 1979). In particular, they contain singular Mach wavefronts traveling with speed β that are radiated from the crack front. The stress at the crack front is still infinite, but the singularity exponent ζ, defined by

$$\tau_{xz}^S(x', 0) \propto x'^{-\zeta}, \tag{2.40}$$

where τ_{xz}^S is the singular part of τ_{xz}, is smaller than the subRayleigh value of $1/2$. It smoothly increases as a function of the crack speed from 0 at $v = \beta$ to $1/2$ as $v \to c_E$ and then again decreases to $\zeta = 0$ at $v = \alpha$.[2] Accordingly, the stress-intensity factor $K_{II} \propto \lim_{x' \to 0^+} x'^{1/2} x'^{-\zeta} = 0$. Hence the energy release rates of these solutions vanish and no energy can be supplied to the crack at these speeds. According to the Irwin or Griffith criteria, propagation of such cracks would only be possible for strictly zero values of K_c (G_c). Therefore, steady-state propagation with speeds $v \in [\beta, \alpha]/\{c_E\}$ is not realistic either. Indeed, disregarding the special speed c_E, c_R is the limiting speed of pure mode II ideally brittle cracks propagating under the Irwin/Griffith

[1] The speed c_R can be defined as the only root of $P(v)$ which is positive, real and smaller then α, see Schröder & Scott, 2001. In general, $c_R < \beta$ and c_R/β is a slowly changing function of ν. For $\nu = 1/4$ (Poisson solids), $c_R \approx 0.92\beta$.

[2] As explained in Rosakis (2002), the underlying mathematical reason for this quantitative change is that the scalar equation governing the steady shear wave potential (expressed in the co-moving coordinates $x' = x - vt$, $t' = t$), changes from an elliptic partial equation to a hyperbolic one as v passes β.

criteria. (Craggs, 1960; Freund, 1979). It is also the limiting speed of mode I cracks (Barenblatt & Cherepanov, 1960; Broberg, 1996), even for cohesive constitutive models.

For mode II cohesive cracks, analytical (Andrews, 1976a; Freund, 1979) and numerical studies (see sections 3.1 and 3.5 and references therein) show that steady supershear rupture speeds are physically plausible. Indeed, when a finite cohesive zone behind the crack front is included, the energy flux can be positive even for $v > \beta$ (Broberg, 1989, 1994; Rosakis, 2002). For the forbidden zone (c_R, β), positive flux is also possible in cohesive models, but likely only for transient (non-steady) propagation. Rapid passage of the crack speed through the forbidden zone has been observed in numerical studies (Geubelle & Kubair, 2001; Bizzarri & Das, 2012; Liu et al., 2014; Payne & Duan, 2015).

For the ideally brittle special case of $v = c_E$, the Mach waves are not present, the solution retains the inverse square root singularity of the subRayleigh propagation and the energy release rate is positive. Therefore, steady brittle propagation is theoretically possible at this speed. Convergence of transient supershear cracks to a steady crack propagating very close to c_E was observed in laboratory experiments of Rosakis (2002).

Finally, we note that ideally brittle mode I and II problems with crack speeds in the interval (c_R, β) in fact admit non-unique solutions (Freund, 1990, ch. 7). In particular, a non-trivial solution with zero energy release rate exists (Freund, 1979). However, as for the $v > \beta$ case, propagation of these cracks according to the traditional Irwin or Griffith criteria would only be possible for strictly zero values of K_c (G_c).

2.1.2 Finite straight cracks

2.1.2.1 Static case

The simplest finite crack problem is that of a static straight anti-plane crack with length $2a$: $\gamma(t) = \{(x, y, z) \in \mathbb{R}^3; |x| \leq a, z = 0\}$ and stress drop equal to $\Delta\boldsymbol{\sigma} = (0, \Delta\sigma, 0)$. At infinity, we require $\lim_{x^2+z^2\to\infty} \tau_{yz}(x, y, z) = 0$. From dimensional analysis (Eq. 2.5) and reflection symmetry of the problem along the plane $x = 0$, we may anticipate that the slip on the crack has the form:

$$s_y(x) = a\frac{\Delta\sigma}{\mu} f(\nu, x/a), \tag{2.41}$$

with f an even or odd function of x/a. Indeed, the exact solution by Knopoff (1958), who derived it based on an analogy with a known solved problem of electrostatics (as both u_y in the static crack problem and the electric potential in absence of charge satisfy the Laplace equation), reads:

$$s_y(x) = 2a\frac{\Delta\sigma}{\mu}\sqrt{1-(x/a)^2}I_{[-a,a]}(x), \tag{2.42}$$

$$\tau_{yz}(x,0) = \Delta\sigma\frac{x}{\sqrt{x^2-a^2}}I_{\mathbb{R}\setminus[-a,a]}(x) - \Delta\sigma, \tag{2.43}$$

where I_A is the indicator function of set A. As in the semi-infinite example, τ_{yz} is infinite at the crack fronts, but non-singular terms are now present as well. For example, introducing the translated coordinate $r = x - a$, the solution (2.43) may be expanded around the right edge of the crack as:

$$\tau_{yz}(a+r,0) = \frac{\Delta\sigma}{\sqrt{r}}\frac{a+r}{\sqrt{2a+r}} - \Delta\sigma = \frac{\Delta\sigma}{\sqrt{r}}\frac{a+r}{\sqrt{2a}}\left(1 - \frac{r}{4a} + o(r)\right) - \Delta\sigma \tag{2.44}$$

$$= \Delta\sigma\left(\sqrt{\frac{a}{2}}r^{-1/2} - 1 + \frac{3}{4\sqrt{2a}}r^{1/2} + \sum_{i=1}^{\infty}k_i(a)r^{(2i+1)/2}\right), \tag{2.45}$$

where $k_i(a)$ are expansion coefficients of the form $f_i a^{-(2i+1)/2}$ for some non-dimensional constants f_i, and the expansion is valid for $0 < r \leq 2a$.

The stress-intensity factor (Eq. 1.13) at the right edge is

$$K_{III}(a) = \lim_{r\to 0^+}\left[\sqrt{2\pi r}\tau_{yz}(a+r)\right] = \Delta\sigma\sqrt{\pi a}. \tag{2.46}$$

It depends on both the stress drop and the geometry of the problem. At the left edge, K_{III} has the same size, but opposite sign.

The energy release rate may be calculated from Eqs. (2.28) and (2.46) as:

$$G = \frac{\pi\Delta\sigma^2}{2\mu}a. \tag{2.47}$$

According to the Griffith criterion, which posits that the crack is stable when $G<G_c$, where G_c is the critical energy release rate, larger cracks are weaker than smaller cracks, sustaining smaller maximum stress drop. From Eq. (2.47), the critical length a_c^{III} above which cracks are

unstable is:

$$a_c^{III} = \frac{2\mu}{\pi\Delta\sigma^2}G_c. \tag{2.48}$$

When the crack size increases towards infinity, the stress drop has to go to zero if K_{III} and G are to remain finite. The solution for slip and traction, expressed in terms of the translated coordinate $r = x - a$, then converges to that of the semi-infinite crack (2.13). Indeed, writing Eq. (2.42) as:

$$s_y(x) = \frac{2\Delta\sigma}{\mu}\sqrt{(a-x)(a+x)}I_{[-a,a]}(x) = \frac{2\Delta\sigma}{\mu}\sqrt{-r(r+2a)}I_{[-2a,0]}(r) \tag{2.49}$$

and calculating the limit for $a \to \infty$ yields:

$$\lim_{a\to\infty} s_y(a+r) = \lim_{a\to\infty} 2\sqrt{2a}\frac{\Delta\sigma}{\mu}\sqrt{-r(1+r/2a)}H(-r) = A\sqrt{-r}H(-r), \tag{2.50}$$

where we have labeled

$$A = \lim_{a\to\infty} 2\sqrt{2a}\frac{\Delta\sigma}{\mu}. \tag{2.51}$$

Similarly, the limit of the stress-intensity factor is, from Eqs. (2.46) and (2.51):

$$\lim_{a\to\infty} K_{III}(a) = \lim_{a\to\infty}(2\sqrt{2a}\frac{\Delta\sigma}{\mu})\frac{\sqrt{\pi}\mu}{2\sqrt{2}} = \frac{\sqrt{2\pi}}{4}A\mu. \tag{2.52}$$

By assumption, the above limit and thus also A are finite. Relations (2.50) and (2.52) therefore correspond to the semi-infinite results (2.13) and (2.14). A similar calculation shows the correspondence for $\tau_{yz}(x,0)$.

The static in-plane case, with $\Delta\boldsymbol{\sigma} = (\Delta\sigma, 0, 0)$, was solved by Starr (1928). It has the same dependence on x as the anti-plane case, but μ is replaced with μ^* (Eq. 2.17):

$$s_x(x) = 2a\frac{\Delta\sigma}{\mu^*}\sqrt{1-(x/a)^2}I_{[-a,a]}(x), \tag{2.53}$$

$$\tau_{xz}(x,0) = \Delta\sigma\frac{x}{\sqrt{x^2-a^2}}I_{\mathbb{R}\setminus[-a,a]}(x) - \Delta\sigma. \tag{2.54}$$

The energy release rate is

$$G = \frac{\pi\Delta\sigma^2}{2\mu^*}a. \tag{2.55}$$

For $\nu > 0$, and mode II, $\mu^* > \mu$. Therefore, the critical crack in mode II:

$$a_c^{II} = \frac{2\mu^*}{\pi\Delta\sigma^2} G_c \tag{2.56}$$

is larger than the critical mode III crack (assuming the values of G_c for mode II and mode III are equal).

2.1.2.2 Steady and self-similar propagation

The solution for a steadily moving finite anti-plane crack, i.e. $\gamma(t) = \{(x, y, z) \in \mathbb{R}^3; |x - vt| \leq a, z = 0\}$ (so-called Yoffe problem, first discussed for mode I cracks by Yoffe, 1951) can be obtained from the static solution discussed above by applying the transformations (2.21) and (2.22) to Eq. (2.42) and (2.43), respectively. The transformations take the static crack with tips $L = -b$ and $R = b$ to a moving crack with tips $L(t) = vt - \gamma(v)b$ and $R(t) = vt + \gamma(v)b$. Since our steadily moving crack has tips $L(t) = vt - a$ and $R(t) = vt + a$, we need to use the solution for the static crack with reduced half-length $b = a/\gamma_\beta(v)$. The result is

$$s_y(t, x) = \frac{2a}{\gamma_\beta(v)} \frac{\Delta\sigma}{\mu} \sqrt{1 - (x')^2/a^2}\, I_{[-a,a]}(x'), \tag{2.57}$$

$$\tau_{yz}(t, x, 0) = \Delta\sigma \frac{x'}{\sqrt{(x')^2 - a^2}} I_{\mathbb{R}\setminus[-a,a]}(x') - \Delta\sigma, \tag{2.58}$$

where $x' = x - vt$.

Since $\gamma_\beta(v) < 1$ for $v > 0$, the slip gets amplified with the crack speed. On the other hand, the on-fault traction is independent of it and the stress-intensity factor is equal to the static case, $K_{III} = \Delta\sigma\sqrt{\pi a}$. In any case, the slip instantaneously returns to zero behind the crack, so the problem does not seem to correspond to a realistic situation.

More physically relevant is the assumption that the *slip rate,* rather than slip, behind the left edge $L(t)$ is zero. In this case, we obtain a simple model of a self-healing *pulse-like* earthquake and the set $\gamma(t)$ defined at the beginning of this subsection should be called a pulse or a slipping zone, rather than a crack. A solution is given in Broberg (1999, ch. 6.4) for the case in which the pulse closes smoothly at the left edge, in the sense that $\partial_x s_y(t, x = -a) = 0$. It

reads

$$s_y(t,x) = \frac{2\pi a}{\gamma_\beta(v)}\frac{\Delta\sigma}{\mu} I_{(-\infty,-a)}(x') + \frac{2}{\gamma_\beta(v)}\frac{\Delta\sigma}{\mu}\left(\sqrt{a^2-(x')^2} + a\arccos(\frac{x'}{a})\right) I_{[-a,a]}(x'), \quad (2.59)$$

$$\tau_{yz}(t,x,0) = \Delta\sigma\sqrt{\frac{x'+a}{x'-a}} I_{\mathbb{R}\setminus[-a,a]}(x') - \Delta\sigma. \quad (2.60)$$

The first formula implies that the slip rate is a pulse of the form:

$$\partial_t s_y(t,x) = \frac{2v}{\gamma_\beta(v)}\frac{\Delta\sigma}{\mu}\sqrt{\frac{a+x'}{a-x'}} I_{[-a,a)}(x'). \quad (2.61)$$

As in the previous problem, s_y is amplified by $1/\gamma_\beta(v)$, and the traction is independent of the pulse speed. The stress-intensity factor at the right edge of the pulse is equal to $2\Delta\sigma\sqrt{\pi a}$, which is twice as large as the crack result. At the left edge, τ_{yz} is continuous and the stress-intensity factor is zero. Nevertheless, the slip acceleration $\partial_{tt} s_y \propto (x'+a)^{-1/2}(x'-a)^{-3/2}$ diverges at both edges. Note that τ_{yz} behind the pulse gradually returns to zero, i.e. the total traction returns to its original value.

Nielsen & Madariaga (2003) considered (among other problems) a related case of a unilateral, self-healing, self-similar pulse which starts propagating from the origin at $t = 0$. The healing front and the rupture front move at speeds $\dot{l} = v_h$ and $\dot{r} = v_r$, respectively. Remarkably, the slip rate function for this problem can be obtained from the solution of the above steady-state problem by replacing a with the instantaneous length of the pulse, $a \to (v_r - v_h)t$. The formula for traction, on the other hand, is far more complicated. Due to the unilateral nature of the problem and the sudden start of the pulse, τ_{yz} has a singularity not only at the rupture front but also at the origin.

Another physically relevant problem is that of a self-similar anti-plane crack expanding in both directions from the origin with constant speed v, i.e. $\gamma(t) = \{(x,y,z) \in \mathbb{R}^3; |x| \le vt, z = 0\}$ (so-called Broberg problem, who first solved it for mode I cracks in Broberg, 1960). The initial displacement and velocity at $t = 0$ are zero. This problem may be used as a model of a bilaterally expanding seismic rupture. It was examined by Broberg (1998) for generally anisotropic media, though he found that solutions only exist for special symmetries of the stiffness tensor. For the case of an isotropic medium, the slip is given by:

$$s_y(t,x) = \frac{2\Delta\sigma}{\mu E\left(\gamma_\beta(v)\right)}\sqrt{(vt)^2 - x^2}\, I_{[-vt,vt]}(x), \tag{2.62}$$

where $E(k) = \int_0^{\pi/2}\left(1 - k^2\sin^2\theta\right)^{1/2} d\theta$ is the complete elliptic integral of the second kind[3]. The stress-intensity factor is:

$$K_{III}(v) = \Delta\sigma\sqrt{\pi vt}\,\frac{\gamma_\beta(v)}{E\left(\gamma_\beta(v)\right)}. \tag{2.63}$$

Therefore, the solution for slip and the singular part of traction is obtained from the static case simply by substituting the instantaneous radius vt for a and multiplying by factors that depend only on the ratio v/β (but we note that the full solution for traction has a more complicated structure). The stress-intensity factor and the energy release rate both vanish at $v = \beta$.

The in-plane case (Kostrov, 1964) has the same temporal and spatial dependence as the anti-plane case but differs in the velocity-dependent proportionality factors. The in-plane stress-intensity factor vanishes at the Rayleigh wave speed.

2.1.3 Spontaneous propagation of a finite straight anti-plane crack

The final straight crack problem we discuss is that of a spontaneous expansion of an anti-plane crack that suddenly appears at $t = 0$ and starts propagating from homogeneous conditions $u_y(0,x,z) \equiv \partial_t u_y(0,x,z) \equiv 0$. The crack surface is defined by $\gamma(t) = \{(x,y,z) \in \mathbb{R}^3; L(t) \le x \le R(t), z = 0\}$, for some non-increasing (non-decreasing) functions L and R, respectively ($L \le R$). These functions may be prescribed or may be left unspecified a priori, modeling spontaneous propagation. The stress drop at the crack is prescribed, but unlike the previous cases, it is allowed to vary with space and time, $\Delta\boldsymbol{\sigma} = (0, \Delta\sigma(t,x), 0)$.

[3] $E(k)$ is equal to one-quarter of the circumference of an ellipse (possibly degenerate) with semi-axes of lengths 1 and $\sqrt{1-k^2}$ (i.e. k is the eccentricity of the ellipse). It is a decreasing function of k such that $E(0) = \pi/2$ and $E(1) = 1$. The complete elliptic integral of the first kind $K(k)$, which turns up in subsection 2.2.1, is defined as $K(k) = \int_0^{\pi/2}(1 - k^2\sin^2\theta)^{-1/2}d\theta$. It appears as a correction in the formula for the exact period T of a mathematical pendulum with amplitude θ_0 and whose small-amplitude period is T_0: $T = \frac{2}{\pi}T_0 K(\sin^2\theta_0/2)$ (Beléndez et al., 2007). It is an increasing function of k, with $K(0) = \pi/2$ and $\lim_{k\to 1} K(k) = \infty$.

Kostrov (1966) solved this general problem with the use of a representation formula for displacement on the fault:

$$u_y(t,x) = \frac{1}{\pi}\int_{S(t,x)} dx'dt' \frac{\tau_{yz}(t',x',0)}{\sqrt{(x-x')^2+(t-t')^2}}, \tag{2.64}$$

where $S(x,t)$ is the domain of dependence of the space-time point (*event*) (t,x), i.e. the set of on-fault space-time events that can reach it by signals propagating no faster than the shear wave speed:

$$S(t,x) = \{(t',x') \in \mathbb{R}\times\mathbb{R};\ |x-x'| \le \beta(t-t')\}. \tag{2.65}$$

However, since τ_{yz} is zero everywhere for $t<0$ and it starts propagating from the crack at $t=0$, with speeds of at most β, $\tau_{yz}(t,x,0)$ vanishes outside the set $K = \{(t',x') \in \mathbb{R}_0^+ \times \mathbb{R};\ x' \in [L(0)-\beta t', R(0)+\beta t']\}$. The integration domain in Eq. (2.64) can therefore be reduced to the set $S_0(t,x) = S(t,x) \cap K$.

For simplicity, let us first restrict ourselves to events to the right of the crack which are not influenced by the left edge of the crack, i.e. events (t,x) for which

$$x > L(0) + \beta t. \tag{2.66}$$

Then $S_0(t,x)$ does not contain points to the left of the crack and can be partitioned into two disjoint connected subsets $S_c(t,x) = \{(t',x') \in S_0(t,x);\ x' \in \gamma(t')\}$ (crack history) and $S_R(t,x) = \{(t',x') \in S_0(t,x);\ x' > R(t')\}$ (the part of S_0 to the right of the crack), such that $S_0(t,x) = S_c(t,x) \cup S_R(t,x)$.

For events in $S_c(t,x)$, $\tau_{yz}(t',x',0)$ is known and equal to the prescribed function $-\Delta\sigma(t',x')$. For points in $S_R(t,x)$, the slip (and hence u_y) is zero by definition, so Eq. (2.64) there leads to the integral identity

$$\int_{S_c(t,x)} dx'dt' \frac{-\Delta\sigma(t',x')}{\sqrt{(x-x')^2+(t-t')^2}} + \int_{S_R(t,x)} dx'dt' \frac{\tau_{yz}(t',x',0)}{\sqrt{(x-x')^2+(t-t')^2}} = 0. \tag{2.67}$$

Eq. (2.67) can be transformed into so-called Abel's integral equation, which in turn allows inverting for τ_{yz} :

$$\tau_{yz}(t,x,0) = \frac{1}{\pi\sqrt{x-R(t_r)}} \int_{x-\beta t}^{R(t_r)} \Delta\sigma\left(t - \frac{x-x'}{\beta}, x\right) \frac{\sqrt{R(t_r)-x'}}{x-x'} dx'. \tag{2.68}$$

Here, t_r is the solution to the equation $x = R(t_r) + \beta(t - t_r)$, i.e. it is the source time of a shear wave sent from the right edge of the crack that reaches x at time t. The formula at points on the left side of the crack is almost identical to Eq. (2.68), except for signs of spatial coordinates. Once the traction is known, displacement (and slip on the crack) can be calculated from equation (2.64).

The stress-intensity factor $K_{III} = \lim_{r\to 0^+} \left[\sqrt{2\pi r}\tau_{yz}(R(t)+r)\right]$ at the right edge turns out to be

$$K_{III}\left(t, R(t), \dot{R}(t)\right) = \sqrt{\frac{2}{\pi}}\sqrt{1 - \dot{R}(t)/\beta}\int_{R(t)-\beta t}^{R(t)} \Delta\sigma\left(t - \frac{R(t)-x'}{\beta}, x'\right)\frac{dx'}{\sqrt{R(t)-x'}}. \quad (2.69)$$

It depends on the instantaneous speed of the right edge, but also on its instantaneous position and on the history of stress drop on the crack. It vanishes for $\dot{R} = \beta$, which is the anti-plane terminal speed. Moreover, unless the integral vanishes (which is possible for cohesive cracks with suitably chosen $\Delta\sigma(t, x)$), β is the only speed that leads to finite traction. Otherwise, the stress once again has the expected inverse square root singularity at the crack edge.

In formula (2.69), the instantaneous crack speed $\dot{R}(t)$ appears only in the square root term in front of the integral, which is equal to 1 for $\dot{R} = 0$. In addition, the history of the crack motion influences the formula only indirectly, through the history of the stress drop. Therefore, the following relationship holds:

$$K_{III}\left(t, R, \dot{R}\right) = \sqrt{1 - \dot{R}/\beta}K^*_{III}\left(t, R\right), \quad (2.70)$$

where K^*_{III} is the stress-intensity factor of the crack with a static right edge R and which has the same history of stress drop as the original crack. Using the generalized Irwin relation (2.28) yields a similar universal identity for the energy release rate:

$$\begin{aligned} G\left(t, R, \dot{R}\right) &= \frac{K^2_{III}\left(t, R, \dot{R}\right)}{\gamma_\beta(v)\cdot 2\mu} \\ &= \frac{1 - \dot{R}/\beta}{\sqrt{1 - \left(\dot{R}/\beta\right)^2}}\frac{\left(K^*_{III}(t, r)\right)^2}{2\mu} \\ &= \sqrt{\frac{1 - \dot{R}/\beta}{1 + \dot{R}/\beta}}G^*\left(t, R\right). \end{aligned} \quad (2.71)$$

Eshelby (1969) studied an alternative problem in which the crack does not appear suddenly at $t = 0$, but has instead existed forever, subject to time-independent loading $\Delta\sigma(x')$. He showed that Eqs. (2.70) and (2.71) are then valid if one interprets K^*_{III} and G^* as the stress-intensity factor and energy release rate, respectively, of a static crack of the same length and subject to the same loading as the moving crack. Relations similar to (2.70) and (2.71) but with a different dependence on $\dot{R}$ also exist for mode II cracks (Fossum & Freund, 1975; Kostrov, 1975, ch. 6). For example,

$$K_{II}(t, R, \dot{R}) = \frac{1 - \dot{R}/c_R}{\sqrt{1 - \dot{R}/\beta}} K^*_{II}(t, R). \tag{2.72}$$

For prescribed propagation, $R(t)$ is known beforehand, and Eqs. (2.67) and (2.64) can be used to calculate the displacement and traction on the fault. For spontaneous rupture, in which $R(t)$ is unspecified, a rupture criterion needs to be supplied instead, as discussed in section 1.5. The evolution of $R(t)$ is then determined from the *crack tip equation of motion*. For example, using the Irwin criterion, this equation is:

$$K_{III}\left(t, R(t), \dot{R}(t)\right) = K_c, \tag{2.73}$$

where K_{III} is given by Eq. (2.69). It is an ordinary first-order differential equation in $R(t)$, which, along with the initial condition $R(0) = R_0$, can be solved for $R(t)$. Similarly, using the Griffith criterion, we obtain the equation

$$G\left(\dot{R}(t), K_{III}\left(t, R(t), \dot{R}(t)\right)\right) = G_c, \tag{2.74}$$

where the function $G(\dot{R}, K_{III})$ is given by Eq. (2.28). Analogical equations can be deduced for mode II cracks (Fossum & Freund, 1975). Indeed, experimental confirmation of such an equation can be found in Svetlizky et al. (2019), who found that it can predict the rupture front position of a laboratory in-plane crack to a good degree of accuracy.

Analytical results of the crack equation of motion are available for simple configurations. For example, for a semi-infinite ($L(t) \equiv -\infty$) crack suddenly appearing at $t = 0$ with uniform stress drop $\Delta\sigma$, the Griffith criterion leads to the result (Kostrov, 1966):

$$R(t) = H(t - t_s)\left(\beta t - \beta t_s\left[1 + 2\arctan(t/t_s) - \pi/2\right]\right), \tag{2.75}$$

where t_s is the time at which the crack starts to propagate:

$$t_s = \frac{\mu\pi G_c}{4\beta\Delta\sigma^2}. \tag{2.76}$$

The velocity v_R of the right-edge is:

$$\dot{R}(t) = H(t - t_s)\beta\left(1 - \frac{2}{1 + (t/t_s)^2}\right). \tag{2.77}$$

Thus, the anti-plane crack starts propagating from zero velocity at $t = t_s > 0$ and asymptotically accelerates to the shear wave velocity as $t \gg t_s$. Slightly different formulae are obtained if Irwin's criterion (i.e., a velocity independent critical stress-intensity factor) is used instead (Das, 2003), but the acceleration from zero to terminal velocity is a persistent feature in homogeneous settings. A similar result holds for in-plane cracks, for which the limiting speed is the Rayleigh velocity (see Fossum & Freund, 1975; Broberg, 1996; Dunham, 2007).

Acceleration of the crack towards terminal speeds is not inevitable in more general settings. If $\Delta\sigma$ is allowed to decrease along the crack path, such as when the crack front travels from areas of high initial stress to areas of low initial stress (assuming complete stress drop), then the crack can be slowed down. The crack equation of motion (2.73) and (2.74) can also be generalized by considering K_c (G_c) as functions of the position, so that $K_c \to K_c(R(t))$ or $G_c \to G_c(R(t))$. This corresponds to heterogeneous resistance to rupture on the fault, which can slow down (when the resistance increases along the crack path) or accelerate (when the resistance decreases) the crack. Curiously, as noted in Eshelby (1969), since no second or higher derivatives of $R(t)$ appear in the equations of motion, the crack front, regarded as a moving particle, has no inertia and its speed can suddenly change upon reaching a discontinuous jump in $\Delta\sigma$ or in rupture resistance.

The formulas (2.68) and (2.69) are exact at all times only for semi-infinite cracks. For finite cracks, it is valid at given x only for times t small enough to satisfy Eq. (2.66), before the arrival of waves from the left of the crack. For events (t, x) to the right of the crack that do not satisfy this condition, the decomposition of the set $S_0(t, x)$ changes to $S_0(t, x) = S_L(t, x) \cup S_c(t, x) \cup S_R(t, x)$ with $S_L(t, x) = \{(t', x') \in S_0(t, x);\ x' < L(t')\}$ and the solution (2.68) is no more applicable, because τ_{yz} is unknown on $S_L(t, x)$. However, if we could calculate the traction there, then we could put $-\Delta\sigma(t', x') = \tau_{yz}(t', x', 0)$ for (t', x') in $S_L(t, x)$ and use the formula (2.68) with $S_c(t, x) \to S_c(t, x) \cup S_L(t, x)$. The traction may be obtained iteratively

(see a similar description in Kostrov, 1975): Let $U^{(1)}$ be the set of points in $A^{(1)} = S_L(t, x)$ whose domains of dependence S include the *right* edge of the crack. Then we can calculate the traction on $A^{(1)} \backslash U^{(1)}$ from the left side analogy of formula (2.68). If $U^{(1)}$ is empty, then we are done. If not, we need to calculate the traction on the set $A^{(2)} = \bigcup_{(t',x')\in U^{(1)}} S_R(t', x')$. To do so, we repeat the iteration on $A^{(2)}$, exchanging the left and right sides. The iteration ends when $U^{(n)}$ is empty for some n. Since traction in each step of this ladder is given by an integral formula, this procedure leads to the appearance of additional multiple (double, triple...) integrals in the result (2.68). They correspond to repeated diffraction at the crack edges. Closed-form solutions of these integrals are typically unavailable and as pointed out by Madariaga (1976), it is more practical to solve the problem with numerical methods.

2.2 Elliptic shear cracks

2.2.1 Static elliptical cracks

Only few 3-D crack problems have known analytical solutions. One of them is that of a static elliptic crack. It is defined by $\gamma = \{(x, y, z) \in \mathbb{R}^3; \frac{x^2}{a^2} + \frac{y^2}{b^2} \leq 1, z = 0\}$ with constant shear stress drop on the crack face with general orientation

$$\Delta\boldsymbol{\sigma} = \Delta\sigma(\cos\psi, \sin\psi, 0). \tag{2.78}$$

At infinity, $\tau_{ij} \to 0$.

Assuming, without loss of generality, that $b \leq a$, the solution for the slip was found by Eshelby (1957, 1963) and can be written as:

$$\boldsymbol{s}(x, y) = b\frac{\Delta\sigma}{\mu}\boldsymbol{A}(b/a, \nu, \psi)\left(1 - \frac{x^2}{a^2} - \frac{y^2}{b^2}\right)^{1/2} I_\gamma(x, y). \tag{2.79}$$

Here, $\boldsymbol{A}$ is a constant vector field given by

$$\boldsymbol{A}(b/a, \nu, \psi) := (A_L(b/a, \nu)\cos\psi, A_T(b/a, \nu)\sin\psi, 0), \tag{2.80}$$

where A_L and A_T are functions of the aspect ratio $p = b/a$ and the Poisson's ratio ν:

$$A_L(p,\nu) = 2/\left(E(k) + \frac{\nu}{1-\nu}\frac{p^2}{k^2}\left[K(k) - E(k)\right]\right), \tag{2.81}$$

$$A_T(p,\nu) = 2/\left(E(k) + \frac{\nu}{1-\nu}\frac{1}{k^2}\left[K(k) - p^2E(k)\right]\right), \tag{2.82}$$

$$k{=}\sqrt{1-p^2}, \tag{2.83}$$

where $K(k)$ and $E(k)$ are the complete elliptic integrals of the first and second kind, respectively. For Poisson solids ($\nu = 1/4$, which is close to the value of $\nu = 0.27$ used in chapters 3 and 6), we plot the functions A_L and A_T in Fig. 2.1 (a similar figure is shown in Madariaga, 1979). They are decreasing functions of the aspect ratio p, with $A_L(p,\nu) > A_T(p,\nu)\ \forall p \in [0,1)$, and

$$A_L(1,\nu) = A_T(1,\nu) = \frac{8(1-\nu)}{\pi(2-\nu)}. \tag{2.84}$$

We point out that Eq. (2.79) has the form (2.8) required by Buckingham's theorem.

For circular crack ($a = b =: r$), we have

$$\Delta\sigma \boldsymbol{A}(b/a,\nu,\psi) = A_L(1,\nu)\Delta\sigma(\cos\psi,\sin\psi) = \frac{8(1-\nu)}{\pi(2-\nu)}\boldsymbol{\Delta\sigma}$$

and the slip is

$$\boldsymbol{s}(x,y) = \frac{\boldsymbol{\Delta\sigma}}{\mu}\frac{8(1-\nu)}{\pi(2-\nu)}r\left(1-\frac{\rho^2}{r^2}\right)^{1/2}, \tag{2.85}$$

where $\rho = \sqrt{x^2+y^2}$. This relation was explicitly derived by Neuber (1937) and Keilis-Borok (1959).

The average slip on the circular crack is:

$$\bar{\boldsymbol{s}} = \frac{1}{\pi r^2}\int_0^r\int_0^{2\pi}\boldsymbol{s}(\rho)\rho d\rho d\phi = \frac{16(1-\nu)}{3\pi(2-\nu)}\frac{\Delta\boldsymbol{\sigma}}{\mu}r. \tag{2.86}$$

Using this expression in the formula for the scalar seismic moment:

$$M_0 = \mu A|\bar{\boldsymbol{s}}|, \tag{2.87}$$

where $A = \pi r^2$ is the area of the crack, we obtain

$$M_0 = \frac{16(1-\nu)}{3(2-\nu)}\Delta\sigma r^3. \tag{2.88}$$

For the usually considered case of Poisson's solid ($\nu = 1/4$), this yields the often used relation (Madariaga & Ruiz, 2016):

$$M_0 = \frac{16}{7}\Delta\sigma r^3. \tag{2.89}$$

For a general aspect ratio, the solution (2.79) contains an important 3-D feature: unlike the simpler half-plane problems, the slip is generally not parallel to the stress drop. The only exception is when the stress drop is parallel to one of the axes of the ellipse, or for circular cracks (Eq. 2.85). The angle ζ between the slip and the semi-major axis is readily obtained from Eqs. (2.79) and (2.80):

$$\tan\zeta = \frac{A_T(b/a,\nu)}{A_L(b/a,\nu)}\tan\psi \tag{2.90}$$

We plot the deviation $\zeta - \psi$ for $\nu = 1/4$ and different aspect ratios b/a in Fig. 2.2. The deviation increases with decreasing aspect ratio, but even in the limit of zero aspect ratio (elongated crack), its maximum value is about $8°$(at $\psi \approx 41°$). For the limiting case of $\nu = 1/2$ (not shown), the maximum deviation increases to $20°$.

Note that since the slip points everywhere in the same direction, the fracture propagation mode is mixed almost everywhere on the crack edge, with pure anti-plane or in-plane fracture obtained only at four special points on the boundary. Taking the limit $a \to \infty$ or $b \to \infty$ yields the static anti-plane and in-plane, respectively, solutions for 2-D cracks (Kostrov & Das, 1984).

The displacement and stress outside of the crack were calculated by Kassir & Sih (1966) and Kostrov & Das (1984). Once again, inverse square root singularities for the stress appear. For stress drop oriented along the semi-major axis, $\Delta\boldsymbol{\sigma} = (\Delta\sigma, 0, 0)$, the stress-intensity factors for modes II and III are:

$$K_{II}(\phi, a, b, \nu) = \frac{1}{2}\sqrt{\pi b}\Delta\sigma A_L(b/a,\nu)\frac{n_x(\phi)}{(1-\nu)\sqrt{\|\boldsymbol{n}(\phi)\|}}, \tag{2.91}$$

$$K_{III}(\phi, a, b, \nu) = \frac{1}{2}\sqrt{\pi b}\Delta\sigma A_L(b/a,\nu)\frac{n_y(\phi)}{\sqrt{\|\boldsymbol{n}(\phi)\|}}, \tag{2.92}$$

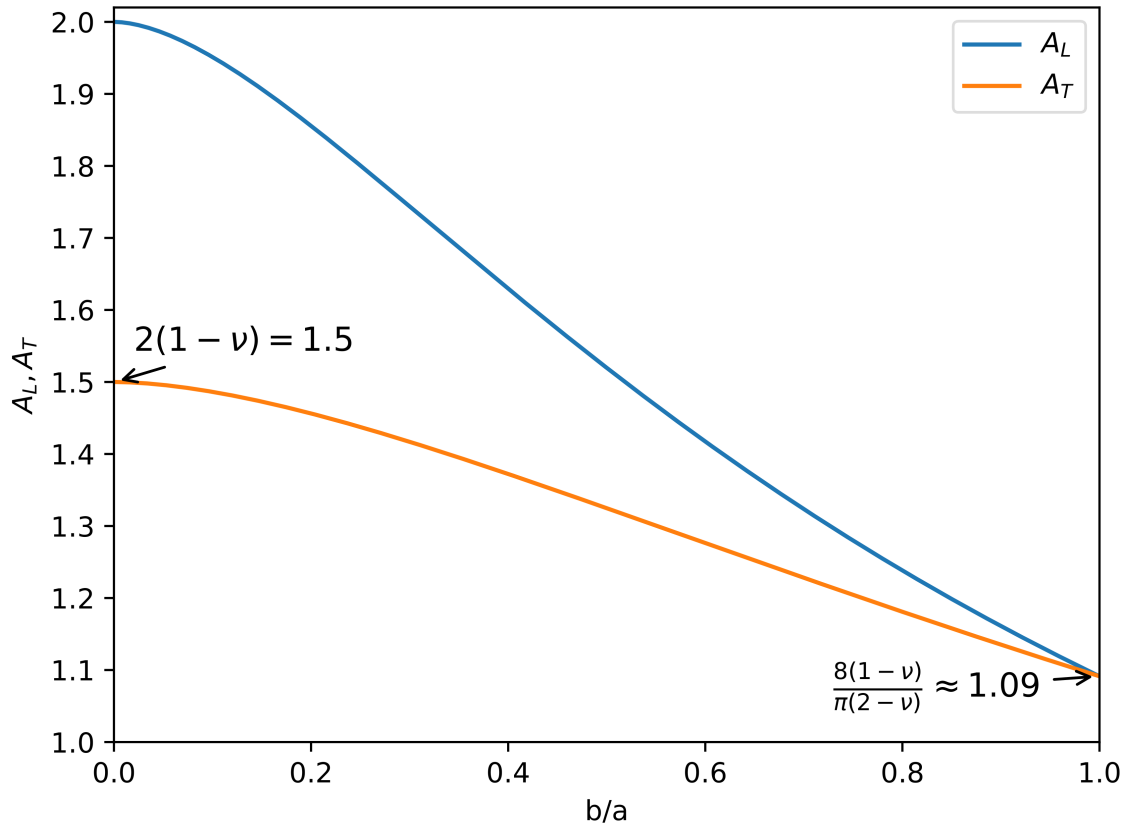

Figure 2.1: The coefficient functions A_L and A_T given by Eqs. (2.81) and (2.82) for $\nu = 1/4$.

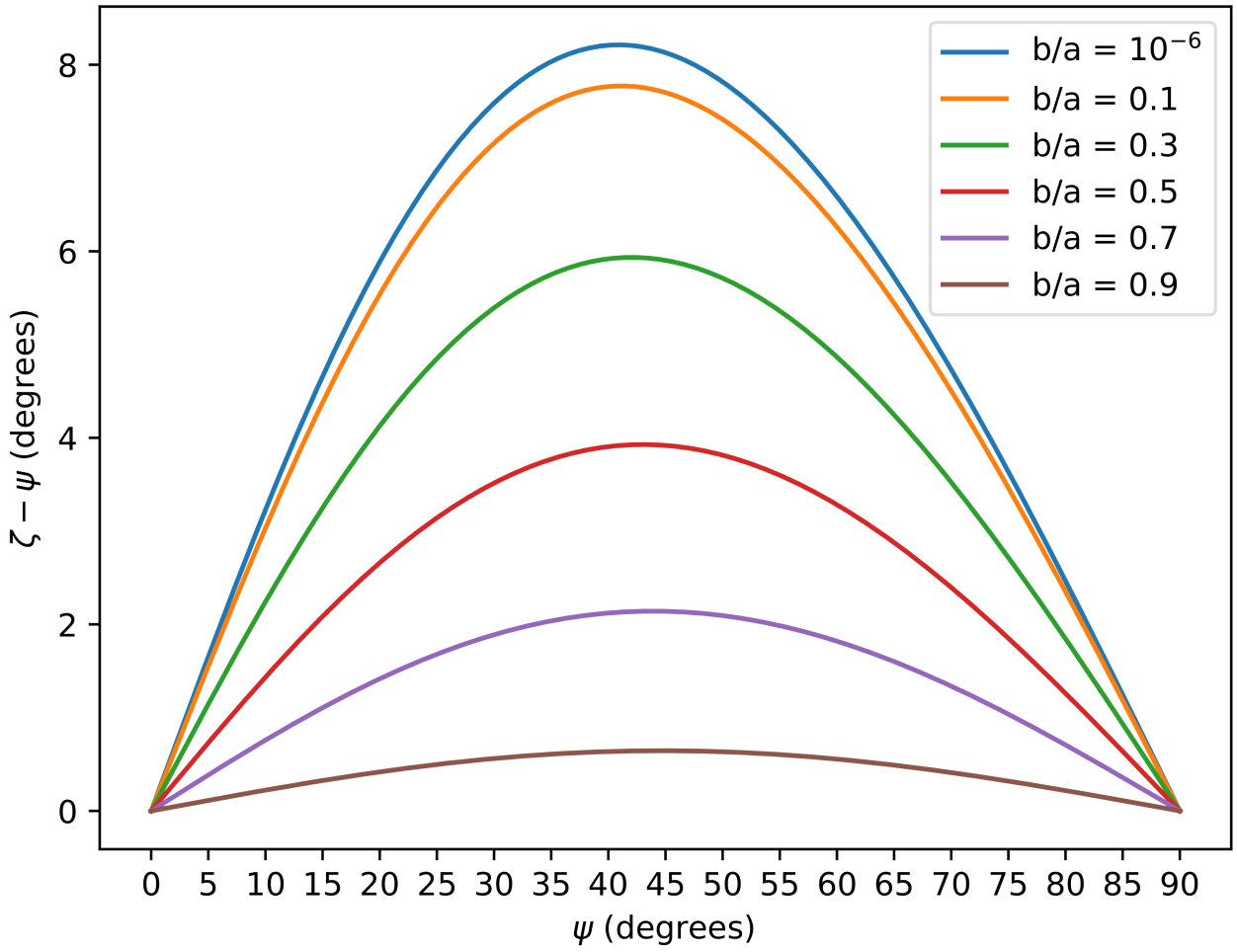

Figure 2.2: The deviation $\zeta - \psi$ between the direction of slip and stress drop as a function of the stress drop angle ψ, calculated from Eq. (2.90) for $\nu = 1/4$.

where ϕ is the parametric angle of the ellipse $x = a\cos(\phi), y = b\sin(\phi)$ and

$$\boldsymbol{n}(\phi) = \left(\frac{b}{a}\cos(\phi), \sin(\phi), 0\right).$$

The total stress-intensity factor

$$K(\phi, a, b, \nu) = \sqrt{K_{II}^2(\phi, a, b, \nu) + K_{III}^2(\phi, a, b, \nu)}$$

varies smoothly and slowly along the edge of the ellipse. It has extremes in the pure in-plane ($\phi \in \{0, \pi\}$) and the pure anti-plane ($\phi \in \{\pi/2, 3\pi/2\}$) directions, with $K(\phi = 0) = K_{II}(\phi = 0) > K_{III}(\phi = \pi/2) = K(\phi = \pi/2)$ if and only if $b/a > (1 - \nu)^2$. We plot $K(\phi, a, b, \nu)$ for $\nu = 1/4$ and four different aspect ratios in Fig. 2.3. For the case of circular crack and $\nu > 0$, the stress-intensity factor in the in-plane direction is always larger (by a factor of $\frac{1}{1-\nu}$) than the stress-intensity factor in the anti-plane direction. According to Irwin's criterion (assuming equal K_c for modes II and III), the circular crack is, therefore, less stable in the in-plane direction. As in the 2-D case, larger cracks are less stable than smaller cracks, since for circular cracks with radius r, K is proportional to $\Delta\sigma\sqrt{r}$. Indeed, the generality of this proportionality can be expected from dimensional analysis.

The energy release rate for the elliptic crack is a function of the position along the edge. Here, we calculate the energy release rate for a self-similarly expanding circular crack, for which we may use the Irwin relation (1.38) with functions (2.37) and (2.29) (Gao, 1988) to calculate the the energy release rate from the stress-intensity factor:

$$G(\phi, r, \mu, \nu) = \frac{K_{II}^2(\phi, r, \nu)(1 - \nu)}{2\mu} + \frac{K_{III}^2(\phi, r, \nu)}{2\mu}. \tag{2.93}$$

Using formulas (2.91) and (2.92) with $a = b = r$, we obtain:

$$G(\phi, r, \mu, \nu) = \frac{\pi r \Delta\sigma^2 A_L^2(1, \nu)}{8\mu}\left(\cos(\phi)^2\frac{1}{1 - \nu} + \sin(\phi)^2\right), \tag{2.94}$$

which again has extremes at the purely in-plane and anti-plane directions, and the in-plane value is larger than the anti-plane value if and only if $\nu > 0$. Averaging (2.94) over the

circumference of the circle and using the formula (2.84) yields:

$$\begin{aligned} G_{avg}(r,\mu,\nu) &= \frac{1}{2\pi}\int_0^{2\pi} G(\phi,r,\mu,\nu)d\phi \\ &= \frac{\pi r\Delta\sigma^2 A_L^2(1,\nu)}{16\mu}\frac{2-\nu}{1-\nu} \\ &= \frac{\pi r\Delta\sigma^2}{16\mu}\left(\frac{8(1-\nu)}{\pi(2-\nu)}\right)^2\frac{2-\nu}{1-\nu} \\ &= \frac{4}{\pi}\frac{1-\nu}{2-\nu}\frac{\Delta\sigma^2}{\mu}r. \end{aligned} \tag{2.95}$$

For the sake of completeness, we note that the stress-intensity factors for stress drop $(0,\Delta\sigma,0)$ along the semi-minor axis can be obtained by replacing A_L with A_T and rotating the coordinate system by 90 degrees. The stress-intensity factors for an arbitrary direction of the stress drop can be obtained as a superposition of the two special cases.

2.2.2 Self-similarly expanding elliptical cracks

As a final example, we look at the problem of an elliptic crack expanding self-similarly with constant speeds v_a and v_b in the directions of the major and minor axes, respectively, i.e. $\gamma(t) = \{(x,y,z) \in \mathbb{R}^3; \frac{x^2}{v_a^2} + \frac{y^2}{v_b^2} \leq t^2, z = 0\}$. The special problem of the expanding circular crack ($v_a = v_b$) was solved by Kostrov (1964) and the general elliptic problem was solved by Burridge & Willis (1969) and Richards (1973).

The solution for the slip is

$$\boldsymbol{s}(t,x,y) = (V_{0x},V_{0y})\sqrt{t^2 - \frac{x^2}{v_a^2} - \frac{y^2}{v_b^2}}I_{\gamma(t)}(x,y), \tag{2.96}$$

where V_{0x}, V_{0y} are proportional to the projections of $\Delta\boldsymbol{\sigma}$ to the semi-major and semi-minor axes, respectively, and are complicated functions of μ, ν and the crack speeds v_a and v_b. At the center of the crack, we have

$$\boldsymbol{s}(t,0,0) = (V_{0x}t, V_{0y}t), \tag{2.97}$$

so slip grows linearly with time and V_{0x}, V_{0y} are the corresponding slip rates. Thus, analogically

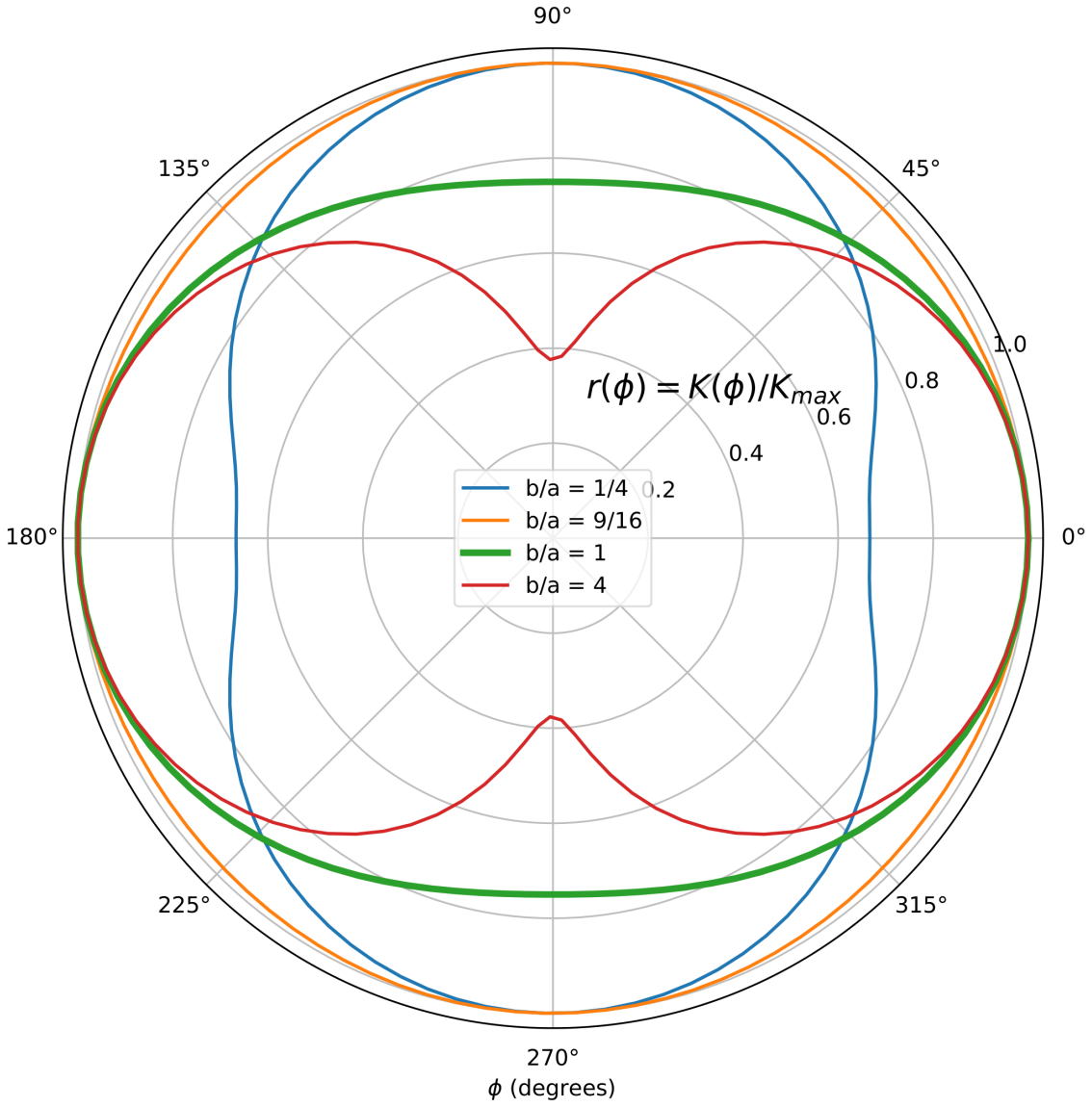

Figure 2.3: The total intensity factor $K(\phi)$ as a function of the elliptic parametric angle ϕ, normalized by its maximum value $K_{max} = \max_\phi K(\phi)$ for $\nu = 1/4$. The stress drop is oriented along $\phi = 0$.

to the case of self-similarly expanding straight crack, the solution is obtained from the static solution by replacing $a \to v_a t$, $b \to v_b t$ and multiplying each component by factors that do not depend on spatial or temporal coordinates.

The expression for the stress-intensity factors are too cumbersome to justify their inclusion here, but the anti-plane stress-intensity factor depends on the function $\gamma_\beta(v_n)$ (Eq. 2.20), evaluated at the local speed of propagation v_n, while the in-plane stress-intensity factor also depends on the function $P(v_n)$ (Eq. 2.33). As in the previous self-similar examples, the anti-plane and in-plane singularities vanish at the shear wave velocity β and the Rayleigh velocity c_R, respectively. These are again the limiting speeds in the pure mode directions. However, in mixed-mode directions, in which the slip is composed of both anti-plane and in-plane components, the in-plane component may surpass the Rayleigh velocity. This is because while the in-plane mode acts as an energy source for $c_R < v_n < \beta$, the anti-plane component acts as a sink, so the overall energy dissipation may still be positive (Richards, 1976; Andrews, 1994). Therefore, the energetic argument forbidding superRayleigh in-plane speed does not strictly apply to fracture at the mixed-mode directions.

In the following two chapters, important features of ruptures governed by the slip-weakening and the rate-and-state constitutive laws are reviewed. Focus is put on the main applications of each law. For the slip-weakening law, examined in chapter 3, this is the fast (seconds to tens of seconds) co-seismic evolution of slip-weakening cracks. We show example calculations in simple settings and review the literature on selected features. In chapter 4, we review basic properties of the rate-and-state law and its application to modeling the long-term evolution of faults, in particular models of seismic cycles.

3 Fast cohesive rupture: The linear slip-weakening law on almost-homogeneous faults

In this chapter, we briefly review important features of rupture governed by the linear slip-weakening constitutive law, which was introduced in subsection 1.3.2.1. Only shear fracture is considered here, i.e. the slip $\boldsymbol{s}$ has no component normal to the fault. The shear traction $\boldsymbol{T}_s$ is then equal to

$$\boldsymbol{T}_s(\boldsymbol{s}, \dot{\boldsymbol{s}}) = -F(s)\frac{\dot{\boldsymbol{s}}}{\|\dot{\boldsymbol{s}}\|}, \tag{3.1}$$

when $\dot{\boldsymbol{s}} \neq \boldsymbol{0}$. When $\dot{\boldsymbol{s}} = \boldsymbol{0}$, only an upper bound on the magnitude of the shear traction is imposed:

$$\|\boldsymbol{T}_s(\boldsymbol{s}, \dot{\boldsymbol{s}})\| \leq F(s). \tag{3.2}$$

Here, F is the shear strength given by:

$$F(s) \coloneqq \begin{cases} (T_u - T_d)(1 - s/D_c) + T_d & \text{for } 0 \leq s \leq D_c \\ T_d & \text{for } s > D_c \end{cases}, \tag{3.3}$$

and s is either the magnitude of slip $\|\boldsymbol{s}\|$ or the slip-path length $\mathfrak{s}$ (Eq. 1.20). The free parameters of the slip-weakening law are the yield strength T_u, the magnitude of dynamic friction T_d, and the characteristic weakening distance D_c (see Fig. 1.2).

In the absence of time-dependent boundary conditions, a completely homogeneous slip-weakening fault model with constant initial traction $\boldsymbol{T_i}$ and zero initial slip and slip rate leads either to a trivial solution (when the magnitude of the initial traction $\|\boldsymbol{T_i}\| < T_u$) or to rupture starting from everywhere on the fault (when $\|\boldsymbol{T_i}\| \geq T_u$), which is not realistic. Therefore, seed heterogeneity is introduced in slip-weakening models such that the slip starts from a small part

of the fault. The preparatory process in which quasi-static rupture transitions to fast, unstable rupture is called *nucleation*. For example, Andrews (1985) (in 2-D), and Bizzarri et al. (2001) or Weng & Ampuero (2020) (in 3-D) use a time-weakening scheme in which a patch of small strength is prescribed that expands from the origin with a constant speed, until spontaneous propagation takes over. Favreau et al. (2002) and Badea et al. (2004) prescribe a small volume of non-zero initial particle velocity. A comparison of different nucleation strategies can be found in Bizzarri (2010).

The most straightforward way of implementing nucleation is to directly introduce an initially overstressed nucleation zone (NZ), so that $\|\boldsymbol{T_i}(\boldsymbol{x})\| > T_u \ \forall \boldsymbol{x} \in \text{NZ}$. The traction inside the NZ can smoothly transition to the values at the rest of the fault, but it is commonly set equal to a constant vector with magnitude T_{nucl}. Moreover, to constrain the extent of the rupture, the fault is sometimes divided into a weakened patch, with low yield strength T_u, and the rest of the fault with a very large strength (e.g., $10 \cdot T_u$), so that rupture cannot propagate outside of the weakened patch.

In this thesis, we restrict our discussion to *almost-homogeneous* models, by which we mean planar fault models with homogeneous properties (either on a weakened patch or on the whole fault), except for the initial heterogeneity needed to initiate rupture. They are characterized by T_u, T_d, D_c, the direction of the initial traction, the magnitudes of initial traction T_e and T_{nucl} outside and inside, respectively, of the nucleation zone (with the constraints that $T_{nucl} \geq T_u \geq T_e > T_d$), and the geometry of the weakened patch and the nucleation zone.

The magnitude of the initial traction T_e is typically replaced by one of the following non-dimensional parameters: The first, so-called S-parameter, is defined as

$$S = \frac{T_u - T_e}{T_e - T_d}. \tag{3.4}$$

When the magnitude of the final traction is equal to T_d, S is the ratio of the distance of the initial stress (outside the NZ) from T_u to the total stress drop (see Fig. 1.2, with $T_i = T_e$). Since $\partial S/\partial T_e = (T_d - T_u)/(T_e - T_d)^2$ and $T_u > T_d$, S is a decreasing function of T_e. The other parameter, which we denote here by γ, is defined as

$$\gamma = \frac{T_e - T_d}{T_u - T_d}. \tag{3.5}$$

When the magnitude of the final traction is equal to T_d, the parameter γ is the ratio between

the total stress drop (outside the NZ) and the breakdown stress drop $T_u - T_d$. The two parameters are related as:

$$\gamma = \frac{1}{S+1}. \tag{3.6}$$

3.1 Example calculations

In this section, we show five example calculations with the linear slip-weakening law, calculated with the program FD3D_TSN (Premus et al., 2020). The code employs finite differences on a staggered grid of 4th order in space and of 2nd order in time. The elastodynamic equation is solved in the cuboid $\Omega = E_L \times E_W \times E_D$, where $E_X = [0, X]$ and L, W, D are its length, width, and depth, respectively. The fault Γ is one of the vertical faces of the cuboid, having dimensions $L \times W$. In the following examples, all the remaining faces are absorbing boundaries; we do not consider the effect of the free surface for simplicity (unlike the simulations in section 3.7 and chapter 6). The absorbing boundaries are implemented using the perfectly matched layers technique (Berenger, 1994). The frictional boundary condition at the fault is implemented using the traction-at-split-node method, following Dalguer & Day (2007). We set the initial particle displacement and velocity to zero and assume a homogeneous isotropic elastic medium. The version of the slip-weakening law that depends on the slip-path length $\mathfrak{s}$ (Eq. 1.20) is assumed. For models without strong heterogeneity, the results are similar to those of the version that depends on the slip magnitude (Bizzarri, 2014). In particular, gross (integral) quantities such as the seismic moment or the energy flux to the crack edge differ by at most 1%. The setup of the calculations is shown in Fig. 3.1 and their parameters are listed in Table 3.1.

In the first calculation (model 1), we set up a pseudo-2-D geometry by prescribing a weakened rectangular patch with initial conditions that are invariant along dip. The initial traction points up-dip and its magnitude T_{nucl} is constant on the whole weakened patch. The dynamic traction T_d is set to a large value of 1000 MPa, which prevents potential rotation of traction during the simulation (as discussed in section 3.7). The initial traction outside the patch is set to T_d.

These conditions lead to the evolution of an anti-plane crack with a fixed size. The traction and slip calculated at selected times along the middle horizontal cross-section of the fault are shown in Fig. 3.2. At the initial stage of rupture, the traction inside the crack starts falling

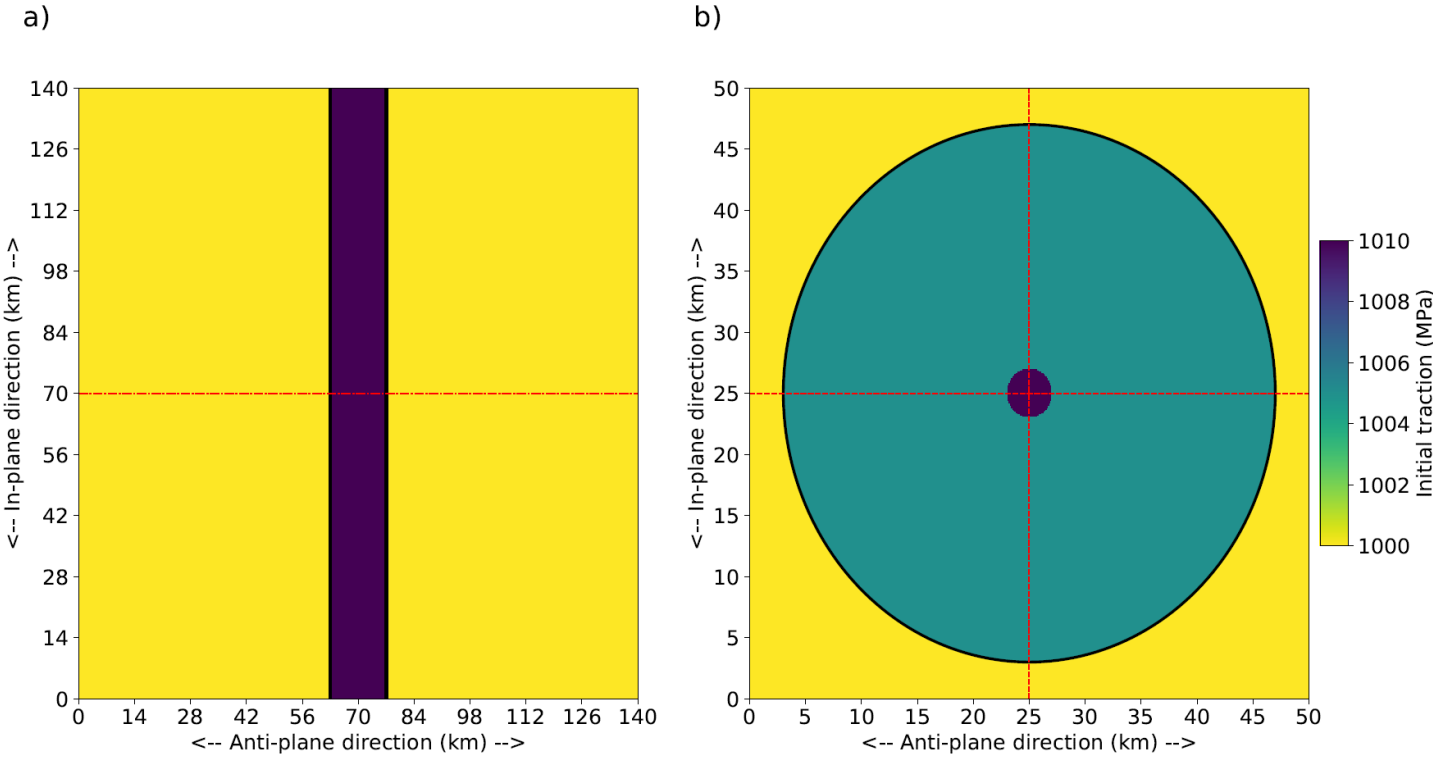

Figure 3.1: The magnitude of initial traction (which points from bottom to top) for a) model 1 and b) model 2b examined in section 3.1. The black curves show boundaries of the weakened patches inside of which rupture can develop. The red lines show cross-sections on which various fields are shown in Figs. 3.2-3.10. Three additional models, 2a, 2b, and 2d, are considered in this section. Model 2a differs from model 2b only by its smaller nucleation zone, while models 2c and 2d differ from model 2b only by the magnitude T_e of the initial traction inside the weakened patch (and outside the nucleation zone), see table 3.1.

Model 1			Models 2a-2d		
Parameter	**Meaning**	**Value**	**Parameter**	**Meaning**	**Value**
x_0 (km)	Along-strike position of the center of the patch	70	x_0 (km)	Along-strike position of the center of the patch	25
y_0 (km)	Along-dip position of the center of the patch	70	y_0 (km)	Along-dip position of the center of the patch	25
a (km)	Half-length of the weakened patch	7	a (km)	Radius of the weakened patch	22
T_u (MPa)	Yield strength	1010	T_u (MPa)	Yield strength	1010
T_d (MPa)	Dynamic friction	1000	T_d (MPa)	Dynamic friction	1000
D_c (m)	Characteristic slip-weakening distance	0.5	D_c (m)	Characteristic slip-weakening distance	0.25
			γ	Non-dimensional initial stress (Eq. 3.5)	0.5 (2a,b), 0.95 (2c), 0.65 (2d)
			x_{nucl} (km)	Along-strike position of the nucleation zone	25
			y_{nucl} (km)	Along-dip position of the nucleation zone	25
			r_{nucl} (km)	Radius of the nucleation zone	1.5 (2a), 2.0 (2b,c,d),
T_{nucl} (MPa)	Traction within the nucleation zone (i.e. the whole weakened patch)	1010.5	T_{nucl} (MPa)	Traction within the nucleation zone	1010.5
L (km)	Length of the fault	140	L (km)	Length of the fault	50
W (km)	Width of the fault	140	W (km)	Width of the fault	50
D (km)	Depth of the box	35	D (km)	Depth of the box	10
Δh (km)	Grid size	0.2	Δh (km)	Grid size	0.1
Δt (s)	Time step	0.003	Δt (s)	Time step	0.003
μ (GPa)	Shear modulus	48.37	μ (GPa)	Shear modulus	48.37
β (km/s)	Shear wave speed	3.95	β (km/s)	Shear wave speed	3.95
ν	Poisson's ratio	0.27	ν	Poisson's ratio	0.27

Table 3.1: Parameters for the example models (see also Fig. 3.1) discussed in section 3.1.

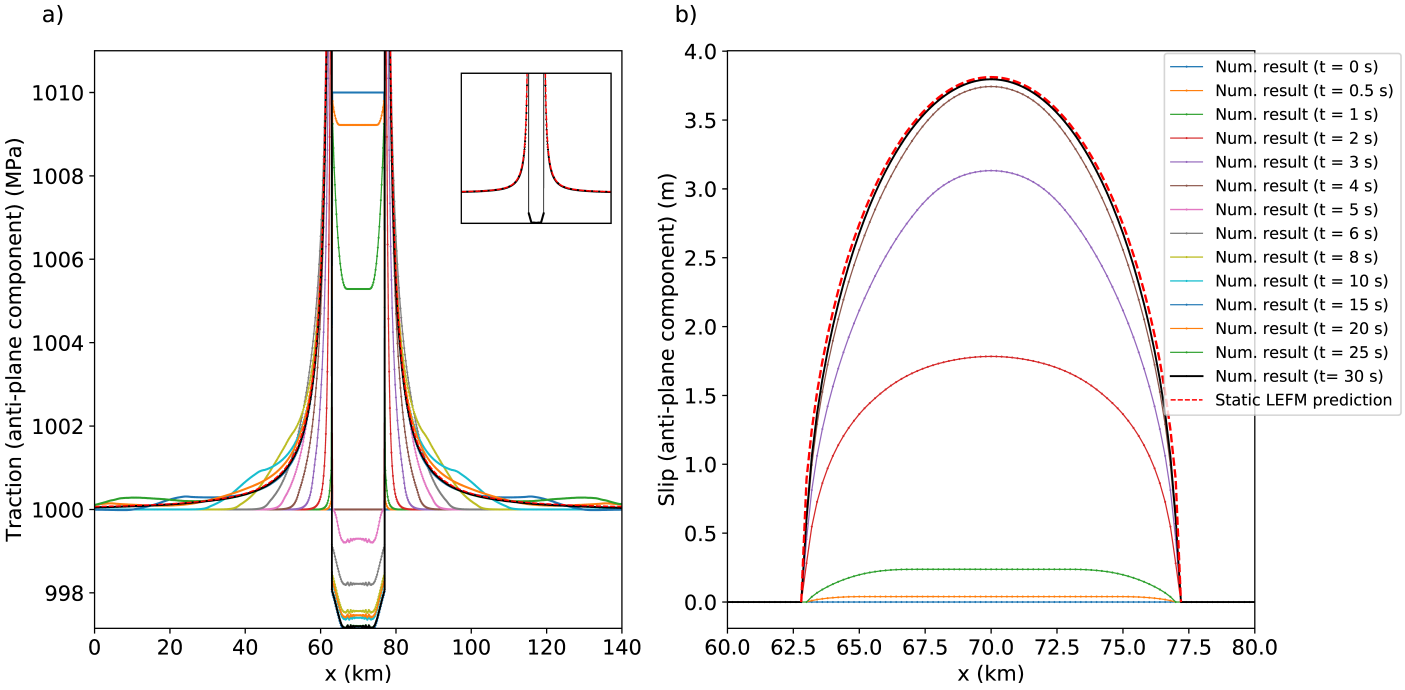

Figure 3.2: Evolution of a) anti-plane traction and b) slip along the middle horizontal cross-section of the pseudo-2-D model shown in Fig. 3.1a. The predictions of LEFM (Eqs. 2.43 and 2.42, respectively) for the final static traction and slip are shown as dashed red lines, see the inset in Fig. a) for a better comparison with the numerical result. Note that figure b) is zoomed to the crack surface.

from T_{nucl} to T_d. By 2 s, the slip on most of the crack has surpassed the value of $D_c = 0.5$ m and the traction has fallen to T_d. At around 5 s, the crack stops slipping and the traction inside the crack starts decreasing below T_d, eventually maintaining a nearly uniform and constant value near the center. Outside of the crack, traction starts increasing above T_d behind a pulse traveling at or near the Rayleigh velocity. At around 20 s a small additional pulse arrives from the lower and upper edges of the patch. By 30 seconds, static traction gets established. The distribution of the final traction outside of the crack has an excellent match with the theoretical static brittle crack distribution (2.43), when we put $\Delta\sigma = T_{nucl} - T_{min}$, where T_{min} is the minimum final traction inside the crack. Similarly, the slip inside the crack matches the theoretical elliptical static brittle distribution (2.42).

For the remaining four examples (models 2a-d) we prescribe the weakened patch and the nucleation zone as concentric circles at the center of the fault (Fig. 3.1b). The only parameters that vary across the models are the nucleation radius r (1.5 km for model 2a and 2.0 km for

models 2b,c,d) and the relative initial stress γ (Eq. 3.5, equal to 0.5 for models 2a,b, 0.95 for model 2c and 0.65 for model 2d), see Table 3.1.

Snapshots of the slip rate at different times for model 2a are shown in Fig. 3.3. The complete evolution of the slip rate at the horizontal (i.e. pure anti-plane) and vertical (i.e. pure in-plane) cross-sections passing through the center of the fault is shown in Fig. 3.4. The slip rate starts from the circular nucleation zone and very slowly expands. At this *initial stage* of rupture, the slip at no part of the fault has yet surpassed D_c. That happens at around 0.6 s at the center of the fault. At that point, the inner edge of the cohesive zone (which corresponds to the portion of the fault on which the slip is between 0 m and D_c) starts propagating outwards, along with the peak of slip rate ($\approx$ 0.8 m/s). By 1.5 s, the crack visibly stops being circular and instead gets elongated in the in-plane direction. However, it soon stops expanding and the rupture gets completely arrested before 3 s. The final length of the crack is 6 km in the anti-plane direction and 7.8 km in the in-plane direction. The final length of the cohesive zone is 1.0 km in the anti-plane direction and 1.4 km in the in-plane direction. Because the crack stops by itself, even before reaching the outer barrier, this style of rupture is called *spontaneously-* or *self-arrested* rupture (Galis et al. 2015; Xu et al. 2015).

The initial setup of model 2b differs from model 2a only by a larger value of the nucleation zone (1.5 km in model 2a vs 2 km in model 2b). The evolution of slip rate for model 2b is shown in Figs. 3.5 and 3.6. During the first second, the slip rate evolves quite similarly to model 2a (though the initial phase is 0.1 s shorter, lasting 0.5 s). However, instead of spontaneously arresting, the crack keeps propagating until it hits the edge of the circular patch. As in the first example, the rupture propagates faster in the in-plane direction at the beginning ($\approx$ 1-5 s), so that the contour of the slip rate resembles an in-plane-elongated ellipse. At later times ($\approx$ 5-7 s), however, the rupture in the pure anti-plane direction accelerates to about 95% of the shear wave speed, while the rupture in the in-plane direction accelerates to about 95% of the Rayleigh-wave speed, see Fig. 3.6. Since these speeds are similar (the Rayleigh speed being about 92% of the shear wave speed), the shape of the rupture starts resembling a circle. At 7 s and 7.5 s, the rupture hits the barrier in the in-plane and the anti-plane directions, respectively. This induces "healing" pulses that propagate from the edges of the patch back to its center and which act to decrease the slip rate. In the in-plane direction, the pulse moves with the P-wave speed (clearly visible in 3.6), while in the anti-plane direction, it moves with the S-wave speed. However, from around 9 s, a 3-D effect starts being visible in which the healing S-wave pulse from the pure anti-plane direction is overtaken by waves from other directions. Since the

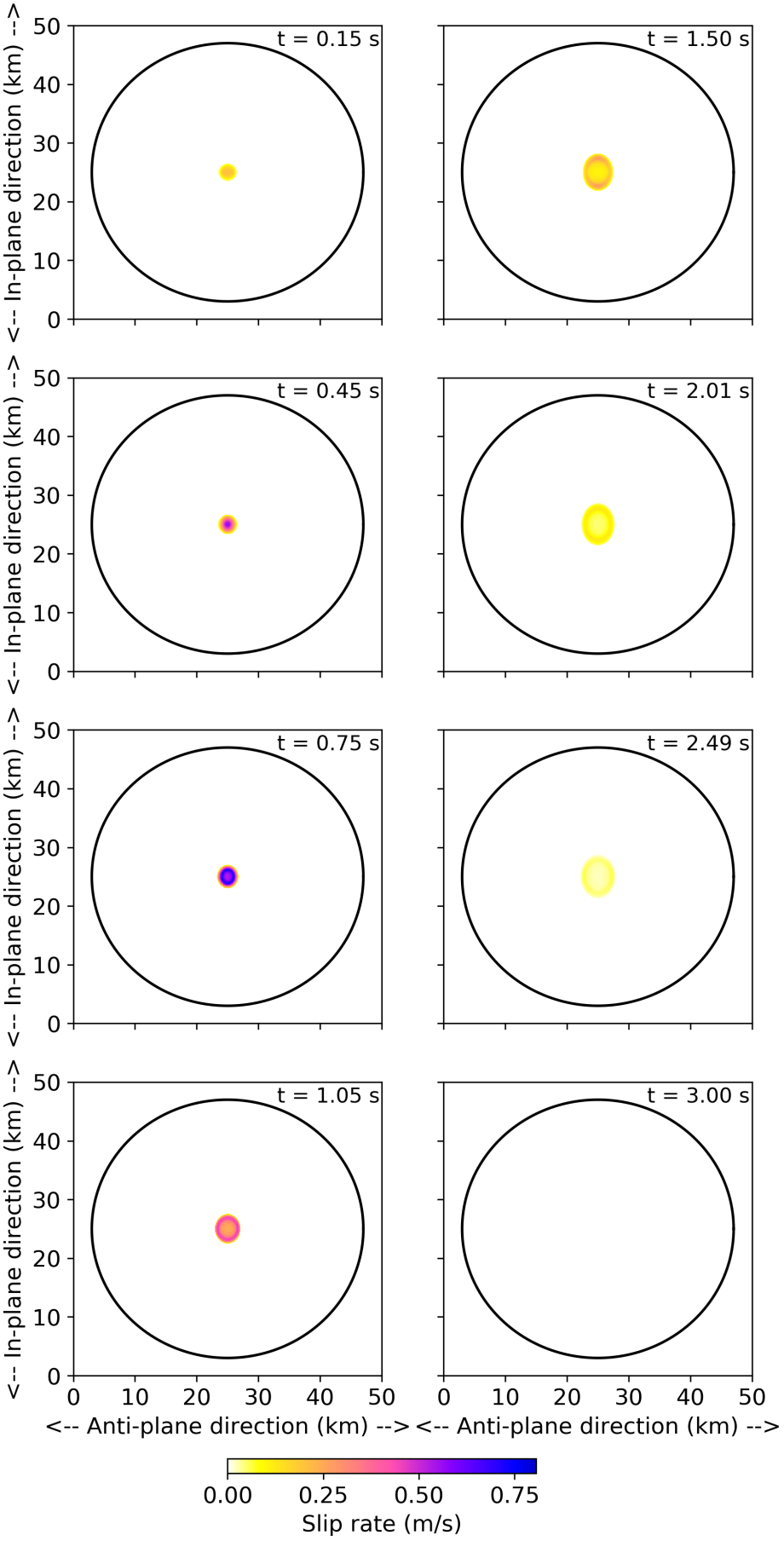

Figure 3.3: Snapshots of the slip rate for model 2a. The large black circle is the boundary of the weakened patch.

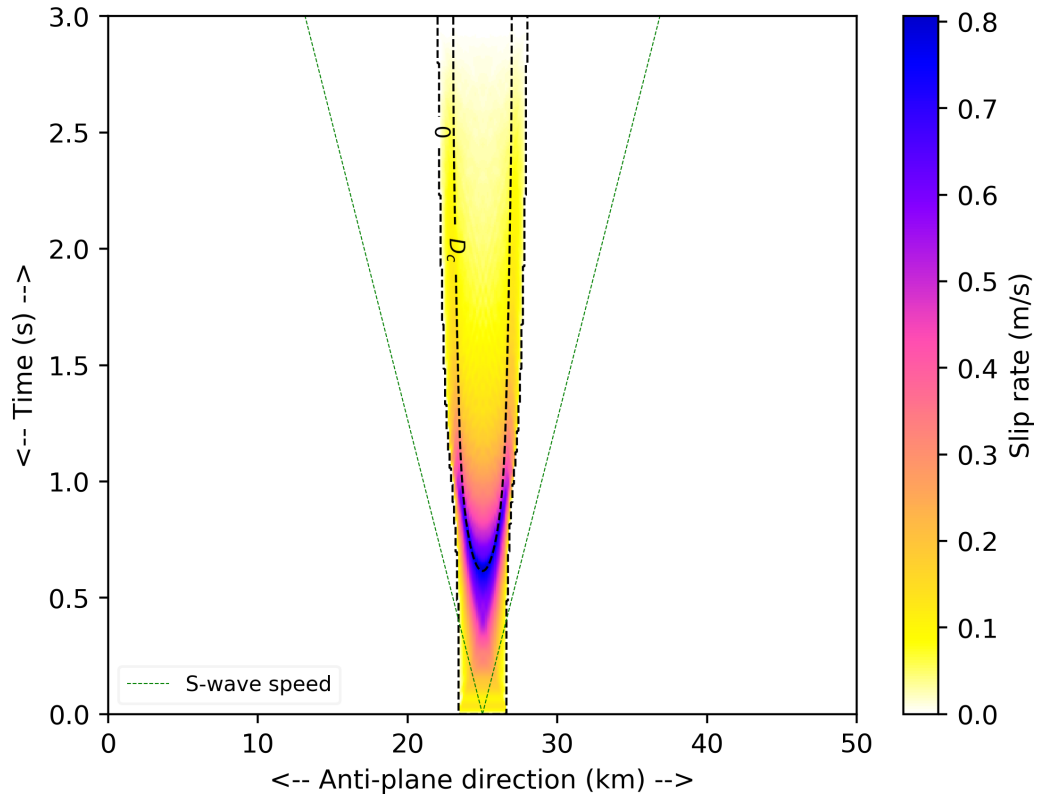

(a)

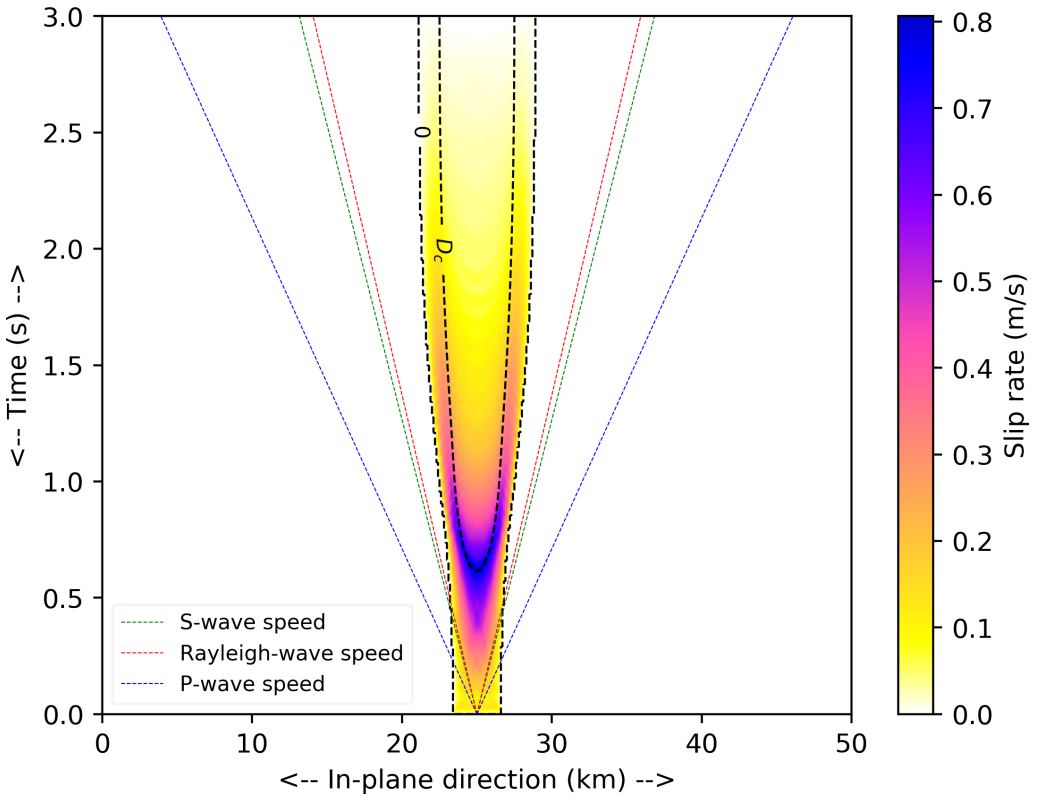

(b)

Figure 3.4: The evolution of slip rate for model 2a in a) the horizontal middle cross-section (pure anti-plane) and b) the vertical middle cross-section (pure in-plane). The dashed straight lines show S-wave (green), Rayleigh-wave (red), and P-wave (blue) speeds. The black dashed lines are contours of slip at $s = 0$ m and $s = D_c$, and delineate the cohesive zone.

healing pulses are faster in the in-plane direction than in the anti-plane direction (and also start propagating sooner), the shape of the slip rate contour again becomes asymmetrical, but this time elongated in the anti-plane direction. Note that there is an additional near-Rayleigh speed pulse, trailing behind the P-wave pulse in the in-plane direction, which momentarily increases the slip rate. However, the slip rate returns to its original value immediately after the passage of the pulse. At around 15 s, the slip stops.

In an absence of the outer barrier or another obstacle, the model would likely propagate indefinitely. The style of rupture of model 2b would then correspond to *sustained sub-shear* propagation. Using the bisection search method, we found that the critical radius separating the self-arresting and sustained sub-shear propagation for the assumed model parameters is about 1.55 km. We review various estimates for the critical radius in section 3.2. Unlike the previous example, the cohesive zone in both directions shrinks with time.

In Figs. 3.7 and 3.8, we show the evolution of slip rate for model 2c. This model differs from model 2b a larger value of the relative initial stress, $\gamma = 0.95$ (about twice as large as in model 2b). Consequently, a much greater amount of strain energy is available for the rupture. Indeed, we can see that at 1 s, the slip patch is already considerably larger than for model 2b. After the initial phase ($\approx$ 0.5 s), the rupture rapidly starts spreading at supershear speeds, nearly reaching the P-wave speed in the pure in-plane direction. In the anti-plane direction, it accelerates to the shear wave speed. As the rupture hits the edges of the circular patch ($\approx$ 3.6 s in the in-plane direction and 5.7 s in the anti-plane direction), the same healing waves appear as for model 2b and the rupture comes to a halt, which is briefly interrupted only by the Rayleigh-wave speed pulses. The maximum slip rate for this model is about twice as large as in model 2b. As in that model, the cohesive zone shrinks as the crack expands, which is especially pronounced in the anti-plane direction, where it almost vanishes, even before the rupture front hits the edge of the patch.

For the final example, we keep the same parameters as in example 2c, but reduce γ to 0.65, which corresponds to smaller initial stress. This results in the peculiar behavior shown in Figs. 3.9 and 3.10. At first, the rupture spreads with subshear speeds. However, at around 3 s, two small rupture fronts appear in the positive and negative in-plane direction ahead of the original front (by fronts, we mean in this context local maxima of slip rate, rather than the edges of the crack). These fronts, to which Madariaga & Olsen (2000) refer as "ears", travel with supershear speed. Once the ears develop, they propagate simultaneously with the original front, which remains subshear. At 5 s, the ears hit the edge of the circular patch. The resulting

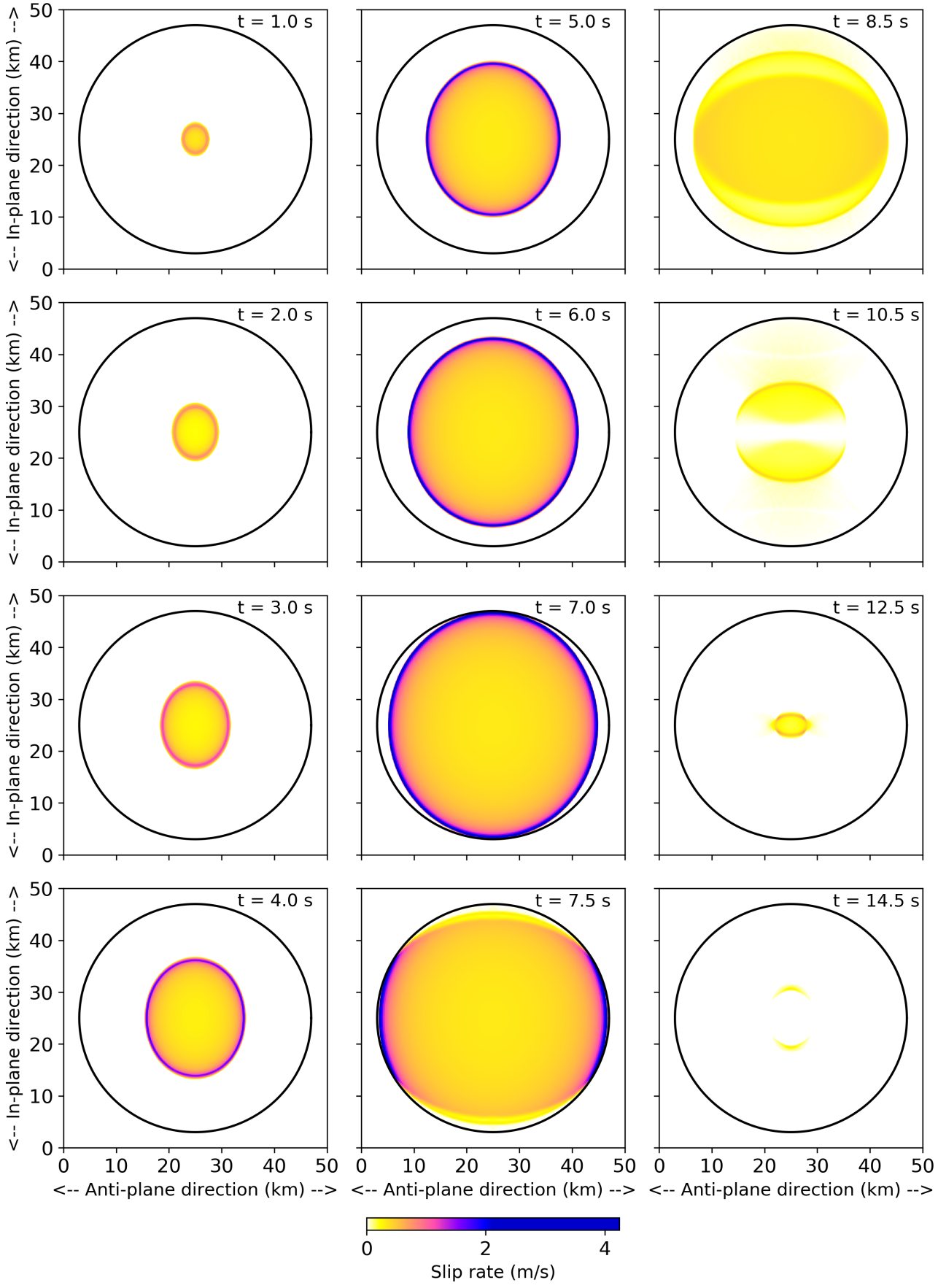

Figure 3.5: Same as Fig. 3.3, but for model 2b.

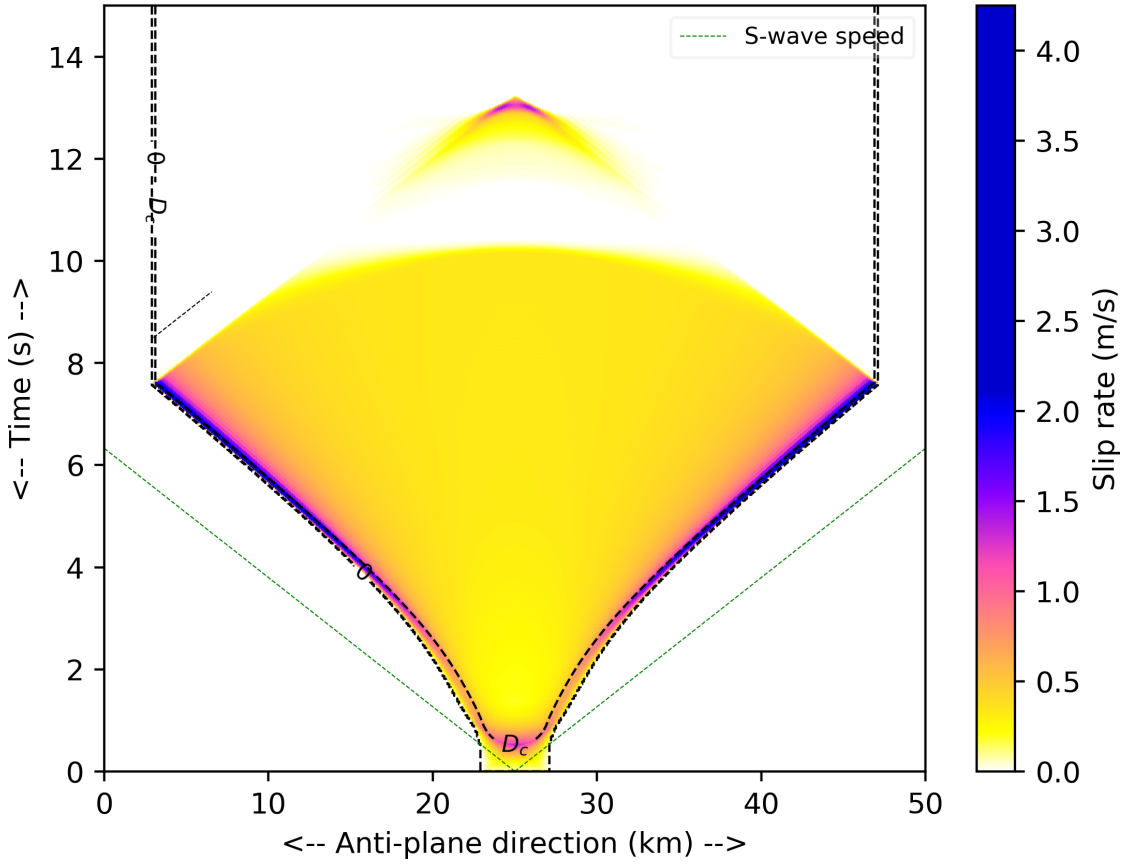

(a)

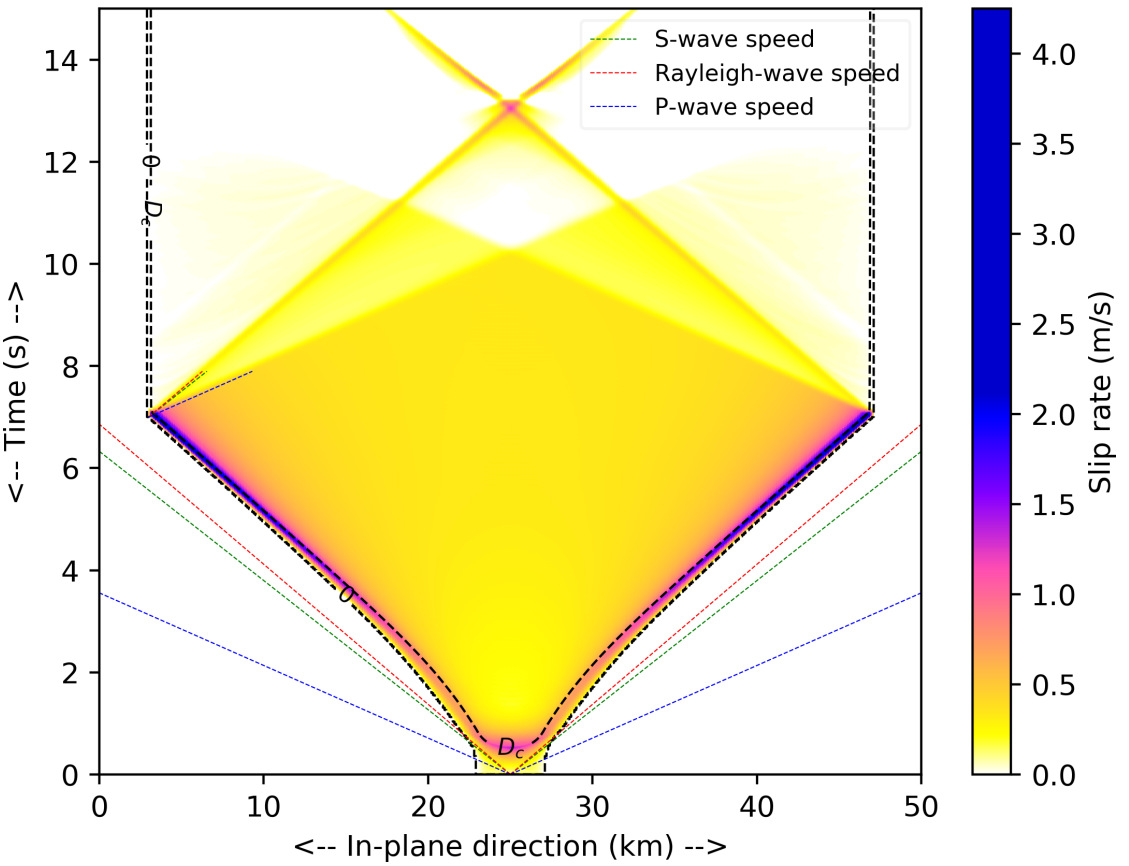

(b)

Figure 3.6: Same as Fig. 3.4, but for model 2b.

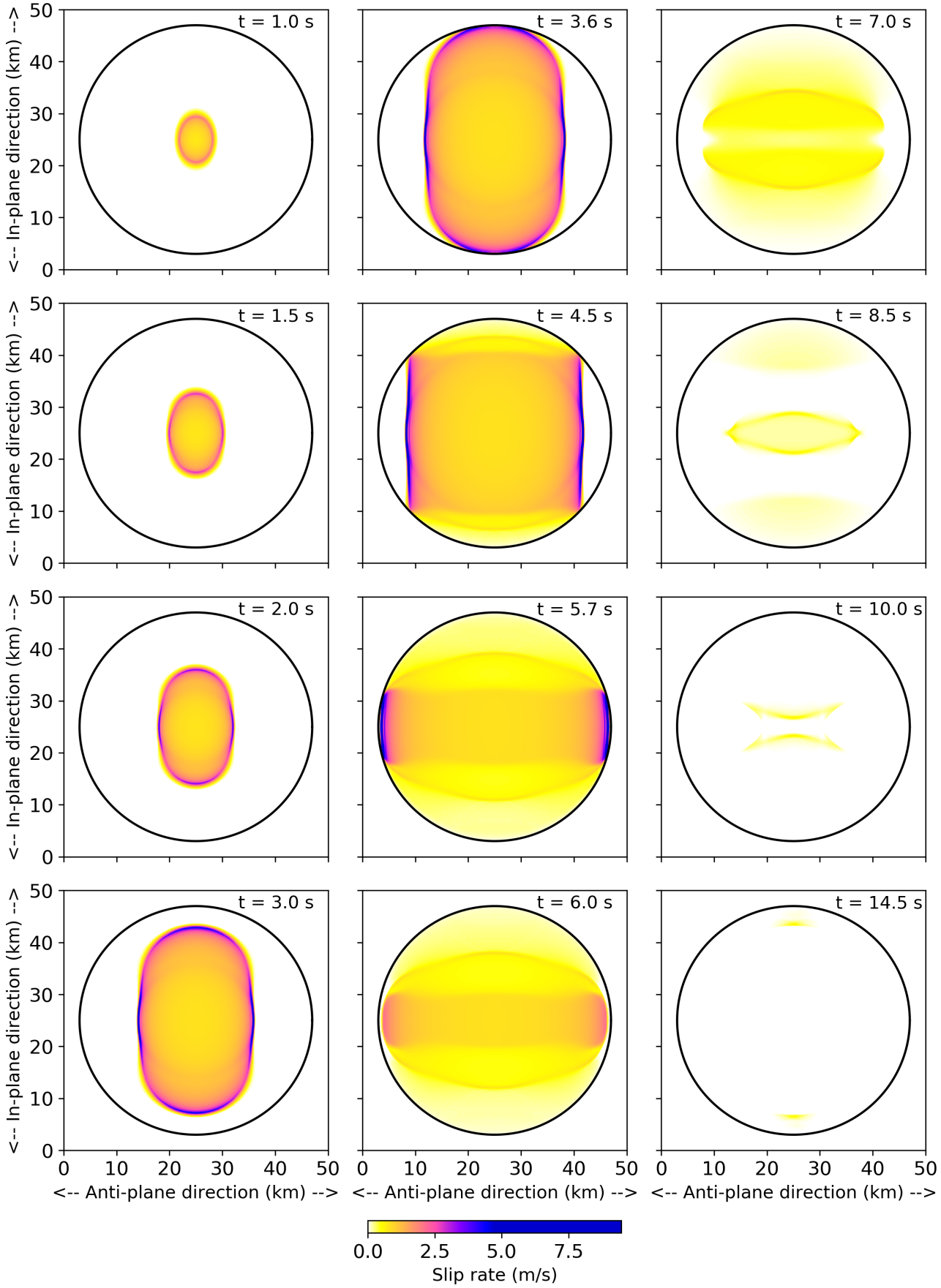

Figure 3.7: Same as Fig. 3.3, but for model 2c.

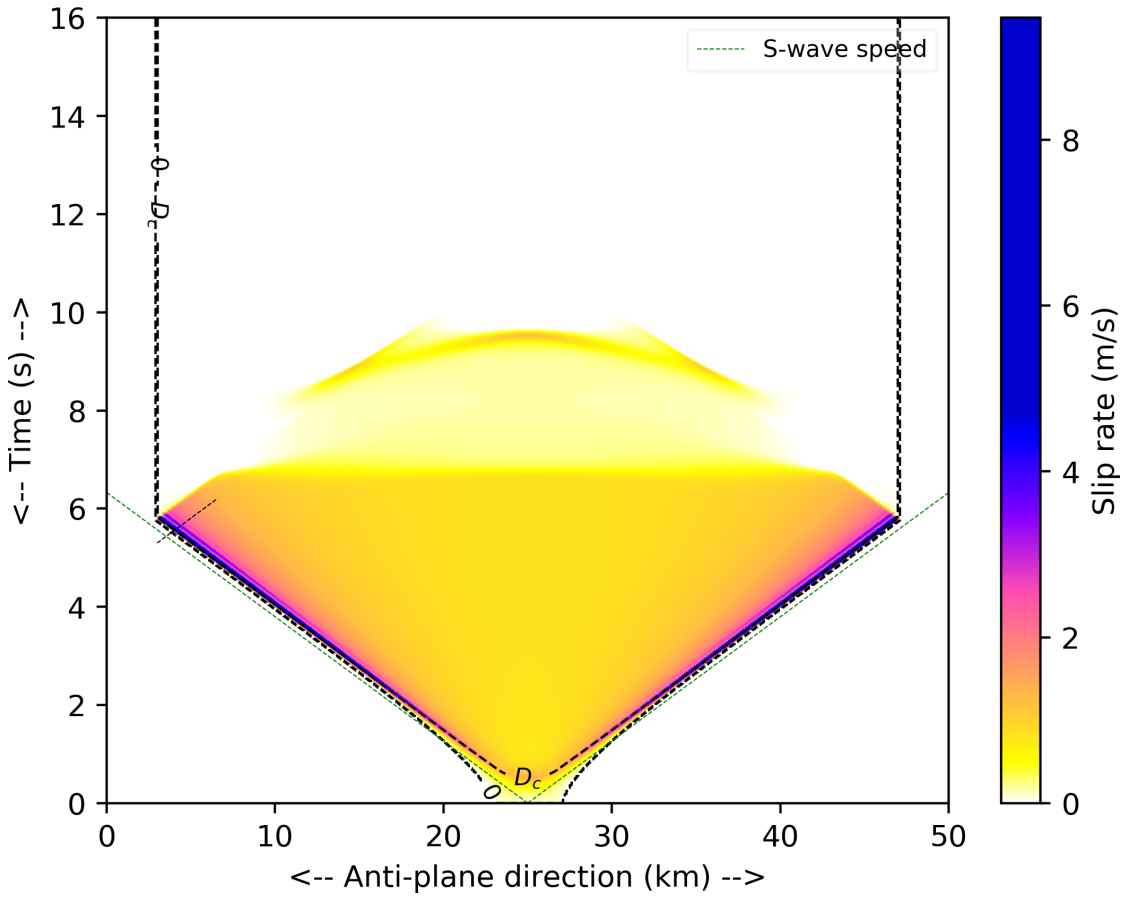

(a)

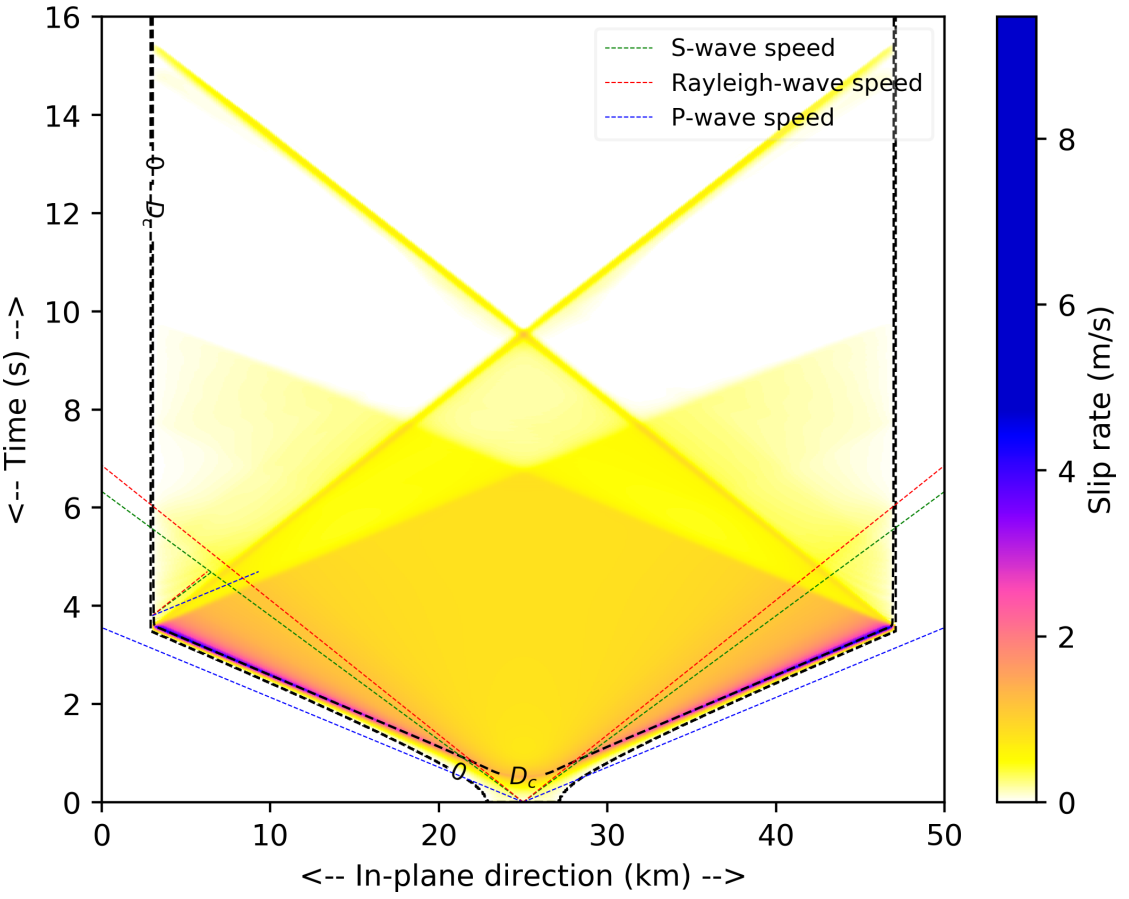

(b)

Figure 3.8: Same as Fig. 3.4, but for model 2c.

healing waves reduce the slip rate at the subshear front but do not slow the front down. Later, the subshear front also hits the boundary of the patch, generating additional healing pulses.

If there were no outer barriers, models 2c and 2d would be examples of *sustained supershear* ruptures. However, in model 2c, a direct transition to a single front supershear propagation is seen, while for model 2d, the transition is more gradual and the supershear front coexists with the original subshear front. We note that setting $\gamma = 0.6$ resulted in pure subshear rupture, while $\gamma = 0.7$ already resulted in the direct supershear transition. The conditions for the appearance of the ears hence seem delicate, though we are not aware of a systematic parametric study exploring this problem.

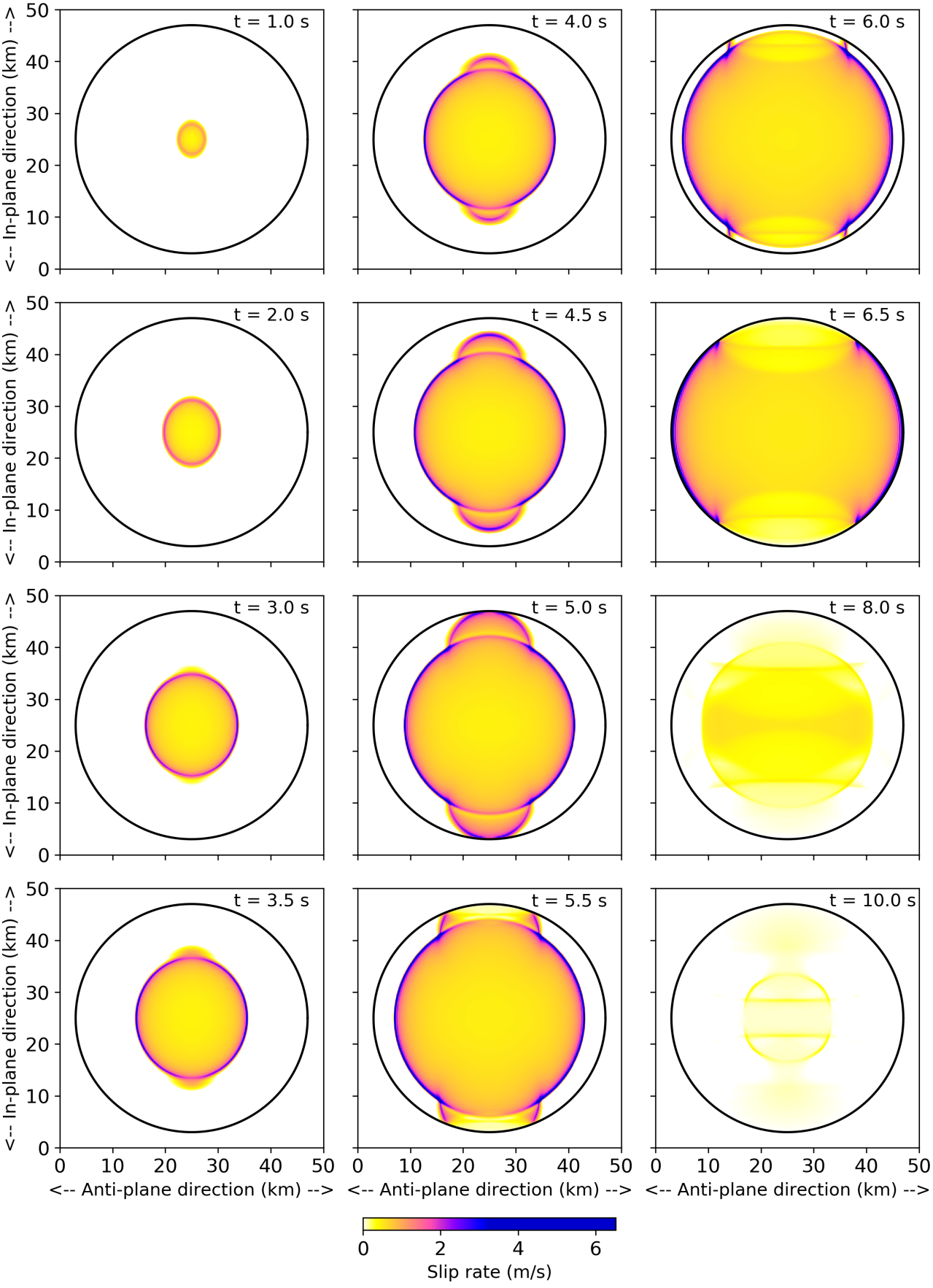

Figure 3.9: Same as Fig. 3.3, but for model 2d.

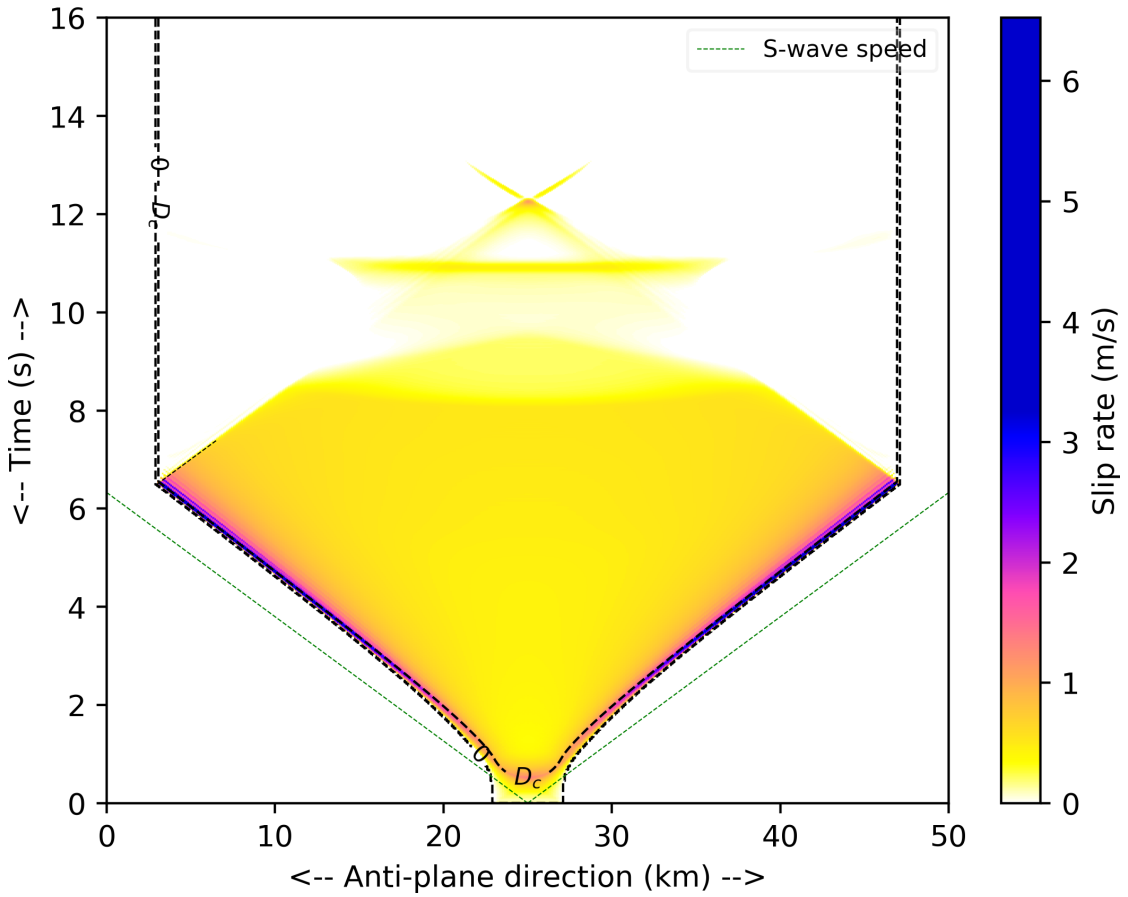

(a)

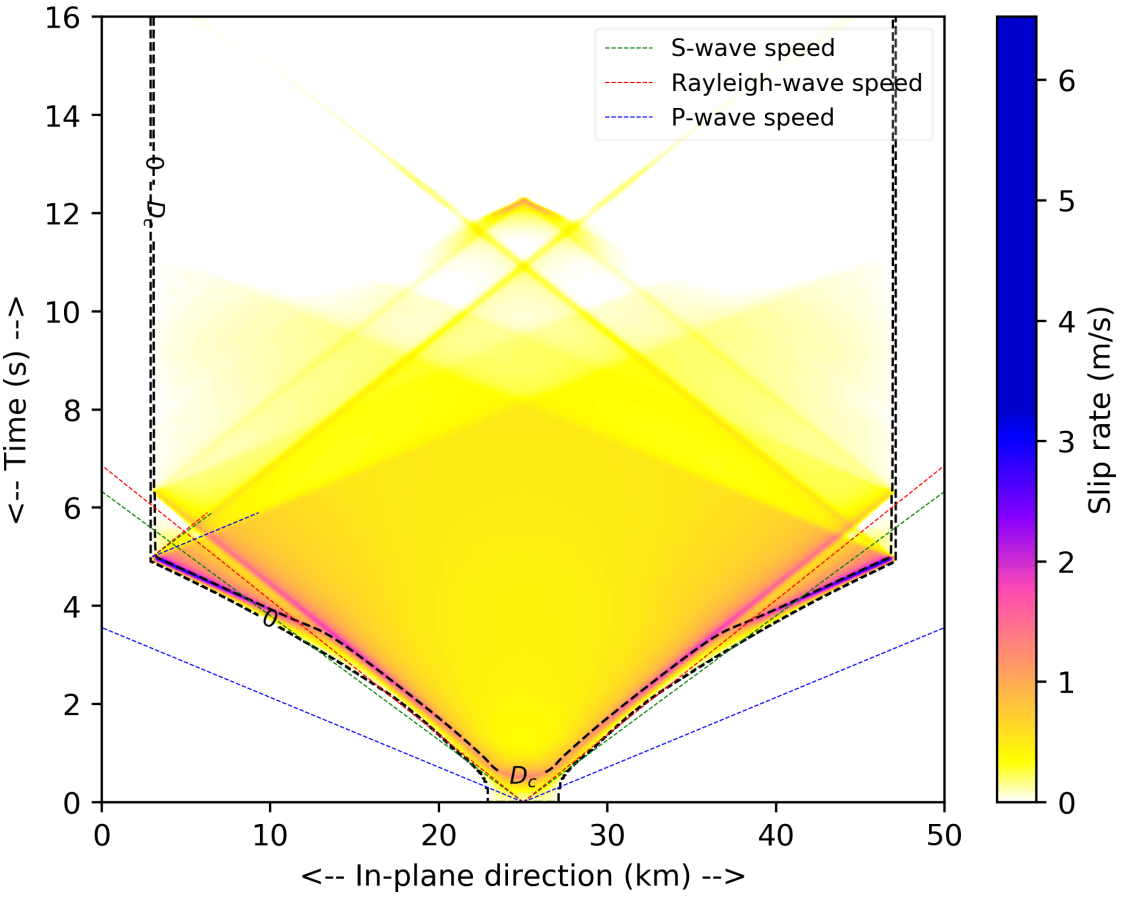

(b)

Figure 3.10: Same as Fig. 3.4, but for model 2d.

3.2 Critical nucleation size

In examples 2a and 2b of the previous section, one value of the nucleation radius resulted in self-arresting rupture, while another resulted in sustained propagation. Indeed, the conditions for successful nucleation have traditionally been described in terms of a critical nucleation size, expressed for a given geometry of the NZ as a function of parameters T_u, T_e, T_d, D_c and possibly T_{nucl}.

The oldest estimates (Andrews, 1976a,b; Day, 1982) for the critical sizes are based on the assumption that the rupture begins from a pre-existing crack with constant stress drop $\Delta\sigma = T_e - T_d$ and a small (relative to the crack size) cohesive zone, so the Griffith criterion for static brittle cracks may be applied. For straight 2-D cracks, the critical crack half-length for both anti-plane and in-plane modes is given by Eq. (2.47):

$$a_c = \frac{2\mu^*}{\pi\Delta\sigma^2} G_c, \tag{3.7}$$

where μ^* is defined in Eq. (2.17) and G_c is the critical energy release rate. An estimate of the latter quantity is obtained for the slip-weakening law by plugging Eq. (3.3) into the expression for the fracture energy density (1.43):

$$\begin{aligned} G_c &= \int_0^{D_c} (T_u - T_d)(1 - s/D_c) ds \\ &= \frac{1}{2}(T_u - T_d) D_c. \end{aligned} \tag{3.8}$$

Using $\Delta\sigma = T_e - T_d$ then leads to the critical nucleation half-length estimate of Andrews (1976b):

$$a_c^A = \frac{\mu^*}{\pi} \frac{(T_u - T_d) D_c}{(T_e - T_d)^2}. \tag{3.9}$$

Similarly, equating the average energy release rate of a circular crack, Eq. (2.95), with the critical rupture energy, Eq. (3.8), leads to the estimate for the critical radius of a circular NZ:

$$r_c^D = \frac{\pi(2-\nu)\mu}{8(1-\nu)} \frac{(T_u - T_d) D_c}{(T_e - T_d)^2}. \tag{3.10}$$

For $\nu = 1/4$, this yields

$$r_c^D = \frac{7\pi\mu}{24}\frac{(T_u - T_d)D_c}{(T_e - T_d)^2}, \tag{3.11}$$

which was presented in Day (1982). However, Madariaga & Olsen (2000); Galis et al. (2015) showed that except for small values of S, this formula overestimates the critical radius. For the example models 2a and 2b considered in section 3.1, it yields 4.5 km, almost three times the value of the actual critical radius, which is around 1.55 km. For model 2c, it yields 1.2 km (vs the actual value of 0.7 km) and for model 2d, it yields 2.6 km (vs the actual value of 0.7 km).

Uenishi & Rice (2003) considered the case of nucleation in 2-D realized by spatially peaked traction, slowly increasing above T_u. In this case, the slip slowly expands from the center of the stress peak, until a critical radius of the crack is reached, at which point the crack starts behaving unstably. It is assumed that up to that instant, the slip on the whole crack is less than D_c (the so-called initiation phase, see section 3.4). This assumption, along with the condition for instability of the slip at the onset of nucleation leads to an eigenvalue problem whose solution yields the critical nucleation half-length

$$a_c^{UR} \approx 0.579\mu^* \frac{D_c}{T_u - T_d}. \tag{3.12}$$

Unlike the Griffith criterion-based estimates, Eq. (3.12) does not depend on the stress drop $T_e - T_d$. Uenishi (2009, 2018) generalized the 2-D estimate to a 3-D case with an elliptical nucleation zone and found that the critical lengths of its semi-axes in the in-plane and anti-plane directions, respectively, are given by

$$a_c^U = h(\nu)\frac{\mu}{1-\nu}\frac{D_c}{T_u - T_d},\ b_c^U = h(\nu)\mu\frac{D_c}{T_u - T_d}, \tag{3.13}$$

where $h(\nu)$ is a function that can be expressed using the complete elliptic integrals and $h(\nu = 1/4) \approx 0.98$. Note that these expressions could again be written compactly using μ^*, but we emphasize here that there are two critical lengths for a single 3-D problem. For the usual case of $\nu > 0$, the critical ellipse is elongated in the in-plane direction.

Galis et al. (2015) investigated the nucleation problem for different shapes (square, circle and an ellipse with the aspect ratio of 4:3) of the nucleation zone in 3-D. From numerical experiments with the three shapes, they found that the critical transition from self-arresting

to sustained rupture is better described by a critical nucleation area, rather than critical length. They also found that for small values of the parameter S ($\lesssim 0.75$, which corresponds to $\gamma \gtrsim 0.57$), the nucleation area is independent of S and coincides with the area $\pi a_c^U b_c^U$ of the critical ellipse (Eq. 3.13) of Uenishi (2009, 2018). For larger values of S, they applied the Irwin criterion to analytically derive an expression for the critical area, which proved to accurately describe their numerical results. The explicit form of the expression is rather cumbersome, but they also provide an approximate formula (which slightly overestimates the exact formula) that reads (for $\nu = 1/4$):

$$A_c^G = \frac{(3\pi)^3}{2^{11}} \frac{(T_u - T_d)^2}{(T_{nucl} - T_e)(T_e - T_d)^3} \mu^2 D_c^2. \tag{3.14}$$

For a circular nucleation zone, this corresponds to the critical radius

$$r_c^G \approx 0.11\pi \frac{\mu(T_u - T_d)D_c}{\sqrt{(T_{nucl} - T_e)(T_e - T_d)^3}}. \tag{3.15}$$

Note that unlike the previous estimates, which were independent of T_{nucl}, r_c^G depends on T_{nucl} as $r_c^G \propto (T_{nucl} - T_e)^{-1/2}$. This leads to the intuitive result that small size of the nucleation zone can be compensated by a large value of T_{nucl}. However, the difference $T_e - T_d$ is more dominant, as $r_c^G \propto (T_e - T_d)^{-3/2}$. For the examples 2a,b in section 3.1 (which have $\gamma = 0.5$), the formula yields 1.65 km, which is 7% larger than the found critical radius. For examples 2c and 2d ($\gamma = 0.95$ and $\gamma = 0.65$), the radius $r_c^U = \sqrt{a_c^U b_c^U}$ corresponding to the area of the ellipse (3.13) (which should be the appropriate estimate, because $\gamma > 0.57$ in both cases) is 1.37 km, which overestimates the found radii by 80% and 17%, respectively.

Galis et al. (2019) further investigated the nucleation problem for rectangular nucleation zones of varying aspect ratios. They found that depending on the aspect ratio, the critical transition is either controlled by the nucleation area (for aspect ratios close to 1, which is the case discussed by Galis et al., 2015), by the shorter length (for very large aspect ratios), or by neither of the two (for intermediate aspect ratios, precise boundaries for these three regimes are described in the paper). In the length-controlled regime, the rupture problem effectively behaves as in 2-D. In this regime, if $S \lesssim 2.75$, the critical length is again independent of S and the results coincide with the 2-D formula (3.12) of Uenishi & Rice (2003). Note that the transitional value of S is larger for the 2-D geometry than for the 3-D geometry. For $S \gtrsim 2.75$, they derived an analytical formula for the critical length. Here, we again show only

the approximate version, which reads

$$a_c^G \approx 0.12\mu^* \frac{D_c(T_u - T_d)}{(T_{nucl} - T_e)(T_e - T_d)}. \tag{3.16}$$

Unlike the 3-D case (3.15), the powers of $T_e - T_d$ and $T_{nucl} - T_e$ are the same in this formula.

3.3 Directional asymmetry of the rupture propagation

As seen in the example calculations shown in Figs. 3.3-3.10, even though the initial crack (i.e. the nucleation zone) is circular, the evolution of rupture is not axially symmetrical - the crack soon becomes elongated along the in-plane direction (which coincides with the direction of initial traction). This could have been anticipated from section 2.2.1, where it is shown that for static brittle circular cracks, the stress-intensity factor and the energy release rate attain maxima and minima in the in-plane and anti-plane direction, respectively. In fact, according to Galis et al. (2015), the rupture becomes elongated regardless of the initial shape. According to Madariaga et al. (1998), the reason for the in-plane elongation is that the radiation pattern of stress S waves radiated from the crack has a peak in the in-plane direction, but not in the anti-plane direction. The in-plane elongation is also seen in the study of Favreau et al. (2002) on the initial phase of rupture, which we discuss in the following section.

3.4 Initial phase of rupture

In the *initial phase* of rupture, when the slip has not yet exceeded D_c at any point on the fault, the traction is an affine function of slip. This was first exploited by Campillo & Ionescu (1997), who found an analytical solution for this phase in a 2-D unbounded anti-plane geometry. They assumed that the initial traction on the fault is everywhere on the verge of instability, $\|\boldsymbol{T}_i(\boldsymbol{\xi})\| = T_u \ \forall \boldsymbol{\xi} \in \Gamma$. The increment of traction on the fault during the initial phase is then negatively linearly proportional to the slip and the fracture problem reduces to a system of linear partial differential equations (with the linear wave equation in the bulk and the linear friction law on the fault). Campillo & Ionescu (1997) were able to transform the problem to a 2-D wave-equation on a half-plane with homogeneous boundary conditions and used the Fourier transform method to find its solution. The solution can be divided into a *wave* part and *a dominant* part. The wave part oscillates with time and soon becomes

negligible in comparison to the dominant part, which has approximately exponential growth. Assuming zero initial displacement and small initial velocity perturbation that quickly decays with distance from the fault, they numerically calculated the evolution of slip rate in the initial phase and compared it to the analytical expression for the dominant part. They found that the two have an excellent match, with maxima of velocity differing at most by a few percent.

An insight into the problem is obtained when it is solved by decomposing the displacement field into functions of the form $\exp(\beta\lambda_k t)u_k(\boldsymbol{x})$. This leads to an eigenvalue-eigenfunction problem with eigenvalues λ_k^2. Campillo & Ionescu (1997) showed that the eigenvalue spectrum (which is continuous, $k \in \mathbb{R}$, as the problem domain is infinite, and real, because the eigenvalue problem is self-adjoint; Favreau et al., 1999) is constrained by the condition

$$\lambda_k^2 < \alpha_c^2, \tag{3.17}$$

where

$$\alpha_c = \frac{T_u - T_d}{\mu D_c} \tag{3.18}$$

is proportional to the weakening rate of the SW law and has the dimension of inverse length. Moreover, the dominant part corresponds to the non-negative part of the spectrum, i.e. $\lambda_k^2 \in [0, \alpha_c^2] \Leftrightarrow \lambda_k \in [-\alpha_c, \alpha_c]$. For an infinite domain, the eigenfunctions are plane-waves and it can be shown that the on fault spatial wavenumbers k lie in the same range as the λ_k, $k \in [-\alpha_c, \alpha_c]$. This can be physically interpreted as the existence of a minimum length-scale for the initiation problem:

$$L_c = \frac{\pi}{\alpha_c}. \tag{3.19}$$

We note that this length is proportional to the critical nucleation length (3.12) of Uenishi & Rice (2003), which is in fact derived from an equivalent eigenvalue problem.

Campillo & Ionescu (1997) also derived an approximate relation (with an error of about 7% when compared to their numerical calculation) for the duration of the initial phase (initiation time), finding that it is approximately proportional to the inverse of $\beta\alpha_c$ and only weakly depends on the amplitude of the initial perturbation. Favreau et al. (1999) directly used the eigenvalue approach to study the same problem for mode II and derived analogical results. They found that the wavenumbers k for the dominant part now lie in the range $[-\alpha_c(1-\nu), \alpha_c(1-\nu)]$, so the in-plane characteristic length $L_c = \pi/k_{max}$ is larger than the characteristic anti-plane length by the familiar factor $\frac{1}{1-\nu}$. To unify the results for the in-plane and anti-

plane, one may thus replace α_c with α_c^*, obtained by simply replacing μ in Eq. (3.18) with μ^* (Eq. 2.17). The bound on the dominant wavenumbers can then be written as:

$$|k| \leq \alpha_c^*. \tag{3.20}$$

The case of the finite 2-D anti-plane fault was examined by Dascalu et al. (2000). He showed that on the finite fault, the spectrum of λ_k^2 is discrete ($k \in \mathbb{N}$) and the number N of eigenvalues corresponding to the dominant part is finite. In addition, if the product $L\alpha_c$, where L is the length of the fault, is less than a certain critical value, then $N = 0$, which means that the dominant part vanishes and the fault is stable. Like Campillo & Ionescu (1997) and Favreau et al. (2002), they derived a formula for the initiation time, which additionally depends on the size of the fault (diverging as L reaches a critical threshold between instability and stability).

Favreau et al. (2002) studied and solved the initiation problem in 3-D. Like for the 2-D problems, the dominant part of their solution fits the numerical solutions very well. On an infinite domain, the dominant wavenumber spectrum is again continuous and bounded, with the bound now depending on the polar angle $\theta = \operatorname{atan2}(k_y, k_x)$ with respect to the pure in-plane direction:

$$\|\boldsymbol{k}\| \leq k_c(\theta) = \frac{\alpha_c}{\frac{1}{1-\nu}\cos(\theta)^2 + \sin(\theta)^2}. \tag{3.21}$$

For in the pure in-plane ($\theta = 0, \pi$) and anti-plane directions ($\theta = \pm\pi/2$), this precisely corresponds to the 2-D result (3.20). In analogy to Eq. (3.19), they defined a characteristic slip patch:

$$r(\theta) \leq \frac{\pi}{k_c(\theta)}, \tag{3.22}$$

which has a roughly elliptical shape elongated in the in-plane direction. Indeed, the maximum wavelength of the dominant mode in the in-plane direction is $\frac{1}{1-\nu}$ times larger than for the anti-plane direction. Their numerical results show that a crack started from a small spherical perturbation of particle velocity centered at the fault rapidly starts extending with a shape similar to $r(\theta)$. After the front passes through $r(\theta)$, the similarity disappears, but the in-plane elongation remains.

Favreau et al. (2002) also studied the case of a finite weakened patch surrounded by areas of infinite yield strength. In this case, the dominant spectrum is discrete. For unstable faults, the slip soon becomes dominated by the mode (eigenfunction) $\boldsymbol{s}_0(\boldsymbol{x})$ with the largest eigenvalue λ_0, i.e. it evolves in time as $\boldsymbol{s}(t, x) = \boldsymbol{s}_0(\boldsymbol{x}) \exp(\lambda_0 t)$. The duration of the initiation phase

scales as λ_0^{-1}. The eigenvalue λ_0 depends on the shape of the patch and non-linearly increases (for a given shape) with the patch area A. As $A \to \infty$, $\lambda_0 \to 1$. On the other hand, $\lambda_0 \to 0$ as $A \to A_c$ for some critical area A_c. Below A_c, the fault behaves stably. For patches geometrically similar to the characteristic slip patch (3.22), A_c is about $1.3 - 1.6$ times of the critical patch area.

3.5 Rupture regimes and supershear propagation

For the purely anti-plane mode of rupture, numerical experiments show that the rupture speed is always smaller than the shear wave speed β (as seen in all the examples in section 3.1 and confirmed by numerical simulations of Andrews, 1976b; Day, 1982; Bizzarri & Das, 2012; Xu et al., 2015; and many others), in accordance with the predictions of linear elastic fracture mechanics. In contrast, supershear rupture speeds appeared in the very first published 2-D in-plane numerical simulations with the slip-weakening law (Andrews, 1976a). In these simulations, the crack first spreads bilaterally and asymptotically accelerates to the Rayleigh speed c_R (which is the limiting speed of steady-state solutions in LEFM under the Griffith or Irwin criteria). A stress-peak propagating at shear wave speed is radiated from the rupture-front. Eventually, the peak gets large enough to surpass the strength T_u and a secondary, *daughter,* crack propagating near the shear wave speed is formed ahead of the main, *mother* crack. The daughter crack is spatially separated from the mother crack, so there is momentarily an unfractured space between the two cracks. After some time, they merge and the new fracture front soon starts propagating at a speed slightly exceeding the Eshelby speed $c_E = \sqrt{2}\beta$. This process of transition from sub-shear to supershear rupture speed was predicted analytically by Burridge, 1973 for self-similarly expanding cracks governed by the classical Coulomb friction model (based on analytic calculations, Burridge et al., 1979 also conjectured that supershear speeds below v_E are unstable). It is referred to as the *mother-daughter*, or the *Burridge-Andrews* mechanism. It was also observed in laboratory experiments (Xia et al., 2005; Mello et al., 2016). The "forbidden zone" of rupture speeds (c_R, β) (subsection 2.1.1.2) is never reached by this mechanism.

Geubelle & Kubair (2001) conducted 2-D numerical experiments in which they also observed the Burridge-Andrews mechanism but discovered that it is not the only way in which rupture can transition to supershear speeds. Their simulations show that the supershear transition can also occur by a direct, sudden acceleration of the crack front from subRayleigh to supershear

speeds (as seen in the 3-D model 2c of section 3.1). In addition, the "forbidden zone" is traversed in a continuous, albeit rapid, manner. The direct transition mechanism was confirmed by subsequent studies (e.g., Festa & Vilotte, 2006; Liu & Lapusta, 2008; Liu et al., 2014). The possibility of pure mode II transient propagation at the forbidden zone was also observed in 3-D simulations (Bizzarri & Das, 2012; Payne & Duan, 2015).

Festa & Vilotte (2006) and Liu et al. (2014) also studied the conditions determining which of the two transition mechanisms occurs. They showed that the direct mechanism is favored by low values of the parameter S (Eq. 3.4) and large values of the nucleation length. When the nucleation length is small, both studies agree that the boundary between the direct mechanism and the Burridge-Andrews mechanism in 2-D lies at $S \approx 0.7 - 0.8$.

The question of whether rupture transitions to supershear speeds or not has been studied in terms of non-dimensional quantities. Andrews (1976a) used the parameter S and showed that as S increases, so does the ratio $L_t/a_c^{A,II}$, where L_t is the length of the main crack at which the supershear transition happens, and $a_c^{A,II}$ is the in-plane critical nucleation half-length (Eq. 3.9). At a critical value S_c of S, the transitional length diverges to infinity so that the rupture is always subshear for $S > S_c$. The existence of the S-dependent transitional length was also found in later numerical 2-D (Andrews, 1985; Festa & Vilotte, 2006; Liu et al., 2014; Geubelle & Kubair, 2001; Weng et al., 2015), 3-D (Dunham, 2007; Kaneko & Lapusta, 2010; Xu et al., 2015) and laboratory (Xia et al., 2004) studies. The critical value S_c depends on the rupture and fault geometry. For bilateral 2-D ruptures on an infinite fault, $S_c \approx 1.77$. For unilateral ruptures, $S_c \approx 1.42$ (Dunham, 2007).

In 3-D slip-weakening numerical simulations, supershear speeds in the in-plane direction were first observed by Day (1982), although the supershear propagation was not sustained, but only momentary. A transition to supershear via secondary fronts ("ears", as exhibited by model 2d of section 3.1) was demonstrated in numerical experiments of Madariaga et al. (1998).

The first systematic study examining the occurrence of various rupture regimes in 3-D was presented by Madariaga & Olsen (2000). Keeping T_u/μ constant and setting $T_d = 0$ MPa, they explored the space of non-dimensional parameters $(D_c/b, \gamma)$ for a long rectangular patch of width $2b$ immersed in full elastic space. The nucleation zone radius r_{nucl} and initial stress T_{nucl} were set to $r_{nucl} = b/2$ and $T_{nucl} = T_u$. They found that the parameter space can be divided into three connected domains that correspond to three rupture regimes: self-arrested rupture (for large values of D_c/b or small values of γ), supershear rupture (small values of

D_c/b or large values of γ) and subshear rupture (an intermediate region). They found that the parameter region for the subshear behavior was quite small, so most ruptures either did not rupture at all or transitioned to supershear speeds. They proposed that the boundary between the rupture regimes could be described by a single non-dimensional *similarity parameter* κ, defined as:

$$\kappa = \frac{(T_e - T_d)^2 b}{\mu (T_u - T_d) D_c}. \tag{3.23}$$

For crack models, this parameter is roughly proportional to the ratio of the average available energy surface density:

$$\Delta W = \frac{1}{2A} \int_{fault} \Delta \boldsymbol{\sigma}(x,t) \cdot \boldsymbol{s}(x,t) dS, \tag{3.24}$$

and the critical fracture energy G_c (Eq. 3.8). This is because for a static crack of characteristic length b, $\boldsymbol{s} \propto \frac{\Delta \boldsymbol{\sigma}}{\mu} b$ (Eq. 2.7), so taking $\Delta\sigma = T_e - T_d$, yields

$$\Delta W \propto \frac{(T_e - T_d)^2 b}{\mu} \tag{3.25}$$

and thus

$$\frac{\Delta W}{G_c} = \frac{\Delta W}{1/2 (T_u - T_d) D_c} = C \frac{(T_e - T_d)^2 b}{\mu (T_u - T_d) D_c} = C\kappa. \tag{3.26}$$

for some constant C that depends on elastic parameters and the geometry of the problem. For an elliptical crack elongated along the stress drop (section 2.2.1), for example, a direct calculation shows that $C = \frac{2}{3} A_L(b/a, \nu)$, with A_L given by Eq. (2.81). For a circular crack with $\nu = 0.25$, $C \approx 0.73$. In Madariaga & Olsen (2000), the boundaries between the no rupture regime and subshear propagation and between the subshear and supershear propagation lie at $\kappa = \kappa_1$ and $\kappa = \kappa_2$, respectively, with $\kappa_1 < \kappa_2$. The critical numbers κ_1 and κ_2 are of order 1 and depend on the geometry. In addition, since only the space $(D_c/b, \gamma)$ was explored in Madariaga & Olsen (2000), they may also depend on other parameters, such as T_u/μ, r_{nucl} and T_{nucl}. Note that if r_{nucl} is used instead of b in Eq. (3.23), then the limiting criterion that $\kappa = \kappa_1$ for successful nucleation is equivalent to Day's (1982) estimate (3.11) of the critical nucleation radius with $\kappa_1 = 7\pi/24$.

Dunham (2007) explored the supershear transition mechanism for different geometries and piecewise power-law slip-weakening constitutive laws (of which the linear slip-weakening is a special case) in full elastic space and found that κ_2 strongly depends on the parameter S, i.e. $\kappa_2 = \kappa_2(S)$. He examined the supershear transition length L_t and found that it is

an increasing function of S that depends on the problem geometry, the direction of rupture (with the pure mode II direction being the most conducive for supershear), and the chosen constitutive law. For elliptical 3-D cracks on unbounded faults, it diverges for $S_c = 1.19$ (i.e. no supershear transition occurs for $S > S_c$), which is smaller than what was found in 2-D. According to Dunham (2007), this is caused by defocusing of stress waves due to the convex shape of the crack (a similar inequality between 2-D and 3-D geometries was already seen for the transitional S value at which the nucleation size starts depending on S, see section 3.2). On the other hand, Dunham et al. (2003) showed that when a circular barrier is encountered by a propagating planar crack, waves are focused at the barrier which can induce supershear transition. For finite faults, Dunham (2007) found that S_c decreases and the transitional length L_t increases with a decrease in the fault width (which is the shorter size of the fault in his model, aligned in the anti-plane direction), so that higher relative stress γ is required for narrow faults to initiate the supershear transition. He proposed that this happens due to healing waves reflected from the edges of the fault, which, for narrow faults, inhibit the crack before the supershear behavior can develop.

A thorough exploration of the rupture regimes was published by Xu et al. (2015). They explored strike-slip and dip-slip (fixing the direction of traction) ruptures in both the full elastic space and in half-space with the free surface, assuming $T_d = 0$ and a square nucleation zone of size a on rectangular faults with a length of 80 km and widths of 40, 30, 20 and 15 km. They explored the space of non-dimensional parameters $(\hat{D}_c, \gamma)$, where

$$\hat{D}_c := \frac{D_c \mu}{r_{nucl}^{eff} T_u}, \tag{3.27}$$

in which $r_{nucl}^{eff} = \sqrt{a^2/\pi}$ is the effective radius of the nucleation zone.

For strike-slip ruptures in the full-space, the situation described by Xu et al. (2015) is similar to that found by Madariaga & Olsen (2000) - three regimes appear: self-arresting (small γ, large $\hat{D}_c$), subRayleigh (intermediate γ, small $\hat{D}_c$), and supershear (large γ, small $\hat{D}_c$). They found that for dip-slip ruptures, there are only two regimes: self-arresting rupture (the same parameter region as in the strike-slip case) or sustained sub-shear propagation. We note that in homogeneous full-space, dip-slip and strike-slip faults of equal dimension differ only by a 90° rotation and should behave the same. The difference between strike-slip and dip-slip faults is therefore likely caused by the assumed rectangularity of their fault geometry, due to which the rupture is predominantly in-plane in the strike-slip case, and predominantly anti-plane in

the dip-slip case.

Xu et al. (2015) also showed that as the width of the fault was decreased, larger values of γ were required for the supershear transition. However, in contrast to the results of Dunham (2007), as long as the transitional length L_t was finite, it did not depend on the fault width. For strike-slip faults in half-space, they found that if the nucleation zone is sufficiently shallow, the ruptures are either self-arresting or supershear, i.e. there is no regime of subRayleigh ruptures. The enhancing effect of the free surface on the generation of supershear ruptures was studied in detail by Kaneko & Lapusta (2010), who found three main contributions: decrease of normal stress and hence the strength near the surface, amplification of slip rate at the surface, and phase conversion of SV-waves to inhomogeneous P-waves. Xu et al. (2015) also studied the influence of the fault dip angle, finding that it has only a negligible effect on the boundaries between the different rupture regimes. On the other hand, faults with lower dip tend to have larger rupture speeds and slip rates, especially for dip-slip faults and ruptures that reach the free surface (see also Chen & Zhang, 2006).

Weng & Ampuero (2020) studied the behavior of rupture on elongated faults with oblique initial traction, i.e. for settings in which the angle θ between the initial traction and the horizontal direction (parallel to the long sides of the fault) may take any value between 0° (dominantly in-plane propagation) and 90° (dominantly anti-plane propagation). They used a finer classification of the rupture behavior than described in this section so far: the self-arresting regime, sustained subRayleigh regime, sustained forbidden regime (when the steady rupture speed v is in the "forbidden" zone between c_R and β), and two types of sustained supershear regimes - slow (when v is between β and the Eshelby speed $c_E = \sqrt{2}\beta$) and fast (when v is greater than c_E). They set the diameter of the nucleation zone (implemented by prescribed time-weakening of the yield strength) equal to the fault width and found that the five regimes could be well described by two main quantities: the angle θ and the energy ratio $e = G_c/G_0^{III}$, where G_c is the critical fracture energy at the cohesive zone (Eq. 3.8), and G_0^{III} is the static energy release rate in mode III. For pure in-plane or anti-plane directions, this energy ratio is proportional to the inverse of the similarity parameter κ given by Eq. (3.23). In the space of these two parameters, the different rupture regimes are associated with connected regions, with the self-arresting regime corresponding to the largest values of e and the fast supershear regime to the lowest (for a fixed and low enough value of θ). When the energy ratio e is larger than ≈ 1.3, the rupture is always self-arresting, regardless of the angle θ. For the pure in-plane mode ($\theta = 0°$), only the fast steady supershear speeds are attainable.

For a certain range of mixed-mode fractures, however, steady speeds in both the forbidden and the slow supershear ranges are possible. When the angle $\theta \gtrsim 60°$, only subshear or self-arresting ruptures are observed. All four boundaries between the regimes can be described as curves $e = B_i(\theta)$, where B_i, $i \in \{1, 2, 3, 4\}$, are monotonously decreasing functions of θ - i.e. it is possible to transition from a slower regime to the faster regime by rotating the initial traction towards the horizontal (in-plane) direction. Remarkably, the functions B_i well match the theoretical curves predicted by fracture mechanics (Weng & Ampuero, 2019).

3.6 The cohesive zone

In the examples of section 3.1, it was shown that the size of the cohesive zone may change during propagation. For the slip weakening law, no exact analytical relationship exists for the evolution of the cohesive zone size d. However, for a steady subshear (mode III) or subRayleigh (mode II) crack with speed v, governed by a constitutive law in which friction linearly decreases with distance from the crack edge (rather than with slip), the following formula was derived (Palmer & Rice, 1973; Rice, 1980):

$$d_{II,III}(v) = C \frac{1}{g_{II,III}(v)} \frac{\mu^*}{(T_u - T_d)} D_c, \tag{3.28}$$

where $C = \frac{9\pi}{16}$, and $g_{II}(v)$ and $g_{III}(v)$ are the in-plane and anti-plane crack speed factors (2.38) and (2.30), respectively. In this model, therefore, d is directly proportional to D_c and inversely proportional to the breakdown stress drop $T_u - T_d$. Since the functions $g_{II}(v)$ and $g_{III}(v)$ are increasing and approach ∞ as v approaches the respective limiting speed (i.e. c_R for mode II and β for mode III), Eq. (3.28) predicts that d decreases with increasing speed, eventually shrinking to zero. Indeed, such a decrease was observed in the example calculations 2b,c,d of section 3.1.

The formula (3.28) is valid when d is small in comparison to the total size of the sliding zone L_s (the area of non-zero slip rate). For general L_s, Rice et al. (2005) have shown that Eq. (3.28) differs by a slowly changing function of d/L_s, so there is about 44% difference in d between the limiting cases $d/L_s \approx 0$ and $d/L_s = 1$. We note that as rupture speed approaches the limiting speeds, the contraction of the cohesive zone makes it harder to resolve. On the

other hand, it should also mean that the problem is better approximated by the ideally brittle theory, in which the size of the cohesive zone has a zero size.

For the step slip-weakening law (1.18), the formula differs only in the constant proportionality factor $C = \pi/4$ (see e.g., Rice, 1980 or Fialko, 2007). Therefore, it can be conjectured that the same form (with a different value of C close to 1) is valid for the slip-weakening law (Udias et al., 2013). For example, the final (zero crack speed) cohesive zone size of model 2b of section 3.1 is 1.0 km and 1.4 km in the anti- and in-plane directions, respectively, compared to the estimates of 1.1 km and 1.5 km predicted by Eq. (3.28). Indeed, Day et al. (2005) showed that the estimate (3.28) with $v = 0$ can be used as an upper bound for slip-weakening cohesive zones.

Huang & Gao (2000) analytically studied supershear cracks governed by the step slip-weakening law that start propagating from the origin with a constant speed. They showed that the cohesive zone length at a given distance of the crack tip is zero at the shear and longitudinal speeds and has a global peak at a certain intermediate speed. Except for the Eshelby speed, it decreases with time. Bizzarri & Das (2012) studied the behavior of the cohesive zone in a finely-discretized 3-D slip-weakening simulation. They found that in the anti-plane direction, d monotonically decreased as the crack accelerated towards the shear wave speed. In the in-plane direction, they observed a decrease in the subRayleigh range, and then an increase and subsequent decrease as the crack transitioned into the supershear range, which is qualitatively consistent with the prediction of Huang & Gao (2000). A peak in the cohesive zone length (near the Eshelby speed) was also observed in laboratory experiments of Fukuyama et al. (2016).

3.7 Dependence on the absolute magnitude of stress

The slip-weakening law posits that the slip rate is anti-parallel to the total traction on the fault. This introduces a dependence of the solution on the total level of traction, not only on the final stress drop. To show the effect of absolute stress, we set up a reference circular patch model whose initial traction is shown at Fig. 3.11, with $T_d = 0$ MPa, $T_u = 10$ MPa (within the patch), $D_c = 0.25$ m and free surface at the top face, and compare five models created from the reference model by shifting T_u, T_d and the magnitude of the initial stress $T_i(\boldsymbol{x})$ on the fault by constant values $\Delta T = 0$, 0.5, 5, 50 and 500 MPa. The final traction and slip at the horizontal slices marked in Fig. 3.11 are shown in Fig. 3.12. The evolution of traction and

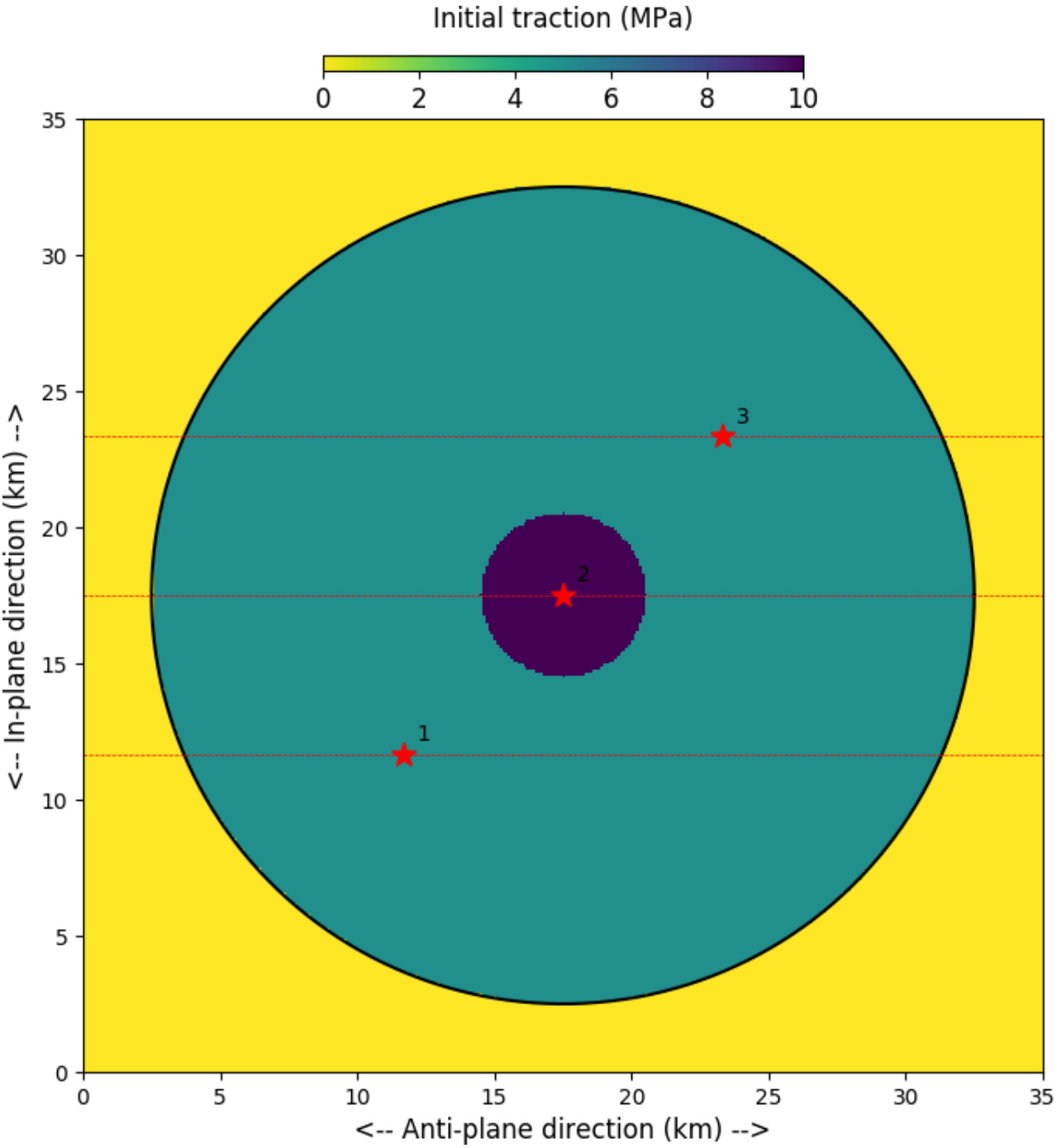

Figure 3.11: The magnitude of initial traction (which points from bottom to top) for the reference model used to assess the effect of the dynamic friction T_d. The black circle is the boundary of the weakened patch inside of which rupture can develop. The red lines are cross-sections on which traction and slip are shown in Fig. 3.12. The red stars are points $P_1 - P_3$ used in Figs. 3.13 and 3.14.

slip at the three points marked in Fig. 3.11 is shown in Figs. 3.13. The resulting rotation of slip rate is shown in Fig. 3.14.

The final spatial distributions and evolution of traction are mostly very similar to each other for models with $T_d \geq 0.5$ MPa (except for the z-component of traction at the nucleation zone, where the $T_d = 0.5$ MPa model differs from the models with larger T_d). However, the traction curves of the $T_d = 0$ MPa model differ significantly. This happens because once the total traction for this model drops to zero, it stays zero (by definition of the slip-weakening law), but it gets readjusted below T_d for the remaining models. The most obvious difference is seen in the final slip, which is rather small for the $T_d = 0$ MPa model, when compared to the $T_d \geq 5$ MPa models. This is because the $T_d = 0$ MPa model shows a significant rotation of the slip vector (Fig. 3.14), especially at the two points P_1 and P_3 outside of the nucleation zone. This causes reversal of the z-component of slip. Rotation and reversal of slip is also seen for the $T_d = 0.5$ MPa model, although it is not as significant as for the 0 MPa model. In contrast, the models with $T_d \geq 5$ MPa do not rotate at all. This may create noticeable differences in gross (integral) quantities characterizing rupture. For example, the seismic moment for the zero T_d model is $4.0 \cdot 10^{19}$ Nm, but it is $4.6 \cdot 10^{19}$ Nm for the $T_d = 0.5$ MPa model and $5.0 \cdot 10^{19}$ Nm for the other models. A difference is also seen in slip-weighted stress drop (5.3 MPa vs 6.1 and 6.6 MPa). For many other quantities, only the 0 MPa model stands out; the differences among the 0.5-500 MPa models are negligible. For example, the energy radiated by the zero T_d model is 1.3×10^{15}J, as opposed to 1.2×10^{15}J for the remaining models.

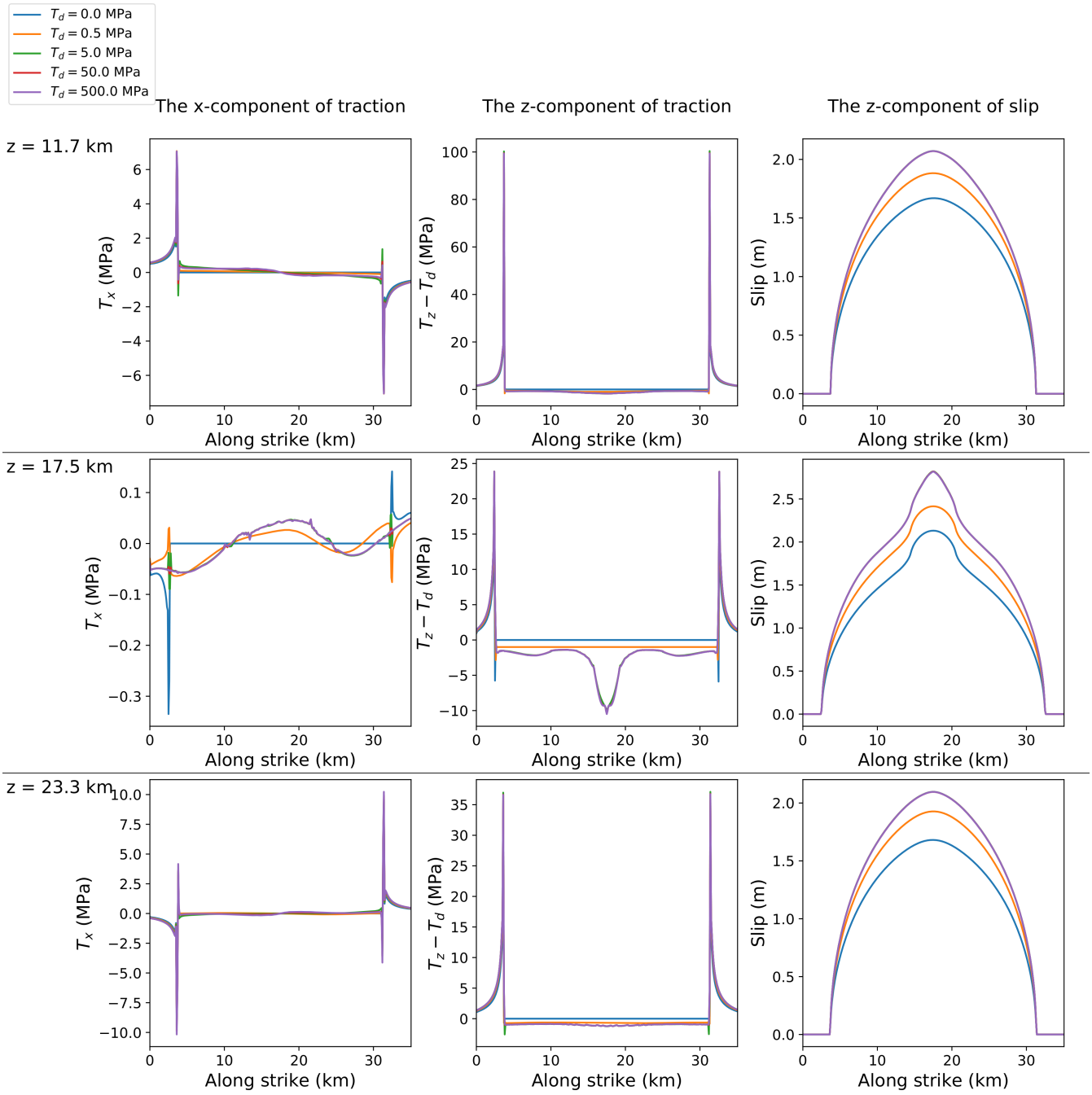

Figure 3.12: The x- and z-components of traction and the final slip for models with different values of T_d (see legend) on the three horizontal slices shown in Fig. 3.11, see annotations at the left part of the figure.

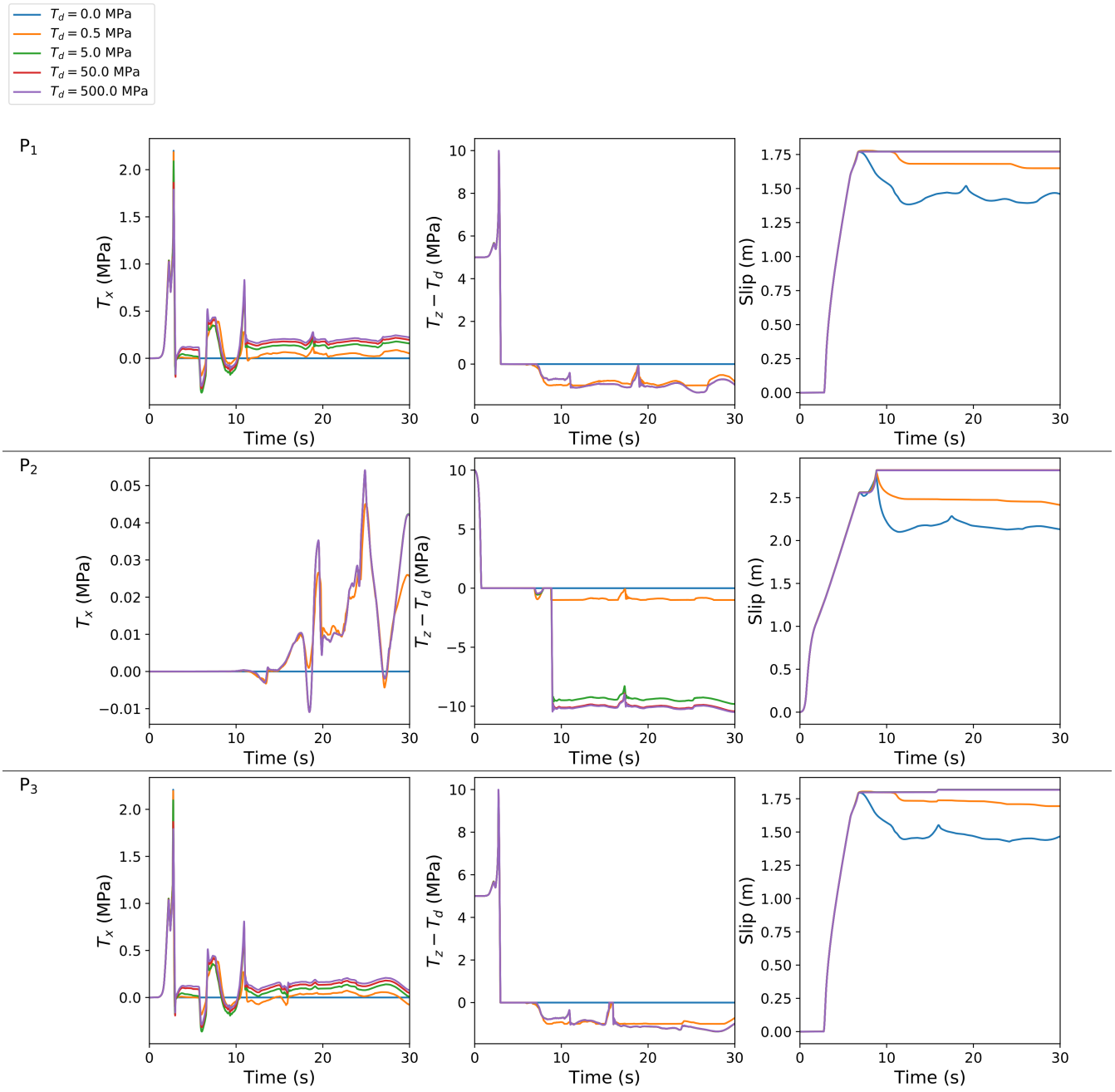

Figure 3.13: The time evolution of the x- and z-components of traction and slip for models with different values of T_d (see legend) at the three points shown in Fig. (3.11), see annotations at the left part of the figure.

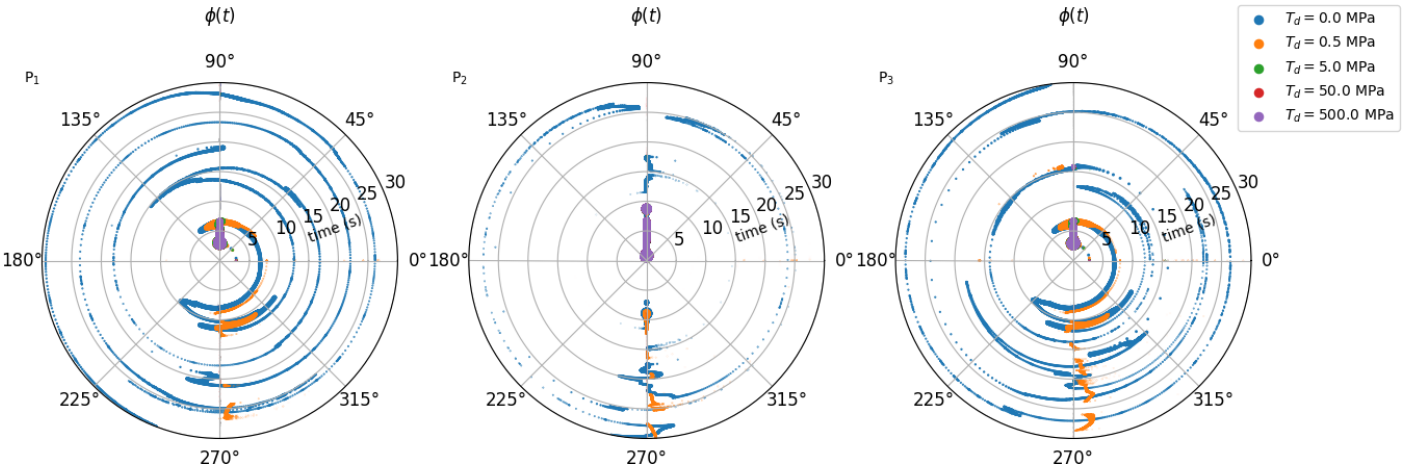

Figure 3.14: Temporal evolution of the direction $\phi(t)$ of the slip rate vector (with respect to the horizontal line) for models with different values of T_d (see legend) at the three points shown in Fig. 3.11. The size of the markers is proportional to the magnitude of the slip rate at a given time.

For comparison, we also show in Figs. 3.15-3.18 analogical figures for one of the best-fitting models found in the inversion of the 2017 Mw 6.3 Lesvos earthquake (chapter 6, $T_u = 7.8$ MPa, $D_c = 0.14$ m). In this case, the $T_d = 0$ MPa model is the only one that stands out, while the $T_d \geq 0.5$ MPa models are very similar to each other, except for the x-component of traction (which is however small in comparison to the z-component). For models with $T_d \geq 0.5$, the

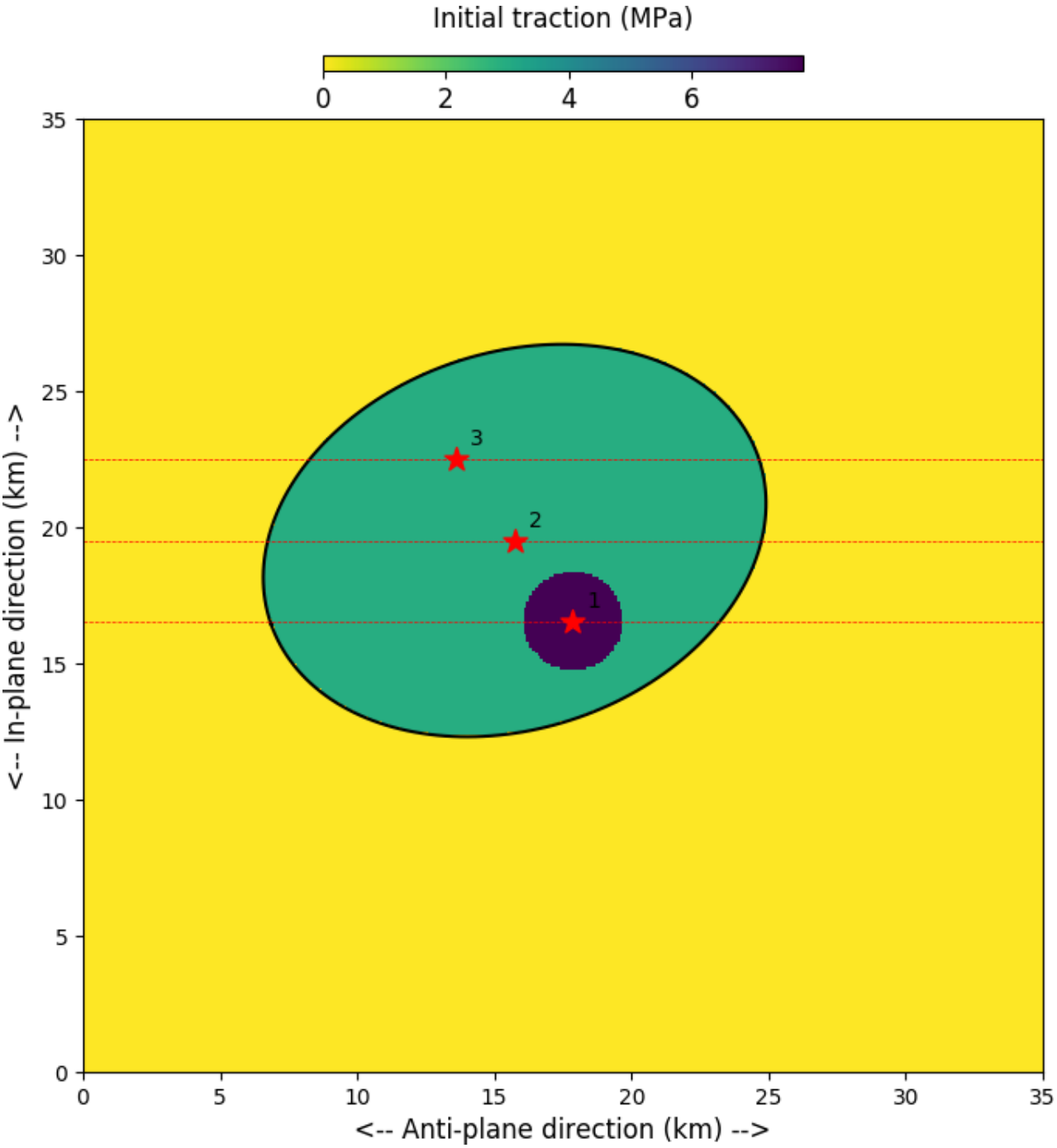

Figure 3.15: The magnitude of initial traction (which points from bottom to top) for one of the best-fitting models found in the inversion of the 2017 Mw 6.3 Lesvos earthquake (chapter 6). The black ellipse is the boundary of the weakened patch inside of which rupture can develop. The red lines are cross-sections on which traction and slip are shown in Fig. 3.16. The red stars are points $P_1 - P_3$ used in Figs. 3.17 and 3.18.

integral quantities are all very close to each other, differing at most by 0.1%.

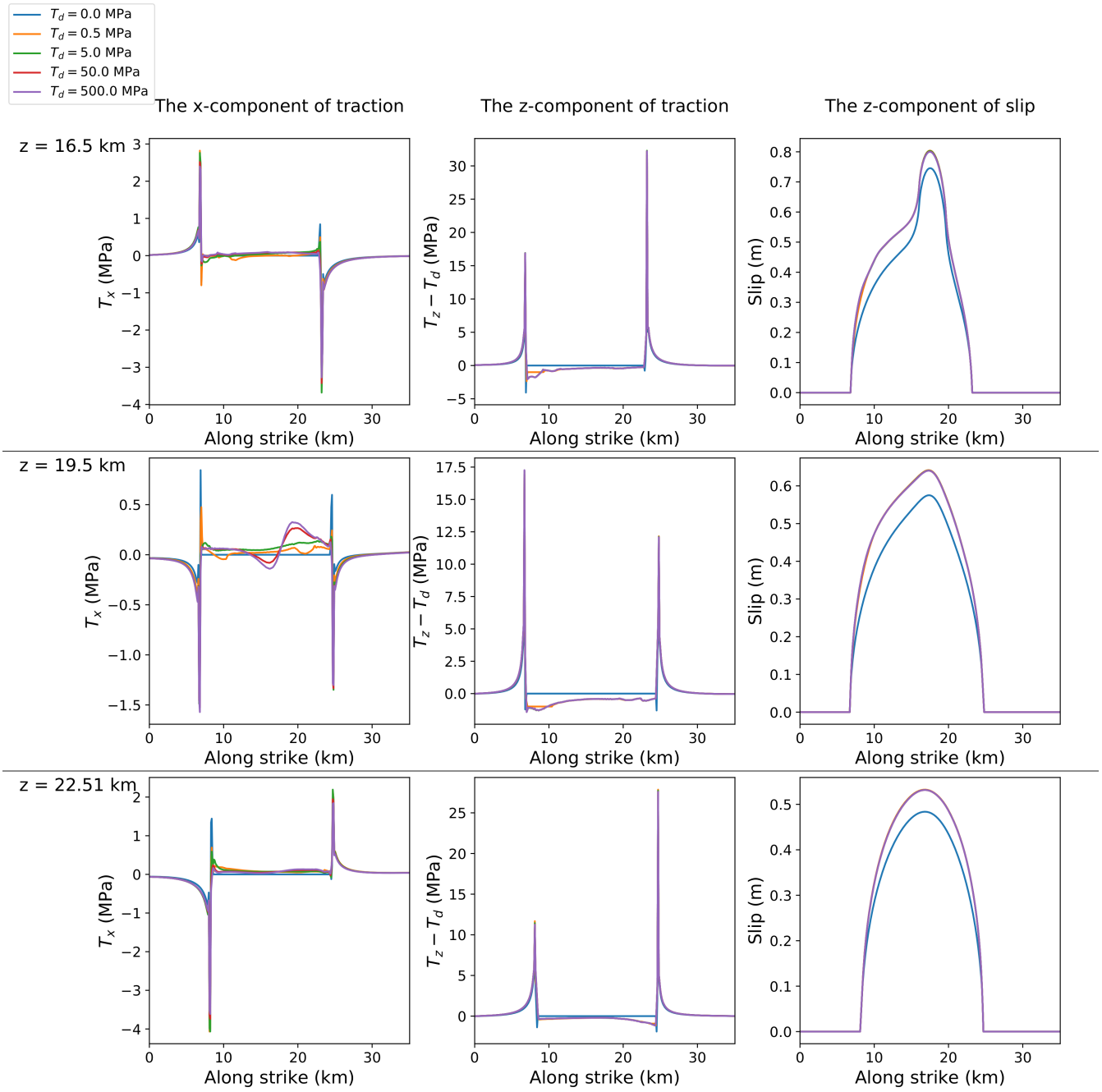

Figure 3.16: Same as Fig. 3.12, but for the model shown in Fig. 3.15.

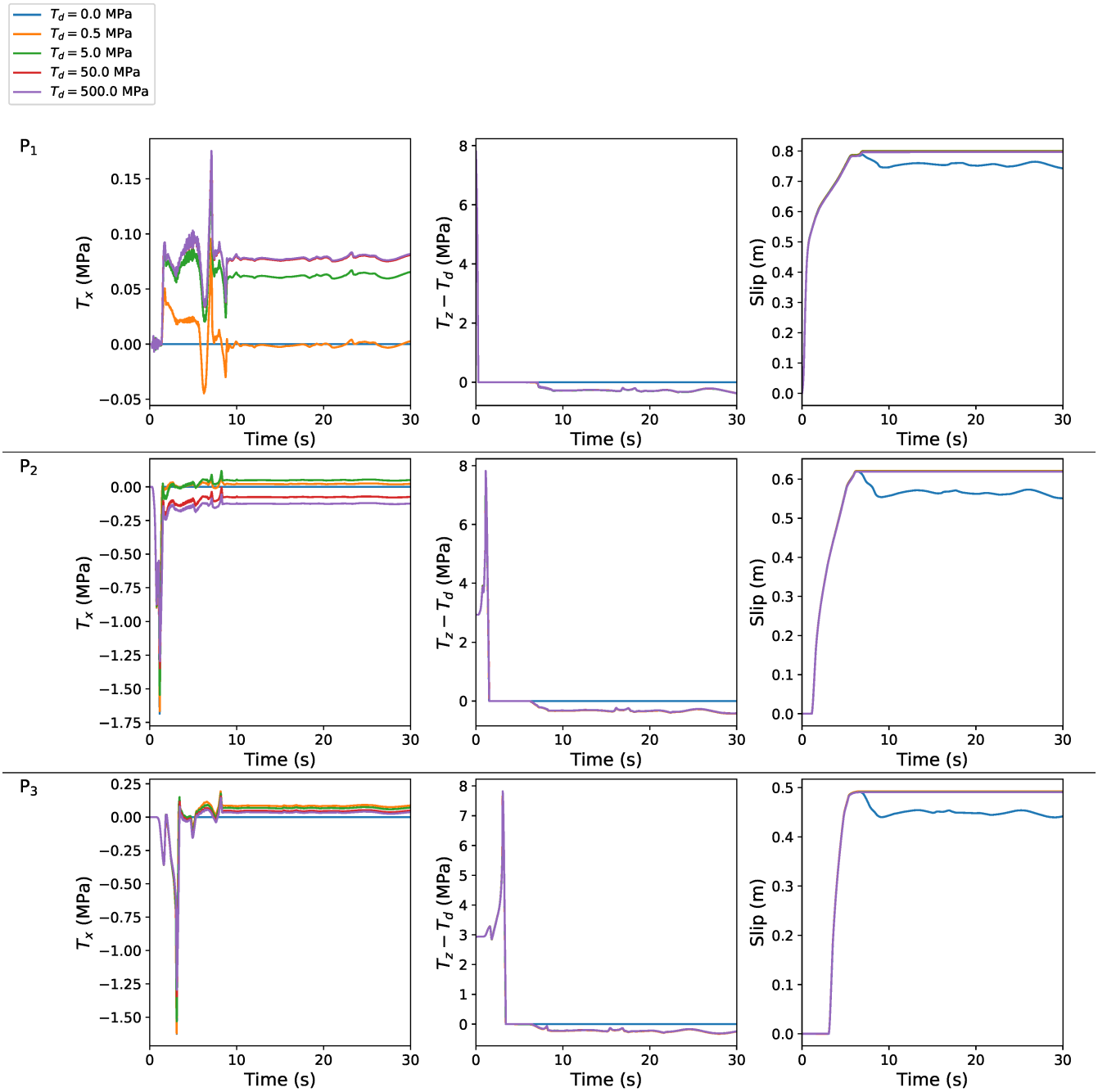

Figure 3.17: Same as Fig. 3.13, but for the model shown in Fig. 3.15.

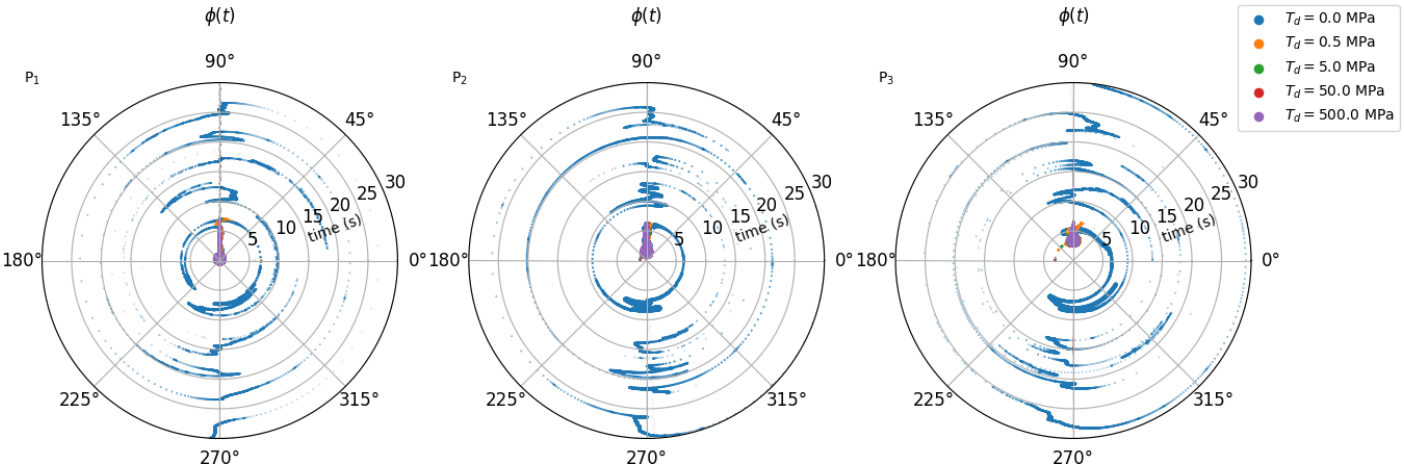

Figure 3.18: Same as Fig. 3.14, but for the model shown in Fig. 3.15.

The influence of the total stress was thoroughly analyzed by Spudich (1992), who suggested that its value on seismic faults could be inferred from temporal rotations of the rake angle of the slip vector. Andrews (1994) studied mixed-mode II and III propagation and found that the results depend on the magnitude of the initial stress. He found that the in-plane component of the solution can be decomposed into smeared-out versions of two singular contributions, one of which increases with rising absolute stress. Moreover, for ruptures spreading at superRayleigh speeds, he observed substantial rotation of the traction vector.

Guatteri & Spudich (1998) studied the dependence on absolute stress in homogeneous and heterogeneous 3-D models (but keeping the stress drop constant and uniform). They found that the main difference between the results at large and small absolute stress was the rotation of the traction vector, which decreases with increasing absolute stress. For a homogeneous direction of initial traction, they found that while the final slip vectors were almost colinear with the initial direction of traction, regardless of the absolute stress, temporal rotations of the traction/slip rate vector do occur for small values of absolute stress. For models with heterogeneous directions of the initial traction direction, the rotations were even larger. Bizzarri & Cocco (2005) found that the greatest temporal rotation of traction occurs at the cohesive zone and that it is significantly larger for supershear ruptures. The maximum rotation shown in Bizzarri & Cocco (2005) is around 20 degrees, for complete stress drop to $T_d = 0$ MPa. An exception to this occurred at points at which the local rupture velocity was parallel to the direction of the initial stress, the slip at these points did not rotate at all.

The rotation of slip rake is a matter of active research in geology. It has been confirmed on

real faults based on observations of slickenlines and fault striations (e.g., Otsubo et al., 2013; Pan et al., 2014; Kearse & Kaneko, 2020; Pollitz et al., 2020).

In dynamic source inversions, the determination of T_d from seismograms is not yet considered a realistic goal, and the value of T_d is set to a fixed value. This is also the case for the inversion of the 2017 Mw 6.3 Lesvos Earthquake presented in chapter 6.

4 Long-term behavior of faults: Rate-and-state friction

In this chapter, we briefly review basic properties of the rate-and-state friction law, particularly as they relate to the modeling of the long-term evolution of slip on planar tectonic faults. As elsewhere in the thesis, we suppose that the slip only has shear components.

4.1 Basic properties of the rate-and-state friction law

The shear traction prescribed by the rate-and-state friction law is given by:

$$\boldsymbol{T}_s(\dot{\boldsymbol{s}}, \theta) = -\sigma_n f(\|\dot{\boldsymbol{s}}\|, \theta) \frac{\dot{\boldsymbol{s}}}{\|\dot{\boldsymbol{s}}\|}, \tag{4.1}$$

where σ_n is the normal component of traction and f is the coefficient of friction, which depends on the magnitude of slip rate $V := \|\dot{\boldsymbol{s}}\|$ and the state-variable θ as (see subsection 1.3.2.2):

$$f(V, \theta) = f^* + a \ln \frac{V}{V^*} + b \ln \frac{V^* \theta}{L}. \tag{4.2}$$

Non-zero V everywhere on the fault ($\gamma = \Gamma$) is assumed.

The aging law governing the evolution of θ reads (Eq. 1.26):

$$\frac{d\theta}{dt}_{|\mathrm{AL}} = 1 - \frac{V\theta}{L}, \tag{4.3}$$

while the slip law reads (Eq. 1.27):

$$\frac{d\theta}{dt}_{|SL} = -\frac{V\theta}{L} \ln \frac{-V\theta}{L}. \tag{4.4}$$

For both evolution laws, steady-state sliding, in which both V and θ are constant, can be achieved only when

$$\theta = \theta_{SS}(V) = \frac{L}{V}. \tag{4.5}$$

To quantify the distance from the steady-state sliding state, Rubin & Ampuero (2005) introduced the non-dimensional quantity

$$\Omega := \frac{V\theta}{L}. \tag{4.6}$$

The steady-state corresponds to $\dot{V} = 0$ and $\Omega = 1$. The right hand side of the evolution laws rewritten in terms of Ω read:

$$\frac{d\theta}{dt}_{|\mathrm{AL}} = 1 - \Omega \tag{4.7}$$

and

$$\frac{d\theta}{dt}_{|\mathrm{SL}} = -\Omega \ln \Omega. \tag{4.8}$$

For V and θ far from the steady-state, i.e. $\Omega \ll 1$ and $\Omega \gg 1$, the two laws significantly differ. On the other hand, writing $\Omega = 1 + \omega$, where ω represents a small deviation from the steady-state, the aging law may be written as

$$\frac{d\theta}{dt}_{|\mathrm{AL}} = -\omega, \tag{4.9}$$

whereas the slip law is

$$\frac{d\theta}{dt}_{|SL} = -(1+\omega)\ln(1+\omega), \tag{4.10}$$

which, for $|\omega| < 1$, is equal to

$$\frac{d\theta}{dt}_{|SL} = -\omega - \frac{\omega^2}{2} + o(\omega^2). \tag{4.11}$$

Therefore, the behavior of both evolution laws agrees to linear order in ω near the steady state.

Plugging the steady-state value of θ (Eq. 4.5), into Eq. (4.2), one obtains the dependence of the steady-state friction coefficient f_{SS} on V:

$$f_{SS}(V) \coloneqq f(V, \theta_{SS}(V)) = f^* + (a-b)\ln\frac{V}{V^*}. \tag{4.12}$$

For $a > b$ ($a < b$), $f_{SS}(V)$ is an increasing (decreasing) function of V. The former case is referred to as the *velocity-strengthening* (VS) and the latter case is referred to as the *velocity-weakening* (VW) parameter regime.

4.2 The spring-slider model

A simple 1-D system in which the dynamics of the rate-and-state friction can be studied is the *spring-slider* model, which consists of a rigid block subject to rate-and-state friction that is connected to an elastic spring. The spring is driven with constant velocity V_{pl}, which simulates loading by distant tectonic motion. The equation of motion for the position $x(t)$ of the block reads (Ruina, 1983; Rice & Tse, 1986):

$$m\ddot{x}(t) + k\left(x(t) - V_{pl}t\right) = -\text{sign}[\dot{x}(t)]\sigma_n f(|\dot{x}|, \theta), \tag{4.13}$$

where m is the mass of the block and k is the spring stiffness, both normalized by the area of the bottom face of the block. This equation is supplemented by an evolution law for θ, either (4.3) or (4.4), which leads to a coupled system of two non-linear ordinary differential equations.

General analytic solutions of this system have not been found, but one particular solution is

$$x_{SS}(t) = V_{pl}t - \frac{\sigma_n}{k} f_{SS}(V_{pl}),\ \theta(t) = \theta_{SS}(V_{pl}), \tag{4.14}$$

i.e. steady-state sliding at the velocity V_{pl}. Heuristically, it can be argued that the slider should be stable in the VS regime because an increase in steady-state slip rate causes an increase in friction, which in turn acts to decrease the slip rate. In the VW regime, on the other hand, we may expect it to behave unstably.

To quantitatively study stability against small perturbations, the system may be linearized around the steady-state (4.14) and tested against deviations from it of the form $x(t) = x_{ss}(t) + \epsilon \exp(st)$ for a given constant $\epsilon \in \mathbb{R}$ and an unknown constant $s \in \mathbb{C}$. Such a linear stability analysis (Ruina, 1983; Rice & Ruina, 1983) shows that the system is linearly stable ($\text{Re}(s) < 0$, so that the slider converges to the steady-state) if and only if k is greater than the *critical*

stiffness k_{crit}:

$$k > k_{crit} = \sigma_n \frac{b-a}{L}(1 + \frac{V_{pl}^2 m}{a\sigma_n L}). \tag{4.15}$$

Thus, the stability of the system depends not only on the parameters of the friction law, but also on the loading rate, normal stress, and the stiffness and mass of the slider. In the quasi-static approximation, the inertial term of Eq. (4.13) is neglected ($m = 0$), and expression (4.15) simplifies to

$$k_{crit} = \sigma_n \frac{b-a}{L}. \tag{4.16}$$

When $a > b$, k_{crit} is negative, so sliding in the VS regime is always stable, in accordance with the heuristic argument. On the other hand, sliding in the VW regime ($a < b$) is only a necessary, not sufficient condition for instability, which occurs if and only if $k < k_{crit}$. For the special case $k = k_{crit}$, the slider is at neutral stability and undergoes undamped harmonic oscillation with circular frequency (Ruina, 1983, eqs. 27 and 32):

$$\omega = \frac{V_{pl}}{L}\sqrt{\frac{b}{a} - 1}. \tag{4.17}$$

The oscillations remain for k in a finite neighborhood of k_{crit}, but they are damped or amplified, according to $k > k_{crit}$ or $k < k_{crit}$, respectively. Their frequency departs from (4.17) as k departs from k_{crit} (see Perfettini et al., 2003b).

For large perturbations, a non-linear analysis needs to be performed and the resulting behavior depends on the assumed evolution law. For the aging law, Ranjith & Rice (1999) showed that, in the quasi-static approximation, the system is stable against any perturbation if and only if $k \geq k_{crit}$, same as in the linear analysis. For the slip law, on the other hand, Gu et al. (1984) showed that the system may become unstable in the VW regime even if $k \geq k_{crit}$, with the necessary destabilizing amplitude growing exponentially with k. Therefore, $k \geq k_{crit}$ is a necessary, but not sufficient condition for stability of slip law spring sliders. Scholz (1998) calls the parameter region with $a < b$ and $k \geq k_{crit}$ *conditionally stable*.

For spring sliders in the unstable regime, a deviation from the steady-state causes the slip rate to diverge to infinity when the quasi-static approximation is used. To remedy this, the so-called *quasi-dynamic* approximation is often assumed, in which the inertial term of the fully dynamic Eq. (4.13) is replaced with a radiation damping term directly proportional to the slip

rate. The equation of motion then takes the form:

$$\eta\dot{x} + k\left(x(t) - V_{pl}t\right) = -\text{sign}[\dot{x}(t)]\sigma_n f(|\dot{x}|, \theta), \tag{4.18}$$

for a constant damping coefficient η. The addition of this rate-dependent term regularizes the system and the unstable slider undergoes *stick-slip* behavior, alternating between sliding at very small speeds below V_{pl} for most of the cycle (stick phase) and a sudden, short acceleration to large speeds (slip phase). The average slip rate of the slider is equal to V_{pl}. The stick-slip behavior corresponds to a limit cycle in the (V, θ) phase space. In fully dynamic simulations, such stick-slip limit cycles are present as well, but more complicated behavior also appears, including aperiodic solutions, quasi-harmonic oscillations, and deterministic chaos (Erickson et al., 2008; Urata et al., 2017; Im et al., 2019). We note that stick-slip is not unique to rate-and-state friction and appears even in the classical Coulomb friction model (Elmer, 1997). Based on the similarity of the stick and slip phases to the inter-seismic and co-seismic phases of earthquakes, respectively, stick-slip was proposed as a possible mechanism for earthquakes as soon as by Brace & Byerlee (1966).

4.3 Rate-and-state faults in 2-D and 3-D

The rate-and-state problem in 2-D and 3-D involves coupling the elastodynamic equation (2.2) with the rate-and-state boundary condition on the fault. In studies of long-term evolution of rate-and-state faults, the fault is typically subjected to loading due to a plate slipping with a constant rate V_{pl}. This can be implemented by imposing this constant slip rate on outer parts of the fault (e.g., Lapusta et al., 2000; Kato, 2001; Hillers et al., 2006; Rubin, 2008; Gallovič, 2008; Lapusta & Liu, 2009), and/or by adding a term to the total traction that represents this loading (e.g., Perfettini et al., 2003b; Rubin & Ampuero, 2005; Ampuero & Rubin, 2008; Gallovič, 2008; Barbot, 2019).

The problem is often studied by boundary integral equation methods (e.g., Cochard & Madariaga, 1994; Perrin et al., 1995; Geubelle & Rice, 1995; Day et al., 2005; Tada, 2009; Lapusta & Liu, 2009), in which the differential equation (2.2) in Ω is converted to an integral

equation on the fault Γ. It has the form:

$$\boldsymbol{\mathcal{I}}[\boldsymbol{s}](t,\boldsymbol{\xi}) + \boldsymbol{T}_l(t,\boldsymbol{\xi}) = \sigma_n(t,\boldsymbol{\xi}) f\left(\boldsymbol{\xi}, V(t,\boldsymbol{\xi}), \theta(t,\boldsymbol{\xi})\right) \frac{\dot{\boldsymbol{s}}(t,\xi)}{\|\dot{\boldsymbol{s}}(t,\xi)\|} \; \forall \boldsymbol{\xi} \in \Gamma, \tag{4.19}$$

where $\boldsymbol{T}_l(t,\boldsymbol{\xi})$ is the contribution of external loading and $\boldsymbol{\mathcal{I}}$ is a linear functional of the slip distribution that takes into account the elastodynamic interaction over the causal history of $(t,\boldsymbol{\xi})$. It can be thought of as a generalization of the inertial and stiffness terms from the spring slider model (Eq. 4.13) to more dimensions.

In the quasi-static approximation, the dynamic effects are neglected and $\boldsymbol{\mathcal{I}}$ only includes static contributions from elastic interaction on the fault, $\boldsymbol{\mathcal{I}} = \boldsymbol{\mathcal{I}}_{el}$. For example, on an in-plane or anti-plane fault of width h, infinite in the anti-plane direction (i.e. an effective 2-D setting), it reads (e.g. Perfettini et al., 2003b; Rubin & Ampuero, 2005):

$$\mathcal{I}_{el}^{2D}[s](t,\xi) = \frac{\mu^*}{2\pi} \int_0^h \frac{1}{\xi - \zeta} \frac{\partial s(t,\zeta)}{\partial \zeta} \, d\zeta. \tag{4.20}$$

In the quasi-dynamic approximation, $\boldsymbol{\mathcal{I}}$ takes the form

$$\boldsymbol{\mathcal{I}}[s](t,\xi) = \boldsymbol{\mathcal{I}}_{el}[s](t,\xi) - \eta \dot{\boldsymbol{s}}(t,\xi). \tag{4.21}$$

The damping coefficient η is typically put equal to (Rice, 1993):

$$\eta = \frac{\mu}{2\beta}, \tag{4.22}$$

which corresponds to the assumption that all radiation has the form of shear waves radiated perpendicularly away from the fault plane.

The results of the stability analysis for the spring-slider model are sometimes extrapolated to higher-dimensional models of geological (sub)faults by replacing the stiffness k of the spring-slider with the *effective stiffness*

$$k_{eff} = \Delta\sigma_c / s_c, \tag{4.23}$$

where s_c and $\Delta\sigma_c$ are the shear slip and stress drop, respectively, at the center of the patch with the same geometry as the (sub)fault, evaluated for some suitable fracture mechanics problem (Dieterich, 1992). For example, s_c may be the slip at the center of a static crack with constant stress drop $\Delta\sigma_c$. Alternatively, $\Delta\sigma_c$ may be taken as the stress drop at the center

of a dislocation with constant slip s_c; this leads to slightly different values of k_{eff}. In fact, at least during the nucleation phase for homogeneous faults with $\Omega \gg 1$, the spring-slider analogy is mathematically justified, because the fault then evolves as if having a single degree of freedom with stiffness k_{eff} (Rubin & Ampuero, 2005). If the geometry of the fault is simple, so that it can be described by some characteristic half-length h, then dimensional arguments and linearity between slip and stress drop (see Eq. 2.5) imply that k_{eff} must have the form:

$$k_{eff} = g(\nu)\frac{\mu}{h}, \tag{4.24}$$

where $g(\nu)$ is a function of the Poisson's ratio ν that depends on the geometry and the assumed fracture mechanical substitution problem. For example, using the static crack solutions (2.42) and (2.53) for a 2-D fault with half-length h yields the effective stiffness

$$k_{eff}^{2D} = \frac{\mu^*}{2h}, \tag{4.25}$$

where μ^* is given by Eq. (2.17). For the constant slip problem, the formula would be multiplied by $2/\pi$ (Dieterich, 1992). When the fault is a circle with radius r, the static crack result (2.85) may be used, yielding

$$k_{eff}^{circle} = \frac{\pi(2-\nu)}{8(1-\nu)}\frac{\mu}{r}. \tag{4.26}$$

These formulas allow defining the *critical patch half-length* h_{crit} as the h corresponding to $k_{eff} = k_{crit}$ (Eq. 4.16):

$$h_{crit} = g(\nu)\frac{\mu L}{\sigma_n(b-a)}. \tag{4.27}$$

For 2-D faults, this yields

$$h_{crit}^{2D} = \frac{\mu^* L}{2\sigma_n(b-a)}, \tag{4.28}$$

while for a circular fault:

$$r_{crit} = \frac{\pi(2-\nu)}{8(1-\nu)}\frac{\mu L}{\sigma_n(b-a)}. \tag{4.29}$$

To the extent that the correspondence between the k of the spring slider model and the effective stiffness k_{eff} holds, a fault should be linearly stable against perturbations from the steady-state if $h < h_{crit}$. Rice (1993) proposed that when continuum rate-and-state problems are discretized, the grid half-size Δh should be much smaller than h_{crit} to achieve correct resolution. This is because a cell of half-size $\Delta h \gtrapprox h_{crit}$ may reach instability on its own,

independently of the elastic interaction with the other cells. Nevertheless, for simulations containing dynamic rupture, an additional criterion on the resolution of the cohesive zone needs to be added (Lapusta et al., 2000; Lapusta & Liu, 2009), which is stricter than the one based on h_{crit}.

long-term behavior of rate-and-state friction is often analyzed on faults that contain a single VW patch enclosed by a VS region (e.g., Tse & Rice, 1986; Rice, 1993; Lapusta et al., 2000; Lapusta & Rice, 2003; Kato, 2003; Perfettini et al., 2003b; Gallovič, 2008; Chen & Lapusta, 2009; Wu & Chen, 2014; Cattania & Segall, 2019; Barbot, 2019). The simplest case in which seismic events (with slip rates on the order of $\sim$ mm/s $-$ m/s, at which the inertial dynamic or quasi-dynamic terms start being significant) occur are simply periodic seismic cycles on faults containing a single homogeneous circular VW patch. In these cycles, the VS regions are steadily slipping (creeping) at the plate velocity. The whole VW region is effectively locked at the beginning of each cycle, slipping at a negligible slip rate. This leads to an accumulation of stress. As time progresses, the creep from the VS region gradually penetrates the VW region and the locked area shrinks towards the center. Finally, a nucleation zone is established, from which fast, seismic sliding eventually spreads to the whole fault, completely releasing the accumulated stress. The system is thus "restarted" and the process repeats, producing periodic cycles of aseismic stress build-up and seismic release. As the earthquakes at the end of each cycle rupture the whole fault and are (almost) identical, they are the ideal examples of *characteristic earthquakes* (Schwartz & Coppersmith, 1984). We note that before the fault settles into these periodic cycles, it may first exhibit irregular behavior, corresponding to a convergence of the system from initial conditions to a limit cycle.

Nevertheless, the actual spectrum of possible fault behaviors is much richer than the simply periodic cycles described above. We briefly review different types of long-term fault behavior and their dependence on parameters of the rate-and-state law in subsection 4.3.3. In the following two subsections, we discuss the co-seismic and nucleation phases of rupture, focusing mainly on the aging law, which we adopt in chapter 5.

4.3.1 The co-seismic phase and equivalent slip-weakening parameters

In the fast, co-seismic phase, the rate-and-state law behaves predominantly as a slip-weakening law (Cocco & Bizzarri, 2002; Bizzarri & Cocco, 2003; Lapusta & Liu, 2009; Bizzarri, 2011). The

weakening is mostly, but not entirely linear and a short strengthening phase is also present, so the traction-slip curve resembles the Ohnaka-Yamashita law (see subsection 1.3.2.1). Bizzarri (2011) simulated the 3-D evolution of spontaneous dynamic ruptures on a homogeneous vertical fault reaching the free surface and compared results for the aging version of the rate-and-state law and for the linear slip-weakening law. The rate-and-state simulation was run first and the parameters of the slip-weakening model were set up to match the a posteriori determined effective yield stress, dynamic friction, and fracture energy density of the rate-and-state simulation. He showed that the two models behave almost identically in terms of (effective) rupture speed and slip rate. Synthetic seismograms, calculated on a free surface synthetic station, were also similar, with only a mild difference at low frequencies, where the slip-weakening simulation produced larger spectral amplitudes.

Due to the similar behavior of the two models in the co-seismic phase, it is sensible to estimate equivalent slip-weakening parameters of the rate-and-state law. For example, assuming that the slip rate is constrained to move in a single direction, the weakening rate

$$w = -\frac{dT}{ds} \tag{4.30}$$

(equal to $[T_u - T_d]/D_c$ for the slip-weakening law) can be evaluated as (using Eqs. 4.1, 4.2):

$$\begin{aligned} w &= -\frac{dT}{dt}\frac{dt}{ds} \\ &= -\sigma_n \left(a\frac{\dot{V}}{V} + b\frac{\dot{\theta}}{\theta} \right) \frac{dt}{ds} \\ &= -\sigma_n \left(a\frac{\dot{V}}{V} + b\frac{\dot{\theta}}{\theta} \right) \frac{1}{V} \end{aligned} \tag{4.31}$$

At the steady-state, the weakening rate is zero ($\dot{V} = \dot{\theta} = 0$). Far from the steady-state, when $\Omega = V\theta/L \gg 1$, the results differ for the aging law and for the slip law (Ampuero & Rubin, 2008). For the aging law (4.3), $\dot{\theta} \approx -V\theta/L$ and so

$$w \approx -\sigma_n \left(a\frac{\dot{V}}{V^2} - \frac{b}{L} \right). \tag{4.32}$$

When $a\dot{V}/V^2$ is small enough so that the first term can be neglected (which is appropriate

in most of the co-seismic phase), the RS law approaches linear slip-weakening with a velocity independent slip-weakening rate:

$$w \approx \frac{b\sigma_n}{L}, \tag{4.33}$$

a relation confirmed numerically by Lapusta & Liu (2009). For the slip law (4.4), $\dot{\theta}$ is additionally proportional to the logarithm of $-V\theta/L$, which results in w depending on the slip rate.

An estimate for the cohesive-zone size can be obtained by replacing the slip-weakening weakening rate $(T_u - T_d)/D_c$ in Eq. (3.28) with the rate-and-state estimate. For the aging law this yields (using Eq. 4.33):

$$d_{II,III}^{RS} \approx C \frac{1}{g_{II,III}(v)} \frac{\mu^*}{b\sigma_n} L, \tag{4.34}$$

where $C \approx 1$ and $g_{II,III}$ are given by Eqs. (2.38) and (2.30).

Assuming that before and after the passage of the cohesive zone, the rock is sliding at steady-slip rates V_i and V_f, respectively, the stress drop can be calculated from Eq. (4.12) as:

$$\Delta\sigma = \sigma_n (b - a) \ln\left(\frac{V_f}{V_i}\right). \tag{4.35}$$

The equivalent value of D_c, i.e. the slip at which the traction drops to the minimum value of T_d^{eq}, was estimated for the aging law by Bizzarri & Cocco (2003) as:

$$D_c^{eq} \approx L \ln \frac{V_m}{V_i}, \tag{4.36}$$

where V_m is the slip rate when traction reaches T_d^{eq} (they propose that V_m is related to the final steady-state velocity V_f as $V_m \approx 2V_f$). This estimate is obtained under the additional assumptions that $\Omega \gg 1$ within most of the cohesive zone and that the state variable θ is close to its steady-state value as the slip reaches D_c^{eq}, as observed in numerical simulations of Bizzarri & Cocco (2003). The estimates of D_c^{eq} and w allow estimating the equivalent breakdown (peak to residual, equal to $T_u - T_d$ for the slip-weakening law) stress drop $\Delta\sigma_{br}^{eq}$ as:

$$\Delta\sigma_{br}^{eq} = D_c^{eq} w \approx b\sigma_n \ln \frac{V_m}{V_i}. \tag{4.37}$$

Using these expressions, the equivalent fracture energy density (critical energy release rate)

can be estimated as:

$$G_c^{eq} = \frac{1}{2} D_c^{eq} \Delta\sigma_{br}^{eq} \approx \frac{1}{2} b\sigma_n L \ln\left(\frac{V_m}{V_i}\right)^2. \tag{4.38}$$

Since $V_m \approx 2V_f$, the energy depends on the second power of the $\ln(V_f)$. This only holds for the aging law. For the slip law, Ampuero & Rubin (2008) showed that G_c^{eq} instead depends only on the first power of $\ln(V_f)$.

4.3.2 Nucleation

The critical fault length $h_{crit} \propto (b-a)^{-1}$ (Eq. 4.27) is an estimate of the minimum size that a fault should assume to exhibit seismic behavior. However, analytical and numerical studies have shown (Dieterich 1992; Rubin & Ampuero 2005; Ampuero & Rubin 2008; Viesca 2016) that the size h_{nuc} of the nucleation zone, i.e. the part of the fault which is slipping (faster than the plate rate) as the fault enters the seismic speed range, is different from h_{crit}, and its scaling with a and b depends on the ratio a/b.

Rubin & Ampuero (2005) and Ampuero & Rubin (2008) numerically and analytically studied the nucleation process governed by the aging and the slip law for quasi-static 2-D faults. For the aging law, they found that when $a/b \lesssim 0.38$, the fault departs from the steady-state and the quantity Ω (Eq. 4.6) increases towards large values, $\Omega \gg 1$, a so-called *no-healing* limit. In this limit, the slip rate evolves approximately as a function separable in time and space on a nucleation zone of fixed length h_{nuc}^{FL}, i.e.

$$V(t,\xi) = V_t(t) V_s(\xi/h_{nuc}^{\mathrm{FL}}) I_{[-1,1]}(\xi/h_{nuc}^{\mathrm{FL}}), \tag{4.39}$$

where $V_s(0) = 1$. The temporal part of the slip rate $V_t(t)$ evolves with time as a single-degree spring-slider model with effective stiffness k_{eff} (Eq. 4.23). During most of the nucleation process, it increases with time. Therefore, this solution corresponds to an accelerating crack of fixed length. Requiring that the stress at the tip of this nucleation zone be finite can be formulated as a requirement that the stress-intensity factor of the equivalent static crack vanish. The stress-intensity factor is given by an integral formula similar to Eq. (2.69) (but for static cracks), so this leads to an integral equation whose numerical solution yields the unique

nucleation half-length (Rubin & Ampuero, 2005):

$$h_{nuc}^{\mathrm{FL}} \approx 1.38 \frac{\mu^* L}{b\sigma_n}. \tag{4.40}$$

Indeed, Rubin & Ampuero (2005) found that in their numerical experiments conducted for a variety of initial and boundary conditions, the actual size of the nucleation zone matches Eq. (4.40) within $\approx 4\%$. Unlike the estimate (4.27), this expression is independent of a, scaling as $h_{nuc}^{FL} \propto b^{-1}$. This scaling is consistent with previous results of Dieterich (1992), who derived it on the basis of the spring-slider analogy. Due to the quasi-static assumption, the slip rate $V_t(t)$ eventually diverges. The time t_∞ at which this happens approximately corresponds to the onset of seismic speeds in fully dynamic models. It is inversely proportional to the initial velocity $V_t(0)$:

$$t_\infty \propto \frac{a}{b} \frac{L}{V_t(0)}. \tag{4.41}$$

The proportionality of t_∞ to the reciprocal value of $V_t(0)$ is approximately also seen in formulas derived for the spring-slider model by Dieterich (1992) and Perfettini et al. (2003b).

Rubin & Ampuero (2005) show that the no-healing limit is only achievable when the effective stiffness of the nucleation zone is smaller than the value of k_{crit} given by Eq. (4.16). They also show that this corresponds to the condition $a/b < 0.38$. As a/b gets larger ($a/b \gtrapprox 0.5$), Ω starts tending towards a constant value close to 1. In this regime, the nucleation zone slowly grows with time, resembling a propagating slip-weakening crack. To obtain an estimate for the limiting half-length of the nucleation zone just as it reaches seismic speeds, Rubin & Ampuero (2005) applied the Griffith criterion for the rate-and-state law and obtained the result:

$$h_{nuc}^{\infty} = \frac{\mu^* L b}{\pi \sigma_n (b-a)^2}. \tag{4.42}$$

This formula can be obtained by using the stress drop estimate (4.35) in the formula for the energy release rate of finite 2-D cracks (Eq. 2.55), equating the latter with an estimate of the effective fracture energy density (4.38) and calculating the limit as the slip rate goes to infinity (which corresponds to the onset of the co-seismic phase; we note that Rubin & Ampuero, 2005 used slightly different estimates to arrive at the same result). The formula fits their numerical results well, except for models with a/b close to 1 and heterogeneous initial distribution of the state variable. For a 3-D circular patch, the result (2.95) for the energy release rate of a

circular crack can be used instead, yielding the nucleation radius:

$$r_{nuc}^{\infty} = \frac{\pi}{8}\frac{2-\nu}{1-\nu}\frac{\mu L b}{\sigma_n (b-a)^2}. \tag{4.43}$$

This estimate was confirmed to a good accuracy by numerical simulations of Noda & Hori (2014). Note that because the square of the difference $b - a$ appears in these formulas, the final nucleation zone for the expanding crack regime can grow much larger than the critical length (4.27) and the no-healing nucleation estimate (4.40) when $a \approx b$. As in the no-healing regime, the time to instability is inversely proportional to the initial velocity.

The existence of the different characteristic length scales h_{nuc}^{FL} and $h_{nuc}^{\infty}$and the dependence on a/b was also found in 2-D stability analysis of the aging law by Viesca (2016). He numerically demonstrated that the two nucleation lengths correspond to fixed-point solutions of the 2-D rate-and-state problem for $a/b < 0.38$ and $a/b \to 1$, respectively. He also pointed out that taking $a/b \to 1$ corresponds to taking the small-scale yielding limit in an equivalent slip-weakening crack problem.

For the slip law, Ampuero & Rubin (2008) showed that the separation into two Ω controlled regimes is present as well. For $\Omega \gg 1$, the initial nucleation zone size is smaller than for the aging law and it shrinks with time until reaching instability. For the $\Omega \approx 1$ regime, the nucleation instead behaves as an accelerating and unilateral pulse.

4.3.3 Seismic cycles

The long-term evolution of rate-and-state fault may exhibit a wide spectrum of qualitatively different behaviors. Systematic studies of these behaviors have often been conducted in terms of one or more non-dimensional parameters. The most studied parameters are the ratios of the size of the VW patch to one of the characteristic sizes described in previous sections, such as h_{crit}^{2D} (Eq. 4.28), h_{nuc}^{FL} (Eq. 4.40), h_{nuc}^{∞} (Eq. 4.42), r_{crit} (Eq. 4.29) or r_{nuc}^{∞} (Eq. 4.43). These parameters are related by the important non-dimensional parameter

$$q = 1 - a/b \tag{4.44}$$

as

$$h_{nuc}^{\mathrm{FL}} \approx 2.75 h_{crit}^{2D} q, \tag{4.45}$$

$$h_{nuc}^{\infty} = \frac{2}{\pi} h_{crit}^{2D}/q, \tag{4.46}$$

and

$$r_{nuc}^{\infty} = r_{crit}/q. \tag{4.47}$$

For example, Kato (2003) considered a homogeneous circular VW patch with radius r and studied, assuming the quasi-dynamic approximation, the behavior of the fault as a function of r/r_{crit}, where r_{crit} is given by Eq. (4.29). Kato (2014) examined the effect of the characteristic slip distance L on the fault behavior, interpreting the results in terms of r/r_{crit} (unlike the following papers which consider the aging law, Kato 2003, 2014 consider a composite version of the aging law and the slip law, see Kato & Tullis, 2001). Liu & Rice (2007) studied a 2-D in-plane fault with VW zone of width h, and the dependence of the fault behavior on a parameter proportional to

$$\tilde{h} = \frac{h}{h_{crit}^{2D}}, \tag{4.48}$$

where h_{crit}^{2D} is given by Eq. (4.28). Wu & Chen (2014) explored the same ratio (for values that produce seismic events), as well as the ratio $a/b = 1 - q$, for anti-plane faults. Chen & Lapusta (2009) studied the effect of the size of a circular VW zone in a fully dynamic 3-D setting. Cattania & Segall (2019) explored the circular problem in a quasi-dynamic setting, focusing on the ratios r/r_{nuc}^{∞} and r/h_{nuc}^{FL}, and $1-q$. Cattania (2019) analytically and numerically explored the behavior of 2-D anti-plane faults in terms of h/h_{nuc}^{∞}. Perhaps the most exhaustive exploration was performed by Barbot (2019), who studied 2-D anti-plane and in-plane 2-D faults as well as 3-D circular faults and examined the parameters q, $\tilde{h}$, as well as the value of the referential coefficient f^*. Clearly then, the behavior of rate-and-state cycles may be very complex and cannot be simply characterized by a single non-dimensional parameter. Nevertheless, at the danger of oversimplification, a summary is attempted below.

When the size of the VW patch is sufficiently small (in comparison to h_{crit}^{2D}, h_{nuc}^{∞}, h_{nuc}^{FL}, r_{nuc}^{∞}, etc.), the faults produce only negligible, aseismic oscillations in slip rate that eventually decay to the plate velocity V_{pl} (Kato, 2003; Liu & Rice, 2007; Barbot, 2019; Wu & Chen, 2014). As the length ratios increase, the decay stops and aseismic slow-slip events appear (Liu & Rice, 2007; Chen & Lapusta, 2009; Barbot, 2019). The duration of these slow slip events may range from days or months (long-term slow-slip) to hours (short-term slow-slip). Next, aseismic bursts with an even shorter duration, but within the aseismic slip rate range (to which Barbot, 2019 refers to as slow earthquakes) appear. Eventually, the regime of seismic events

is reached. In the lower range of the seismic regime ratios, the seismic events are bilateral, nucleating from the center of the VW patch and rupturing the whole patch. However, as the length ratio increases, the faults start rupturing unilaterally from the edges (Chen & Lapusta, 2009; Barbot, 2019; Wu & Chen, 2014; Cattania & Segall, 2019). Eventually, some of these unilateral events begin rupturing the fault only partially. The evolution of the fault then starts containing both whole-fault and partial earthquakes. The seismic events may be accompanied by slow slip and aseismic burst precursors. The complexity of the cycles and the regularity of the event recurrence times also depend on the length ratios. On 2-D faults, the recurrence time of the events seems to progress from simply periodic to aperiodic, so that increasing the length ratios leads to greater complexity. On 3-D finite faults, the situation is more complicated and two-periodic (event recurrence times follow the pattern $ABABAB...$), multi-periodic and aperiodic patterns of whole system seismic ruptures appear, possibly even before the simply periodic cycles (Kato, 2014; Barbot, 2019).

Cattania (2019) invoked brittle crack models and the Irwin criterion to derive that the number of partial earthquakes per one cycle should scale as $\sqrt{h/h^{\infty}_{nuc}}$ for large h/h^{∞}_{nuc}. This estimate fits her numeric experiments fairly well. Heuristically, this monotonous dependence on h/h^{∞}_{nuc} arises because the slip required to nucleate a partial event scales with h^{∞}_{nuc}, whereas the slip required to rupture the whole fault scales with h. Cattania (2019) also showed that the distribution of inter-event times T_i for large h/h^{∞}_{nuc} is well approximated by a truncated power law. Cattania & Segall (2019) used crack models and arguments based on the Irwin criterion to show that T_i should scale with the seismic moment M_0 of each event as

$$T_i \sim M_0^{1/6}. \tag{4.49}$$

This is satisfied by their own numerical experiments as well as those by Chen & Lapusta (2009) and real observations of small repeating earthquakes (Nadeau & Johnson, 1998). Remarkably, the mechanism that leads to this scaling is different for small and large earthquakes.

The transition between aseismic and seismic behavior can also be achieved by increasing the parameter q, i.e. low values of q at fixed and moderate values of $\tilde{h}$ tend to produce slow slip events and aseismic bursts, and increasing q moves the fault towards seismicity (Wu & Chen, 2014; Barbot, 2019). A possible explanation for the effect of q is its influence on the nucleation regime. For $q < 1/2$, the nucleation is in the growing crack regime and h^{∞}_{nuc} is the relevant nucleation length. The ratio of the VW patch size to the actual nucleation size $h/h^{\infty}_{nuc} \propto \tilde{h}q$

(Eqs. 4.46 and 4.48) decreases with decreasing q, which might explain why aseismic cycles are produced at low values of q. At $q \approx 0.62$, the fixed crack regime is reached and h^{FL}_{nuc} is the relevant nucleation length. Indeed, no quantitative changes in behavior seem to occur in the simulations of Barbot (2019) for fixed $\tilde{h}$ and $q \gtrapprox 0.7$.

Even though the parameters $\tilde{h}$ and q can compensate each other to an extent, their effects are not interchangeable. The ratio $\tilde{h}$ seems to control the complexity of the seismic cycle, with large values corresponding to great complexity, regardless of the value of q. The ratio q, on the other hand, rather seems to be connected to the transition between slow and fast rupture, though it also controls complexity to a degree (on 3-D faults, for example, its change may induce a transition between one-period and two-period seismic cycles). In any case, the fault depends on the combination of the two parameters in a complicated manner.

In the above discussion, it was assumed that the external load $\boldsymbol{T_l}$ acting on the system throughout the seismic cycle is exclusively due to the constant external plate loading. When an additional load perturbs the stress on the fault, the behavior of the cycles can significantly depart from the unperturbed case (e.g., Dieterich, 1988; Gomberg et al., 1998; Kato & Hirasawa, 2000; Perfettini et al., 2003b; Gallovič, 2008; Cho et al., 2009; van der Elst & Savage, 2015; Yoshida et al., 2020). In particular, when an external stress perturbation is suddenly applied to the fault, the next event can be delayed, advanced, or even instantly triggered. The difference in the earthquake occurrence times of the unperturbed and the perturbed case is called the *clock advance*. It has been conjectured that the effect of both shear and normal perturbations, $\Delta\tau$ and $\Delta\sigma_n$, respectively, can be characterized by the *Coulomb stress change* ΔCS:

$$\Delta CS = \Delta\tau - f^* \Delta\sigma_n, \tag{4.50}$$

see, e.g., King et al. (1994); Harris (1998); Cattania et al. (2015). In chapter 5, we examine the effect of changes in Coulomb stress, realized by shear stress perturbations, on the clock advance of faults undergoing simply periodic earthquakes.

Original research

5 Static Coulomb stress load on a three-dimensional rate-and-state fault: Possible explanation of the anomalous delay of the 2004 Parkfield earthquake

This chapter was published as Kostka & Gallovič (2016). Minor corrections, including notational and stylistic edits, were made.

Abstract

We perform quasi-dynamic modeling of earthquake cycles using laboratory-derived rate-and-state laws of friction on a homogeneous three-dimensional fault model. We study the effects of the static Coulomb stress load on clock advance and clock delay of the subsequent event. We carefully investigate the dependence of the clock advance on the onset time of the stress load, its amplitude, area, and place of application of the load. We find that this dependence is complex, being controlled by the actual slip velocity on the fault, especially at the domain of the stress load. In particular, the stress (un)load can initiate the occurrence of quasi-periodic creep-like episodes, which could be associated with episodic increases of microseismicity on real faults, such as observed on the locked Parkfield segment of the San Andreas Fault. Depending on the load parameters, including its timing within the earthquake cycle, one of such creep-like events may trigger the next (clock advanced) system-size earthquake. In some cases, the nucleation of the main shock can fail, and the fault experiences one or several seismic events of

smaller magnitudes instead. In such a case the next main shock becomes significantly delayed. We speculate that such a mechanism could have contributed to the extreme delay of the M_w 6 2004 Parkfield earthquake. Indeed, the Parkfield segment was subject to Coulomb stress unload due to the 1983 Coalinga-Nuñez earthquakes and then experienced M_w 4.9 events in 1993–1994, when the system-size event was expected. Instead, these failed main shock nucleations delayed the Parkfield earthquake by another ≈10 years.

5.1 Introduction

Many earthquake faults undergo a quasi-periodic seismic cycle, where long-term tectonic loading is released in a form of characteristic earthquakes (Wesnousky, 1994; Stirling et al., 1996). The characteristic earthquakes are believed to be large enough to dominate the seismic moment release and substantially reduce the average stress. Such behavior is especially evident for subduction zone megathrusts, where the characteristic earthquakes have large magnitudes (>8) and relatively short recurrence times. Nevertheless, even smaller (intraplate), mainly mature, faults have characteristic earthquake distributions with maximum magnitude earthquakes occurring quasi-periodically. Correct estimation of the timings of such characteristic (or system-size) earthquakes in terms of a probability density function is one of the main keys to improving seismic hazard assessment. The shape of the probability density function is controlled by two main phenomena. First, real faults are characterized by frictional and geometrical complexities that result in heterogeneity in the stress redistribution along the fault, altering the occurrence of the characteristic earthquakes. Second, the faults do not exist individually, and thus the earthquake occurrence is affected by stress load/unload due to slip on nearby faults. Understanding these effects is thus one of the main goals of earthquake physics. In the present paper, we address the effect of stress load and unload by means of earthquake cycle simulations on a planar 3-D rate-and-state fault model. The effect of stress transfer is typically associated with increasing or decreasing rate of occurrence of small events (Freed, 2005; Steacy et al., 2005, and references therein). For larger-magnitude events, the effect of stress transfer on earthquake triggering can be assessed by the so-called clock advance (CA), i.e., the change of the occurrence time of the next earthquake on the fault under study. CA can be potentially taken into account in time-dependent earthquake forecasting (Stein et al., 1997) and in renewal models of characteristic earthquakes in seismic hazard assessment (Gomberg

et al., 2005; Console et al., 2009; Pace et al., 2014).

From simple considerations assuming a standard Coulomb criterion and spring slider model, it follows that the clock advance CA_S due to a static Coulomb stress increase $\Delta\mathrm{CS}$ is given by:

$$\mathrm{CA}_S = \frac{\Delta\mathrm{CS}}{\dot{\tau}_f} = \frac{\Delta\mathrm{CS}}{k_{eff} V_{pl}}, \tag{5.1}$$

where $\dot{\tau}_f = k_{eff} V_{pl}$ is a constant shear stressing rate due to far field loading, and V_{pl} is the plate velocity. The effective fault stiffness k_{eff} is related to the length of the fault R as

$$k_{eff} = c\mu/R, \tag{5.2}$$

where μ is the rigidity of the medium and $c \approx 1$ is a geometric constant. In this model, the clock advance is independent of the onset time of the stress load within the earthquake cycle. Gomberg et al. (1998) employed a simple single degree-of-freedom (1-D) spring slider model governed by the rate-and-state friction, obtaining CA_S as a monotonously decreasing function of the load onset time. We point out that such a model is still too simplified, neglecting effects related to the finite geometry of the real earthquake faults. For example, it cannot take into account possible spatial inhomogeneity of the stress load. Therefore, the clock advance needs to be analyzed considering a more realistic fault model in order to correctly take such effects into account in advanced time-dependent earthquake hazard models.

An examination of the effect of external stress perturbation on a finite-extent fault with rate-and-state friction was first presented by Kato & Hirasawa (2000), considering a two-dimensional dip-slip fault embedded in a half-space. They analyzed the effect of stress change due to a nearby compressional or tensional outer rise event on the earthquake cycle, finding that the clock advance depends non-linearly on the timing of the stress change. They reported that tensional earthquakes advance the occurrence of the next earthquake, and compressional earthquakes delay it, except for later parts of the cycle, where clock advance occurs. The research was followed by Kato (2004) and Kuroki et al. (2004), who examined the effects of nearby earthquakes on earthquake cycles of large interplate earthquakes at subduction zones. Kuroki et al. (2004) used a realistic 3-D fault geometry and evaluated the effects of three large earthquakes on the Tōkai earthquake, which is expected to occur in central Japan. Perfettini et al. (2003b) systematically analyzed CA on a 2-D rate-and-state fault by means of loading the whole fault at various onset times within the earthquake cycle. They found that while the

CA is constant when the load is applied at the beginning of the earthquake cycle, it exhibits oscillations when the fault is loaded later. The authors associated this effect with oscillations of an equivalent spring slider model. Liu & Rice (2007) simulated aseismic transients on a plate boundary caused by static stress changes. Cho et al. (2009) extensively investigated the effect of static stress changes on the occurrence of the next earthquake for various times and amplitudes of the static stress load, reporting discontinuities in the dependence of CA on the loading time.

Gallovič (2008) analyzed the position of the nucleation point of the event following the stress load on a 3-D rate-and-state fault model, confirming the oscillatory character of the CA. He also noticed the dependence of the CA on the spatial extent of the stress load.

Here we extend these studies by performing a detailed systematic analysis of the clock advance on a 3-D rate-and-state strike-slip fault model. We investigate the dependence of the clock advance on the onset time of the stress load, its amplitude, area, and place of application. We point out that many of the observed dependencies are related to 3-D effects of the slip velocity/stress evolution and thus cannot be modeled by a simple spring slider model (in accordance with earlier studies). We recognize that in some cases the advanced event may rupture only a portion of the fault (having a smaller magnitude), causing a significant clock delay of the next main shock. We suggest that a related mechanism may have played a role in the surprisingly long delay of the 2004 M_w 6 Parkfield earthquake (Bakun et al., 2005).

5.2 Model

5.2.1 Quasi-Dynamic Rate-and-State Fault Modeling

We use a model of a two-dimensional square vertical fault of dimensions $R \times R$ embedded in a homogeneous isotropic half-space. The fault is discretized into $N \times N$ equally sized square cells with dimensions $\Delta R = R/N$. The frictional stress on cell i is given by the well-established Dieterich-Ruina constitutive rate-and-state law (Dieterich, 1979; Ruina, 1983):

$$\tau_i \left(V_i(t), \theta_i(t)\right) = \sigma_i \left(f^* + a_i \ln \frac{V_i(t)}{V^*} + b_i \ln \frac{\theta_i(t) V^*}{L_i} \right), \tag{5.3}$$

where V_i and θ_i represent the slip velocity and state variable, respectively, at cell i, σ_i is the normal stress, L_i, a_i and b_i are frictional parameters, and f^* and V^* are the referential values of the frictional coefficient and velocity, respectively. The evolution of the state variables is governed by the Dieterich aging law:

$$\frac{d\theta_i(t)}{dt} = 1 - \frac{V_i(t)\theta_i(t)}{L_i}. \tag{5.4}$$

On the fault, the frictional stress must be balanced by both elastic and radiative contributions, as well as the externally imposed stress $\Delta\tau_i(t)$:

$$\tau_i(t) = \sum_j K_{ij}\left(\delta_j(t) - V_{pl}t\right) - \frac{\mu}{2\beta}V_i(t) + \Delta\tau_i(t), \tag{5.5}$$

where δ_j is the slip on the cell j, V_{pl} is the constant driving plate velocity, μ is the Young shear modulus, and β is the S-wave velocity. Kernel K_{ij} of elastic interactions represents static stress induced on cell i by unit slip on cell j, which we evaluate using the analytical solutions by Okada (1992). The middle term on the right-hand side of Eq. (5.5) corresponds to the (standardly added) viscous term introduced by Rice (1993), also called the radiation damping term, which approximates the effect of seismic wave radiation. Outside the model fault zone, continuous stable sliding is assumed ($V = V_{pl}$).

After setting (5.3) and (5.5) equal, differentiating, and doing simple algebra, one arrives at a system of ordinary differential equations (see a detailed description in Perfettini et al., 2003b or Gallovič, 2008). This system is solved using the Runge-Kutta algorithm with fifth-order adaptive step-size control (Press et al., 1992).

5.2.2 Catalog Extraction

During the earthquake cycle simulation, we extract a seismic catalog by breaking the slip velocity history into separate events using criteria similar to those described by Hillers et al. (2006). Specifically, an event is comprised of cells with slip rates greater than a given threshold and that share a common hypocenter. If two cells belonging to different events touch each other, they are merged into a single event. For each event, we record its hypocentral time and calculate its moment magnitude M_w.

One possibility of defining the threshold slip velocity is to use the critical velocity $2\beta a\sigma/\mu$ for which the forces of radiation damping and friction compensate (Noda & Hori, 2014). This would result in 0.23 m/s in our setting. Nevertheless, we use a smaller value of 1 mm/s as a standard value also considered by other authors when performing similar simulations (Perfettini et al., 2003b; Hillers et al., 2006; Gallovič, 2008; Murphy et al., 2013). We note that the conclusions of this work are not affected by this choice.

5.2.3 Stress Load and Clock Advance

We pick a reference time t_r after several earthquake cycles. Without applying external Coulomb stress, an event occurs at time $t_u > t_r$. Starting from time t_0 such that $t_u > t_0 > t_r$, we apply stress perturbation $\Delta\tau_i(t)$ at cell i of the form

$$\Delta\tau_i(t) = \begin{cases} \frac{1}{2}\Delta\mathrm{CS}_i \left(1 - \cos\pi\left(\frac{t-t_0}{\Delta t}\right)\right) & \text{for } t_0 < t < t_0 + \Delta t \\ \Delta\mathrm{CS}_i & \text{for } t \geq t_0 + \Delta t \end{cases}. \tag{5.6}$$

The stress perturbation thus increases during the time interval Δt from $\Delta\tau(t_0) = 0$ to $\Delta\tau(t_0 + \Delta t) = \Delta\mathrm{CS}_i$, where $\Delta\mathrm{CS}_i$ is the amplitude of the static Coulomb stress change.

As a result of the stress perturbation, one or more events will nucleate at hypocentral times which will generally differ from t_u. The magnitudes of the events will also generally differ from the unperturbed case. The clock advance CA is defined as

$$\mathrm{CA} = t_u - t_p, \tag{5.7}$$

where t_p refers either to the occurrence time of the subsequent event regardless of its magnitude (referred to as a magnitude-unconstrained CA), or the subsequent event with magnitude larger than threshold magnitude M_{tr} (referred to as the magnitude-constrained CA). Negative values of CA are also called clock delay.

Note that we have tried to apply shear stress and normal stress perturbations that correspond to the same amplitude of Coulomb stress change, obtaining almost identical results (as also observed by Perfettini et al. 2003b). Therefore, we only apply shear stress perturbations to realize the Coulomb stress change.

Quantity	Notation	Value
Fault dimensions	$R \times R$	25×25 km^2
Fault discretization	$N \times N$	128×128
Shear modulus	μ	30 GPa
Lamé's first parameter	λ	20 GPa
Friction parameters	a	0.015
	b	0.019
	L	2 cm
Referential friction coefficient	f^*	0.6
Referential velocity	V^*	1 µm/s
Loading plate velocity	V_{pl}	3.5 cm/year
S-wave velocity	β	3 km/s
Normal stress	σ	75 MPa

Table 5.1: Parameters of the fault model. The setup leads to periodic occurrences of M_w 6.9 earthquakes.

5.3 Modeling results

We consider a homogeneous fault in the velocity-weakening regime ($a - b = 0.004$) embedded in a homogeneous elastic space with constant normal stress σ. The model parameters are listed in Table 5.1. The fault homogeneity allows us to focus solely on the effect of the properties of Coulomb stress change (i.e., amplitude, placement, duration, etc.), without introducing additional complexities due to, e.g., the effect of heterogeneity of frictional parameters or free surface. At the beginning of the simulation, the model is initiated by setting slip velocities to twice the plate velocity V_{pl} on the whole fault. After one or two earthquakes, the fault reaches a stable cycle of repeating events of magnitude $M_w = 6.9$. The average stress drop $\Delta\tau_{avg}$ of these events is 6.2 MPa according to the formula $\Delta\tau_{avg} = (b - a)\sigma \ln(V_{co}/V_{int})$, where $V_{co} = 1\,m/s$ is the co-seismic slip velocity and $V_{int} = V_{pl}$ is the estimate of the average inter-seismic slip velocity (Barbot et al., 2012, supplemental material); this value is similar to the actual difference between maximum and minimum values of average shear stress, which gives the stress drop of 5.2 MPa. The duration of the unperturbed inter-seismic cycle is approximately 89 years. The graph of the average and maximum velocities on the fault is shown in Fig. 5.1a, and the graph of slip velocities at five regularly spaced points on the fault are shown in Fig. 5.1b. Just after an event ends, the slip rates decrease to values about 4 orders smaller than V_{pl}, bringing the fault into an effectively locked state. Then, slip velocities at the fault start to

increase to $\approx V_{pl}$, and this creep gradually penetrates into the locked area, building conditions for nucleation of the subsequent system-size event in the center of the fault (Rubin & Ampuero, 2005). This nucleation style corresponds to the bilateral rupture propagation style described by Lapusta & Liu (2009). Therefore, our simulation results are to be considered representative of models of this type. We point out that in the modeling of the Parkfield fault in subsection 5.4.2, the rupture behavior rather corresponds to the second style described by Lapusta & Liu (2009), where the velocity-weakening regions are penetrated by only a small amount of aseismic creep, the events nucleate closer to the fault borders, and rupture unilaterally.

5.3.1 Clock Advance Due to Stress Perturbation

We set the origin of the time coordinate to $t_r = 733.0$ years since the start of the simulation, which corresponds to the beginning of the eighth earthquake cycle. To see the effect of the stress load on the clock advance (CA), we run the earthquake cycle 500 times, applying the shear stress increase or decrease of magnitude $\Delta\mathrm{CS} = \pm 0.01\ \sigma$ (i.e., approximately 14% of the main shock stress drop) to the whole fault at various onset times t_0 and measure the resulting CA. We let $\Delta t = 10$ s, which effectively corresponds to an instantaneous Coulomb stress change. Fig. 5.2 shows the dependence of the magnitude-constrained ($M_w > M_{tr} = 6$) and the magnitude-unconstrained CA on the load time t_0 for both positive and negative loads. After an interval corresponding to constant CA, the dependence has an oscillatory character. Such behavior of the (unconstrained) CA was first observed by Perfettini et al. (2003b) and later by Gallovič (2008) on 2-D and 3-D rate-and-state faults, respectively. Here we analyze the behavior of the CA in more detail.

The magnitude-unconstrained CA curves in Fig. 5.2 can be separated into three to four phases: static, increasing, and decreasing. The fourth phase, corresponding to instantaneous triggering, is present only in the case of positive stress load. The increasing and decreasing phases are jointly referred to as the oscillatory phase of CA.

During the static phase, CA is a constant independent of t_0. In each decreasing phase, CA decreases approximately linearly, with a slope close to -1. Recalling the definition of clock advance (5.7), this means that events occur after approximately constant time intervals from the CS load application. In the static and decreasing periods, the subsequent earthquake corresponds to a system-size event with magnitudes ranging from 6.5 to 7. This means that

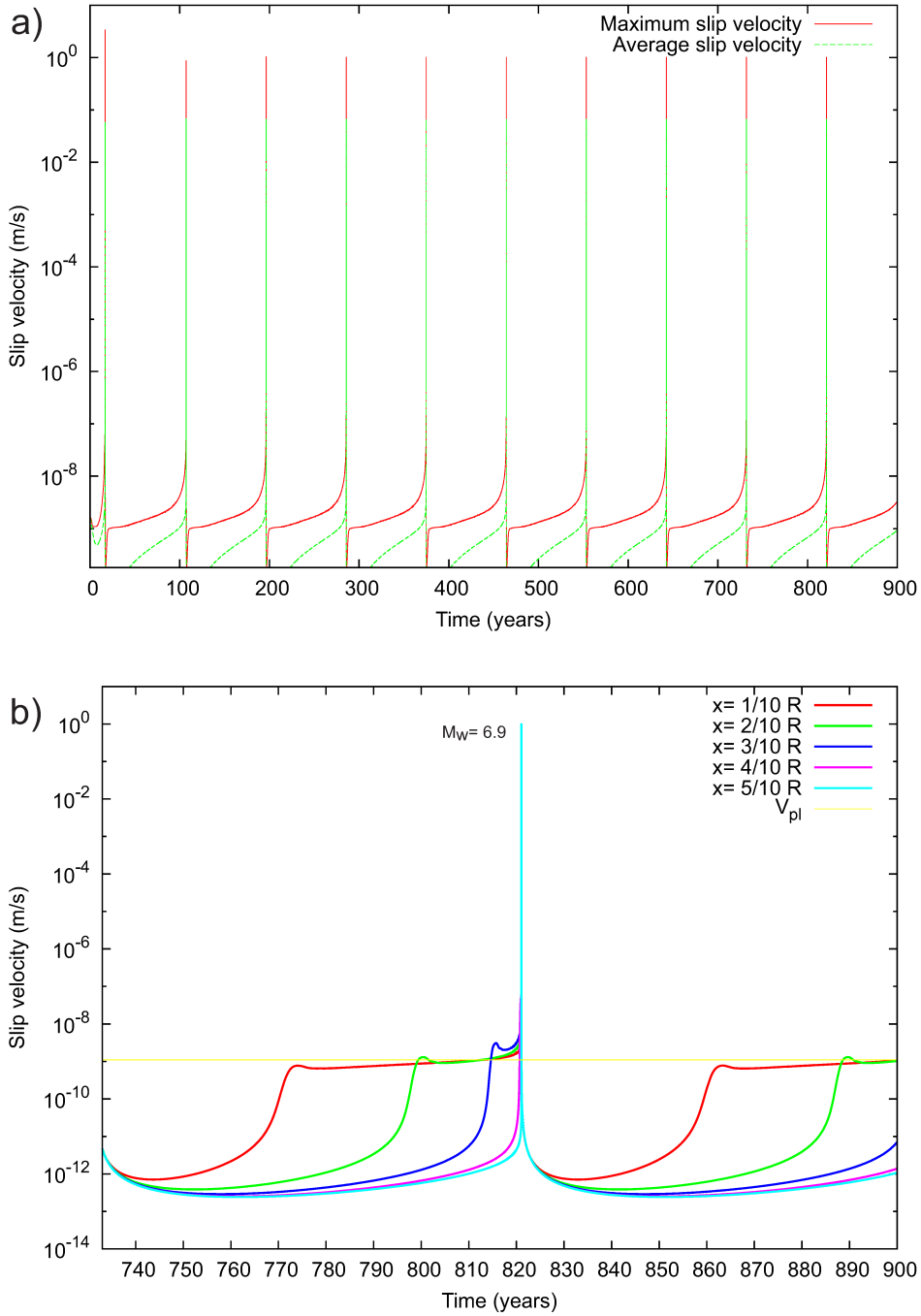

Figure 5.1: a) Evolution of the average (green) and maximum (red) slip velocities on the homogeneous rate-and-state fault model (see Table 5.1 for its parameters). b) Evolution of slip velocities from $t_r = 733$ to 900 years at five equidistant points in the middle width of the left half of the fault (see legend); note that the two halves of the fault evolve in the same way due to the symmetry of the problem. Just after an event, the slip velocities on the fault decrease to values about 4 orders of magnitude smaller than V_{pl}. Velocity at the borders of the asperity then starts increasing to values close to V_{pl}, and this creep gradually penetrates into the locked area, building conditions for nucleation of the subsequent system-size event in the center of the fault.

the magnitude-constrained and magnitude-unconstrained CA curves coincide (see Fig. 5.2). However, the situation is more complex in the increasing phase, where the smooth magnitude-unconstrained CA is related to the occurrence of events with magnitudes between 3.5 and 6 (see Fig. 5.2). In the magnitude-constrained case, i.e., when considering the occurrence of the system-size event, CA is characterized by abrupt changes with significant values of clock delay. We note that the intervals of t_0 associated with such clock delays are rather short, 1.3 years on average in the present example. Nevertheless, since there are six such intervals within the earthquake cycle (with average time spacing of 7.0 years), they altogether amount to 7.6 years, which corresponds to 8.5% of the whole cycle.

5.3.2 Fault Evolution After Stress Perturbation

To better understand the behavior of the CA, we analyze the evolution of slip velocities on the fault after the stress load. We do not discuss here the effect of instantaneous triggering, which is, in the present context, relatively straightforward.

Fig. 5.3 shows maximum velocity as a function of time for several examples of (positive) stress onset times t_0. In Fig. 5.4a we plot slip velocities at five different equidistant points located in the middle width of the fault. Immediately after the stress load, the slip velocities increase at the affected cells. For a simple spring slider model, one can derive an approximate formula for the change of velocity following Coulomb stress steps ΔCS (e.g., Perfettini et al. 2003b):

$$V(t_0^+) = V(t_0^-) \exp\left(\frac{\Delta \mathrm{CS}}{a\sigma}\right), \tag{5.8}$$

where $V(t_0^-)$ and $V(t_0^+)$ are the slip velocities before and after the stress step, respectively. The formula predicts that the response to the stress step depends not only on its amplitude ΔCS (exponentially) but also linearly on the actual slip velocity $V(t_0^-)$. We remind the reader that during the earthquake cycle, the slip velocities increase inward from the borders of the asperity from values corresponding to the locked fault to values corresponding to a creeping ($\approx V_{pl}$) fault, which differ by approximately 4 orders of magnitude. Therefore, the effect of the load is the most significant when applied to the creeping portion of the fault. For example, Fig. 5.4a demonstrates that only the creeping parts of the fault at the fault edge start to oscillate after the stress load. This response then in turn alters the stress field, which may lead

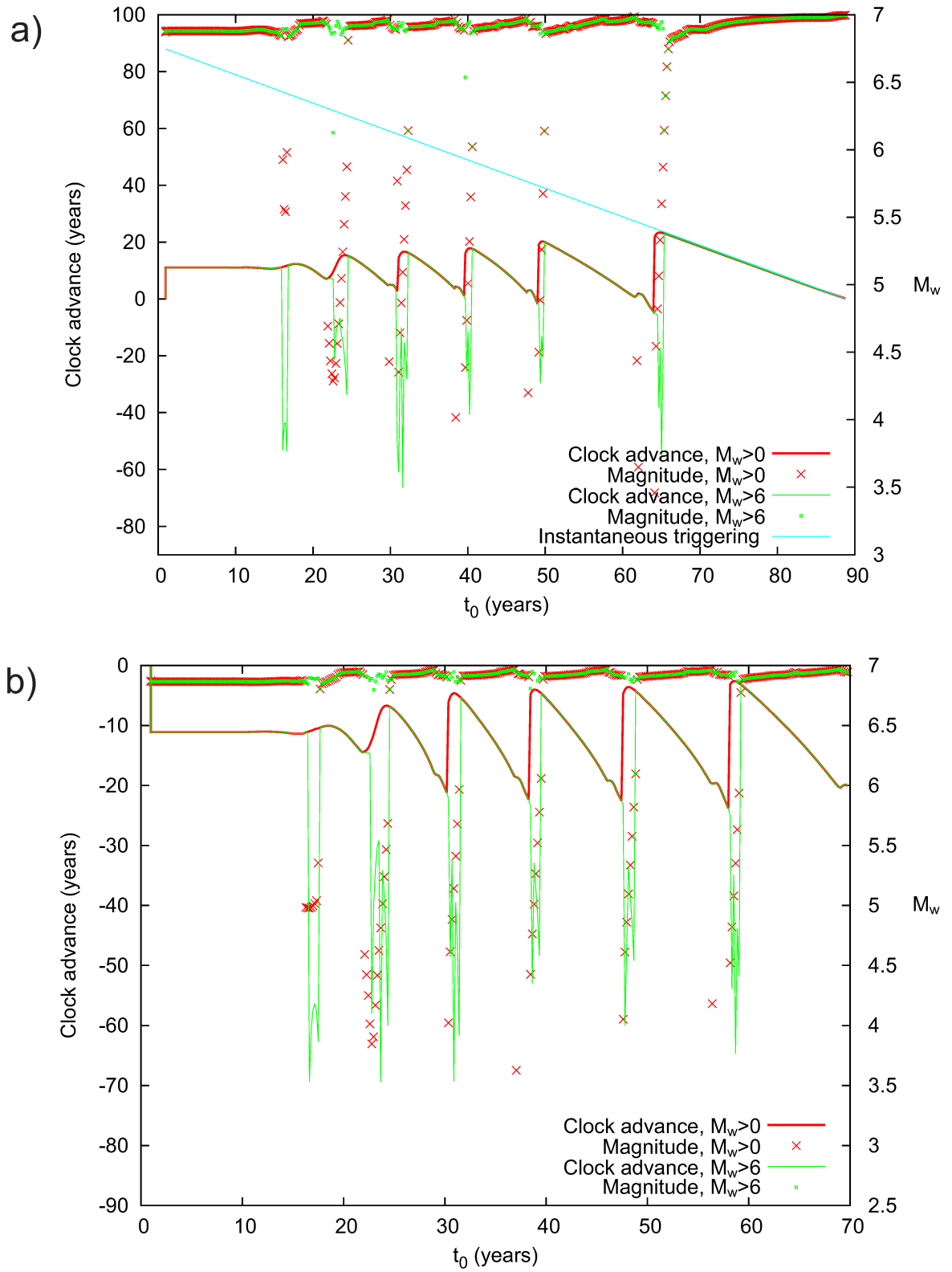

Figure 5.2: Clock advance CA (lines, left axes) and magnitude of the triggered events (symbols, right axes) as functions of stress load onset time t_0 for a) positive and b) negative loads. The red lines represent CA corresponding to the very first subsequent (triggered) event, regardless of its magnitude. The green lines correspond to CA of the first subsequent event with a magnitude larger than 6 (so-called magnitude-constrained CA). Note that the two curves depart only in the intervals of increasing CA, where the system-size events are significantly delayed for both the load and unload. The blue line corresponds to instantaneous triggering.

to destabilization of the fault.

In particular, when the stress load is applied early after an event, the initial velocity jump is relatively small, because the fault is locked almost everywhere. In such a case the resulting slip velocity perturbations are relatively weak and get damped after a relatively short time (see Fig. 5.3a). Nevertheless, the overall velocity (and thus stress) increase remains stored in the system, leading to the observed independence of the CA on t_0 in the constant CA phase (see Fig. 5.2).

During the oscillatory phase of CA, the initial velocity jump results in quasi-periodic oscillations in maximum slip velocity, which do not get damped. Depending on the timing of the CS load, one of the episodic slip velocity increases, taking place close to the occurrence of the regular event, can either trigger the system-size event or fail in doing so. The former case would correspond to the decaying part of the CA curve (see Fig. 5.2), while the latter case would correspond to the increasing part of the magnitude-unconstrained CA curve. During the failed (small magnitude) event, the slip velocities reach normal seismic values ($\approx$1 m/s), just as during the system-size event, but only on a part of the total fault area. Moreover, several such small events can happen in a relatively short time. Since the small earthquakes can release a relevant part of the accumulated stress on the fault, the system-size event may get delayed by a significant fraction of the whole earthquake cycle duration.

A similar example of such failed nucleation is shown in Fig. 5.4b for a shear stress perturbation of amplitude $+0.01\sigma$ applied to the fault edge at $t_0 = 39.0$ years. The figure shows slip velocity histories at five equidistant points on the fault. We can observe that the slip velocities at the perturbed points at the right edge of the asperity gain an immediate increase. As a result of the perturbation, the point at $9/10R$ undergoes oscillatory creep, whereas the slip velocity at the other side of asperity at $1/10R$ remains steady until 83 years, where a small peak is observed. At 84 years, the center of the fault reaches seismic velocities, but this rupture is confined to a small area around the center and does not spread to either of the points close to the borders of the asperity (although the slip velocities at both points undergo small sharp peeks a few years before this event). This results in an event of magnitude 4.9. Later, another event is produced at 106 years, rupturing a larger area (but not the whole asperity) and having a magnitude of 5.3. Eventually, the whole asperity is ruptured at 149 years, causing an event of magnitude 6.9, corresponding to the magnitude of the unperturbed main shock. Thus, this perturbation results in a delay of 60 years.

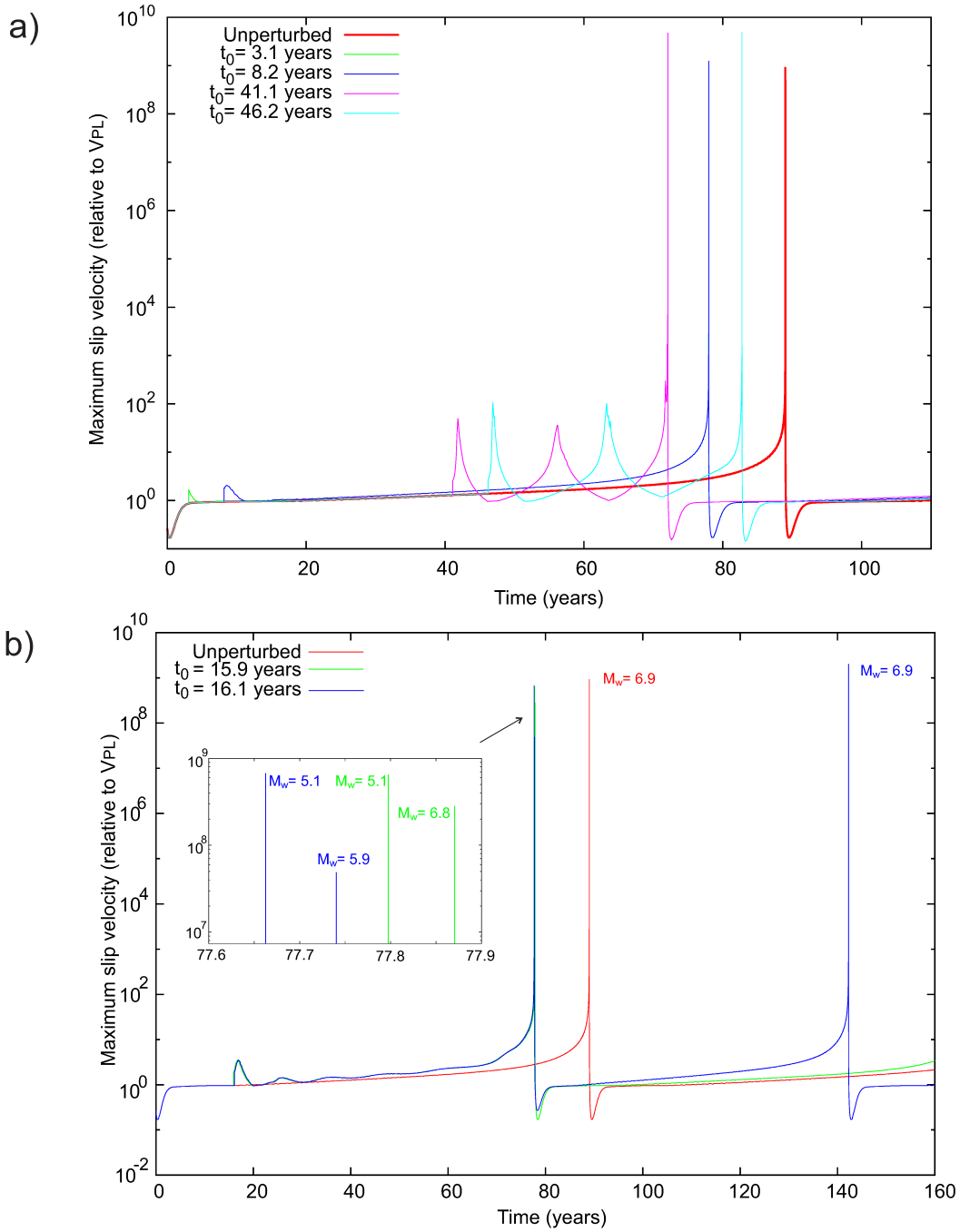

Figure 5.3: a) Evolution of the maximum slip velocities over the fault for selected stress loading times t_0 (see legend), corresponding to various parts of the CA plot in Fig. 5.2a. Loading times of 3.1 and 8.2 years correspond to the flat phase of the CA (see Fig. 5.2a). Loading times of 41.1 and 46.2 years were selected from the period of the CA decrease in Fig. 5.2a. The evolution of the slip velocities at five points for the case of loading at 41.1 years (here in magenta) is shown in Fig. 5.4a. b) The evolution of maximum slip velocities for two scenarios with t_0 only 2 months apart, at the boundary between the decreasing interval of the CA and the clock delay interval (Fig. 5.2a). Until the occurrence of the first smaller event, the evolution of the maximum slip velocities is very similar. Nevertheless, while for the smaller t_0, the first event is followed by a (clock advanced) system-size rupture of $M_w = 6.8$, for the larger t_0, the second event fails to rupture the whole fault (thus having smaller magnitude), even though its maximum slip velocity is larger than for the main shock triggered in the case of the smaller t_0. The whole fault is then ruptured 65 years later.

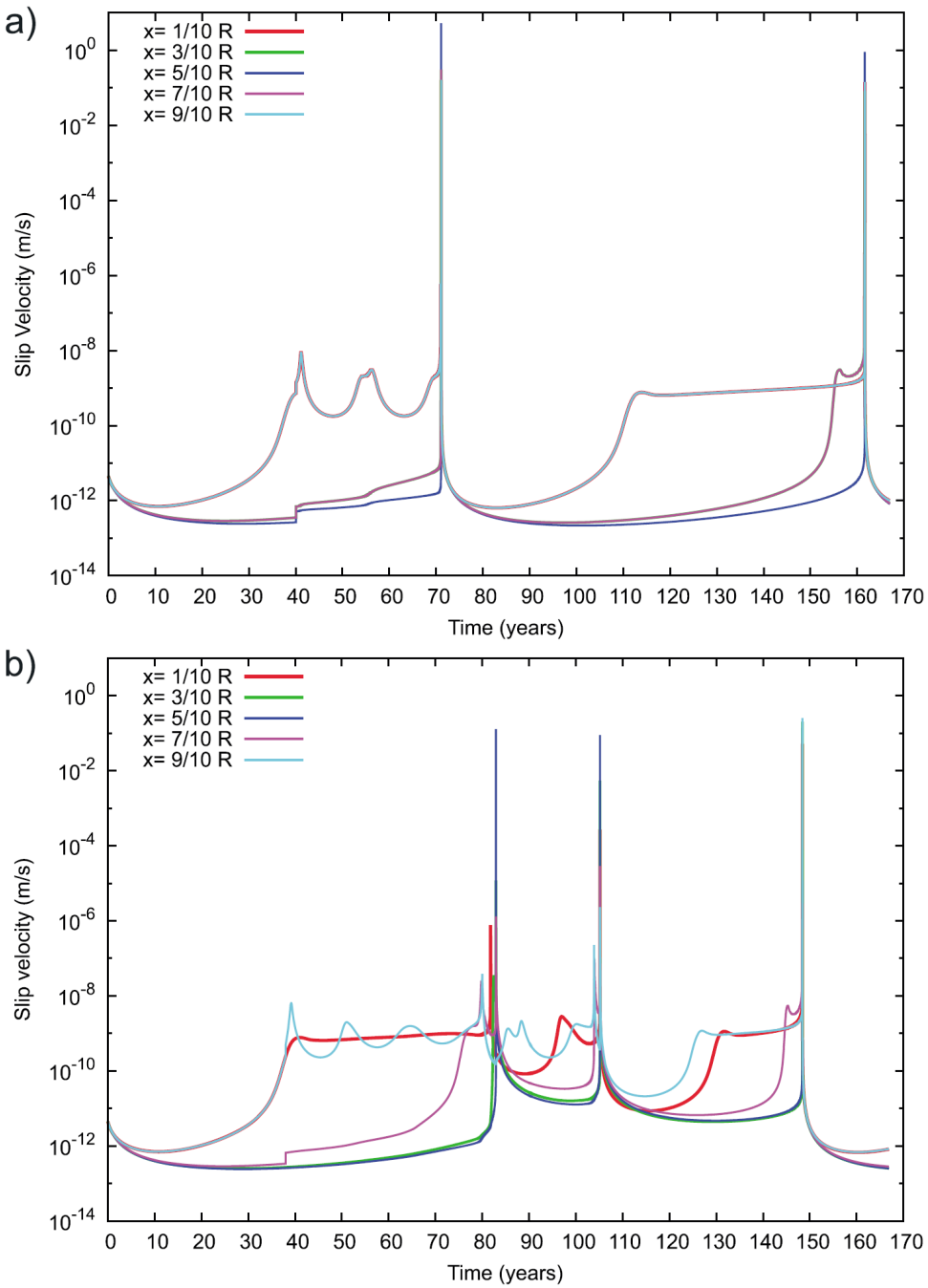

Figure 5.4: a) Evolution of slip velocities at five equidistant points along the middle horizontal cross-section of the fault (see legend) assuming a shear stress perturbation of amplitude $+0.01\sigma$ applied to the whole fault at $t_0 = 41.1$ years. The curves corresponding to the opposite sides of the fault overlap due to the symmetry of the model and the perturbation. Note the slow-slip oscillations at the edges of the fault. After the whole fault has been ruptured, it starts evolving in the same way as the unperturbed fault. b) Evolution of slip velocities at the same points as in a) when a shear stress perturbation of the same amplitude is applied to the edge of the fault at $t_0 = 39.0$ years. In this case, the oscillations are present only at the side of the fault affected by the stress increase. At 84 years only the center of the fault reaches seismic velocities, resulting in an event of magnitude 4.9. It is followed at 106 years by another event of magnitude 5.3, which ruptures a larger area. Eventually, the whole fault ruptures at 149 years, causing an event of magnitude 6.9 (equal to the original unperturbed magnitude), which is thus delayed by 60 years.

5.3.3 Dependence of Clock Advance on the Stress Load Parameters

In this section, we explore the dependence of CA on parameters of the shear stress loading, such as its amplitude and domain of application. For the sake of clarity, we show here only the magnitude-unconstrained CA curves. In all cases, the relatively narrow intervals of increasing CA are always associated with significantly delayed system-size events. Fig. 5.5a shows the dependence of the magnitude-unconstrained CA on t_0 for different values of the stress load amplitude ΔCS applied to the whole fault. Fig. 5.5b shows the same dependence as Fig. 5.5a but considering the application of the load on the central square covering one-half of the fault area. The stress drop during the mainshock, 5.2 MPa, corresponds to about 7% of the confining normal stress. For perturbations greater than this, there is instantaneous triggering for all t_0. Below we discuss the static and oscillatory phases separately in detail. We also interpret the observed dependences using arguments developed in subsection 5.3.2.

Static Phase

The static phase is observed for early onset times of the stress load in all cases. We denote the CA during this phase by CA_0 and calculate it for the onset time $t_0 = 1$ year. The dependence of CA_0 on ΔCS is explored in Fig. 5.6, assuming loading over the whole fault and at two smaller rectangular areas located in the middle of the fault or at its corner. As we can see, CA_0 depends approximately linearly on ΔCS as predicted by the standard Coulomb failure model (see Eq. 5.1). However, the slope of the curve, which should only depend on the fault stiffness, varies according to the extent of the loaded area and its position. The steepest slope is for the case of loading the whole fault. In the case of partial loading, CA_0 is larger for the central loading than the corner loading (for the same ΔCS). Assuming $\mathrm{CA}_0 = \Delta\mathrm{CS}/(k_a V_{pl})$, as suggested by the Coulomb failure model (5.1) but with k_{eff} replaced by k_a, we can obtain the "apparent" stiffness k_a by means of linear regression. For the whole fault loading we obtain the minimum value of $k_a^{min} = 1.93$ MPa/m, which is larger than the effective fault stiffness $k_{eff} \approx \mu/R = 1.2$ MPa/m. For loading the central half of the fault $k_a = 2.38$ MPa/m.

To explore the role of the loading area further, Fig. 5.6b shows the dependence of CA_0 on the extent of the loading (square) area, assuming three locations of the load—center, middle edge, and corner. The loading amplitude is constant in this case, $\Delta\mathrm{CS} = 0.2\sigma$. Generally, CA_0 is an increasing, yet nonlinear function of the loading area. Moreover, we can also see that

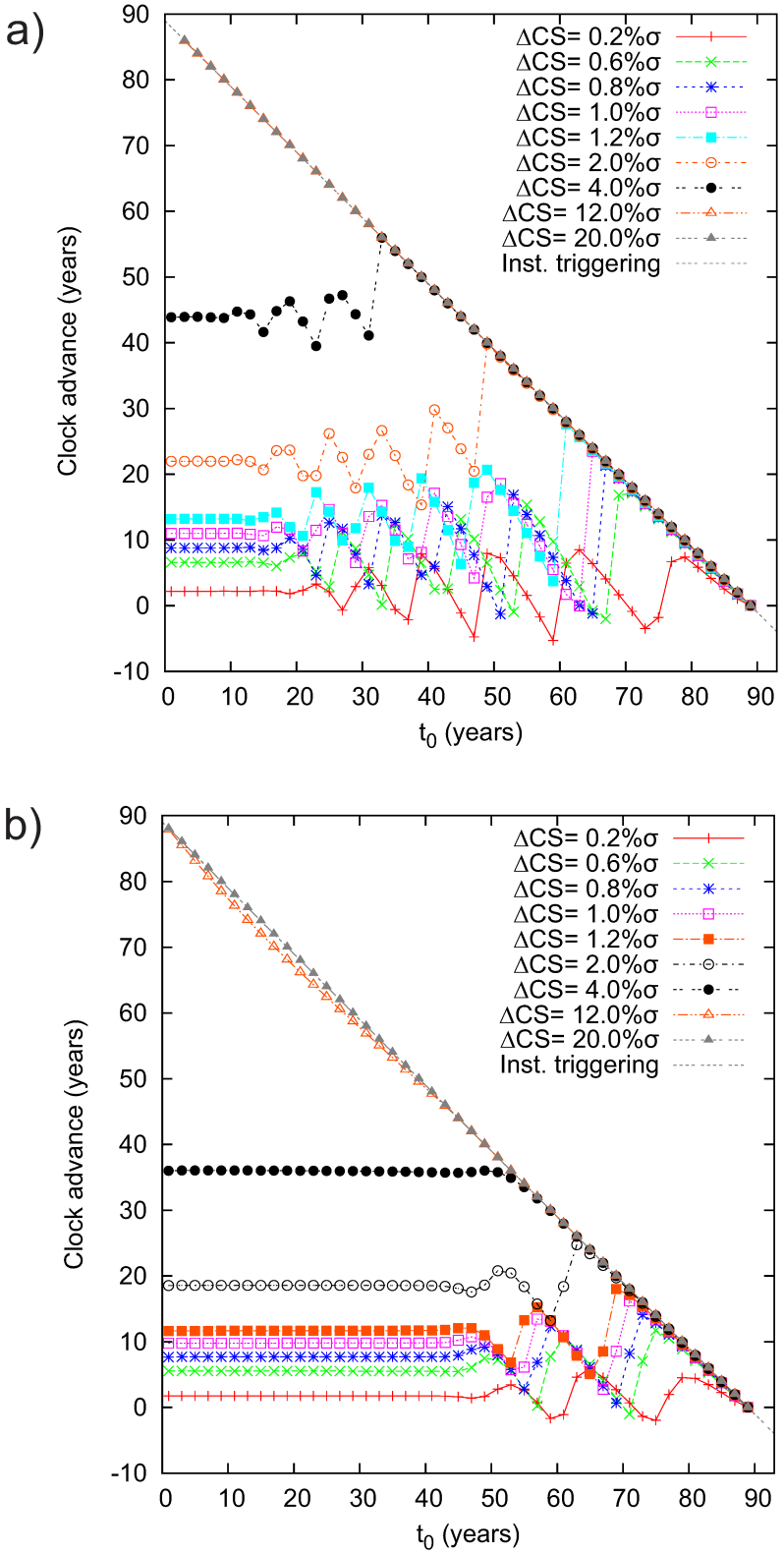

Figure 5.5: Dependence of the magnitude-unconstrained CA on the loading time t_0 for various amplitudes of the stress load expressed as a fraction of the normal stress σ (see legend). The load is applied either a) to the whole fault or b) to a square covering the central half of the total fault area.

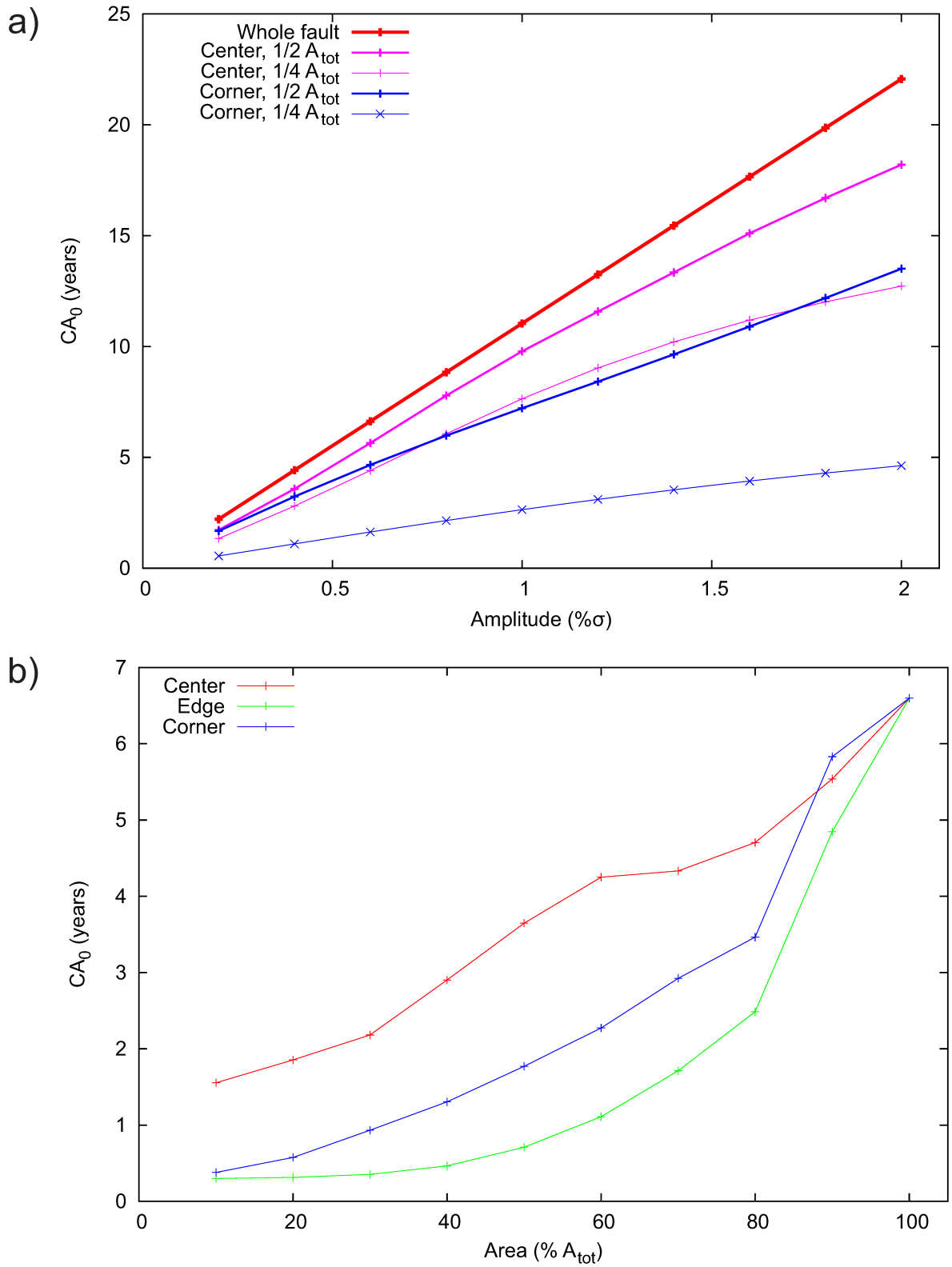

Figure 5.6: a) The dependence of CA_0 (the value of CA corresponding to the flat phase of the CA graph, see, e.g., Fig. 5.5) on the stress load amplitude ($x-$axis) and the loading area (see legend), evaluated for a stress load application at $t_0 = 1$ year. The loading is applied to the whole fault (red line) and at two smaller rectangular areas located at the middle of the fault (pink lines) and at its corner (blue lines) with areas equal to one half (thick lines) and one fourth (thin lines) of the total fault area A_{tot}. b) Dependence of CA_0 on the area of the stress load for three different locations of the loading domains (see legend), assuming fixed stress load amplitude of 0.2% σ.

the dependence of CA_0 on the loading area differs according to the particular location of the load. We interpret the behavior of CA_0 following the argumentation in subsection 5.3.2. Slip velocities affected by the stress load increase according to Eq. (5.8). In particular, the increase is linearly dependent on the slip velocities prior to the stress load. Since the slip velocity is inhomogeneously distributed along the fault (e.g., at the beginning of the earthquake cycle, large values are constrained to the fault borders), the change in the velocities (and stress) is also inhomogeneous. Although any consequent slip velocity oscillations diminish in time, the additional stress heterogeneity introduced by the load is preserved by means of the memory effect of the friction state variable, which leads to the complex behavior of CA_0.

Oscillatory Phase

The onset of the oscillatory phase t_{osc} strongly depends on the extent and position of the CS loading area. To explore this issue, Fig. 5.7 shows CA for various Coulomb stress loading amplitudes ΔCS applied to square areas of three sizes located at the center of the fault (Fig. 5.7a) and at its edge (Fig. 5.7b). For the stress load at the fault center (Fig. 5.7a) the larger the CS area, the smaller the t_{osc}. On the other hand, when the CS load is applied at the edge of the fault, t_{osc} is rather small and independent of the load area.

The observed behavior can again be related to the stronger response of the creeping part of the fault to the applied load, as discussed in subsection 5.3.2. Indeed, t_{osc} is the smallest when the loading is applied at the edge of the fault (Fig. 5.7a), since the fault edges are the first to start creeping after the preceding event. Contrarily, if the stress load is applied at the fault center (Fig. 5.7b), the smaller the area, the later the CA oscillations begin. This happens because the load is applied to the locked section of the fault for a longer fraction of the earthquake cycle period.

5.4 Discussion and Conclusions

We have studied the effect of static Coulomb stress change on the clock advance or delay of a characteristic earthquake on a 3-D fault model with rate-and-state friction. The present dynamic fault model is rather simple (planar fault, homogeneous frictional parameters, etc.) to isolate the effect of the stress load from other features. Despite this simplification, the

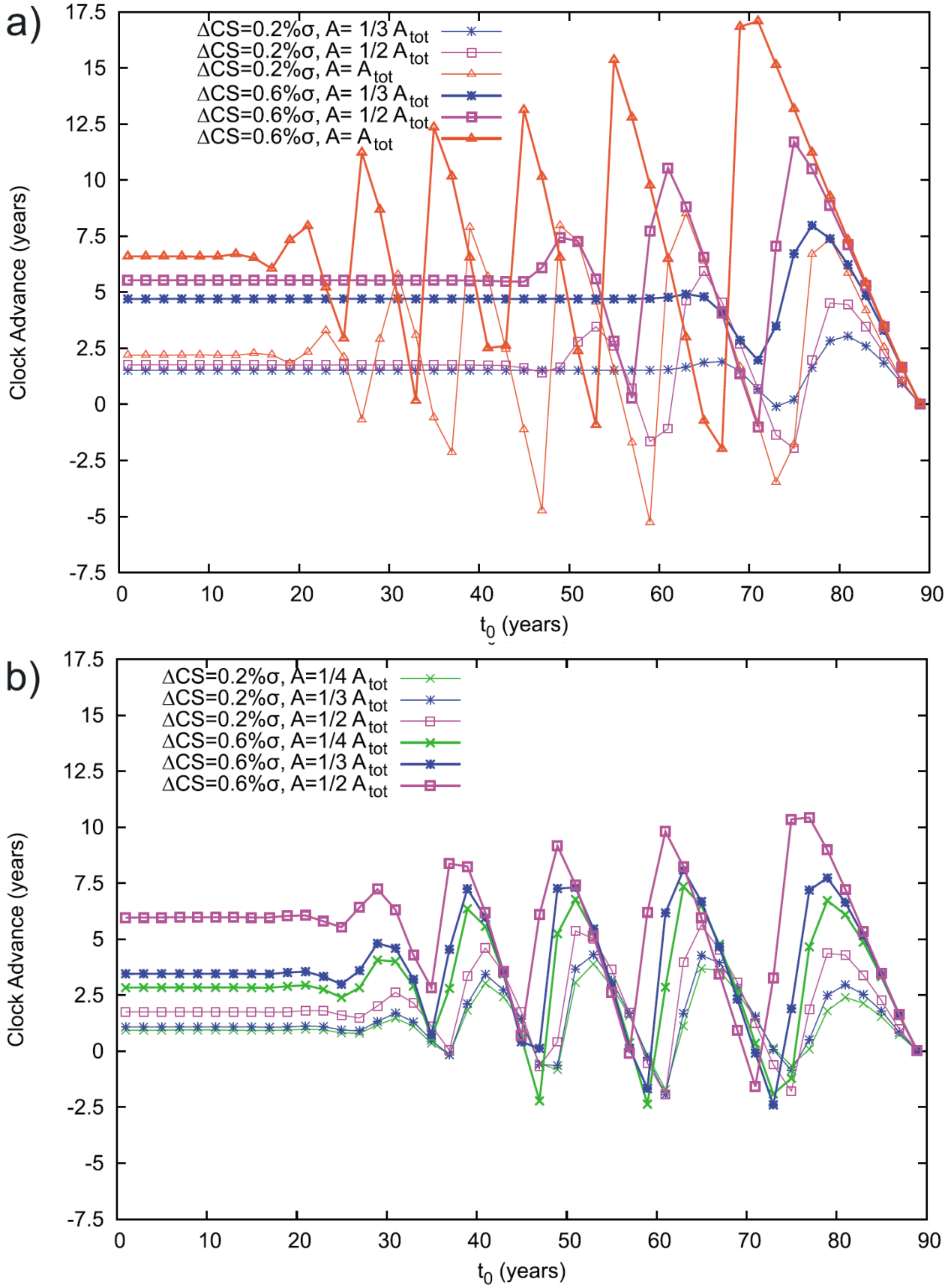

Figure 5.7: a) Dependence of the magnitude-unconstrained CA on the loading time t_0. The stress load has various amplitudes expressed as a fraction of the normal stress σ and sizes of the loading domains (see legend). The load is applied either a) at the central part of the whole fault or b) at the fault corner.

response of the fault to the stress load is complicated. For example, in agreement with other studies (Perfettini et al., 2003b; Gallovič, 2008), we observe that the clock advance (CA) is an oscillatory function of the stress load onset time t_0. We point out that such a complexity of the CA is related not only to the nonlinear character of the rate-and-state friction model but also to the 3-D fault geometry. Indeed, a simple spring slider model with rate-and-state friction law predicts CA due to a static stress loading to be a monotonously decreasing function of t_0 within the whole earthquake cycle (Gomberg et al., 1998). We observe that the stress load disturbs the otherwise stable fault evolution by increasing slip velocity on the loaded part of the fault. The elevated slip velocities may lead to instantaneous nucleation of the main (system-size) earthquake. If the fault is not ready to go, the nucleation is arrested and such a failed nucleation becomes a creep-like event, introducing an additional heterogeneity in the stress distribution on the fault. If the load is applied at the beginning of the earthquake cycle, the fault returns to its stable evolution. Otherwise, the stress heterogeneity leads to an excitation of a quasi-periodic occurrence of additional creep events traveling along the fault. Eventually, one of these events leads to the nucleation of a seismic event. Depending on the timing and the amplitude of the stress load, this earthquake may rupture the whole fault (system-size event), or just a part of it, corresponding to a smaller-magnitude event. We demonstrate that in the latter case, the next system-size earthquake can be significantly delayed from its regular (unperturbed) occurrence. We note that such delayed occurrence of the main shock can happen for both the positive and negative loads (Fig. 5.2).

5.4.1 Induced Slip Velocity Oscillations

Inter-seismic slip velocity oscillations of an apparently locked fault seem to be an intrinsic feature of the rate-and-state friction on finite-extent faults (see examples in Figures 5.3 and 5.4). They can be induced even on a fault with homogeneous frictional parameters and previously stable evolution by an external stress load, especially if the load has a spatially inhomogeneous amplitude and if the load is applied later in the earthquake cycle. Perfettini et al. (2003b) associated the slip velocity oscillations with oscillations of a spring slider model governed by the rate-and-state friction. We were not able to match the fault oscillations to those of a spring slider model with stiffness equal to the effective stiffness of the fault. Moreover, the observed complex spatial evolution of the stress/slip velocity field on the fault suggests that

the oscillations are related to the multidimensional character of the fault. During the slip velocity oscillations, the fault undergoes quasi-periodic creep events. The question is whether such behavior is realistic and whether it could be proven by observations. We note that the creep events are hardly detectable by surface measurements due to very small associated slip. Nevertheless, they might be manifested by other related phenomena such as episodic increases of microseismicity as observed on the locked Parkfield segment (Nadeau et al., 1995; Nadeau & Guilhem, 2009). We note that similar variations of recurrence intervals of characteristically repeating microearthquakes have been observed on the creeping section of the San Andreas Fault (SAF) (Nadeau & McEvilly 1999, 2004). These slip rate oscillations have been recently confirmed by modern geodetic data (Turner et al., 2015).

5.4.2 Possible Explanation of the Anomalous Delay of the Parkfield Earthquake

Our study is to be understood as a qualitative analysis of conceptual fault behavior after being perturbed by a stress load or unload. Nevertheless, particularly the observed significant clock delays, occurring when the stress (un)load is applied at specific periods within the seismic cycle, prompt for comparison with real fault observations. A perfect candidate is the locked Parkfield segment of the SAF. This fault is well known for its quasi-periodic occurrence of $M_w \approx 6$ events with a mean interval of about 22 years (see Fig. 5.8a). The striking similarity of waveforms recorded in the 1922, 1934, and 1966 events suggests that the ruptured area of the fault is similar for all those events (Bakun et al., 2005). After the 1966 earthquake, the next M_w 6 event was anticipated to take place between 1988 and 1993. Interestingly, the event occurred as late as 2004, being delayed by approximately 15 years (Fig. 5.7b). The reason for this exceptional delay, representing a significant portion of the whole seismic cycle, remains enigmatic. Here we link it with the perturbation of the stress field by two nearby strong earthquakes that occurred northeast of the Parkfield section of SAF in 1983, M_w 6.5 Coalinga and M_w 6.0 Nuñez. Toda & Stein (2002) studied the response of SAF to these events. Their Coulomb stress calculations showed that these two earthquakes increased stress on the creeping section of the SAF, raising the rate of small shocks for the next ≈18 months. Conversely, the Coalinga-Nuñez earthquakes decreased stress on the locked Parkfield segment up to 0.5 bars, causing surface creep and a drop of occurrence rates of small earthquakes for more than 6

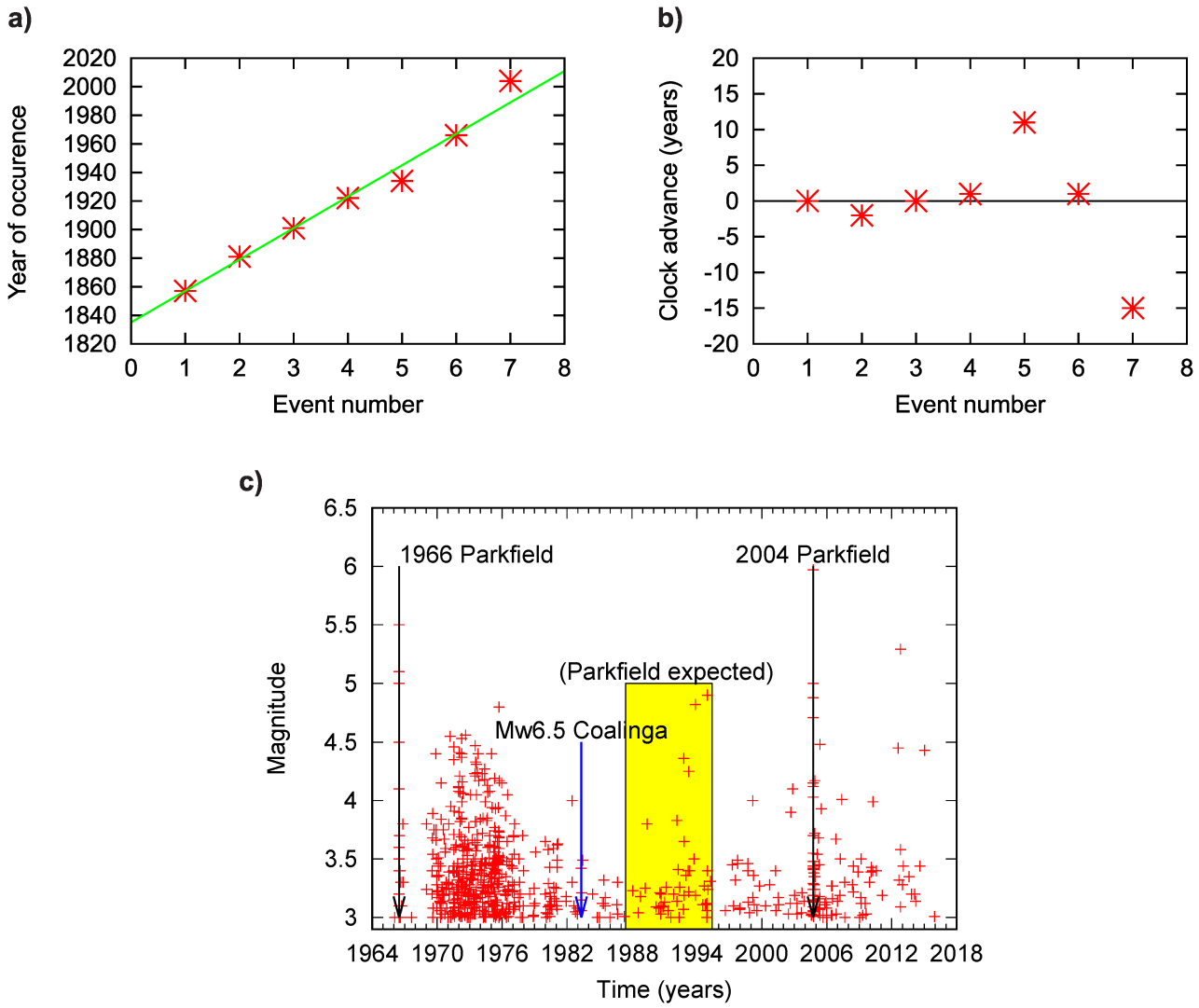

Figure 5.8: a) Occurrence time of the main shocks on the locked Parkfield segment of the San Andreas Fault. The green line corresponds to a recurrence time of 22 years. b) Clock advance of the main shocks evaluated as a difference between the actual year of occurrence and the estimated one from the 22 year recurrence period (green line in Fig. 5.8a). c) Real seismicity on the Parkfield fault (red symbols, obtained from the NCEDC archive, 2014). Black arrows denote the occurrence of the last two Parkfield main shocks. The blue line denotes the time of the nearby M_w 6.5 Coalinga earthquake (followed by the M_w 6.0 Nuñez shock), which unloaded the Parkfield fault by approximately 0.15 bars (Toda & Stein, 2002). The time period in yellow denotes the expected occurrence of the next main shock after the 1966 event. Note that instead of the large system-size event, smaller earthquakes of $M_w \lessapprox 4.9$ occurred in that period.

years. Toda & Stein (2002) converted the Coulomb stress decrease to a 22% drop of 10-year probability of the next M_w 6 Parkfield earthquake. This hardly explains the absence of the main shock until 2004. Barbot et al. (2012) developed a rate-and-state dynamic model of the seismic cycle of the Parkfield segment of SAF. The authors replicated basic characteristics of the cycle including the swap of hypocenters of the 1966 and 2004 events. Nevertheless, they did not explain the anomalous delay of the latter event. Although they neglected the external unloading due to the nearby 1983 Coalinga-Nuñez events, the authors also raised the possibility that the delay of the 2004 M_w 6.0 Parkfield event may have been at least partially caused by smaller earthquakes occurring from 1993 to 1994, being perhaps a series of arrested M_w 6 nucleations (see Fig. 5.8c).

To support this hypothesis by simulation, we consider a fault model with conditions closer to the properties of the Parkfield segment, following Barbot et al. (2012). In particular, we assume a strike-slip model with dimensions of 36 km $\times$ 18 km, which covers both seismogenic and aseismic parts of the SAF. For the sake of computational efficiency, we simplify the distribution of frictional parameters of Barbot et al. (2012), removing small seismogenic patches and using a simple rectangular seismogenic zone of 24 $\times$ 4 km (see Figures 5.9a and 5.9b). We use the same depth dependence of effective normal stress as Barbot et al. (2012); see Fig. 5.9c. The fault is discretized by 256 $\times$ 128 cells corresponding to a meshing twice as coarse in each dimension as that considered by Barbot et al. (2012). We assume larger $L = 6$ mm, constant along the fault.

After initialization, the fault quickly settles into a periodic regime with a period of 20.4 years. We apply a negative Coulomb stress change of 0.6 MPa to the velocity-weakening zone at 130 equidistant onset times t_0. The resulting dependence of both magnitude-constrained and magnitude-unconstrained CA on t_0 is shown in Fig. 5.9d, which is analogous to Fig. 5.2. We observe three intervals of significant clock delay. As in the homogeneous model, the large earthquake is delayed by one or two preceding smaller events. Their hypocenters generally differ from that of the main shock; in most cases, the main shock hypocenter is located closer to the edges of the velocity-weakening area. The stress perturbations also generate creep episodes with irregularly spaced peaks in slip velocity with intervals ranging between 0.4 and 3 years, i.e. covering the 2 year period of the repeating microearthquakes observed at Parkfield (Nadeau & McEvilly 1999, 2004). Nevertheless, we stress that the qualitative behavior of the fault is quite sensitive to variations of the model parameters. For example, no significant delays appear when considering a purely rectangular velocity-weakening zone. More comprehensive

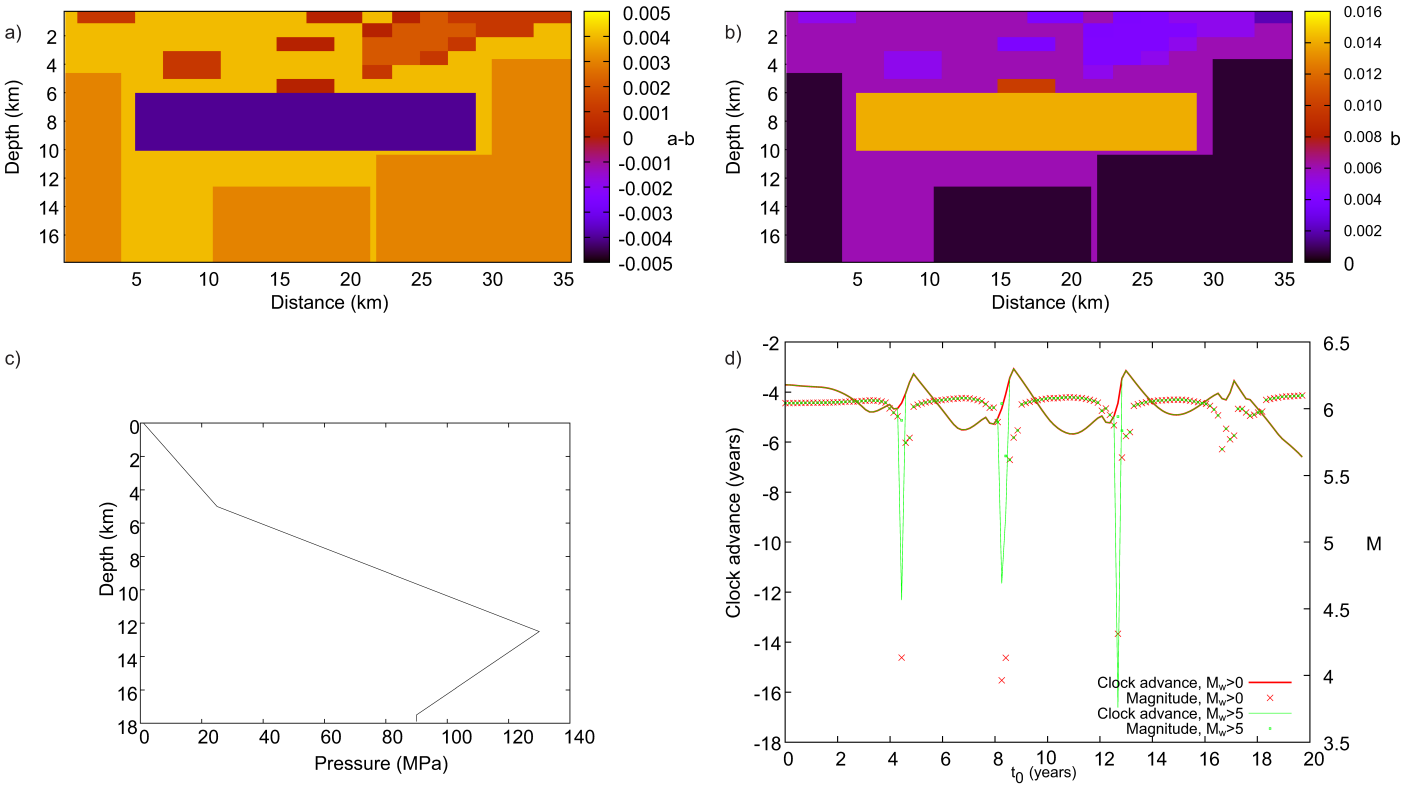

Figure 5.9: Parameters and the results for our model of the Parkfield fault segment. a) The spatial distribution of friction parameter $a-b$, simplified after Barbot et al. (2012). The blue area corresponds to the velocity-weakening zone. b) The spatial distribution of friction parameter b simplified from Barbot et al. (2012). c) Depth dependence of the effective normal stress, adopted from Barbot et al. (2012). d) The dependence of the clock advance CA and magnitude of the triggered events as a function of stress load onset time t_0. We apply a negative Coulomb stress change on the velocity-weakening zone. The figure is analogous to Fig. 5.2. Note the significant time delays of the system-size ($M_w \approx 6$) events, which are preceded by $M_w < 5$ events, within the three intervals of load time t_0.

modeling of the Parkfield segment that would explain the fault behavior in full detail is left for further study.

Our results support the hypothesis of Barbot et al. (2012), suggesting that the stress unload due to the 1983 Coalinga-Nuñez earthquakes took place during a specific phase of the Parkfield seismic cycle (corresponding to the increasing phase of the CA curve; see Fig. 5.2). This resulted in the failure of the $\approx M_w$ 4.9 events from 1993 to 1994 to rupture the whole fault. Instead, they significantly delayed the 2004 M_w 6 main shock. We note that this proposed mechanism is not unique. For example, simulations by Ben-Zion et al. (1993) showed that accounting for viscoelasticity below the brittle crust can also produce a delay of the 2004 M_w 6 Parkfield earthquake; for some parameters, their calculations predicted the next Parkfield earthquake to occur in the time interval 1995 $\pm$ 11, which includes 2004.

5.4.3 Clock Advance Concept in Earthquake Hazard Assessment

The present results pose a challenge for time-dependent earthquake forecasting and for building characteristic earthquake renewal models in seismic hazard assessment. Both of those practical applications need an estimate of the CA of the next earthquake due to the Coulomb stress change invoked by a nearby event. Complex dependencies of CA, including the possibility of a clock delay as observed in the present study, seem to preclude a simple prediction. Indeed, CA is strongly affected by the actual state of the stress/slip velocities on the fault at the time of the stress load, especially on the part of the fault to which the stress load is applied. Details of the fault behavior are also controlled by the actual frictional parameters of the fault, which are hard to obtain.

A promising way to overcome this problem in the future is a "full" simulation of the earthquake cycle. Such a dynamic simulation of a single fault was performed for the Parkfield segment of SAF in the above-mentioned paper by Barbot et al. (2012); considering the rate-and-state friction law. Another possibility is to avoid trying to explicitly estimate the CA for a given fault. Instead, the potential hazard study can rely on dynamic simulations of whole earthquake fault systems. For example, Richards-Dinger & Dieterich (2012) introduced the earthquake simulator RSQSim, which takes into account all known mutually interacting locked and creeping faults in California governed by the rate-and-state friction. The model successfully reproduces basic characteristics of the real earthquake catalog. In principle, such

physics-based models take into account the complex behavior of CA inherently by considering the complex stress interactions among the faults in the fault system.

Data and Resources

Waveform data, metadata, or data products for this study were accessed through the Northern California Earthquake Data Center (2014), doi:10.7932/NCEDC.

6 Assessing the role of selected constraints in Bayesian dynamic source inversion: Application to the 2017 M_w 6.3 Lesvos earthquake

A version of this chapter, mainly differing by a slightly shorter methodical part, was published as Kostka et al. (2022).

Summary

A dynamic finite-fault source inversion for stress and frictional parameters of the M_w 6.3 2017 Lesvos earthquake is carried out. The mainshock occurred on June 12, offshore the southeastern coast of the Greek island of Lesvos in the north Aegean Sea. It caused 1 fatality, 15 injuries, and extensive damage to the southern part of the island. Dynamic rupture evolution is modeled on an elliptic patch, using the linear slip-weakening friction law. The inversion is posed as a Bayesian problem and the Parallel Tempering Markov Chain Monte Carlo algorithm is used to obtain posterior probability distributions by updating the prior distribution with progressively more constraints. To calculate the first posterior distribution, only the constraint that the model should expand beyond the nucleation patch is used. Then, we add the constraint that the model should reach a moment magnitude similar to that obtained from our centroid moment tensor inversion. For the final posterior distribution, 15 acceleration records from Greek and Turkish strong-motion networks at near regional distances ($\approx$ 30-150 km) in the frequency range of 0.05-0.15 Hz are used. The three posterior distributions are compared to understand how much each constraint contributes to resolving different quantities. The most probable

values and uncertainties of individual parameters are also calculated, along with their mutual trade-offs. The features best determined by seismograms in the final posterior distribution include the position of the nucleation region, the mean direction of rupture (towards WNW), the mean rupture speed (with 68% of the distribution lying between 1.4-2.6 km/s), radiated energy (12-65 TJ), radiation efficiency (0.09-0.38), and the mean stress drop (2.2-6.5 MPa).

6.1 Introduction

Dynamic inversions of earthquake rupture aim at finding parameters governing frictional and stress conditions on a fault. This can be done in two ways. In the first approach, the stress on the fault is calculated from the history of slip obtained via inversion for a kinematic model, and the two fields are then used to estimate parameters of the constitutive law relating slip and friction (e.g. Fukuyama & Mikumo, 1993; Ide & Takeo, 1997; Pulido & Irikura, 2000; Peyrat et al., 2001; Tinti et al., 2005; Burjánek & Zahradník, 2007). A more recent approach, used here, is the fully dynamic inversion (e.g. Peyrat & Olsen, 2004; Di Carli et al., 2010; Ruiz & Madariaga, 2011, 2013; Díaz-Mojica et al., 2014; Twardzik et al., 2014; Herrera et al., 2017; Gallovič et al., 2019a,b; Mirwald et al., 2019; Gallovič et al., 2020). In this approach, simulations in which the elastodynamic equation is coupled with the constitutive law are used and the parameters describing the law and the initial stress on the fault are searched directly. The history of slip during the rupture is obtained as a by-product and it is guaranteed to be consistent with physical laws. Solving a fully dynamic inversion problem thus solves an associated kinematic inversion problem. However, dynamic inversions also permit interpretation of the earthquake properties in terms of physics. This is crucial for understanding processes of rupture nucleation, propagation, and arrest, eventually enabling realistic simulations of near-source ground motions (e.g. Aochi & Ulrich, 2015).

There are several issues with dynamic inversions that complicate interpretations of their results and prevent their widespread use. First, the appropriate form of the constitutive law that describes friction on geological faults is still a topic of intense research. Widely applied empirical friction laws have been derived from small-scale laboratory experiments (Dieterich, 1979; Ruina, 1983; Ohnaka & Yamashita, 1989; Chen & Spiers, 2016, etc.), but little is known about their applicability to the Earth's crust (see Perfettini et al., 2003a; Marone et al., 2009; Viesca & Garagash, 2015 for an extensive discussion on the topic). Since the differences between

the relevant laws are negligible at low frequencies and hard to distinguish within the precision and accuracy of current seismological data, we use the linear slip-weakening law (Ida, 1972), which was introduced to regularize problems in fracture mechanics. Owing to its simplicity, it has been used in almost all dynamic inversions published to date. For an overview of other important friction laws, we refer the reader to Bizzarri (2011).

Second, just as kinematic inversions, dynamic inversions are non-unique, and it is desirable to describe their uncertainty (Ruiz & Madariaga, 2013; Gallovič et al., 2019a,b). We achieve this by casting the problem in a probabilistic, Bayesian framework and expressing the information about model parameters in the form of a *posterior probability density function*. This function provides a formal basis for analyzing uncertainties of model parameters and their trade-offs. Another advantage of the Bayesian framework is that it enables researchers to clearly formulate their prior assumptions (in the form of the prior probability density function) and to identify how they affect the resulting inference.

Third, running a fully dynamic rupture simulation (representing the forward part of the inverse problem) is computationally demanding. Due to the non-linear relationship between model parameters and data, many such simulations must be run to solve the inverse problem, even in non-Bayesian methods. That is why the dynamic rupture solver must be as fast as possible. To achieve this, we use the highly efficient finite difference code FD3D_TSN (Premus et al., 2020), which utilizes GPU acceleration and requires approximately 1 s of seconds to finish a single GPU computational time per 1 s of rupture simulation in our application. An important strategy for making the inversion computationally feasible is to keep the dimension of the parameter space low; there have been only a few inversions directly seeking a discretized distribution of stress and friction on the fault (Fukuyama & Mikumo, 1993; Peyrat et al., 2001; Peyrat & Olsen, 2004; Corish et al., 2007; Gallovič et al., 2019a,b, 2020). Instead, simple parametrization is typically considered, such as models consisting of one or two elliptic sub-faults (Ruiz & Madariaga, 2011, 2013; Twardzik et al., 2014; Di Carli et al., 2010; Díaz-Mojica et al., 2014; Herrera et al., 2017).

Finally, and most importantly for this study, interpreting the results of the inversion is difficult because it is not clear which constraints are responsible for the appearance of particular features. For example, anti-correlation between the average slip and the ruptured area is likely to be observed in every earthquake with a well-constrained seismic moment. In contrast, fine geometric and temporal features of the rupture propagation may only be constrained by using detailed seismic waveforms specific to the earthquake. We investigate this issue by using

progressively more information to calculate three posterior distributions. For the first posterior distribution, we use only the constraint that the rupture breaks at least twice the area of the nucleation zone and lasts more than 1 second. This condition removes uninteresting models that produce negligible wave radiation. For the second distribution, we add information about the moment magnitude. The resulting distribution will characterize models with mechanisms and magnitude similar to the one from the moment tensor inversion, regardless of the observed waveforms. For the final posterior distribution, we use both moment magnitude and waveforms observed at near-regional seismic stations. Comparing the three posterior distributions allows us to separate features that are determined by the rupture condition, those determined by magnitude, and those determined by waveforms.

We apply our method to the M_w 6.3 Lesvos earthquake that occurred on June 12, 2017, 12:28 GMT, offshore the southeastern coast of the Greek island of Lesvos in the Lesvos Basin, Aegean Sea. According to the Geophysical Institute of the National Observatory of Athens (GI-NOA), it was a shallow crustal event with a hypocentral depth of 12.0 $\pm$ 1.7 km. The stress state in the area is characterized as transtensional, with minimum principal stress axis σ_3 oriented in the NNE-SSW direction (Konstantinou et al., 2017). The earthquake likely ruptured the eastern segment of the Lesvos Basin fault, oriented perpendicular to σ_3, dipping SSW with a normal faulting mechanism (Kiratzi, 2018). We show a map of the epicentral area in Fig. 6.1.

Most of the damage caused by the earthquake occurred on the southern coast of Lesvos. In what has been called the "Vrisa paradox" (Papadimitriou et al., 2018), the heaviest structural damage was observed in the small village of Vrisa about 20 km toward NW from the mainshock epicenter, despite the presence of closer towns and villages. (e.g., Plomari, Akrasi, Vatera, etc.). One woman in Vrisa died, and at least 15 people were injured. This has been attributed to site effects, vulnerable infrastructure (Lekkas et al., 2017), and the large spatial extent of slip and source directivity. The last two have been examined by a kinematic inversion of seismic data (Kiratzi, 2018), a kinematic inversion of GPS data (Chousianitis & Konca, 2018), and an analysis of the aftershock sequence (Papadimitriou et al., 2018). Both kinematic inversions conclude that the slip was concentrated in a large patch with unilateral propagation of rupture from the hypocenter toward the northwest, as also indicated by centroid position reported shortly after the event at EMSC by Sokos & Zahradník (2017). Here we use data from local Greek and Turkish stations to reanalyze the earthquake in a fully dynamic, Bayesian framework.

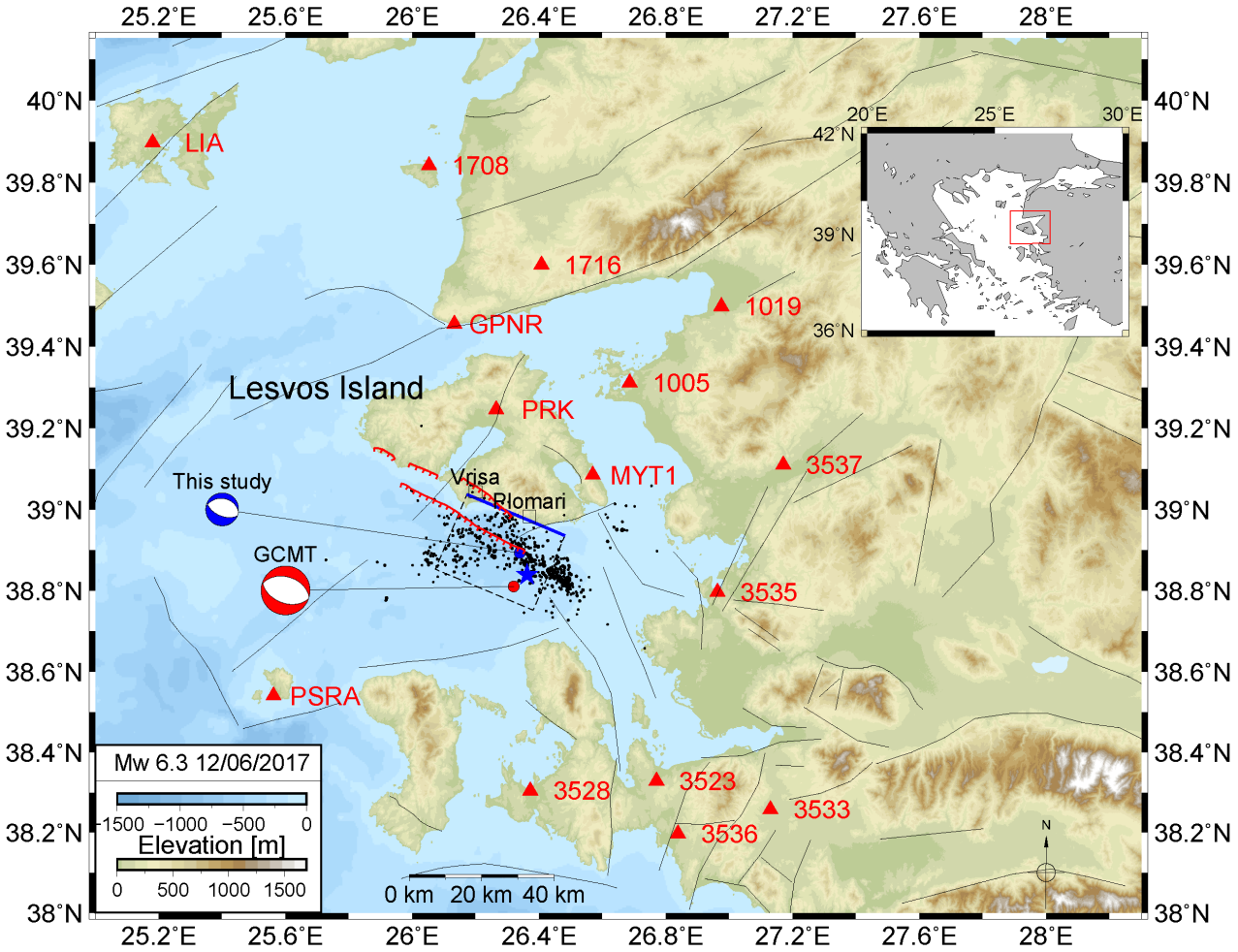

Figure 6.1: Map of the epicentral area of the 2017 M_w 6.3 Lesvos earthquake (see the inset for a wider geographic view). Strong-motion stations used for the dynamic inversion are shown as red triangles. The black rectangle shows the projection of the assumed fault plane used in the inversion. The blue solid line is the top fault edge at the surface. The blue beachball shows the centroid moment tensor of the M_w 6.3 mainshock inferred in this study, while the red beachball shows the GCMT centroid for the same event. Black dots are the aftershocks within two months after the event, as determined by GI-NOA. The hypocenter located by GI-NOA is denoted by a blue star. Fault traces from The European Database of Seismogenic Faults (EDSF; Basili et al., 2013) are shown as black lines. The red lines show inferred and mapped faults from Chatzipetros et al. (2013) and Ganas et al. (2013).

6.2 Method

6.2.1 Forward problem

The forward problem consists of a dynamic rupture simulation and a calculation of synthetic waveforms in a layered isotropic medium. For the former, we use the Fortran code FD3D_TSN (Premus et al., 2020), which employs finite differences on a staggered grid of 4th order in space and of 2nd order in time. The code solves the elastodynamic equation in a 3-D box, allowing for discontinuous displacement (slip) on a pre-defined fault. The mechanical conditions on the fault, which is placed at one of the vertical faces of the box and implemented using the traction-at-split-node approach, are governed by the linear slip-weakening friction law (Ida, 1972). This law relates shear traction $\boldsymbol{T}(\boldsymbol{x},t)$ and slip $\boldsymbol{s}(\boldsymbol{x},t)$ at each point $\boldsymbol{x}$ on the fault and time t and consists of two parts:

1. The rupture criterion: The slip rate at $\boldsymbol{x}$ is zero until the magnitude of shear traction at that point reaches the strength T_u.

2. Constitutive law: The on-fault traction during slip is a function of the accumulated slip (slip-path length)
$$\mathfrak{s}(t,\boldsymbol{x}) = \int_0^t \|\dot{\boldsymbol{s}}(t',\boldsymbol{x})\|dt' \tag{6.1}$$
and the slip rate direction:
$$\boldsymbol{T}(t,\boldsymbol{x}) = -f(\mathfrak{s}(t,\boldsymbol{x}))\frac{\dot{\boldsymbol{s}}(t,\boldsymbol{x}))}{\|\dot{\boldsymbol{s}}(t,\boldsymbol{x})\|}, \tag{6.2}$$
where (see Fig. 6.2a):
$$f(\mathfrak{s}) \coloneqq \begin{cases} (T_u - T_d)(1-\mathfrak{s}/D_c) + T_d & \text{for } 0 \leq \mathfrak{s} \leq D_c \\ T_d & \text{for } \mathfrak{s} > D_c \end{cases}. \tag{6.3}$$
Here D_c is the so-called characteristic slip distance and T_d is dynamic friction.

The initial shear traction $\boldsymbol{T_i}$ points in the up-dip direction (to represent normal faulting), approximating the centroid rake direction of the event (-83°, see subsection 6.2.3.4). The direction of traction is not fixed, but it changes only negligibly during the dynamic simulation.

We set T_d to zero, as is commonly done in dynamic inversions (e.g. Ruiz & Madariaga, 2011, 2013; Twardzik et al., 2014; Gallovič et al., 2019a,b). However, we also include a small stabilizing cohesion term of 0.5 MPa, which effectively moves T_d to 0.5 MPa. Indeed, we have verified that shifting $\|\boldsymbol{T}_i\|$, T_u and T_d by a fixed positive value has a negligible effect on the simulation results. The friction law is summarized in Fig. 6.2.

The boundary conditions at the remaining faces of the computational box consist of a free surface enforced by the stress-imaging technique (Levander, 1988; Graves, 1996; Kristek et al., 2002) at the top face, and perfectly matched layers (Berenger, 1994) as absorbing conditions at the remaining faces. We note that a significant speed-up in FD3D_TSN is achieved by assuming that the fault is vertical. To partially compensate for neglecting the actual dip of the fault, we stretch the along-dip positions of the velocity model interfaces, so that they conform to the actual depths along the fault. Since the synthetic ruptures do not reach the surface, the error caused by ignoring the actual dip in the first stage of the calculation is negligible (Gallovič et al., 2019b). As a result of the dynamic rupture simulation, we obtain the evolution of traction and slip rate at each grid point on the fault. The slip rates are then convolved with Green's functions pre-calculated using the Axitra software (Cotton & Coutant, 1997). But unlike the FD3D_TSN simulation, we supply Axitra with the centroid dip and rake to calculate the Green's functions (see application and validation of this approach by Gallovič et al., 2019b). The resulting elementary seismograms are summed over every grid point and as a result, synthetic displacements on specified stations are obtained. As a final step, we apply the fourth-order causal Butterworth filter to each of the seismograms, the same as used for the data (see subsection 6.2.3.4).

6.2.2 Dynamic model parametrization

The distribution of friction and initial stress on the fault is defined by a single elliptic patch model Ruiz & Madariaga, 2011, 2013; Díaz-Mojica et al., 2014; Herrera et al., 2017, see Fig. 6.2b. It is relatively simple, which is appropriate due to the small complexity of the event indicated by i) previous studies of the earthquake (Kiratzi, 2018; Chousianitis & Konca, 2018), ii) our moment tensor inversion (performed by J. Zahradník and E. Sokos, see text S1.1), and iii) the limited frequency range we use. In addition, the limited number of parameters makes the elliptic patch model suitable for a Bayesian inversion. The geometry of the patch is

parameterized by five parameters (Fig. 6.2b): The position of its center along strike, x_c, and along dip (measured from bottom to top), y_c, the components of the vector connecting the center and the tip of the semi-major axis, a_x, a_y, and the length of the semi-minor axis, b. The strength is set to a constant value of T_u inside the patch and to a very large value outside of it, so the patch is the only region in which rupture may propagate. The characteristic slip distance is set to a constant value of D_c everywhere on the fault. The magnitude of the initial shear traction T_i inside the patch is a piecewise constant function:

$$T_i(\boldsymbol{x}) = \begin{cases} T_u(1+\delta) & \text{for } \boldsymbol{x} \in \text{NZ} \\ T_u\gamma & \text{for } \boldsymbol{x} \notin \text{NZ} \end{cases}, \tag{6.4}$$

where $\delta > 0$, and $\gamma \in [0, 1]$ are parameters and NZ is a small circular nucleation zone from which rupture begins. Finally, the geometry of the nucleation zone is determined by 3 parameters: the along-strike and along-dip locations x_{nucl}, y_{nucl} of its center and its radius r_{nucl}. To sum up, we parameterize the model by 12 model parameters (Fig. 6.2b): 8 that describe the geometry of the elliptic patch and the nucleation zone (x_c, y_c, a_x, a_y, b, r_{nucl}, x_{nucl}, y_{nucl}), 2 that define the magnitude of the initial shear stress (γ, δ), and 2 that define frictional properties (T_u, D_c).

6.2.3 The inverse problem

6.2.3.1 Bayesian framework

We describe our knowledge about the parameters in terms of a *probability density function* on the 12-dimensional space M of model parameters defining the elliptic models described in subsection 6.2.2. This is a function $f : M \to \mathbb{R}_0^+$ such that the true value of the parameter combination $\boldsymbol{m} = (m_1, m_2..., m_{12})$ is contained in a Borel set $A \subset M$ with probability:

$$P(A) = \int_A f(m_1, m_2, ..., m_{12}) d\boldsymbol{m}. \tag{6.5}$$

For the sake of brevity, we also refer to probability density functions as (probability) distributions or simply *pdf*s.

The parametrization of the model space M presented in subsection 6.2.2 is not unique.

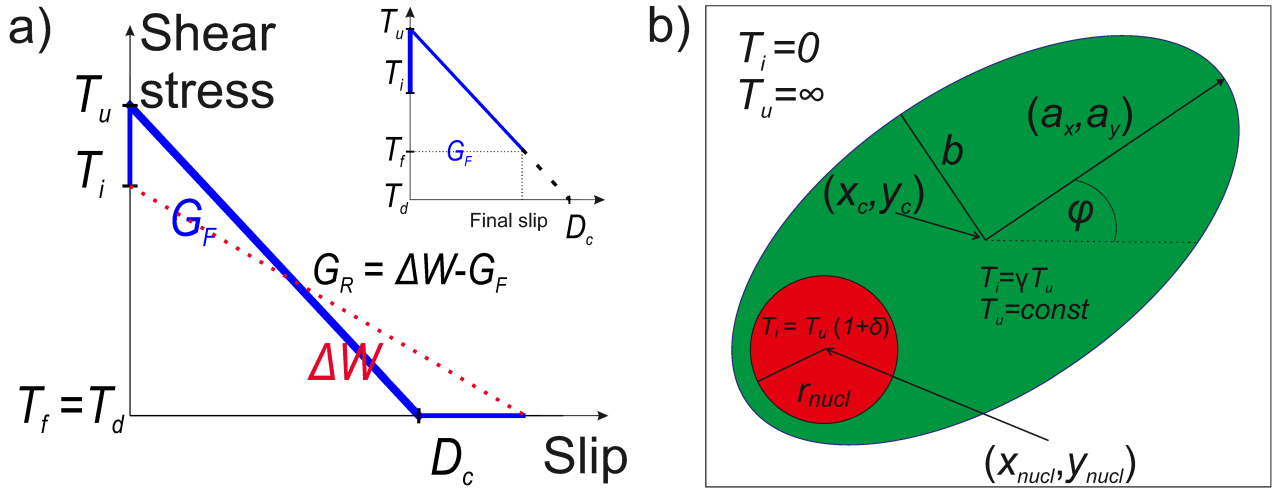

Figure 6.2: a) The linear slip weakening friction law. The magnitude of the shear stress at each point $\boldsymbol{x}$ on the fault has the initial value $T_i(\boldsymbol{x})$ (see Fig. b) and obeys linear elasticity until it is larger than or equal to T_u (yield strength). It then decreases linearly with accumulated slip (slip-path) $\mathfrak{s}$ until it reaches the final stress $T_f = T_d$ at $\mathfrak{s} = D_c$. The inset shows the case when slip stops before reaching D_c, in which case $T_f > T_d$. Stress drop is defined as $T_i - T_f$. The area ΔW under the red dotted line is the available strain energy surface density. The area G_F under the blue curve is the dissipated fracture energy surface density (energy dissipated from ΔW per area of rupture). The quantity $G_R = \Delta W - G_F$ is the radiated energy density. Integrals of these quantities over the fault plane are the available strain energy change ΔE, the dissipated fracture energy E_F, and radiated energy E_R, respectively. For the extension to 3-D, see Ripperger et al. (2007) and Eq. (6.35). b) The elliptic parametrization used for the dynamic inversion. The yield strength T_u is finite and constant inside an elliptic patch and infinite elsewhere. The geometry of the ellipse is defined by the along-strike and along-dip coordinates of its center, x_c and y_c, the along-strike and along-dip components a_x and a_y of the semi-major axis, and the length of the semi-minor axis, b. The angle between the semi-major axis and the horizontal line is denoted by ϕ. The geometry of the nucleation zone (red) is parameterized by the coordinates of its center x_{nucl}, y_{nucl}, and the radius r_{nucl}. The magnitude of the shear stress inside the nucleation zone is defined relatively to T_u by the positive parameter δ: $T_i = T_u(1 + \delta)$. Elsewhere on the patch, T_i has a constant value of γT_u. Outside of the patch, it is zero.

When a different parametrization is used, the probability $P(A)$ is left invariant. Therefore, since the volume element $d\boldsymbol{m}$ in Eq. (6.5) is transformed upon a change of coordinates, the pdf also needs to transform, but in an inverse manner. Specifically, let $\{x_i, i = 1, \ldots, 12\}$ and $\{y_i, i = 1, \ldots 12\}$ be two coordinate systems on M. Let $y_i = \psi_i(x_1, x_2, \ldots x_{12}\}$, where $\boldsymbol{\psi} : \mathbb{R}^{12} \to \mathbb{R}^{12}$ is an invertible differentiable function. Then the pdf f with respect to $\{x_i\}$ and the pdf g with respect to $\{y_i\}$ are related as (Gelman et al., 2004):

$$g(\boldsymbol{y}) = f\left(\boldsymbol{\psi}^{-1}(\boldsymbol{y})\right) |J_{\boldsymbol{\psi}^{-1}}(\boldsymbol{y})|, \tag{6.6}$$

where $J_{\boldsymbol{\psi}^{-1}}(\boldsymbol{y})$ is the Jacobian determinant of $\boldsymbol{\psi}^{-1}$, evaluated at $\boldsymbol{y}$:

$$J_{\boldsymbol{\psi}^{-1}}(\boldsymbol{y}) := \det\left(\frac{\partial(\psi^{-1})_j}{\partial y^i}(\boldsymbol{y})\right). \tag{6.7}$$

Consequently, a uniform pdf with respect to one set of coordinates typically results in a non-uniform pdf with respect to a different set of coordinates.

Even before analyzing the observational constraints $\boldsymbol{c}$ on the earthquake in detail, we have some prior knowledge about the parameters. For example, we know that the hypocenter of the earthquake is located near Lesvos island, we have some estimates about the extent of the rupture, maximum stress drop, etc. We formalize this knowledge in terms of a *prior probability density function* $\rho_{pr}(\boldsymbol{m})$, which we fully describe in subsection 6.2.3.3. We then update our prior knowledge by taking $\boldsymbol{c}$ into account. Mathematically, this is represented by passing to the *posterior probability density function* $\rho(\boldsymbol{m}|\boldsymbol{c})$ using *Bayes' formula*:

$$\rho(\boldsymbol{m}\,|\,\boldsymbol{c}) = kL(\boldsymbol{m}\,|\,\boldsymbol{c})\rho_{pr}(\boldsymbol{m}). \tag{6.8}$$

Here,

$$L(\boldsymbol{m}\,|\,\boldsymbol{c}) = p(\boldsymbol{c}|\boldsymbol{m}) \tag{6.9}$$

is the *likelihood function*, which represents the probability density function of $\boldsymbol{c}$ given that the true model parameters are equal to $\boldsymbol{m}$, and k is a normalizing constant such that $\rho(\boldsymbol{m}\,|\,\boldsymbol{c})$ integrates to 1.

In this study, we divide our updating process into three steps. In the first step, we assume that we have no information about the earthquake other than that it lasted for at least one second and ruptured more than twice the area of the nucleation zone. This rupture condition,

which we label r, leaves only models that successfully rupture beyond their nucleation zone and excludes uninteresting models that cannot produce any ground displacements at seismic stations. Formally, the likelihood function for this condition can be written as

$$L_0(\boldsymbol{m}\,|\,r) \propto I_R(\boldsymbol{m}), \tag{6.10}$$

where R is the set of all models that meet the rupture condition and I_R is its indicator function. Plugging Eq. (6.10) into Eq. (6.8) with $\boldsymbol{c} = r$, we obtain the posterior distribution

$$\rho_0(\boldsymbol{m}|r) = k_0 I_R(\boldsymbol{m})\rho_{pr}(\boldsymbol{m}), \tag{6.11}$$

where k_0 is a normalizing constant. Since the exact shape of R is unknown, neither the value of k_0 nor the precise form of I_R can be determined beforehand. However, this is not important when estimating the distribution with a suitable Monte-Carlo method, such as the Parallel Tempering algorithm (see the next part of this subsection).

In the second step, we add to $\boldsymbol{c}$ an estimate of the earthquake's moment magnitude M_w^0, so that $\boldsymbol{c} = (r, M_w^0)$. When we solve the forward problem with model $\boldsymbol{m}$, we obtain the corresponding moment magnitude $M_w(\boldsymbol{m})$. Due to observational and modeling errors, neither M_w^0 nor $M_w(\boldsymbol{m})$ will be exact. However, if we suppose that the errors are normally distributed, it turns out (Tarantola, 2005) that the combined error is also normally distributed with variance $\sigma^2_{M_w}$ equal to the sum of the original variances. The likelihood function is then:

$$L_1(\boldsymbol{m}|M_w^0) \propto \exp\left(-\frac{\left(M_w(\boldsymbol{m}) - M_w^0\right)^2}{2\sigma^2_{M_w}}\right). \tag{6.12}$$

Using ρ_0 as the prior distribution and updating it using Eq. (6.8), we obtain the posterior distribution

$$\rho_1(\boldsymbol{m}|r, M_w^0) = k_1 L_1(\boldsymbol{m}|M_w^0)\rho_0(\boldsymbol{m}|r) = k_1 \exp\left(-\frac{\left(M_w(\boldsymbol{m}) - M_w^0\right)^2}{2\sigma^2_{M_w}}\right) I_R(\boldsymbol{m})\rho_{pr}(\boldsymbol{m}), \tag{6.13}$$

where k_1 is again a normalizing constant. This pdf is independent of ground displacement observations, except for the information about the moment magnitude. As such, it allows us to identify model parameters and features that are required for the earthquake to rupture with approximately the given magnitude, but are not necessarily specific to the actual earthquake.

In the final step, we supplement the preceding constraints with the observed seismograms $\boldsymbol{d_{obs}}$, i.e. $\boldsymbol{c} = (r, M_w^0, \boldsymbol{d_{obs}})$. The vector $\boldsymbol{d_{obs}}$ consists of the three components of displacement at each time sample and at each station. Assuming normally distributed errors as before, the likelihood function for this update is

$$L_2(\boldsymbol{m}|\boldsymbol{d_{obs}}) \propto \exp\left(-\frac{\|\boldsymbol{d}(\boldsymbol{m}) - \boldsymbol{d_{obs}}\|^2}{2\sigma_d^2}\right), \tag{6.14}$$

where $\boldsymbol{d}(\boldsymbol{m})$ are synthetic seismograms calculated from the model $\boldsymbol{m}$, $\|\cdot\|$ is the regular Euclidean norm and σ_d^2 is the total observational and modeling variance. Using this likelihood function and using ρ_1 as the prior distribution, Eq. (6.8) now yields

$$\rho_2(\boldsymbol{m}|r, M_w^0, \boldsymbol{d_{obs}}) = k_2 I_R(\boldsymbol{m}) \exp\left(-\frac{\|\boldsymbol{d}(\boldsymbol{m}) - \boldsymbol{d_{obs}}\|^2}{2\sigma_d^2} - \frac{(M_w(\boldsymbol{m}) - M_w^0)^2}{2\sigma_{M_w}^2}\right) \rho_{pr}(\boldsymbol{m}), \tag{6.15}$$

where k_2 is another normalizing constant. In subsection 6.3.2, we compare the prior distribution and the three posteriors to extract information obtained by each piece of observational data.

Since the model space M has 12 dimensions, the pdfs are hard to visualize and interpret. Nevertheless, if we decompose M as a Cartesian product of spaces A and B such that $M = A \times B$, we can calculate, for any pdf ρ on M, its *marginal pdf* $\rho^A(\boldsymbol{m_A}|\boldsymbol{y})$ for $\boldsymbol{m_A} \in A$ by integrating $\rho(\boldsymbol{m_A}, \boldsymbol{m_B}|\boldsymbol{y})$ over B:

$$\rho^A(\boldsymbol{m_A}|\boldsymbol{y}) = \int_B \rho(\boldsymbol{m_A}, \boldsymbol{m_B}|\boldsymbol{y}) d\boldsymbol{m_B}. \tag{6.16}$$

Plots of the marginal distributions give us a picture about the original (joint) distribution, but they must be approached with caution because some information is lost by the integration. In particular, that the marginal distribution ρ^A has a maximum at some $\boldsymbol{m_A} \in A$ is neither a sufficient nor necessary condition for the joint distribution to have a maximum at $(\boldsymbol{m_A}, \boldsymbol{m_B})$ for some $\boldsymbol{m_B} \in B$. To simplify notation in the following text, we use the same symbols for both the marginal and the joint distributions.

6.2.3.2 Sampling the posterior distributions with the Parallel Tempering algorithm

Even though formulas (6.11), (6.13), and (6.15) show the theoretical form of the sought posterior pdfs, a major complication immediately arises when one wants to calculate them in practice. The values of the functions $I_R(\boldsymbol{m})$, $M_w(\boldsymbol{m})$ and $\boldsymbol{d}(\boldsymbol{m})$ which appear in these formulas are only available through costly numerical simulations; we do not have analytical expressions for them. If we try to numerically evaluate the distributions on a regular grid spanning the model space, the calculation quickly becomes unfeasible as the dimension of the model space increases and most time is spent on models with negligible probability density (curse of dimensionality). Moreover, the values of the normalizing constants are unknown.

Monte Carlo methods solve this problem by efficiently drawing samples of a posterior distribution and using the obtained ensemble to approximately characterize the distribution. A popular technique employed for Monte Carlo sampling is the Metropolis-Hastings (MH) algorithm (Metropolis et al., 1953; Hastings, 1970; see also Sambridge & Mosegaard, 2002), which employs a random walker that moves through the model space according to a prescribed proposal distribution, and accepts or rejects models according to a mathematically derived rule. The rule guarantees that given enough steps, the accepted models will sample the target distribution. However, the original MH algorithm works best for distributions with a single local maximum. For distributions with multiple local maxima, the walker may get trapped in a close neighborhood of a particular one without ever exploring the others.

One of the extensions of the MH algorithm that solve this problem, already utilized for dynamic source inversion by Gallovič et al. (2019a; 2019b), is the Parallel Tempering algorithm (also known as Replica exchange Monte Carlo; Swendsen & Wang, 1986). This algorithm samples the target distribution by performing the MH algorithm on multiple chains, each of which, if working independently, would sample a tempered distribution

$$\rho_T(\boldsymbol{m}|\boldsymbol{y}) := k_T \left[\rho(\boldsymbol{m}|\boldsymbol{y})\right]^{1/T} . \tag{6.17}$$

Here, T is a parameter called temperature, generally different for each chain, and k_T are normalizing constants, the knowledge of which is not required by the algorithm. The target distribution is sampled by chains at $T = 1$. The chains at higher temperatures are auxiliary and their purpose is to help the $T = 1$ chains jump over areas of low probability. This is achieved by allowing the chains at different temperatures to randomly swap their models. Indeed, since the tempered distributions, sampled by chains at $T > 1$, are flatter than the target distribution

(converging to the uniform distribution as $T \to \infty$), these chains can traverse areas that would be unavailable for chains at $T = 1$. For more details, see Sambridge (2013).

Once a large enough ensemble of samples is obtained, it can be used to approximate the important integrals characterizing the distribution, including the normalizing constant. For example, the mean and the variance of the distribution are estimated by calculating the mean and the variance, respectively, of the sampled ensemble. Samples of the marginal probability density functions (see Eq. 6.16) are obtained by projecting samples of the joint distribution to the target space of interest.

To approximately reconstruct the original pdf from its samples, we use the kernel density estimation technique (KDE, see, e.g., Zambom & Dias, 2013). In the case of one-dimensional spaces (generalization to higher dimensions is straightforward), the pdf is estimated by the formula:

$$\rho_{est}(x) = \frac{1}{|S|h} \sum_{s \in S} K\left(\frac{x - s}{h}\right), \tag{6.18}$$

where S is the collection of the obtained samples, $|S|$ is its size, h is a positive real parameter called the bandwidth, and $K(x)$ is a smooth even function with unit integral, called the *kernel*. Here we use the Gaussian kernel:

$$K(x) = \frac{1}{\sqrt{2\pi}} \exp\left(-\frac{x^2}{2}\right). \tag{6.19}$$

Compared to the more standard method of plotting histograms of the samples, KDE estimates are smooth functions and on average, converge faster to the true distribution as the number of samples increases (Wasserman, 2004). Nevertheless, the dependence on the bin width is replaced by the dependence on the bandwidth h. We choose h equal to $1/40$ of the respective parameter range. This value is similar to the bandwidths calculated according to the rule of thumb suggested by Scott (1992).

6.2.3.3 Prior pdf on the model space

The joint prior distribution ρ_{pr}, with respect to the model parameters introduced in subsection 6.2.2, is assumed to be uniform on the set $P \subset M$ defined by the following 4 constraints:

1. All parameters lie within the intervals specified in Table 6.1.

2. The parameter b specifying the length of the semi-minor axis is smaller or equal to the length of the semi-major axis a:

$$b \leq a = \sqrt{a_x^2 + a_y^2}. \tag{6.20}$$

3. The center of the nucleation zone lies within the patch.

4. The patch is completely contained within the fault.

The purpose of constraint #2 is to avoid ambiguity in specifying the semi-major and semi-minor axes. Constraint #3 ensures that rupture always initiates within the patch, which represents a weakened area on the fault. Constraint #4 ensures that the patch always has an elliptic shape (i.e. the ellipse is not cropped). We note that we allow both a_x and a_y to take positive and negative values, permitting occurrences of pairs (a_x, a_y) and $(-a_x, -a_y)$, which represent the same model. This introduces redundancy into the inversion, but it is nevertheless convenient as it eliminates unnecessary barriers in the Monte Carlo sampling.

We sample the prior distribution ρ_{pr} with a random number generator, uniformly generating models within the bounds given by constraint #1 and then only accepting those that satisfy constraints #2-4. KDE estimates of 1-D marginal priors of ρ_{pr}, reconstructed from 100 000 samples, are shown as black curves in Fig. 6.3.

The 1-D pdfs of Cartesian components a_x and a_y are not very informative about the size and orientation of the semi-major axis. Similarly, x_c and y_c have, due to constraint #3, very similar distributions to x_{nucl} and y_{nucl}. We therefore transform these four parameters to more illustrative ones. Instead of a_x and a_y, we use the quantities a (length of the semi-major axis, Eq. 6.20) and ϕ, which is the angle between the vector (a_x, a_y) and the horizontal line. We also identify values of ϕ differing by 180°, since they describe the same model, that is:

$$\phi = \text{atan2}(a_y, a_x) \mod 180°. \tag{6.21}$$

Instead of x_c and y_c we show two derived quantities that characterize the connecting vector

$$\Delta\boldsymbol{r} = (x_c - x_{nucl}, y_c - y_{nucl}). \tag{6.22}$$

The first quantity, C_{dist}, is the length of $\Delta\boldsymbol{r}$ relative to the elliptic patch (equal to 0 when the

nucleation is at the center of the patch and equal to 1 when it is at the boundary). Formally,

$$C_{dist} = \sqrt{\left(\frac{\Delta r_x^{'}}{a}\right)^2 + \left(\frac{\Delta r_y^{'}}{b}\right)^2}, \tag{6.23}$$

where $\Delta r_x^{'}$ and $\Delta r_y^{'}$ are the orthogonal projections of $\Delta \boldsymbol{r}$ on the semi-major and semi-minor axis, respectively. The second quantity, C_{ang}, is the angle between $\Delta \boldsymbol{r}$ and the horizontal axis:

$$C_{ang} = \text{atan2}(\Delta r_y, \Delta r_x). \tag{6.24}$$

The 1-D marginal priors for this new set of parameters are shown as black curves in Fig. 6.4.

We note that while the *joint* prior pdf of the model parameters is uniform on P, marginal distributions of the geometric model parameters (except for r_{nucl}) shown in Fig. 6.4 are non-uniform. There are two reasons for this. First, due to constraints #2-4, P has a non-rectangular shape, and the effective bounds over which the joint distribution is integrated (Eq. 6.16) may depend on the value of the target parameter. Second, the derived parameters a, ϕ, C_{dist} and C_{ang} were obtained by a coordinate transformation, and the joint distribution is therefore modified by the Jacobian factor (6.7).

As an example of the former effect, consider the 2-D marginal prior pdf $\rho_{pr}^{(a_x,a_y)}$ of the pair (a_x, a_y). If condition #1 were the only constraint, $\rho_{pr}^{(a_x,a_y)}$would be uniform. However, for a given value of (a_x, a_y), the conditions #2-#4 constrain the allowed ranges of the parameters b, x_c, y_c, x_{nucl} and y_{nucl}. Integrating the joint pdf over the constrained ranges according to Eq. (6.16) results in the pdf $\rho_{pr}^{(a_x,a_y)}$ shown in Fig. S6. Conditions #2 and #3 cause it to be denser at large values of a_x and a_y, while condition #4 has the opposite (but smaller) effect. Finally, integrating $\rho_{pr}^{(a_x,a_y)}$ over a_y (a_x) yields the 1-D pdfs for a_x (a_y) shown in Fig. 6.3.

The joint pdf $\rho_{pr}^{(a,\phi)}$ for (a, ϕ) can be obtained by transforming $\rho_{pr}^{(a_x,a_y)}$ according to Eq. (6.6) with $(a_x, a_y) = \boldsymbol{\psi}^{-1}(a, \phi) = (a\cos\phi, a\sin\phi)$, $J_{\boldsymbol{\psi}^{-1}}(a, \phi) = a$:

$$\rho_{pr}^{(a,\phi)}(a, \phi) = \rho_{pr}^{(a_x,a_y)}(a\cos\phi, a\sin\phi)a. \tag{6.25}$$

When approximating the pdf from its samples via histogram estimation or the KDE method, the above mathematical transformation is taken care of automatically. Integrating $\rho_{pr}^{(a,\phi)}$ over ϕ and a yields the 1-D marginal distributions for a and ϕ, respectively, shown in Fig. 6.4.

Let us remark that, conversely, for any non-uniform positive pdf $f(\boldsymbol{x})$ on $P = [0, 1]^n$,

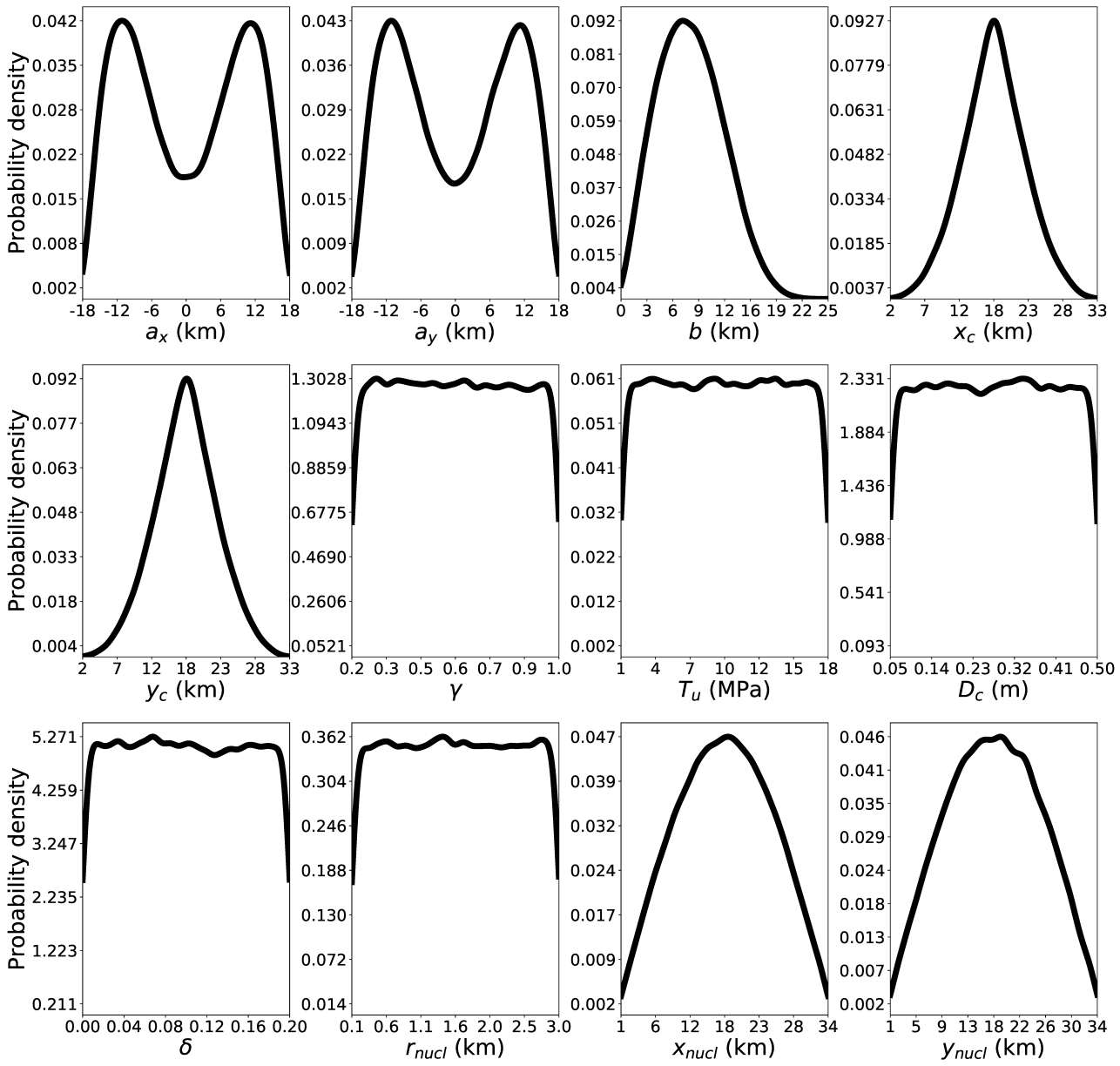

Figure 6.3: KDE estimates of 1-D marginal prior distributions for the model parameters.

we can always find coordinates $\boldsymbol{y} = \boldsymbol{\psi}(\boldsymbol{x})$ with respect to which the transformed pdf $g(\boldsymbol{y})$ is constant. Indeed, it can immediately be seen from the transformation law (6.6) (using $|J_{\psi^{-1}}(\boldsymbol{y})|=|J_{\psi}(\psi^{-1}(\boldsymbol{y}))|^{-1}$ and $\boldsymbol{x} = \boldsymbol{\psi}^{-1}(\boldsymbol{y})$):

$$g(\boldsymbol{\psi}(\boldsymbol{x}))\,|J_{\psi}(\boldsymbol{x})| = f(\boldsymbol{x}),$$

that requiring $g \equiv 1/c$ for an arbitrary positive constant $c > 0$ amounts to:

$$|J_{\boldsymbol{\psi}}(\boldsymbol{x})| = cf\,(\boldsymbol{x})\,, \tag{6.26}$$

This is a non-linear partial differential equation for the vector function $\boldsymbol{\psi}$. There are infinitely many functions $\boldsymbol{\psi}$ satisfying Eq. (6.26). Indeed, every function of the form $\boldsymbol{U} \circ \boldsymbol{\psi}^p$, where $\boldsymbol{U}$ is a volume preserving transformation (e.g., a rotation or translation) and $\boldsymbol{\psi}^p$ is a particular solution, is also a solution. Here we find a particular solution $\boldsymbol{\psi}^p$ by specializing to the case when only one (for example the first) component is transformed:

$$\boldsymbol{\psi}^p(x_1, x_2, ..., x_n) = (\chi(x_1, x_2, ..., x_n), x_2, x_3, ..., x_n), \tag{6.27}$$

where χ is a scalar function of $x_1, x_2, ..., x_n$. We then obtain

$$J_{\boldsymbol{\psi}}(\boldsymbol{x}) = \begin{vmatrix} \partial\chi/\partial x_1 & \partial\chi/\partial x_2 & \cdots & \cdots & \partial\chi/\partial x_n \\ 0 & 1 & 0 & 0 & 0 \\ 0 & 0 & 1 & 0 & 0 \\ \vdots & \ddots & \ddots & \ddots & \vdots \\ 0 & \cdots & \cdots & 0 & 1 \end{vmatrix} (\boldsymbol{x}) = \partial\chi/\partial x_1(\boldsymbol{x}). \tag{6.28}$$

Therefore, Eq. (6.26) simplifies to

$$|\partial\chi/\partial x_1(\boldsymbol{x})| = cf(\boldsymbol{x}), \tag{6.29}$$

which has a particular solution

$$\chi(x_1, x_2, ..., x_n) = c\int_0^{x_1} f(x_1', x_2, ..., x_n)dx_1'. \tag{6.30}$$

As an example, we consider the pdf $f(x, y) = \frac{3}{2}(x^2 + y^2)$ on $P = [0, 1]^2$ and sample it

with the ordinary Metropolis-Hastings algorithm. The KDE estimate of f obtained from the samples is shown in Fig. S7a.

Applying the transformation (6.30) with $x = x_1, y = x_2$, we obtain

$$\chi(x, y) = \frac{x^3}{2} + \frac{3}{2}y^2 x. \tag{6.31}$$

The pdf g w.r. to the transformed coordinates $\boldsymbol{\psi}(x, y) = (\chi(x, y), y)$ is shown in Fig. S7b. We see that g is indeed constant on the transformed domain $\boldsymbol{\psi}(P)$ (bounded by the green curves), which is however no longer a square.

Note that the transformation $\boldsymbol{\psi}$ can be used to obtain samples of a non-uniform pdf by sampling a uniform pdf on $\boldsymbol{\psi}(P)$ and then applying the inverse transformation $\boldsymbol{\psi}^{-1}$ to the obtained samples. This assumes that $\boldsymbol{\psi}$ is known analytically. Moreover, in large dimensions, most samples will likely be transformed to values close to zero due to the curse of dimensionality. Therefore, Monte Carlo methods are more suitable for our inversion. In 1-D, the described procedure reduces to the so-called inverse sampling method (e.g., Tarantola, 2005).

6.2.3.4 Data and model setup

Based on the full-waveform centroid moment tensor (CMT) inversion performed before the dynamic inversion by the software ISOLA (Zahradník & Sokos, 2018), as summarized in the supplementary text S1.1, we adopt the fault plane geometry and mechanism with strike/dip/rake values 113°/40°/-83° and $M_w^0 = 6.24$ (Eqs. 6.12, 6.13 and 6.15). The map projection of the fault plane is shown in Fig. 6.1.

Within 150 km from the centroid, the earthquake was recorded by 55 strong-motion stations of the Geodynamic Institute of the National Observatory of Athens (GI-NOA) and Bogazici University Kandilli Observatory and Earthquake Research Institute (KOERI). For the dynamic inversion, we excluded stations very close to each other (with almost the same waveforms) to reduce station redundancy.

For the computation of Green's functions, we adopt a five-layer model after Karagianni et al. (2002), Fig. S8. Many of the recordings are affected by significant basin and site effects, which are not accounted for in the 1-D model. To select stations suitable for the inversion, we used Axitra to calculate synthetic seismograms for a point source located at the GI-NOA hypocenter in the low-frequency range of 0.05-0.08 Hz and excluded stations with visibly poor

fits with the observed seismograms. For example, stations in the city of Izmir were removed because of a significant path effect likely caused by the presence of the Izmir basin, which cannot be reproduced in our 1-D model. In the end, we selected the 15 stations shown in Fig. 6.1. The event has good angular coverage of stations to the east (azimuths from -10° to 170°), but poor coverage to the west as that direction corresponds to the open sea.

Acceleration records were tapered with a rectangular time window starting at the origin time of 2017/06/12 12:28:37 GMT and with a duration of 80 s. The records were then bandpass filtered between 0.05 and 0.15 Hz by the 4th order Butterworth filter, and integrated into displacements. The lower frequency bound is necessary to remove low-frequency instrumental noise from the data. The upper bound is chosen to lower the influence of the imperfect velocity model, as well as uncertainties in fault geometry.

We set the standard deviation σ_{M_w} (Eqs. 6.12, 6.13 and 6.15) to 0.1, representing roughly the variability of magnitudes from different studies/agencies, see Table S1. The total seismogram standard deviation σ_d (Eqs. 6.15 and 6.15) is set to 2.5 cm. A similar relative estimate of seismogram uncertainty was also used in the dynamic inversions by Gallovič et al. (2019a,b). We note that it is close to the theoretical estimate by Hallo & Gallovič (2016), which is based on synthetic simulations with randomly varied velocity models. To account for the uncertainty in the origin time and to balance for relatively weak or strong nucleation of dynamic rupture, we uniformly shift synthetic seismograms at all stations by the time Δt within (-3.2 s,3.2 s) that results in the minimum misfit.

6.3 Results

Let us describe the sampling of the individual posterior distributions ρ_0, ρ_1 and ρ_2. For the rupture-constrained posterior distribution ρ_0, we took 100 000 samples of the prior distribution and accepted only models that satisfied the predefined rupture condition r, i.e. with rupture lasting at least one second and breaking more than twice the area of the nucleation zone. About 70% of prior samples did not meet the condition, leaving approximately 30 000 samples of ρ_0.

We sampled the posterior distributions ρ_1 and ρ_2 by two independent runs of the Parallel Tempering algorithm, employing Eqs. (6.13) and (6.15), respectively. Initial models (different for each chain) were randomly picked from the prior distribution ρ_{pr}. MCMC proposals for

each parameter were sampled from normal probability densities centered around the present value of the parameter and with a standard deviation equal to 2% of its allowed range. We employed parallel computing on 6 GPUs of our in-house cluster, with 2 MPI threads per GPU and 8 MCMC chains per MPI thread. The temperature of two chains in each thread was set to 1, so they sampled the target distribution, while the remaining temperatures were randomly sampled from a log-normal distribution between 1 and 100. An additional MPI thread controlled the swapping of models among the chains.

For each distribution, the number of models visited by all chains was approximately 2 500 000 within 35 days. To ensure more accurate sampling, only every tenth accepted sample was recorded and the first sixth of the recorded samples were discarded to account for the so-called burn-in phase. Finally, we discarded the samples that did not satisfy the rupture condition r and kept only models sampled at $T = 1$. This way, about 50 000 samples were obtained for ρ_1 and ρ_2 each.

The quantities which emerge as results of dynamic simulations and are not analytically calculable from the model parameters, are denoted as emergent quantities. The main emergent quantities we discuss here are the scalar seismic moment:

$$M_0 = \int_{S_{el}} \mu(\boldsymbol{x}) \|\boldsymbol{s}_f(\boldsymbol{x})\| dS, \tag{6.32}$$

where $\boldsymbol{s_f}$ is the final slip distribution, the moment magnitude

$$M_w = \frac{2}{3} \left(\log_{10}(M_0) - 9.1 \right), \tag{6.33}$$

the area of rupture S_{rupt} (defined as the area of the portion of the fault with non-zero slip), the slip-weighted average stress drop:

$$\overline{\Delta\sigma} = \frac{\int_{S_{el}} \Delta\boldsymbol{\sigma}(\boldsymbol{x}) \cdot \boldsymbol{s}_f(\boldsymbol{x}) dS}{\int_{S_{el}} \|\boldsymbol{s}_f(\boldsymbol{x})\| dS}, \tag{6.34}$$

where $\Delta\boldsymbol{\sigma}(x)$ is defined as the difference between the shear stress at the beginning and the end of the simulation (see Fig. 6.2), the radiated energy (Ripperger et al., 2007):

$$E_R = -\frac{1}{2} \int_{S_{el}} \Delta\boldsymbol{\sigma}(\boldsymbol{x}) \cdot \boldsymbol{s}_f(\boldsymbol{x}) dS - \int_0^{t_f} \int_{S_{el}} (\boldsymbol{T}(t, \boldsymbol{x}) - \boldsymbol{T_i}(\boldsymbol{x})) \cdot \dot{\boldsymbol{s}}(t, \boldsymbol{x}) dt dS, \tag{6.35}$$

where t_f is the duration of rupture, the ordinary average $\overline{G_F}$ of the dissipated surface energy density G_F:

$$G_F = \int_0^{\mathfrak{s}_f} (T(s) - T_d) ds = \begin{cases} T_u \mathfrak{s}_f (1 - \frac{\mathfrak{s}_f}{2D_c}) & for\ 0 < \mathfrak{s} < D_c \\ T_u D_c / 2 & for\ \mathfrak{s} \geq D_c \end{cases} dS, \tag{6.36}$$

where $\mathfrak{s}_f$ is the final slip-path length, the total dissipated surface energy:

$$E_F = \int_{S_{el}} G_F(\mathfrak{s}_f(\boldsymbol{x})) dS, \tag{6.37}$$

the radiation efficiency

$$\eta = \frac{E_R}{E_R + E_F}, \tag{6.38}$$

and the slip-weighted average rupture speed:

$$\overline{V_r} := \frac{\int_{S_{el}} \frac{1}{\|\boldsymbol{p}(\boldsymbol{x})\|} \|\boldsymbol{s_f}(\boldsymbol{x})\| dS}{\int_{S_{el}} \|\boldsymbol{s_f}(\boldsymbol{x})\| dS}, \tag{6.39}$$

where $\boldsymbol{p}$ is the gradient of rupture time.

To explore rupture directivity, we examine the slip-weighted mean direction of rupture $\overline{\psi}$, defined as the angle between the horizontal line and the slip-weighted mean rupture velocity vector:

$$\overline{\psi} = \text{angle}\left(\boldsymbol{e_1}, \int_{S_{el}} \|\boldsymbol{s_f}(\boldsymbol{x})\| \frac{\boldsymbol{p}(x)}{\|\boldsymbol{p}(\boldsymbol{x})\|^2} dS\right), \tag{6.40}$$

where $\boldsymbol{e_1}$ is the unit horizontal vector pointing along strike.

To quantify the fit of synthetic data $\boldsymbol{d}(\boldsymbol{m})$ and the observed data $\boldsymbol{d_{obs}}$, we calculate the *variance reduction* (VR):

$$\text{VR}\left(\boldsymbol{d}(\boldsymbol{m}), \boldsymbol{d}_{obs}\right) := 1 - \frac{||\boldsymbol{d}(\boldsymbol{m}) - \boldsymbol{d}_{obs}||^2}{||\boldsymbol{d}_{obs}||^2}. \tag{6.41}$$

Unlike the misfit $||\boldsymbol{d}(\boldsymbol{m}) - \boldsymbol{d}_{obs}||^2$, the variance reduction is not additive over stations. Instead, the total variance reduction is a weighted average of variance reductions at individual stations. To see this, write

$$M^s = ||\boldsymbol{d}^s(\boldsymbol{m}) - \boldsymbol{d}^s_{obs}||^2 \tag{6.42}$$

and

$$N^s = ||\boldsymbol{d}^s_{obs}||^2, \tag{6.43}$$

where $\boldsymbol{d}^s(\boldsymbol{m})$ and $\boldsymbol{d}^s_{obs}$ are the synthetic and observed data, respectively, at station s. Then

$$\|\boldsymbol{d}(\boldsymbol{m}) - \boldsymbol{d}_{obs}\|^2 = \sum_s M^s, \tag{6.44}$$

$$\|\boldsymbol{d}_{obs}\|^2 = \sum_s N^s, \tag{6.45}$$

and the variance reduction $\mathrm{VR^s}$ at station s is

$$\mathrm{VR^s} = 1 - \frac{M^s}{N^s}. \tag{6.46}$$

The total variance reduction (6.41) can therefore be written as

$$\begin{aligned} \mathrm{VR} &= 1 - \frac{\sum_s M^s}{\sum_s N^s} \\ &= 1 - \frac{\sum_s N^s \frac{M^s}{N^s}}{\sum_s N^s} \\ &= 1 - \frac{\sum_s N^s(1 - \mathrm{VR^s})}{\sum_s N^s} \\ &= 1 - \frac{\sum_s (N^s - N^s \mathrm{VR^s})}{\sum_s N^s} \\ &= \sum_s \frac{N^s}{\sum_s N^s} V_R^s \end{aligned}, \tag{6.47}$$

which shows that is the average of variance reductions at individual stations, weighted by the sum of squares of the data. Therefore, closer stations with larger amplitudes have greater effect on the total variance reduction than far away stations with small amplitudes.

6.3.1 Best-fitting models

To provide the reader with an intuitive sense of the parameters and robust features of the sampled models, we first examine three models sampled from ρ_2 that best fit the observed seismograms. Spatial distributions of their slip, stress drop, and rupture time are shown in

Fig. 6.5. The fits between the observed and the synthetic waveforms for these models have variance reductions of 63-64%. In Fig. 6.6 we plot the waveform fit of the best-fitting model along with KDE estimates of synthetic seismograms generated from the whole ensemble. The KDE of variance reduction for ρ_2 is shown in Fig. 6.4. We note that 65%, 30% and 3% of models have variance reductions larger than 50%, 55% and 60%, respectively.

The feature in which the models are the most similar is the center coordinates of their nucleation zones, within 2 km. The dimensions of the elliptic patch are similar for the best-fitting models, though model #1 is somewhat more elongated than the other two. However, the rupture in model #1 only breaks 85% of the whole patch, stopping before reaching its lower left tip. The inclination angles ϕ of each elliptic patch differ quite strongly and this parameter is rather broadly distributed in the ρ_2 ensemble. Nevertheless, for all three models, the nucleation zone is to the right of the center of the ellipse, as is the case for 90% of models in the ensemble. The rupture propagates predominantly to the WNW, as it is soon arrested at the ESE edges of the patch. However, in contrast to the relatively robust directional preference with respect to the strike direction, the data do not seem to distinguish between upward or downward spreading. We note that kinematic inversions of Kiratzi (2018) and Chousianitis & Konca (2018) suggest even more pronounced unilateral rupture propagation.

The average slip-weighted stress drops $\overline{\Delta\sigma}$ of the three models are 5.7 MPa, 3.4 MPa, and 3.1 MPa, respectively. Model #1 has the lowest slip-weighted average rupture speed $\overline{V_r}$ (1.25 km/s vs 1.38 km/s and 1.91 km/s). It also has larger values of both T_u and D_c than the other two models (9.6 MPa vs 8.5 MPa vs 7.8 MPa, and 0.43 m vs 0.12 m vs 0.14 m). Consequently, model #1 also has the largest average fracture energy surface density $\overline{G_F}$ (1.6 MJ/m^2 vs 0.7 MJ/m^2 vs 0.6 MJ/m^2). The total radiated energies (see Fig. 6.2 here or fig. 1 and eq. C2 of Ripperger et al., 2007) of all three models range from 20 TJ (model #1) to 40 TJ (model #2). As we discuss below, this is the quantity best resolved by the seismograms. The seismic moments of the models are similar (3.4-3.7 $\times 10^{18}$ Nm). All three models have pronounced nucleation, which is a common feature in the ρ_2 ensemble.

6.3.2 Characteristics of the posterior pdfs

In this subsection, we analyze various parameters and how well they are constrained when incrementally updating the prior distribution ρ_{pr} by the rupture condition (posterior distribu-

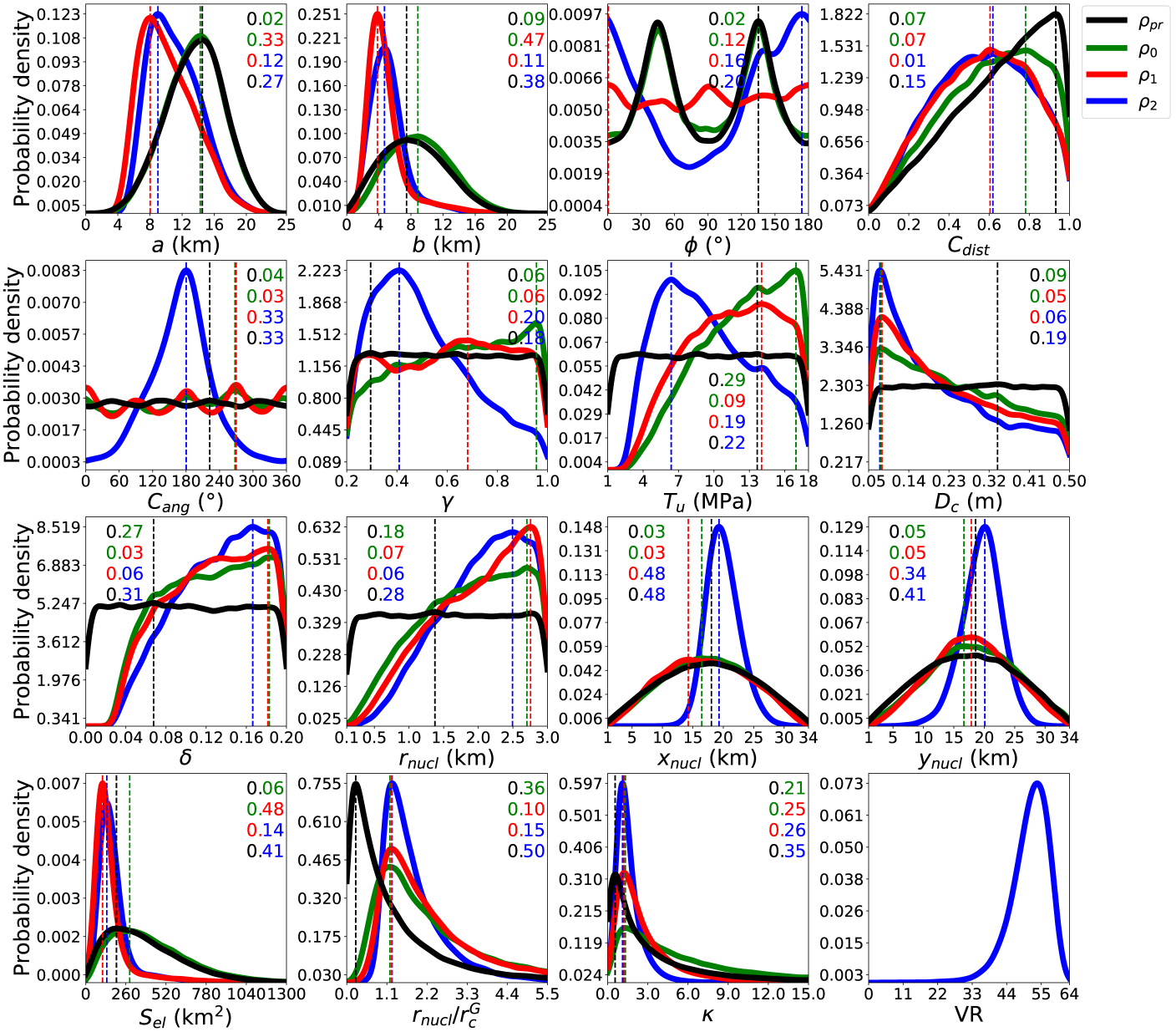

Figure 6.4: KDE estimates of 1-D marginal distributions for the model parameters and quantities derived from them, obtained with the Parallel Tempering algorithm. Different colors correspond to the prior distribution (ρ_{pr}) and posterior distributions incrementally constrained by the rupture condition (ρ_0), moment magnitude (ρ_1), and seismograms (ρ_2) (see legend). Vertical bars show the modes of each distribution. The numbers show the Hellinger distances between distributions, with color-coding representing the respective pair of distributions under comparison (for example, the distance between ρ_{pr} and ρ_0 is shown as a black-and-green number). Only the 12 parameters in the first three rows are independent, the quantities $S_{el} = \pi ab$, r_{nucl}/r_c^G (Eq. 6.51) and κ (Eq. 6.52) were calculated from them. The KDE of seismogram variance reduction (VR) for samples of ρ_2 is shown at the bottom right.

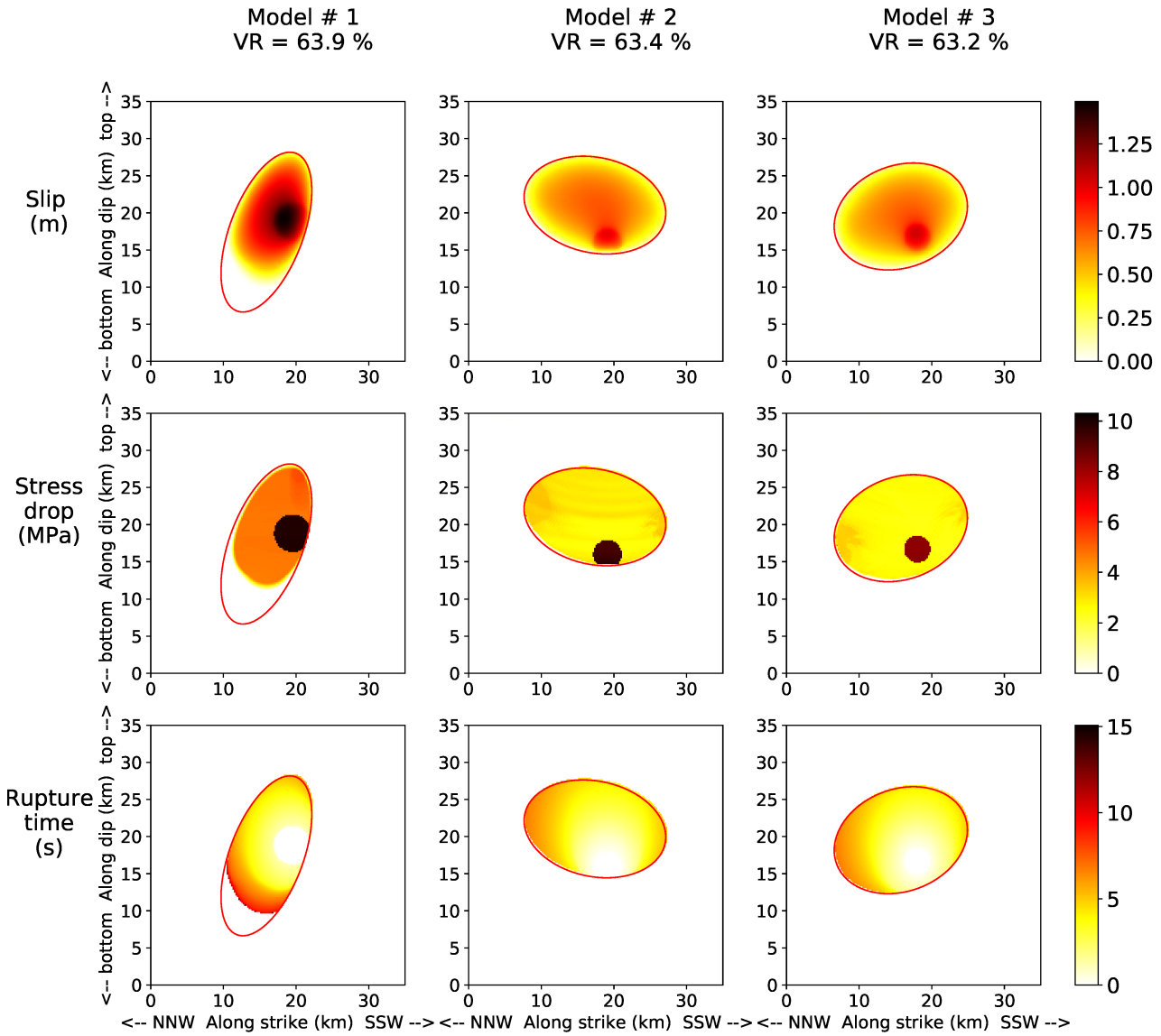

Figure 6.5: Distributions of the final slip, stress drop, and rupture time (rows) for the three best-fitting models (columns). Only the positive part of the stress drop is shown. The red ellipses show the boundaries of the elliptic patches within which rupture may propagate.

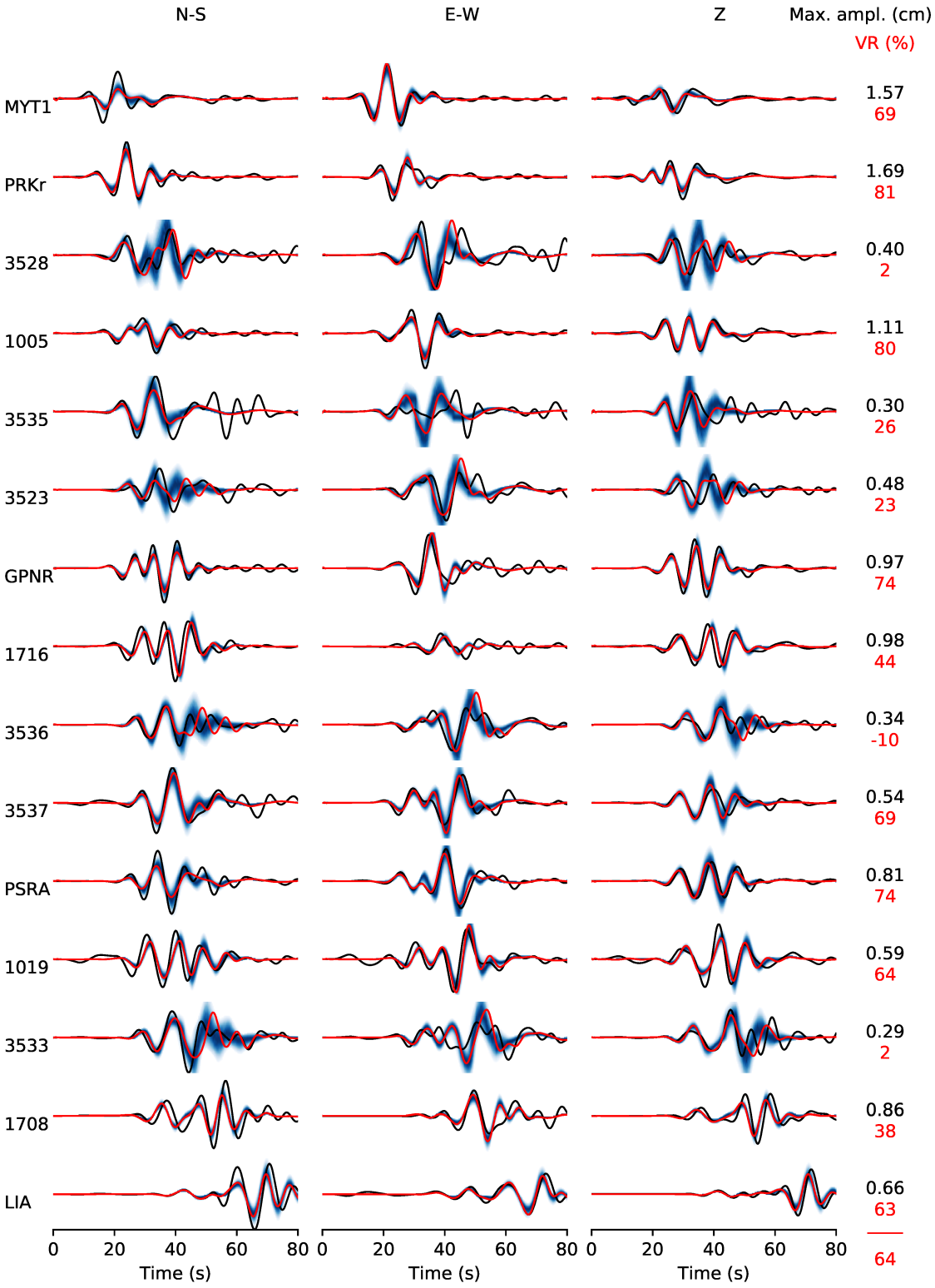

Figure 6.6: Displacement seismograms at the 15 selected stations in the frequency range of 0.05-0.15 Hz. Observed seismograms are black, synthetic seismograms of the best-fitting model are red. KDE estimates of synthetic seismogram posterior distribution, calculated at each time step, are blue. Numbers on the right show the maximum amplitude of the observed seismograms (black) and variance reduction at individual stations for the best-fitting model (red). The red number at the bottom is the overall variance reduction of the best-fitting model. The time axis begins on 12 Jun 2017, 12:28:38.26 GMT.

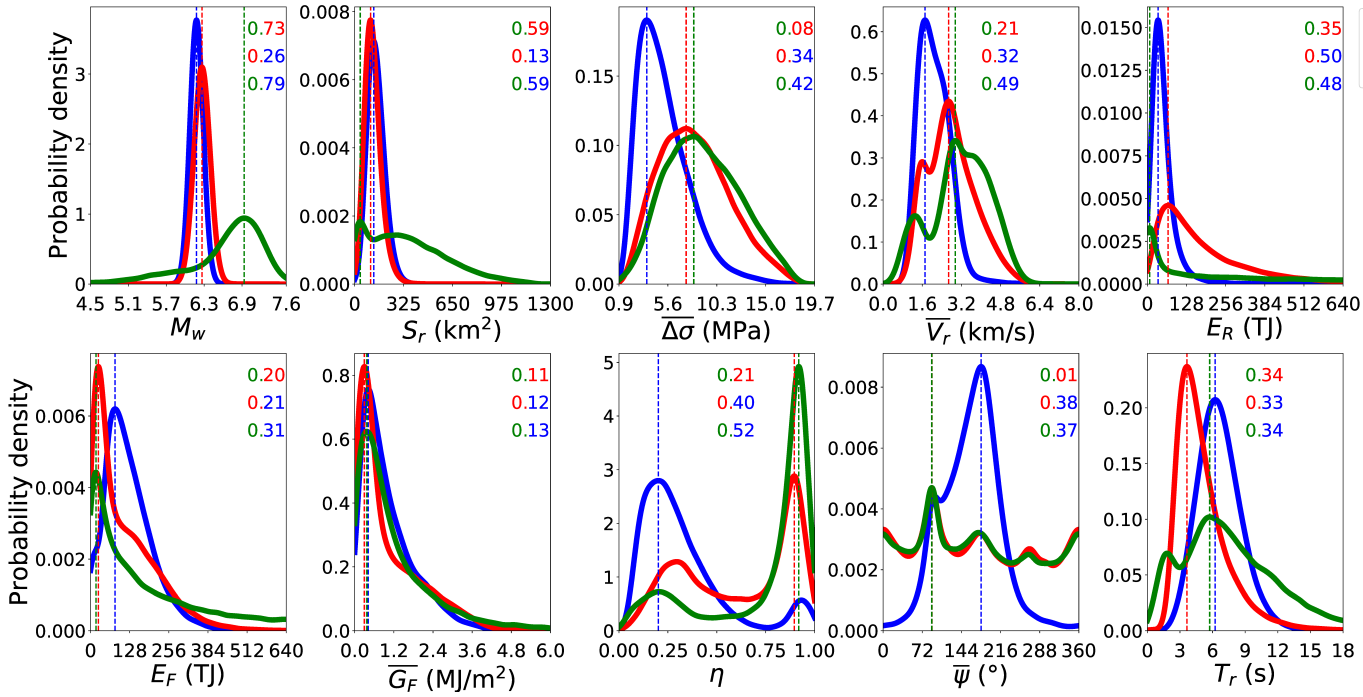

Figure 6.7: KDE estimates of 1-D marginal distributions for emergent quantities obtained with the Parallel Tempering algorithm. Different colors correspond to the posterior distributions incrementally constrained by the rupture condition (ρ_0), moment magnitude (ρ_1), and seismograms (ρ_2) (see legend). Vertical bars show the modes of each distribution. The numbers show the Hellinger distances between distributions, with color-coding representing the respective pair of distributions under comparison.

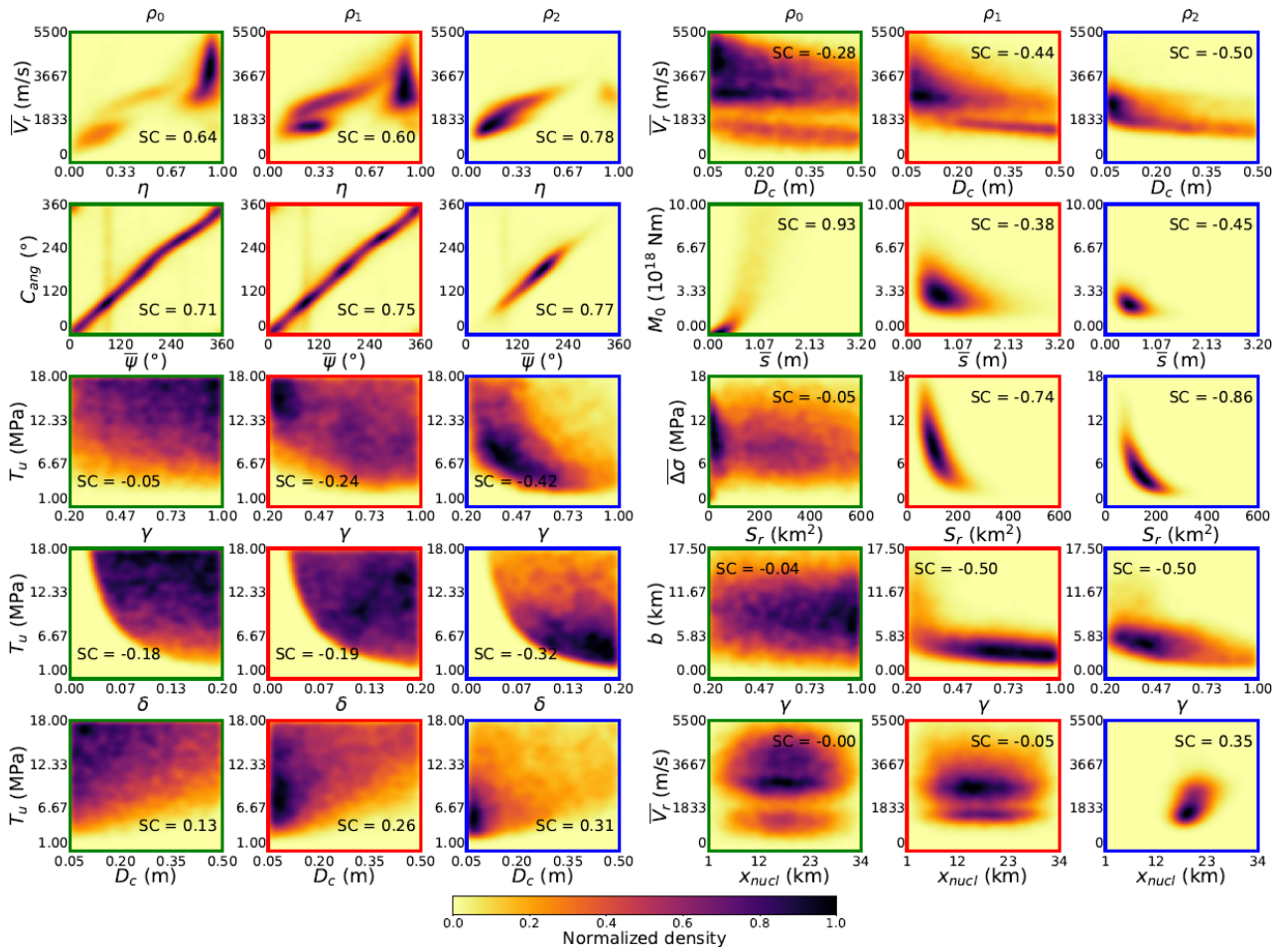

Figure 6.8: KDE estimates of 2-D marginal distributions of the posteriors ρ_0, ρ_1 and ρ_2 for selected pairs of quantities. The distributions are normalized by their respective maxima. SC denotes the value of the Spearman correlation coefficient.

tion ρ_0), the constraint on the moment magnitude (ρ_1), and the observed seismograms (ρ_2). A comparison of KDE estimates of marginal distributions of ρ_{pr}, ρ_0, ρ_1 and ρ_2 for model parameters (or parameters derived from them, such as a, ϕ, C_{ang} and C_{dist}) is shown in Fig. 6.4. Fig. 6.7 shows marginal posterior distributions for emergent quantities.

To compare the information contained in ρ_{pr}, ρ_0, ρ_1 and ρ_2, we measure their mutual dissimilarity in terms of the Hellinger distance H (Shemyakin, 2014):

$$H(\rho_i, \rho_j) = (1 - \int_{\mathbb{R}} \sqrt{\rho_i(x)\rho_j(x)}dx)^{1/2}. \tag{6.48}$$

It is a metric on the space of probability density functions, equal to 0 for (almost everywhere) identical pdfs and 1 for (a.e.) disjoint pdfs. For the sake of conciseness, we use the notation

$$H_{i,j} = H(\rho_i, \rho_j). \tag{6.49}$$

Large values of $H_{1,2}$, for example, suggest that the information contained in seismograms is very different from that contained in the moment magnitude. Evaluating data informativeness by comparing the prior and posterior distributions was also emphasized by Minson et al. (2014) in their Bayesian kinematic inversion of the great Tōhoku earthquake. In Tables 6.3 and 6.4 we list each model parameter and emergent quantity, respectively, sorted by $H_{0,1}$ and $H_{1,2}$. We note that since H is a metric, it satisfies the triangle inequality, e.g., $|H_{0,1} - H_{1,2}| \leq H_{0,2} \leq H_{0,1} + H_{1,2}$.

To quantify the uncertainty of the parameters, we evaluate the size of their 68% *highest density regions* (HDR). These are the regions that contain 68% of the posterior density, such that the density within them is always larger than the density outside (Hyndman, 1996). In particular, they always contain the largest mode of the distribution. For Gaussian distributions, the size of the HDR corresponds to two times their standard deviation. We list the modes and the HDRs of ρ_0, ρ_1 and ρ_2 in Tables 6.1 and 6.2. We use the notation $p \sim [_l M_u]$ to denote that the distribution of parameter p has mode M and l and u are the lower and upper bounds of its HDR. To compare the relative resolution of a parameter in distribution ρ_i and in its updated distribution ρ_j, we calculate the inverse ratios of their HDR sizes:

$$\text{rHDR}_{i,j} = \frac{|\text{HDR}_j|}{|\text{HDR}_i|}. \tag{6.50}$$

Low values of $\mathrm{rHDR}_{i,j}$ signify good relative resolution. We list the values of $\mathrm{rHDR}_{0,1}$ and $\mathrm{rHDR}_{1,2}$ in Table 6.3 (for model parameters) and in Table 6.4 (for emergent quantities).

2-D marginal distributions for selected 2-D pairs of quantities are shown in Fig. 6.8. To quantify their correlation, we use the Spearman correlation coefficient (SC). 2-D distributions for a more extensive list of quantities are shown in Figs. S9-S11.

6.3.2.1 Model parameters

The model parameters whose distributions appreciably change upon transition from ρ_{pr} to ρ_0 ($H_{pr,0} > 0.1$) are T_u, δ and r_{nucl} (Fig. 6.4). In ρ_{pr}, the distributions are flat, while in ρ_0 they are increasing (the sharp decay to zero at the boundaries is an artifact of the KDE method). This transition from a uniform to a monotonous distribution is also seen in parameters γ (increasing) and D_c (decreasing), although there the change is only small. Distributions of these 5 parameters change only negligibly upon the update from ρ_0 to ρ_1 (Fig. 6.4), which shows that they are not further affected by the magnitude. Nevertheless, distributions of parameters T_u and γ do visibly change after the seismogram ($\rho_1 \to \rho_2$) update ($H_{1,2} \approx 0.2$), developing peaks in the lower halves of their allowed ranges.

The only model parameters that strongly change in the transition from ρ_0 to ρ_1 are the lengths of the semi-major axis a and the semi-minor axis b, with $H_{0,1} = 0.33$ and 0.47, respectively. The ρ_1 distributions of both parameters peak at lower values than the ρ_0 distributions. In the case of a, the shift in the mode position is the main contributor to the change, and the uncertainty does not decrease very much ($\mathrm{rHDR}_{0,1} = 0.93$). In the case of b, there is a significant reduction of uncertainty ($\mathrm{rHDR}_{0,1} = 0.42$), the largest among model parameters in the $\rho_0 \to \rho_1$ transition. Nevertheless, the total area of the elliptic patch, $S_{el} = \pi ab$ (whose KDE is also shown in Fig. 6.4), gets resolved even more sharply than a or b individually ($\mathrm{rHDR}_{0,1} = 0.28$). The distributions of these three quantities are adjusted only a little when passing to the posterior ρ_2. Hence, they are mostly determined by moment magnitude.

The only other parameter for which ρ_0 and ρ_1 appreciably differ ($H_{0,1} > 0.1$) is the inclination angle of the patch, ϕ. In ρ_0, it peaks near 45° and 135°, as more elliptic patches fit within the fault (prior constraint #4 in subsection 6.2.3.3) at these angles. Contrarily, the ρ_1 distribution of ϕ is much flatter, probably because the elliptic patches sampled from this posterior tend to be smaller, so their orientation only weakly affects the probability of them fitting within the fault. In ρ_2, ϕ has a single peak around 0° (≡180°), suggesting that elon-

Parameter	Meaning	Prior min.	Prior max.	Mode and 68% HDR		
				ρ_0	ρ_1	ρ_2
a_x (km)*	Along-strike component of the semi-major axis	-17.5	17.5	$-11.1[18.8]$	$-6.0[17.0]$	$-8.6[15.5]$
a_y (km)*	Along-dip component of the semi-major axis	-17.5	17.5	$-11.3[18.4]$	$5.9[16.5]$	$[_{-7.5}-0.3_{7.5}]$
a (km)	Length of the semi-major axis	-	-	$[_{10.1}14.3_{17.4}]$	$[_{5.9}8.0_{12.6}]$	$[_{7.11}9.0_{13.5}]$
b (km)*	Length of the semi-minor axis	0.0	24.75	$[_{12.9}17.6_{22.1}]$	$[_{10.2}17.4_{23.3}]$	$[_{15.2}17.6_{20.0}]$
ϕ (degrees)	Angle of the semi-major axis	-	-	$[_{13.2}17.7_{22.3}]$	$[_{11.7}17.6_{23.6}]$	$[_{18.0}20.9_{22.9}]$
x_c (km)*	Along-strike position of the elliptic center	1	34	$[_{0.46}0.78_{0.96}]$	$[_{0.35}0.60_{0.85}]$	$[_{0.33}0.62_{0.84}]$
y_c (km)*	Along-dip position of the elliptic center	1	34	$268[232]$	$270[227]$	$[_{115}180_{226}]$
C_{dist}	Elliptic distance of the nucleation zone and the elliptic center	-	-	$[_{0.50}0.96_{0.99}]$	$0.68[0.51]$	$[_{0.24}0.41_{0.61}]$
C_{ang} (degrees)	Angle of the vector connecting the nucleation zone with the elliptic center	-	-	$268[232]$	$270[227]$	$[_{115}180_{226}]$
γ*	Initial background shear traction in the elliptic patch, relative to T_u	0.2	1.0	$[_{0.50}0.96_{0.99}]$	$0.68[0.51]$	$[_{0.24}0.41_{0.61}]$
T_u (MPa)*	Yield strength	1	18	$[_{10.4}16.9_{17.8}]$	$[_{8.8}14.0_{17.1}]$	$[_{3.9}6.4_{12.0}]$
δ*	Initial shear stress excess at the nucleation zone, relative to T_u	0.0	0.2	$[_{0.09}0.18_{0.20}]$	$[_{0.10}0.18_{0.19}]$	$[_{0.11}0.17_{0.19}]$
r_{nucl} (km)*	Radius of the nucleation zone	0.1	3	$[_{1.5}2.7_{2.9}]$	$[_{1.6}2.8_{3.0}]$	$[_{1.7}2.5_{2.9}]$
D_c (m)*	Characteristic slip-weakening distance	0.05	0.5	$0.08[0.26]$	$[_{0.05}0.08_{0.28}]$	$[_{0.05}0.08_{0.25}]$
x_{nucl} (km)*	Along-strike position of the nucleation zone	1	34	$[_{10.0}16.5_{25.1}]$	$[_{9.1}14.2_{24.2}]$	$[_{16.9}19.3_{22.3}]$
y_{nucl} (km)*	Along-dip position of the nucleation zone	1	34	$[_{11.0}16.7_{25.7}]$	$[_{11.0}17.9_{24.7}]$	$[_{16.6}20.1_{23.0}]$
S_{el} (km)	Area of the elliptic patch	-	-	$[_{97}285_{550}]$	$[_{53}109_{182}]$	$[_{77}137_{215}]$
r_{nucl}/r_c^G	Ratio of r_{nucl} to r_c^G (Eq. 6.51)	-	-	$[_{0.56}1.18_{2.60}]$	$[_{0.78}1.23_{2.60}]$	$[_{0.90}1.24_{2.10}]$
κ	Similarity parameter (Eq. 6.52)	-	-	$[_{0.29}1.32_{6.10}]$	$[_{0.33}1.23_{3.17}]$	$[_{0.51}1.11_{1.97}]$

Table 6.1: Prior ranges of model parameters and modes and 68% high density regions of posterior distributions ρ_0, ρ_1 and ρ_2 for model quantities. The symbols denoted by asterisks are the model parameters directly searched in the inversion, the rest is derived from them using explicit formulas. In the last three columns, we use the notation $[_lM_u]$, where l and u are the lower and upper bounds of the 68% HDR and M is the mode of the distribution. When the HDR is not an interval, we instead write $M[S]$, where S is the size of the HDR.

Parameter	**Meaning**	**Mode and 68% HDR**		
		ρ_0	ρ_1	ρ_2
M_w	Moment magnitude	$[_{6.43}6.93_{7.34}]$	$[_{6.14}6.27_{6.39}]$	$[_{6.08}6.18_{6.28}]$
S_r (km^2)	Ruptured area	$[_{0}36_{463}]$	$[_{57}105_{161}]$	$[_{76}126_{187}]$
$\overline{\Delta\sigma}$ (MPa)	Slip-weighted mean stress drop	$[_{4.8}8.1_{12.1}]$	$[_{4.1}7.4_{10.9}]$	$[_{2.2}3.6_{6.5}]$
$\overline{V_r}$ (km/s)	Slip-weighted mean rupture speed	$[_{2.3}3.0_{4.7}]$	$[_{1.4}2.7_{3.4}]$	$[_{1.4}1.7_{2.6}]$
E_R (TJ)	Radiated energy	8[272]	$[_{15}68_{210}]$	$[_{12}35_{65}]$
E_F (TJ)	Dissipated fracture energy	$[_{0}18_{217}]$	$[_{0}26_{149}]$	$[_{38}80_{174}]$
$\overline{G_F}$ (MJ/m^2)	Mean fracture energy surface density	$[_{0.0}0.4_{1.4}]$	$[_{0}0.3_{1.3}]$	$[_{0.1}0.4_{1.3}]$
η	Radiation efficiency	$[_{0.75}0.92_{1.00}]$	0.90[0.44]	$[_{0.09}0.20_{0.38}]$
$\overline{\psi}$ (°)	Slip-weighted mean rupture direction	89[222]	90[222]	180[103]
T_r (s)	Equivalent duration of rupture	5.7[8.2]	$[_{2.4}3.6_{6.0}]$	$[_{4.4}6.2_{8.3}]$

Table 6.2: The 68% high density regions of posterior distributions ρ_0, ρ_1 and ρ_2 for emergent quantities. We use the notation $[_lM_u]$, where l and u are the lower and upper bounds of the 68% HDR and M is the mode of the distribution. When the HDR is not an interval, we instead write $M[S]$, where S is the size of the region.

Rank	Parameter	$H(\rho_0, \rho_1)$	$\text{rHDR}_{0,1}$	Parameter	$H(\rho_1, \rho_2)$	$\text{rHDR}_{1,2}$
1	S_{el}	0.48	0.28	x_{nucl}	0.48	0.36
2	b	0.47	0.42	y_{nucl}	0.34	0.47
3	a	0.33	0.93	C_{ang}	0.33	0.48
4	κ	0.25	0.49	κ	0.26	0.51
5	ϕ	0.12	1.17	γ	0.20	0.72
6	r_{nucl}/r_c^G	0.10	0.89	T_u	0.19	0.98
7	T_u	0.09	1.13	ϕ	0.16	0.72
8	C_{dist}	0.07	1.02	r_{nucl}/r_c^G	0.15	0.66
9	r_{nucl}	0.07	0.90	S_{el}	0.14	1.07
10	γ	0.06	1.04	a	0.12	0.95
11	D_c	0.05	0.91	b	0.11	1.15
12	y_{nucl}	0.05	0.93	r_{nucl}	0.06	0.91
13	x_{nucl}	0.03	1.00	D_c	0.06	0.87
14	δ	0.03	0.94	δ	0.05	0.91
15	C_{ang}	0.03	0.98	C_{dist}	0.01	1.00

Table 6.3: Model parameters and derived quantities sorted according to the value of the Hellinger distance $H_{0,1}$ between posteriors ρ_0 and ρ_1, and the Hellinger distance $H_{1,2}$ between posteriors ρ_1 and ρ_2. The ratios of the sizes of the respective HDRs, $\text{rHDR}_{0,1}$ and $\text{rHDR}_{1,2}$, are also shown.

Rank	Parameter	$H(\rho_0, \rho_1)$	$\text{rHDR}_{0,1}$	Parameter	$H(\rho_1, \rho_2)$	$\text{rHDR}_{1,2}$
1	M_w	0.73	0.28	E_R	0.50	0.27
2	S_r	0.59	0.22	η	0.40	0.66
3	E_R	0.35	0.72	$\overline{\psi}$	0.38	0.46
4	T_r	0.34	0.44	$\overline{\Delta\sigma}$	0.34	0.63
5	η	0.21	1.79	T_r	0.33	1.07
6	$\overline{V_r}$	0.21	0.83	$\overline{V_r}$	0.32	0.61
7	E_F	0.20	0.69	M_w	0.29	0.82
8	$\overline{G_F}$	0.11	0.94	E_F	0.21	0.91
9	$\overline{\Delta\sigma}$	0.08	0.93	S_r	0.13	1.07
10	$\overline{\psi}$	0.01	1.00	$\overline{G_F}$	0.12	0.94

Table 6.4: Emergent quantities sorted according to the value of the Hellinger distance $H_{0,1}$ between posteriors ρ_0 and ρ_1, and the Hellinger distance $H_{1,2}$ between posteriors ρ_1 and ρ_2. The ratios of the sizes of the respective HDRs, $\text{rHDR}_{0,1}$ and $\text{rHDR}_{1,2}$, are also shown.

gation of the patch along strike (anti-plane direction) is preferred when the seismograms are included (most patches in ρ_1 and ρ_2 tend to be elongated, with the aspect ratio $b:a$ peaking around $1:3$ and having a median of about $1:2$). However, the peak in ϕ is rather broad (the size of the HDR is 86°, which is 48% of its possible range, and $\mathrm{rHDR}_{1,2} = 0.72$). As we have shown in subsection 6.3.1, ϕ considerably varies even among the best-fitting models.

Finally, the ρ_2 distributions of the parameters x_{nucl}, y_{nucl}, and C_{ang} are strongly determined by seismograms only, with $H_{1,2}$ of 0.48, 0.34 and 0,33, respectively. The along-strike location of the nucleation zone, x_{nucl}, has the greatest reduction in uncertainty among model parameters, $\mathrm{rHDR}_{1,2} = 0.36$. Its HDR size is 5.4 km, compared to the 6.4 km observed in the along-dip location y_{nucl} ($\mathrm{rHDR}_{1,2} = 0.47$). The distance of the most probable nucleation zone location and the GI-NOA hypocenter (see the 2-D distribution of (x_{nucl}, y_{nucl}) in Fig. S9c) is 6.3 km. Finally, parameter C_{ang}, which is better resolved than ϕ (with the absolute HDR size equal to 31% of its allowed range and $\mathrm{rHDR}_{1,2} = 0.48$), peaks around 180°. This corresponds to the nucleation zone being located to the ESE from the center of the ellipse. We consider the fact that we can resolve the position of the nucleation zone and the rupture direction as evidence that the seismograms are sensitive to finite-fault features of the source.

6.3.2.2 Emergent quantities

For emergent quantities, the differences between the ρ_0 posterior and the other two posteriors are often more pronounced than for most model parameters, and their Hellinger distances are larger on average (see Fig. 6.7 and Table 6.4). The ρ_0 posterior for M_w is wide and asymmetric, spanning values from 4.5 to 7.6, with a peak at 6.93. The ρ_1 posterior for M_w has a symmetric peak at 6.27, only slightly larger than the target value of $M_w^0 = 6.24$. The size of its HDR is 0.25. The ρ_2 posterior has a slightly lower mode (6.18) and smaller HDR (0.2).

Ruptures sampled from ρ_0 are fast, with mean slip-weighted rupture speed $\overline{V_r} \sim [_{2.3}3.0_{4.7}]$ km/s and tend to have large radiation efficiency η ($[_{0.75}0.92_{1.00}]$). Both quantities (which are strongly correlated in all distributions, see Fig. 6.8) are shifted towards lower values in the remaining two posteriors, especially in ρ_2.

Since the shear wave speed β is between 3.36-3.95 km/s on most of the fault, an appreciable fraction of models sampled from ρ_0 and even ρ_1 have a supershear average rupture speed. For ρ_2, this is true only for a negligible number of models. We note that for some models in ρ_2 with subshear average speed, the rupture speed does surpass β on a small part of the fault,

but this supershear propagation is unsustained.

The total ruptured area S_r has similar distributions to S_{el} and like that parameter, it is strongly resolved by magnitude ($\mathrm{rHDR}_{0,1} = 0.22$, the lowest among all emergent quantities). However, the distributions of S_r are slightly denser in lower values, because not all models rupture the whole elliptic patch. Note that some distributions of the quantities η, $\overline{V_r}$, S_r, and T_r have two peaks; the minor peaks correspond to the partially ruptured models.

The distributions of the slip-weighted mean stress drop $\overline{\Delta\sigma}$ are similar for ρ_0 and ρ_1. In ρ_2, the peak of the distribution gets shifted to lower values by about 50% and narrowed ($\mathrm{rHDR}_{1,2} = 0.63$, $\overline{\Delta\sigma} \sim [_{2.2}3.6_{6.5}]$ MPa).

The quantity whose uncertainty is reduced the most when seismograms are used, having $\mathrm{rHDR}_{1,2} = 0.27$, is the radiated energy E_R ($[_{12}36_{65}]$ TJ in ρ_2). Its Hellinger distance $H_{1,2}$ is 0.50, the largest among both model and emergent quantities. In contrast, the fracture energy E_F ($[_{38}80_{174}]$ TJ) and its average area density $\overline{G_F}$ ($[_{0.1}0.4_{1.3}]$ MJ/m^2) have $\mathrm{rHDR}_{1,2} = 0.91$, $H_{1,2} = 0.21$ and $\mathrm{rHDR}_{1,2} = 0.94$, $H_{1,2} = 0.12$, respectively. This makes E_F and $\overline{G_F}$, together with S_r, the emergent quantities whose distributions are the least resolved by the seismogram information.

Marginal distributions of ρ_0 and ρ_1 for the mean direction of rupture $\overline{\psi}$ are nearly identical. It is strongly correlated to the model parameter C_{ang}, with SC > 0.7 for all posterior distributions (Fig. 6.8). Local peaks are distributed at multiples of 90°, but only the peaks at 0° and 180° have the same height. This is not surprising, because the dynamic problem is symmetric only with respect to the strike. The distribution of $\overline{\psi}$ changes substantially in the $\rho_1 \rightarrow \rho_2$ ($H_{1,2} = 0.38$) transition. Its $\mathrm{rHDR}_{1,2}$ is 0.46, the second-largest reduction in uncertainty among emergent quantities after E_r. The HDR of the ρ_2 distribution lies approximately between 112° and 215°, which shows a strong seismogram preference for rupture spreading in the negative strike direction (towards WNW).

The final important quantity which is strongly affected by the waveform data is the equivalent duration of rupture T_r, calculated by dividing the seismic moment of each model by the maximum of its source time function. Even though the sizes of its ρ_1 and ρ_2 HDRs are similar ($\mathrm{rHDR}_{1,2} = 1.07$), the ρ_2 posterior peaks at ≈ 6.2 s, which is about 70% larger than for ρ_1. We plot the KDEs of source time functions sampled from ρ_1 and ρ_2 in Fig. 6.9, in which the different duration is clearly visible. While the ρ_1 STFs (Fig. 6.9a) form a diffuse large peak at the beginning, the ρ_2 STFs (Fig. 6.9b) are sharper, consisting of two lower peaks connected by a 3-4 s long plateau.

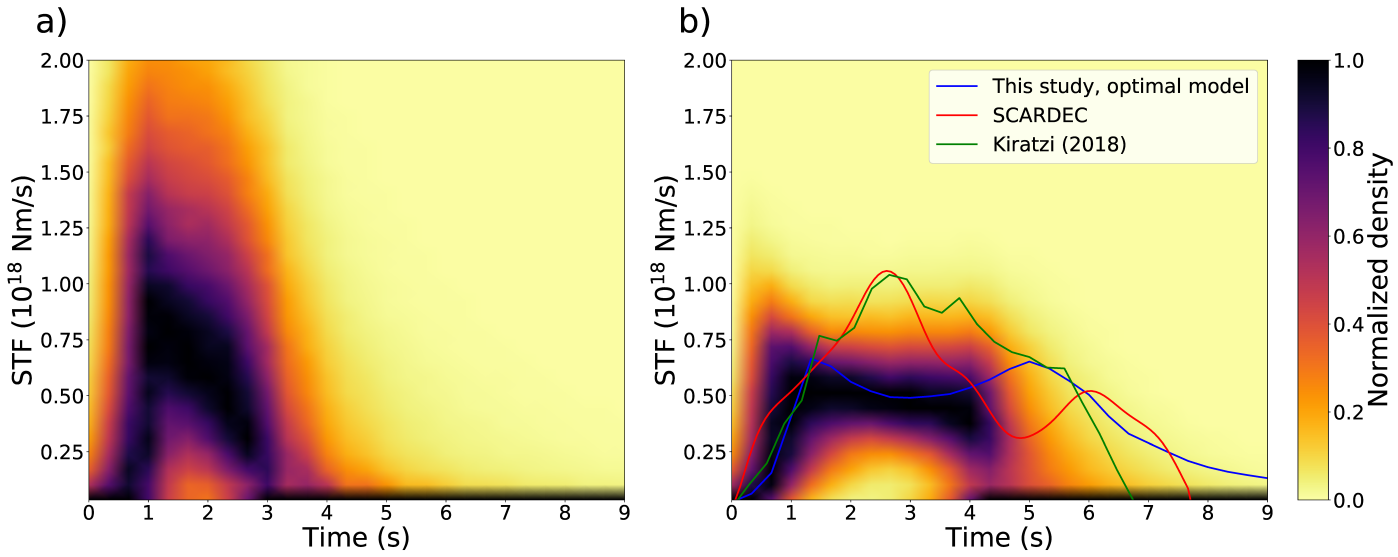

Figure 6.9: KDE estimates of source-time functions for a) ρ_1 and b) ρ_2, normalized at each time instance by the respective maximum. The source time function for the best-fitting model of this study is shown as the blue curve. The source time functions from the SCARDEC database (Vallée & Douet, 2016) and Kiratzi (2018) are shown as the red and green curves, respectively.

6.4 Discussion

We have performed a detailed Bayesian analysis of the dynamic inversion of the 2017 M_w 6.3 Lesvos earthquake, assuming an elliptic patch model. Thanks to careful sampling with the Parallel Tempering algorithm, we have identified how different quantities become resolved as progressively more information is added into the inversion. In particular, we analyze the chain of distributions $\rho_{pr} \rightarrow \rho_0 \rightarrow \rho_1 \rightarrow \rho_2$, corresponding to updating the prior (ρ_{pr}) by constraints on the rupture condition (ρ_0), magnitude (ρ_1) and seismograms (ρ_2), according to the Bayes' formula (6.8). We emphasize that if the inversion were performed by considering only the final posterior distribution, ρ_2, one could mistakenly attribute the resolution of a particular parameter only to the seismograms, even though the parameter may have gotten resolved mainly by the rupture or the magnitude constraints. Therefore, careful interpretation of results is needed.

We found that the final marginal posteriors ρ_2 of every model parameter are appreciably different from the prior distributions ρ_{pr}, with the minimum value of Hellinger distance $H_{pr,2}$ equal to 0.15 for parameter C_{dist} (see the black-and-blue numbers in Fig. 6.4). However, the

update causing the biggest change varies among parameters. The quantities whose distributions are mainly affected by the rupture criterion (i.e., the greatest change happens in the $\rho_{pr} \rightarrow \rho_0$ transition, while the ρ_1 and ρ_2 distributions are very close to ρ_0) are δ and r_{nucl}. Parameters a and b are mostly constrained by the moment magnitude ($\rho_0 \rightarrow \rho_1$), as is the total ruptured area S_r. The distributions of the model parameters x_{nucl}, y_{nucl}, C_{ang} and γ, and emergent quantities E_r, η, $\overline{\psi}$, $\overline{\Delta\sigma}$ and $\overline{V_r}$ are mainly affected by seismograms ($\rho_1 \rightarrow \rho_2$). Finally, the distributions of parameters D_c and C_{dist} do not change very much in either transition, but the small changes accumulate and their ρ_2 distributions are appreciably different from ρ_{pr}.

The seismogram information seems to push both T_u and γ towards lower values. This may be because seismograms require lower values of the background initial stress $T_e = T_u\gamma$, in accordance with the preference of lower values of the slip-weighted stress drop $\overline{\Delta\sigma}$ in ρ_2 (Fig. 6.7). Indeed, T_u and γ are weakly negatively correlated in ρ_2 (see Fig. 6.8), suggesting a tendency to keep $T_u\gamma$. Low values of γ mean large contrast between the stress at the nucleation zone and the rest of the patch. They are also more likely to lead to subshear rupture speeds (e.g., Andrews, 1976a; Dunham, 2007; Xu et al., 2015; see section 3.5 of this thesis) which could be significant for fitting the observed seismograms.

The change in distributions of parameters T_u, δ and r_{nucl} due to the rupture condition ($\rho_{pr}\rightarrow\rho_0$ transition, see subsection 6.3.2.1) calls for an explanation. A natural way to interpret it is that there exists a parameter-dependent minimum nucleation radius, r_m, such that a model does not meet the rupture condition unless $r_{nucl} > r_m$. Since there is no analytic formula for r_m, we adopt an approximate closed-form expression for the critical radius from Galis et al. (2015), presented in this thesis as Eq. (3.15). In the parametrization of this study, it reads

$$r_c^G = \sqrt{\frac{3^3}{2^{11}}} \frac{\pi\mu D_c}{T_u\gamma^{3/2}\sqrt{1+\delta-\gamma}}. \tag{6.51}$$

It was derived for runaway ruptures, which break the whole patch, and should be considered as an upper bound for r_m. We plot the KDE of the non-dimensional ratio r_{nucl}/r_c^G in Fig. 6.4. The distribution of the parameter changes significantly between ρ_{pr} (in which it is essentially decreasing from zero since the small peak is an artifact of the KDE method) and ρ_0, in which it peaks at ≈1.2. The remaining posteriors also peak near that value. Importantly, less than 1% of all models sampled from ρ_0 have r_{nucl}/r_c^G smaller than ≈ 0.3. We interpret this as the nucleation condition choosing only models with r_{nucl}/r_c^G greater than this minimum value.

It also explains why the ρ_0 distribution of D_c is decreasing, while the ρ_0 distributions of parameters T_u, δ and r_{nucl} are increasing. Further, since the parameters in Eq. (6.51) can mutually compensate their effects on r_c^G, we can expect that they are not independent in the posteriors (as they are in ρ_{pr}.) This is most noticeable in the 2-D marginal distributions of the pair (δ, T_u), which have a roughly semi-circular shape with non-zero values only when both T_u and δ are large enough (Fig. 6.8).

Another non-dimensional parameter, which was shown to control the transition between failed and successful rupture in elongated homogeneous barrier patches with sufficient width (Madariaga & Olsen, 2000) is the *similarity* parameter κ (Eq. 3.23), defined in our parametrization as:

$$\kappa = \frac{bT_u\gamma^2}{\mu D_c}. \tag{6.52}$$

Ruiz & Madariaga (2011, 2013); Twardzik et al. (2014); Herrera et al. (2017); Mirwald et al. (2019) and Mirwald et al. (2019) inverted for its value and obtained relatively similar values for well-fitting models, between 1.0 and 2.0. We plot its marginal distributions in Fig. 6.4. We find that its HDR in the ρ_2 posterior is [0.5, 2.0], compared to its ρ_{pr} HDR of [0.14,3.5], which is a good reduction in uncertainty. The peak in all three posterior distributions is centered around similar values ($\approx$ 1.1-1.3), but it gets narrower in both the $\rho_0 \rightarrow \rho_1$ ($\text{rHDR}_{0,1} = 0.49$) and the $\rho_1 \rightarrow \rho_2$ ($\text{rHDR}_{1,2} = 0.51$) transitions. The first sharpening is likely related to the resolution of parameter b by the magnitude information ($\text{rHDR}_{0,1} = 0.49$), while the second is either caused by the resolution of γ ($\text{rHDR}_{1,2} = 0.72$), or it cannot be attributed to a single parameter.

The quantity whose uncertainty is reduced the most when seismograms are used is the radiated energy E_R. That E_R is better resolved by seismograms than the fracture energy E_F seems reasonable, as it is the energy carried away from the fault by elastic waves that reach seismic stations. In addition, since for a fully fractured patch, the fracture energy is proportional to $T_u D_c S_r$, and S_r is well determined, there are two ways in which E_F could be resolved. Either both T_u and D_c need to be well resolved, or they may be individually unresolved, but mutually anti-correlated so that their product is approximately constant. Instead, neither parameter is strongly resolved and their correlation coefficients are small and positive in all posterior distributions (Fig. 6.8). The chosen frequency band (0.05-0.15 Hz) may be the reason for this weak (relative to other parameters) resolution. As higher frequencies become available, finer details of the earthquake might become visible, possibly permitting

better resolution of D_c (Guatteri & Spudich, 2000), and consequently E_F.

As seen above, statistical dependencies between pairs of parameters can be explored by examining 2-D marginal distributions. However, like the 1-D marginals, these need to be interpreted carefully. Some dependencies are observed in all three posteriors (Fig. 6.8), such as the positive correlation between $\overline{V_r}$ and η, expected from simple rupture-mechanical models (e.g., Kanamori & Brodsky, 2004), or the weak negative correlation between $\overline{V_r}$ and D_c (noted also by Mirwald et al., 2019, in their inversion of the 2017 M_w 7.1 Puebla-Morelos earthquake). However, conservation of correlations across successive distributions should not be taken for granted, even when we might expect the correlations from physical considerations. For example, since for constant μ, $M_0 = \mu S_r \overline{s_f}$, where $\overline{s_f}$ is the average magnitude of the final slip (Eq. 6.32), we would expect M_0 to be positively correlated to $\overline{s_f}$. Indeed, the two parameters are strongly positively correlated in ρ_0 (SC > 0.9). But when passing to ρ_1 and ρ_2, M_0 and $\overline{s_f}$ become weakly negatively correlated instead. We note the parameters M_0 and S_r remain positively correlated, but the correlation weakens in the transition from ρ_0 to ρ_1 and ρ_2 (see Fig. S10).

On the other hand, quantities that are almost completely uncorrelated in ρ_0 may become correlated in ρ_1 and ρ_2 (Fig. 6.8). For example, we observe a weak positive correlation between x_{nucl} and $\overline{V_r}$ in ρ_2, i.e. models sampled from ρ_2 tend to rupture faster when nucleating farther along strike. The quantities $\overline{\Delta\sigma}$ and S_r are other examples; a strong negative correlation (also observed by Mirwald et al., 2019) appears upon the passage from ρ_0 to the magnitude constrained ρ_1. This scaling is what we would expect from the circular crack model, in which $M_0 \propto \Delta\sigma S_r^{3/2}$ (Eq. 2.89 with $r = \pi^{-1/2} S_r^{1/2}$). The anti-correlation between emergent parameters $\overline{\Delta\sigma}$ and S_r translates to an anti-correlation between model parameters γ and b (Fig. 6.8). We note that one of these parameters is geometric, while the other controls initial shear stress. Therefore, fixing geometric model parameters (e.g., to those of the best fitting model, Twardzik et al., 2014), and exploring only stress-frictional parameters underestimates the uncertainty of the latter, though faster exploration is obtained as a trade-off.

6.5 Conclusion

We have carried out a Bayesian dynamical inversion of the 2017 M_w 6.3 Lesvos earthquake using a single elliptic model with stress and friction defined by 12 parameters. We have cal-

culated three different posterior probability distributions for those parameters by requiring 0) only that the model they describe continues to rupture after nucleation, 1) that it produces moment magnitude close to a value determined from a CMT inversion, and 2) that it produces displacement waveforms that fit recordings from near regional stations.

We compared the distributions to assess the degree to which each piece of information constrains various parameters. We found that the parameters δ (nucleation stress overshoot relative to yield strength) and r_{nucl} (radius of nucleation zone) are sensitive mainly to the rupture condition, so neither the magnitude nor the seismograms strongly constrain them further. Lengths of the semi-major and semi-minor axes of the elliptic patch, a and b, are mainly determined by moment magnitude. Finally, the along-strike and along-dip coordinates of the nucleation zone x_{nucl}, y_{nucl}, the relative angle between nucleation and center of the patch C_{ang}, the yield strength T_u and the ratio γ of the initial traction to the yield strength are determined chiefly by seismograms.

We also examined emergent quantities, obtained as results of dynamic rupture simulations. The surface area of rupture is the emergent quantity best resolved by the magnitude information. The quantity best resolved by the seismogram information is the radiated energy, with its final posterior distribution peaking at 35 TJ and with 68% of values between 12 TJ and 65 TJ. Most models sampled from the final posterior are characterized by slow mean rupture velocity (1.4-2.6 km/s), low radiation efficiency (10-40%), and low slip-weighted mean stress drop (2.2-6.5 MPa). The rupture is further characterized by pronounced nucleation and subshear propagation directed predominantly towards WNW.

The presented analysis of resolvability of source parameters is limited to the considered elliptic models and seismogram frequency range and station distribution similar to this study. Nevertheless, our approach to assessing the roles of various constraints in Bayesian inversion by comparing 1-D distributions can be generalized to other dynamic earthquake source studies. Even for more complex source models with a large number of possibly correlated model parameters, the approach could prove useful for analyzing gross rupture properties, such as radiated energy, seismic moment, average stress drop, or average rupture velocity.

Acknowledgments

We are grateful to two anonymous reviewers for suggestions that helped improve the manuscript. We thank the personnel of the Hellenic Seismic Network, National Seismic Network of Turkey (DDA) and Bogazici University Kandilli Observatory and Earthquake Research Institute (KOERI) for their work on the installation, operation, and maintenance of stations whose waveforms were used in this study. We thank Jan Premus for codeveloping the dynamic rupture simulation code FD3D_TSN and assisting with its use. We thank Malcolm Sambridge for making available his Fortran subroutines for the Parallel Tempering algorithm. We acknowledge financial support from the Charles University (projects GA UK No. 1698218 and SVV 115–09/260581). This work was supported by The Ministry of Education, Youth and Sports (cze) of the Czech Republic through the e-INFRA CZ (ID:90140).

DATA AVAILABILITY All waveforms and seismic event locations used in this paper are publicly available from the Hellenic Seismic Network (National Observatory of Athens doi:10.7914/SN/HL, ITSAK doi:10.7914/SN/HI), National Seismic Network of Turkey (DDA), and Bogazici University Kandilli Observatory and Earthquake Research Institute (KOERI) (doi:10.7914/SN/KO). The dynamic rupture simulation code FD3D_TSN is publicly available at https://github.com/JanPremus/fd3dTSN. The Parallel Tempering subroutines are available, upon registration, at http://www.iearth.org.au/codes/ParallelTempering/. The files containing all the probability distribution samples, as well as the Python scripts used for their visualization and statistical analysis, will be shared on request to the corresponding author.

S1 Supplemental material

S1.1 Estimation of M_w^0 and the fault plane based on centroid moment tensor inversion

To determine the fault plane geometry and obtain an estimate of the moment magnitude of the Lesvos earthquake, we performed a full-waveform centroid moment tensor (CMT) inversion

with the help of the software ISOLA (Zahradník & Sokos, 2018). We summarize the analysis below.

We used non-clipped broadband records from stations located 180 to 350 km away from the epicenter, filtered between 0.01 and 0.05 Hz, finding the centroid position shifted from the GI-NOA epicenter by ∼7 km in the NW direction. Then we used strong-motion stations located 30 to 90 km away from the hypocenter (Fig. S1) to improve the CMT solution. Using a 3D grid search and records filtered between 0.03 and 0.07 Hz, we found the optimum centroid position at a depth of 8 km, shifted 2 km west and 6 km north of the GI-NOA epicenter, centroid time of 3.76 s after origin time; we found the moment magnitude to be 6.24 ($M_0 = 2.89 \cdot 10^{18}$ Nm), see Figs. S2 and S3. We use this value for our estimate of M_w^0 in the Bayesian inversion (Eqs. 6.12, 6.13 and 6.15). The double-couple percentage (although not a priori constrained) was very high, DC≥90%.

Of the two moment-tensor nodal planes of our CMT, we adopt the fault with strike/dip/rake values 113°/40°/-83° for the following reasons: i) it has been preferred by seismic, geologic and bathymetric data in previous studies (Kiratzi, 2018), and ii) the distance of the GI-NOA hypocenter (H) from this fault plane passing through the centroid (C) is only 0.03 km. The latter is the so-called H-C consistency (Zahradník et al., 2008), a useful tool for identifying fault planes. A comparison of our solution for the centroid with other studies is shown in Table S1.

In the dynamic inversion, we assume a fault plane with a dimension of 35×35 km (spatial sampling of 200 m), which is large enough to encompass the rupture within a comfortable margin. During initial tests, it became evident that models tend to rupture in the WNW direction from the centroid. For this reason, the fault center was shifted along the strike direction by 5 km from the inferred centroid to allow more space for rupture. The map projection of the fault is shown in Fig. 6.1 of the main text.

Having obtained the centroid solution, it is also useful to increase the frequency range and check a multiple-point source model, because it can provide a preliminary estimate of rupture propagation and rupture complexity. We used the range 0.05-0.10 Hz, calculated a three-point model (see Figs. S4 and S5), and found a stable normal-faulting mechanism, indicating a simple rupture geometry of the mainshock and rupture propagation towards the northwest.

	Lat. (°)	Lon. (°)	Depth (km)	M_0 (10^{18} Nm)	M_w	Strike (°)	Dip (°)	Rake (°)
This study	38.8928	26.3392	8	2.89	6.24	113	40	-83
SCARDEC	38.93	26.365	11	4.02	6.34	118	41	-74
Papadimitriou et al. (2018)	38.8529	26.3509	13	3.49	6.3	122	40	-83
GCMT	38.81	26.32	12	4.31	6.36	110	77	-87
GFZ	38.83	26.34	10	4.3	6.36	112	42	-84
USGS	38.93	26.365	11.5	3.98	6.33	114	57	-82

Table S1: Comparison of centroid solutions found by different studies. Only the nodal plane used in this study is shown.

S1.2 Supplemental figures

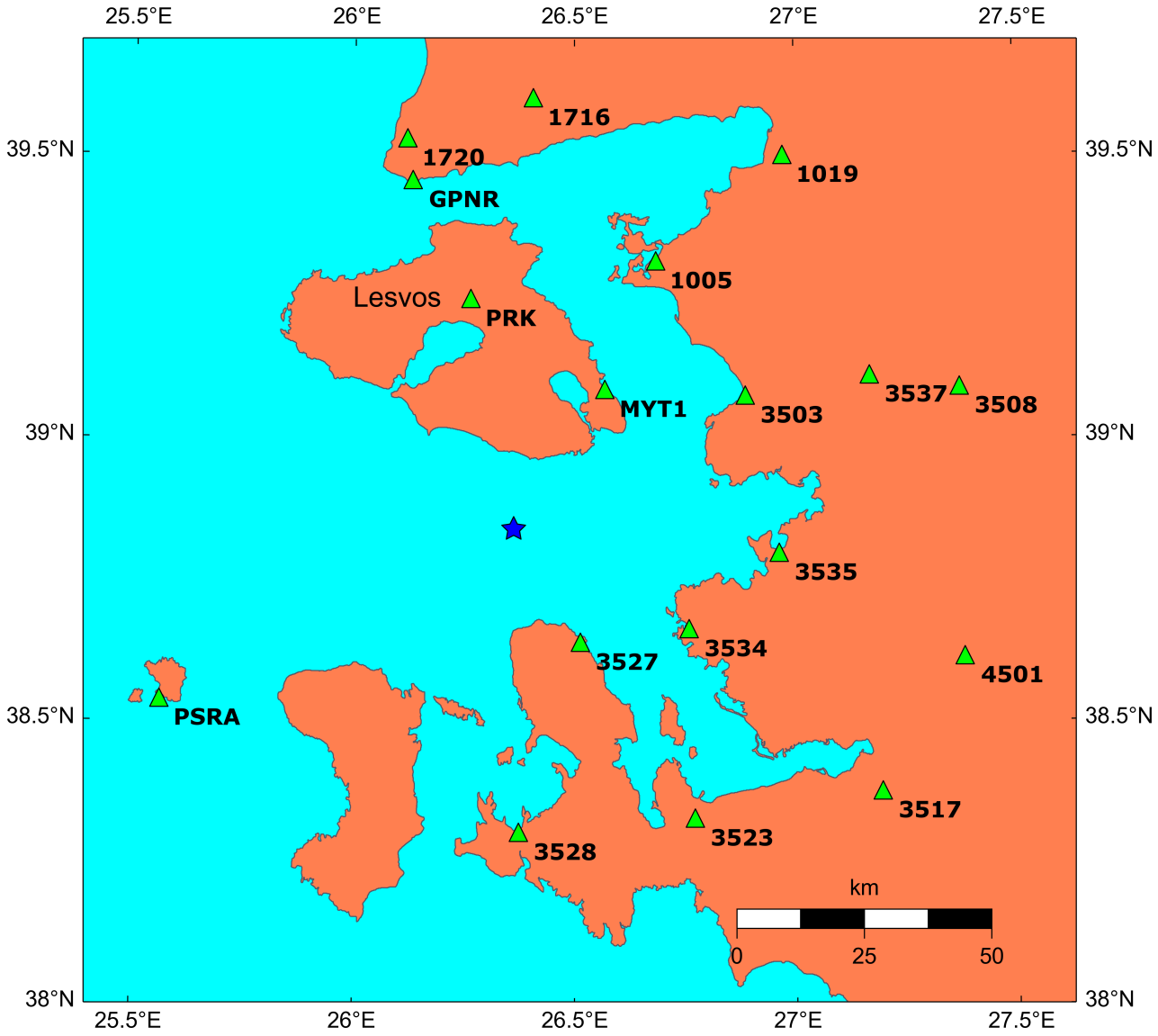

Figure S1: Map view of the stations used in the centroid moment tensor inversion (text S1.1 and Figs. S2-S5). The blue star is the GI-NOA hypocenter.

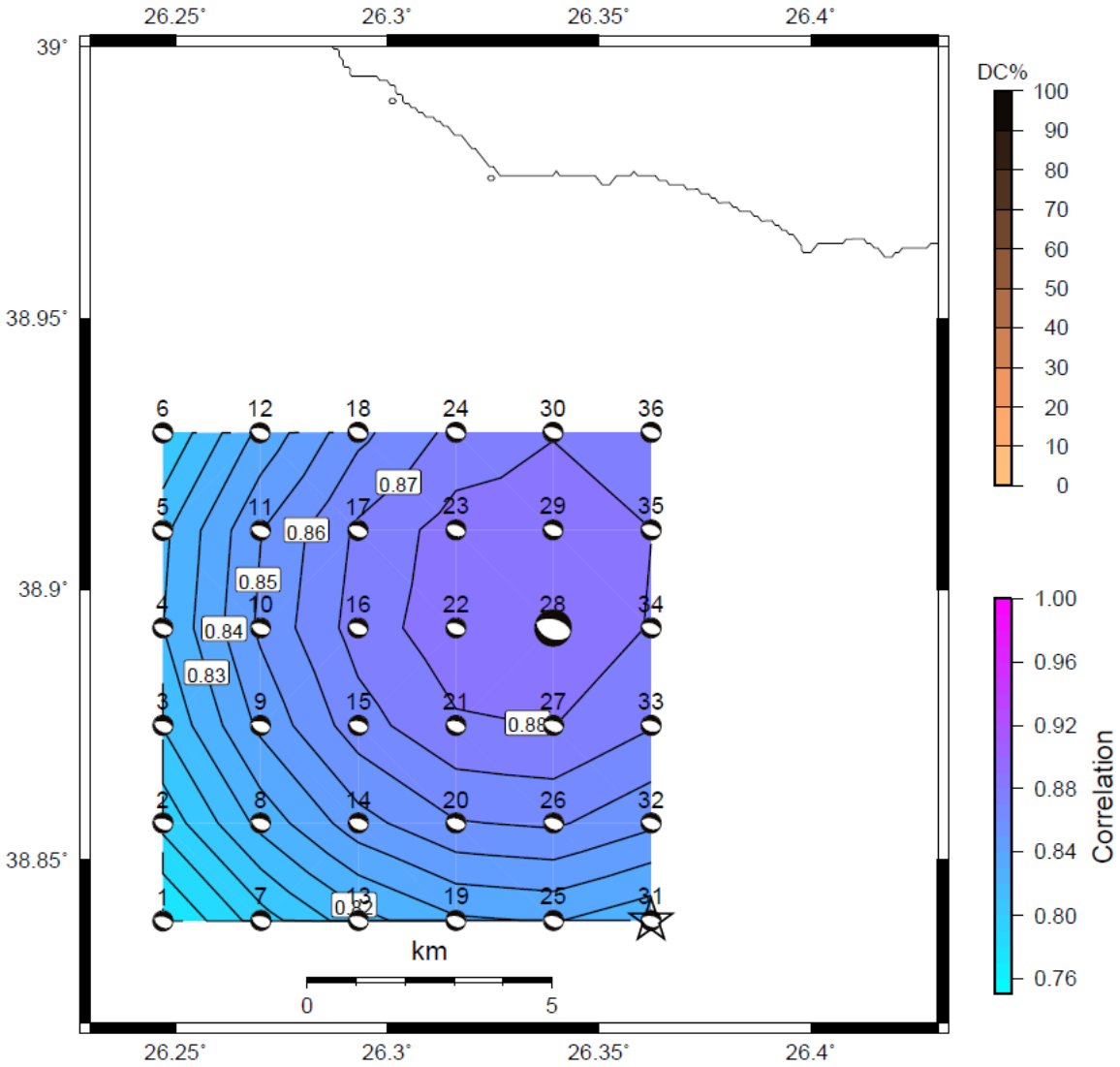

Figure S2: Horizontal grid search (36 trial positions, increments of 2 km) for the centroid at a depth of 8 km. The star shows the NOA epicenter for reference. The centroid position, characterized by the largest correlation between observed and synthetic displacements in the frequency range of 0.03 and 0.07 Hz, located 2 km west and 6 km north from the epicenter, is shown by the largest beachball, trial position #28. The balls are color-coded according to the double-couple percentage (all $>$ 90%). Note the stability of the focal mechanism across the grid.

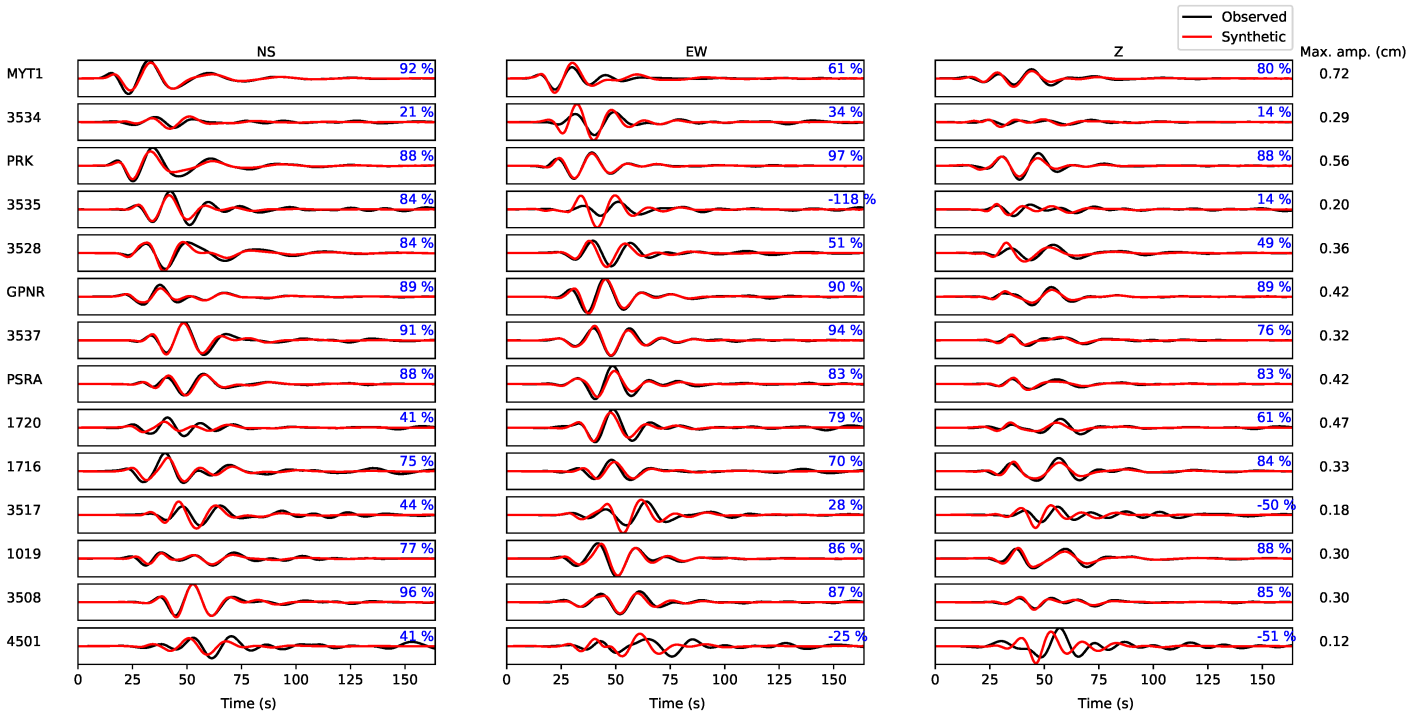

Figure S3: Waveform fit for the CMT solution (position #28 in Fig. S2, strike/dip/rake = 113°/40°/-83°, frequency range from 0.03 Hz to 0.07 Hz, the total variance reduction VR=79%). Real and synthetic displacements are shown as black and red lines, respectively. The blue numbers denote the variance reductions of the individual components.

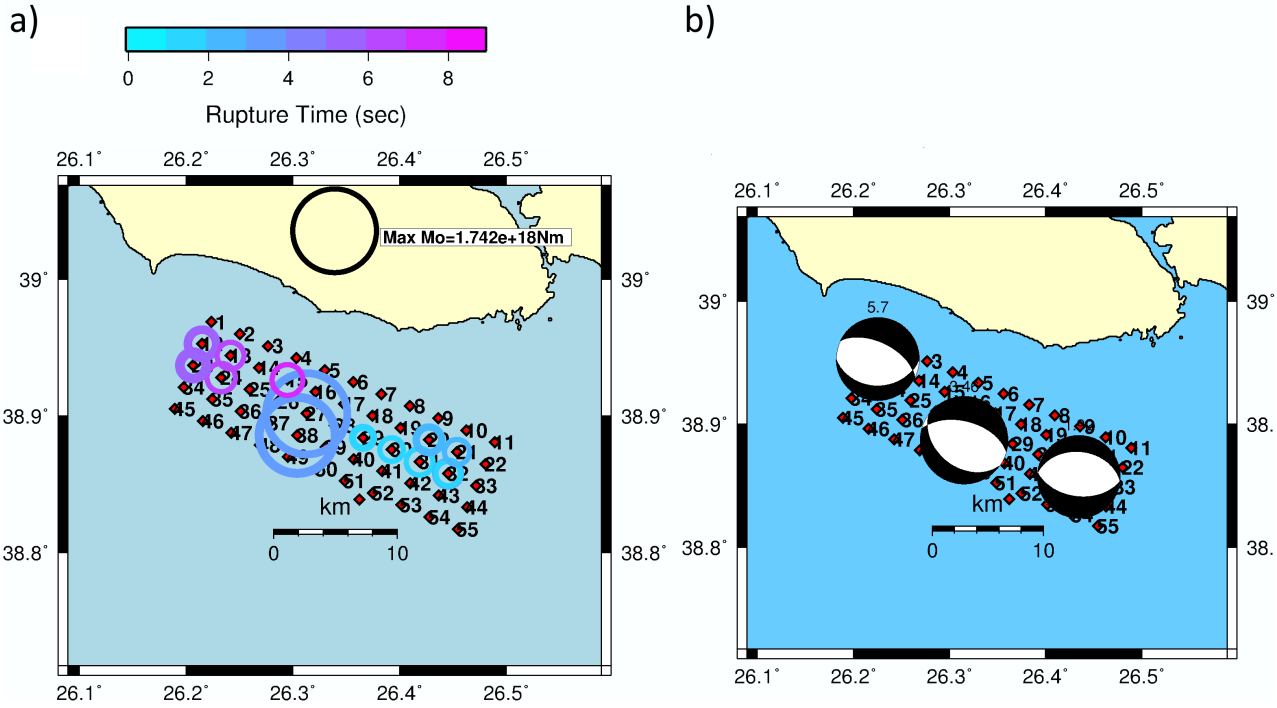

Figure S4: a) A three-point source model. Three point-source models with deviatoric moment tensors are searched by iterative deconvolution of ISOLA (Zahradník & Sokos, 2018) software in the assumed fault plane, using the frequency range of 0.05-0.10 Hz. The sources are shown by circles, sized according to their scalar moment, and color-coded according to their rupture time ($t = 0$ s is the origin time). The large black circle at the top is a referential moment scale, not a solution. The 3-point solution was calculated repeatedly, each time removing one station (jackknifing), thus producing multiple triplets of circles (some of them coincide) to estimate uncertainty. The plot demonstrates a stable evolution of the rupture from the southeast to the northwest. The process starts with an early subevent (turquoise-colored) near the epicenter (marked by an isolated diamond near the trial position #52), continues with the major subevent in the middle of the fault, and ends with a third moment-release episode at about 6-8 seconds after origin time. Variance reduction from the stations shown in Fig. S5 varied during jackknifing from VR = 0.69 to 0.76. The focal mechanism of the major subevent was almost constant, the mechanisms of the remaining two subevents varied within 30° Kagan angle from the CMT solution during the jackknifing. b) The mechanisms of the best solution from all stations. The largest subevent is at position #38, followed by positions #32 and #12. Strong stability of the mechanism is seen.

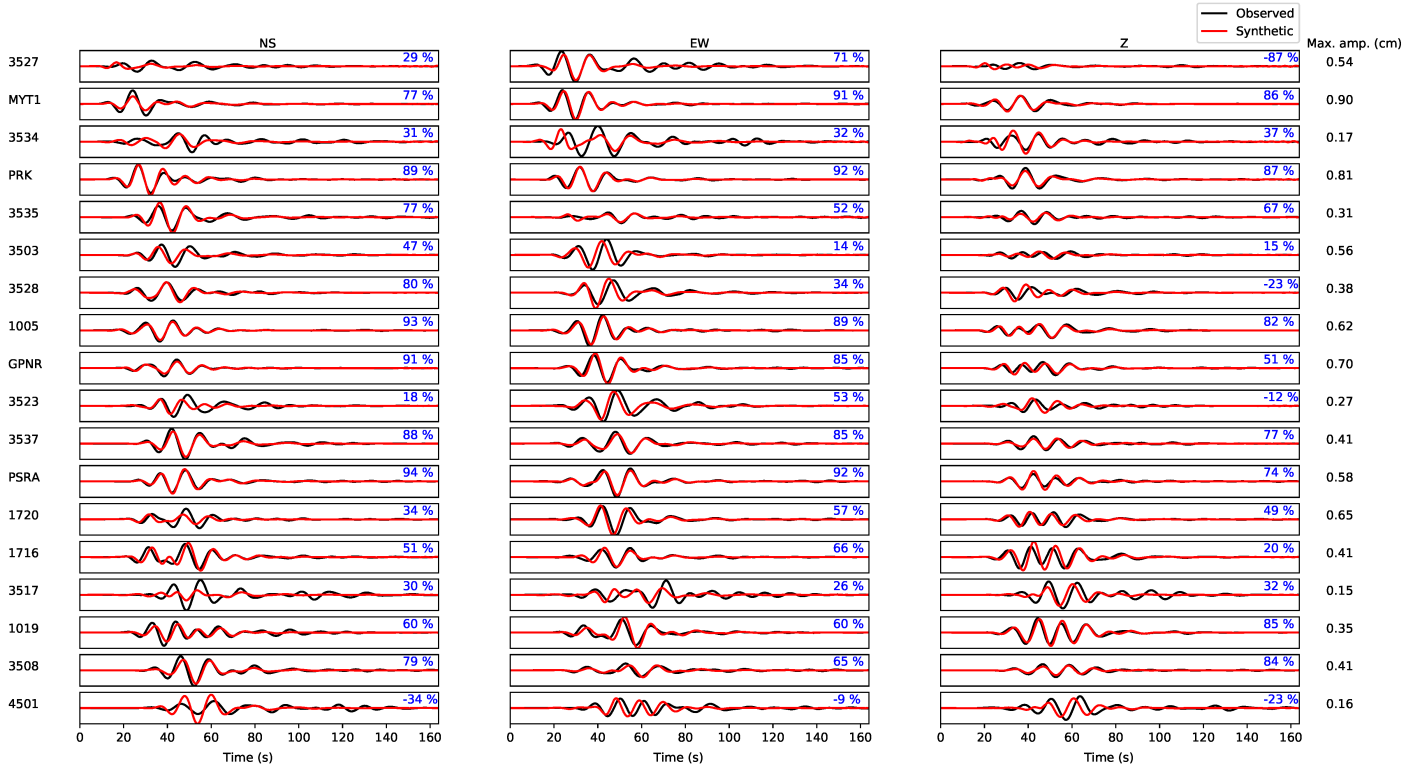

Figure S5: Waveform fit for the three-point source model of Figure S4b. The frequency range is 0.05-0.10 Hz, the total variance reduction VR=71% (when considering only the two largest subevents, or just a single largest subevent, variance reduction drops to VR = 66% and 60%, respectively). The real and synthetic displacements are shown as black and red lines, respectively. The blue numbers denote the variance reductions of the individual components.

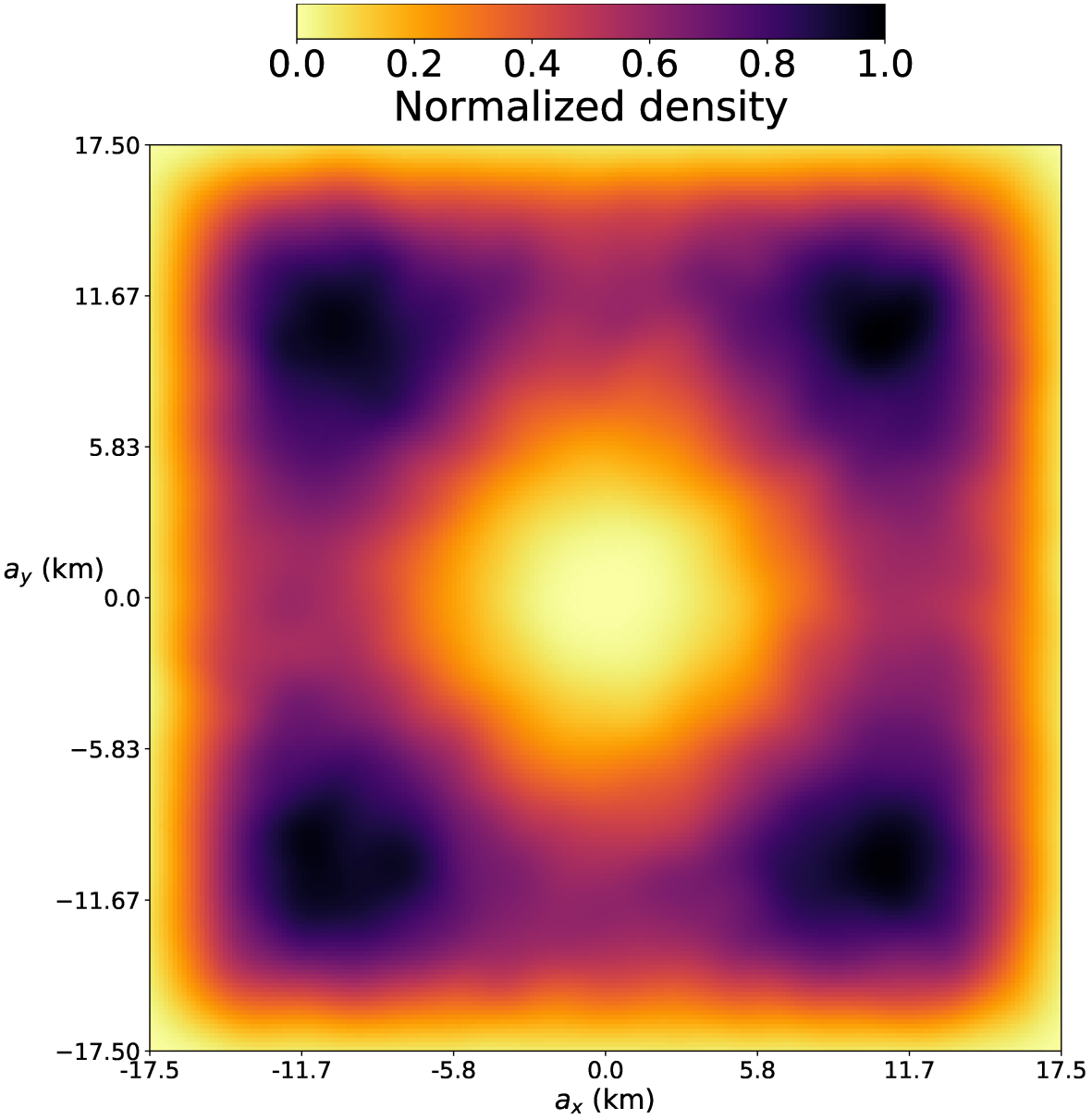

Figure S6: KDE estimate of the 2-D marginal prior pdf for the model pair (a_x, a_y) discussed in subsection 6.2.3.3.

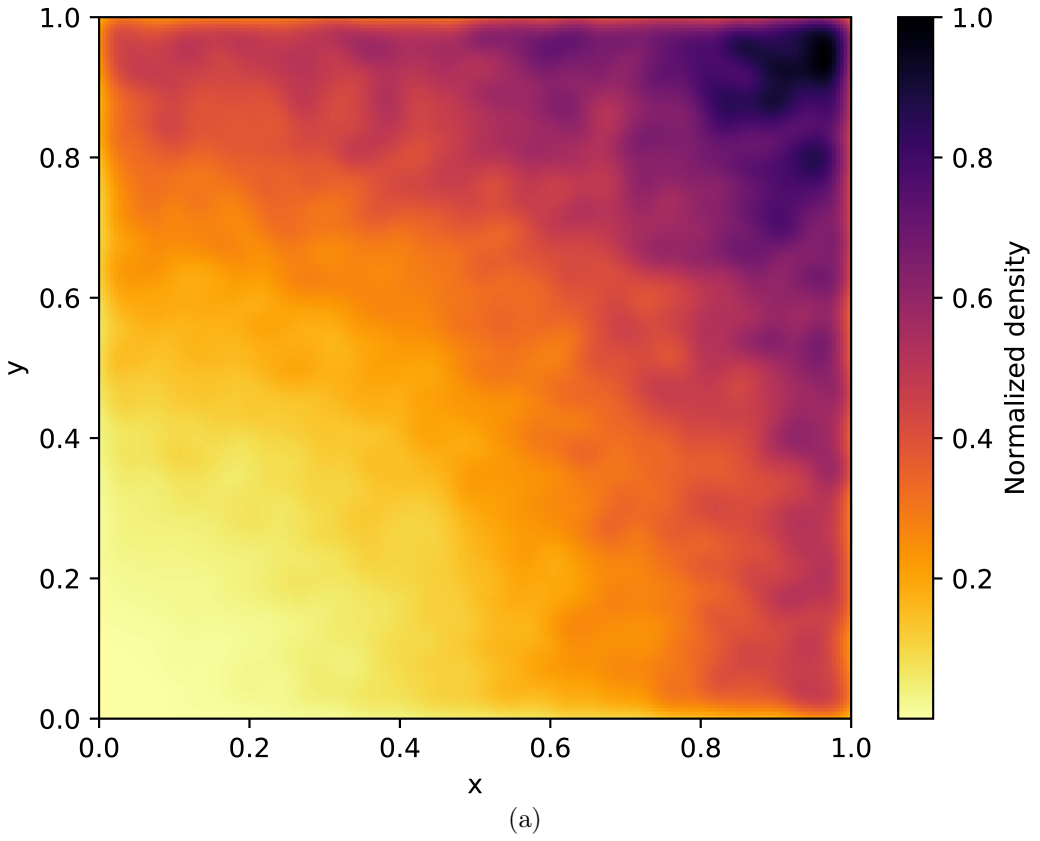

(a)

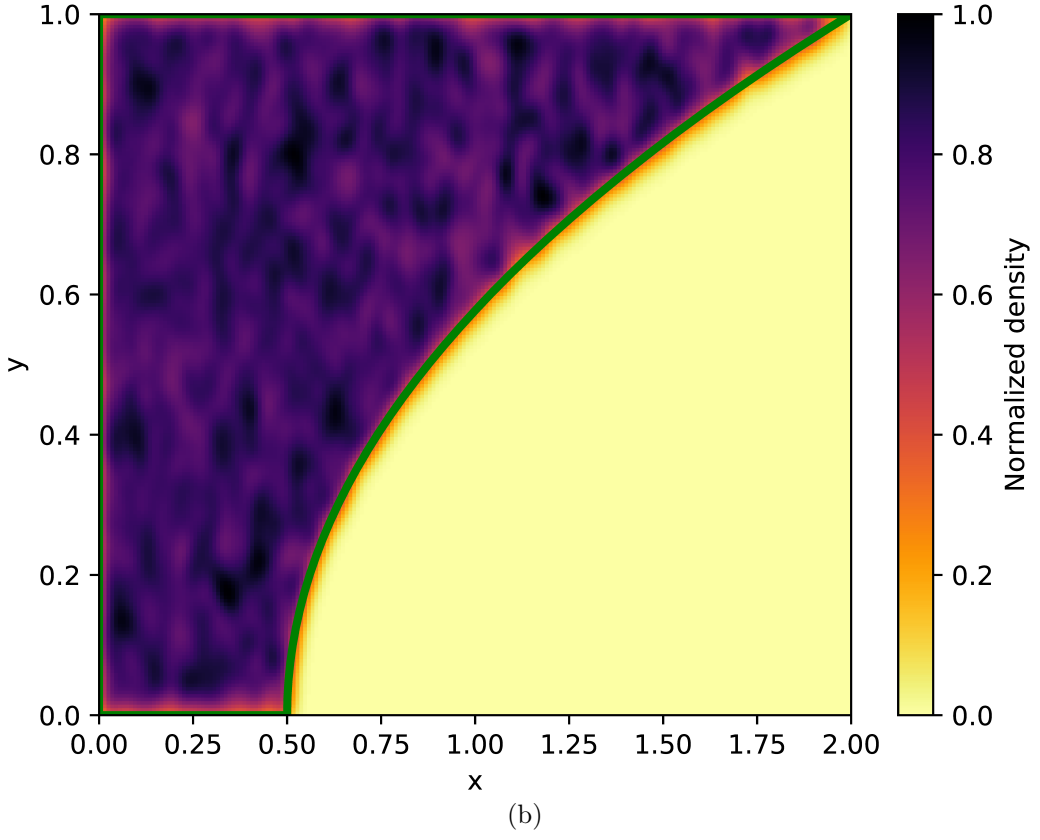

(b)

Figure S7: a) KDE estimate for samples drawn with the ordinary MC algorithm from the pdf $f(x, y) = \frac{3}{2}(x^2 + y^2)$. b) The KDE estimate from the samples in a) transformed according to Eq. (6.30). The support of the latter pdf is bounded by the green curves. Both pdfs are normalized by their maximum values.

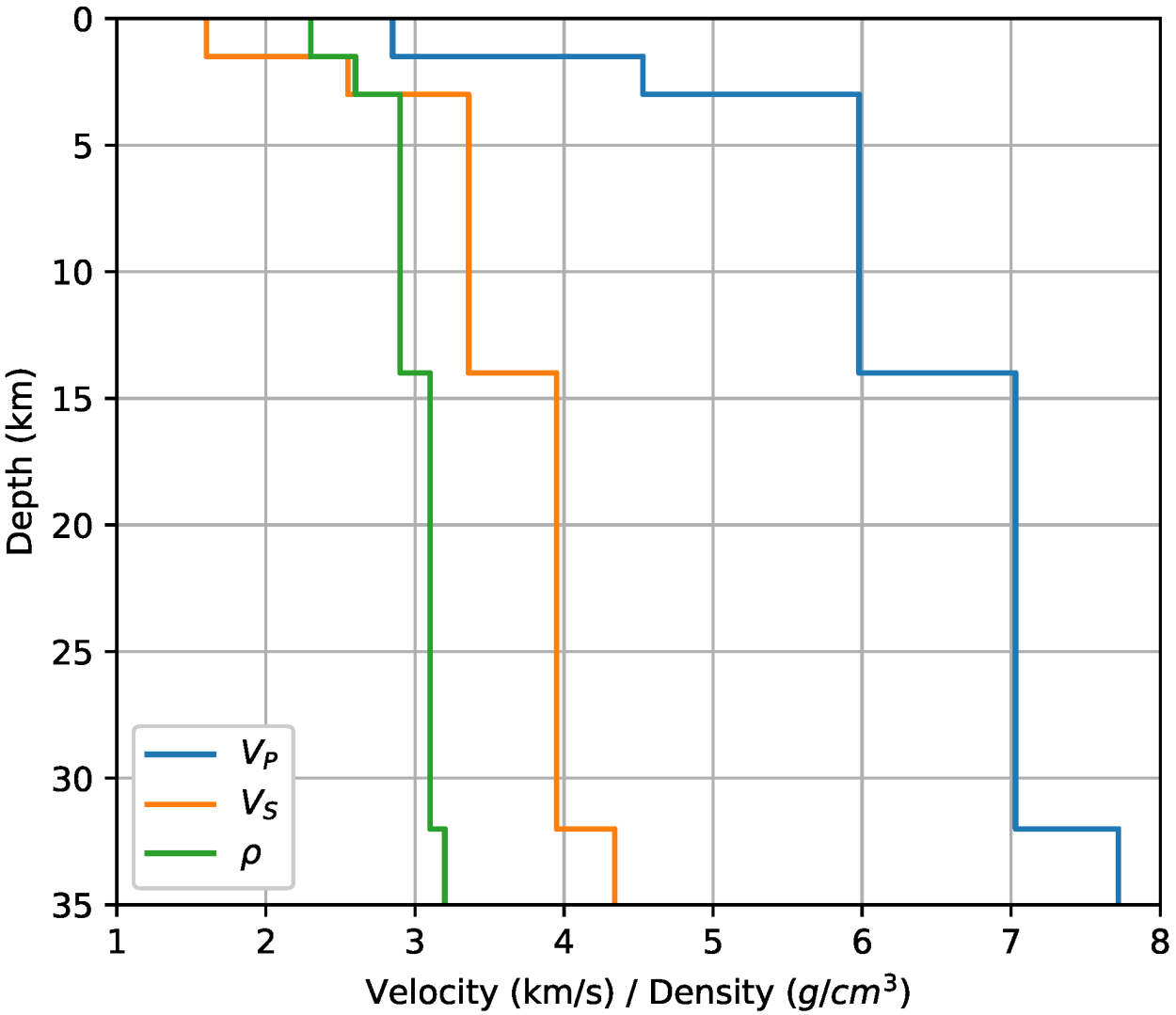

Figure S8: The seismic velocity and mass density model assumed in the inversion adapted from Karagianni et al. (2002) by removing its low-velocity channel. The quality factors are $Q_P = 300$ and $Q_S = 150$ for depths smaller than 32 km. At larger depths, $Q_P = Q_S = 1000$.

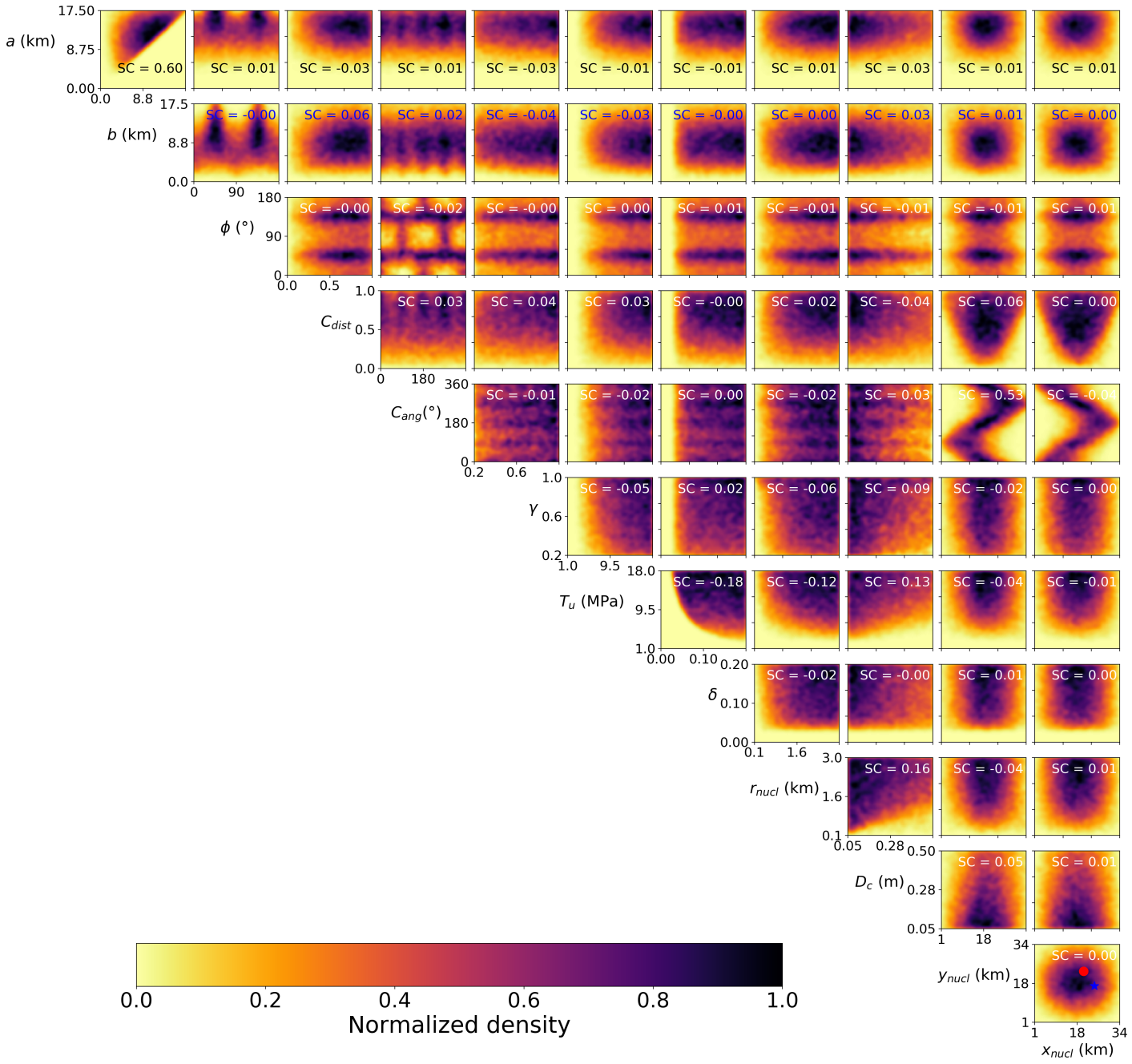

(a) ρ_0

Figure S9: KDE estimates of 2-D marginal posteriors of a) ρ_0 b) ρ_1 c) ρ_2 for pairs of model parameters. The letters SC stand for Spearman's correlation coefficient. The color scale is relative to the maximum value of the distribution in each plot. The blue star and the red circle in the last panel of each figure denote the position of the GI-NOA hypocenter and the centroid inferred by our CMT inversion, respectively.

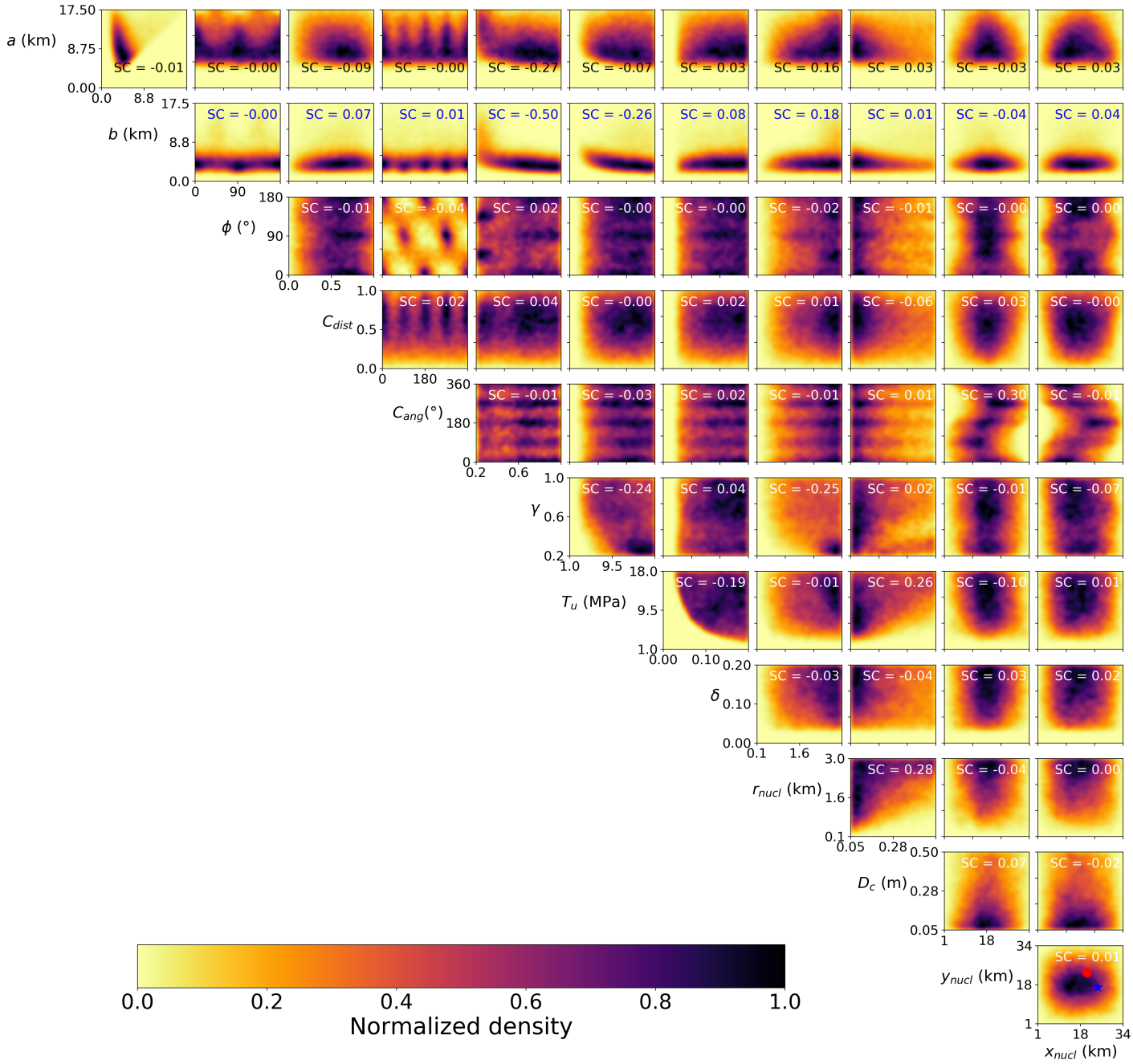

(b) ρ_1

Figure S9

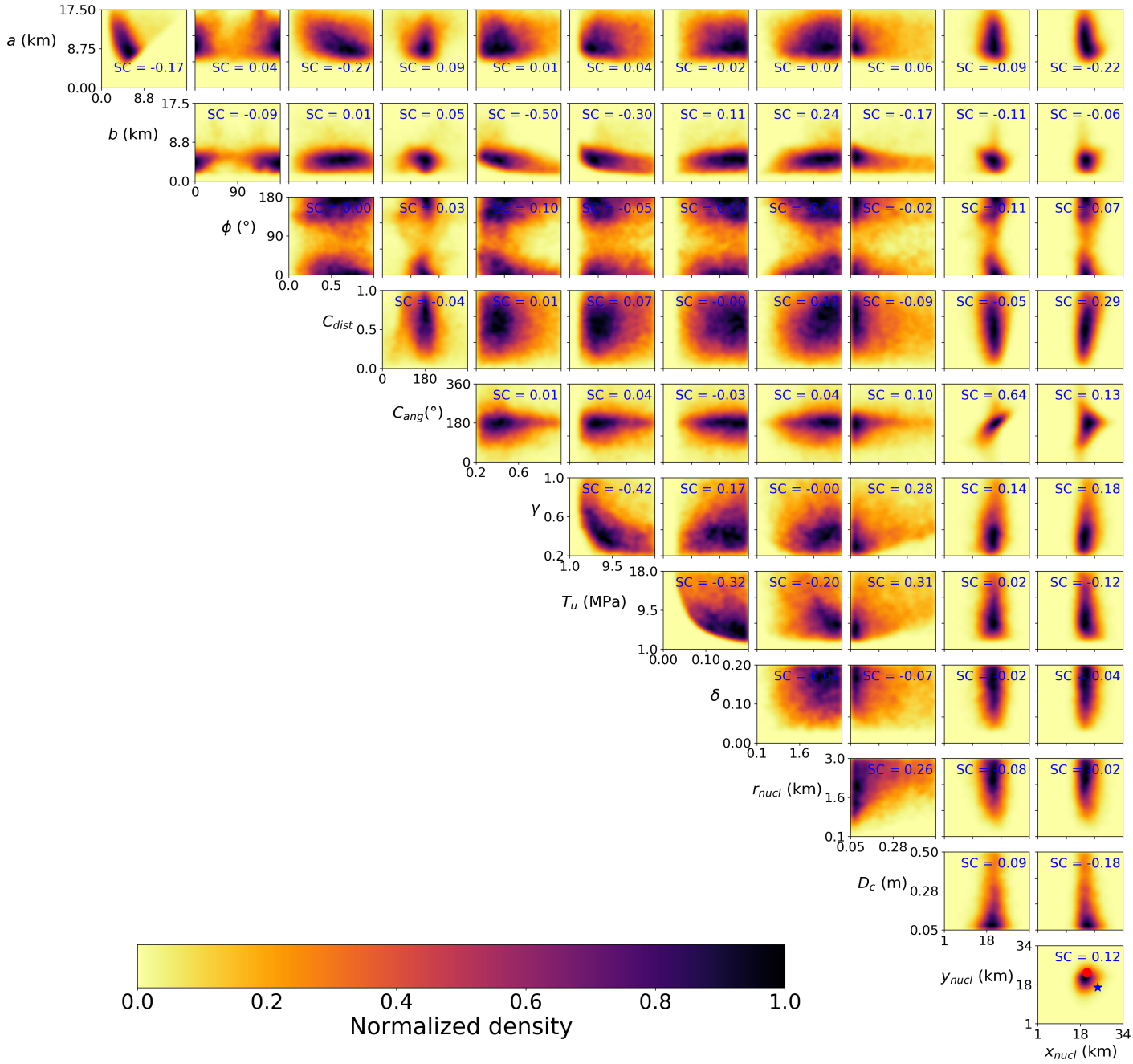

(c) ρ_2

Figure S9

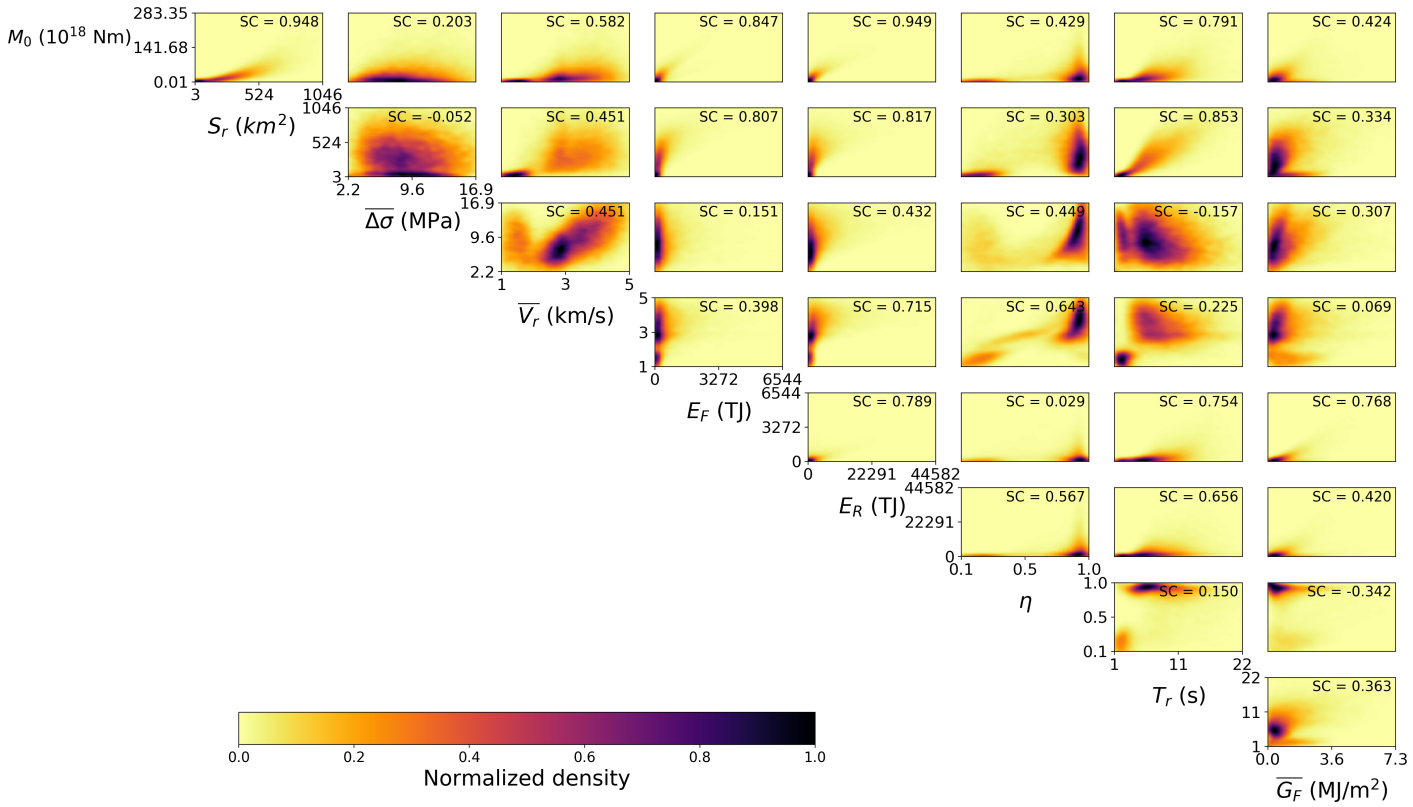

(a) ρ_0

Figure S10: KDE estimates of 2-D marginal posteriors of a) ρ_0 b) ρ_1 c) ρ_2 for pairs of emergent quantities. The letters SC stand for Spearman's correlation coefficient. The color scale is relative to the maximum value of the distribution in each plot.

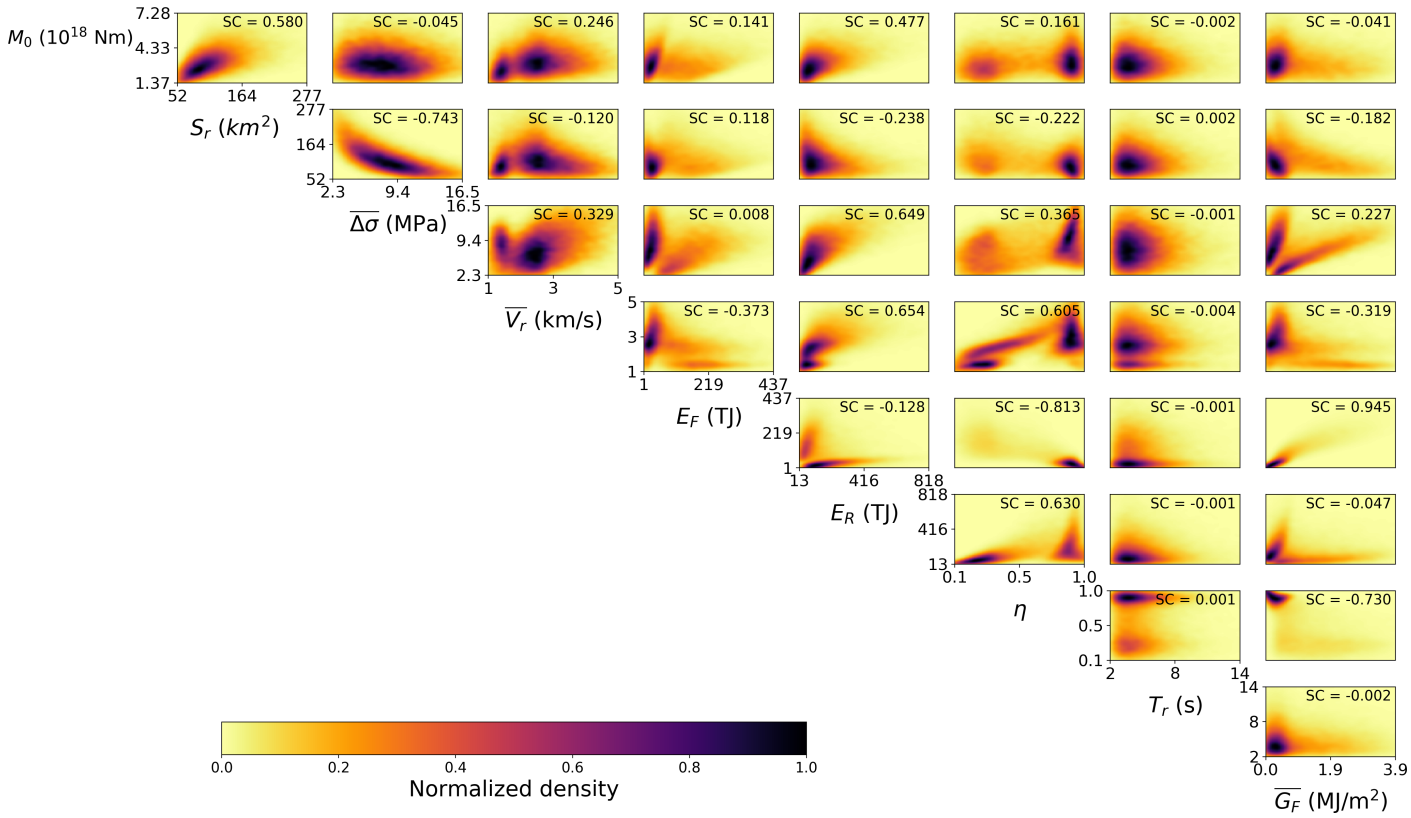

(b) ρ_1

Figure S10

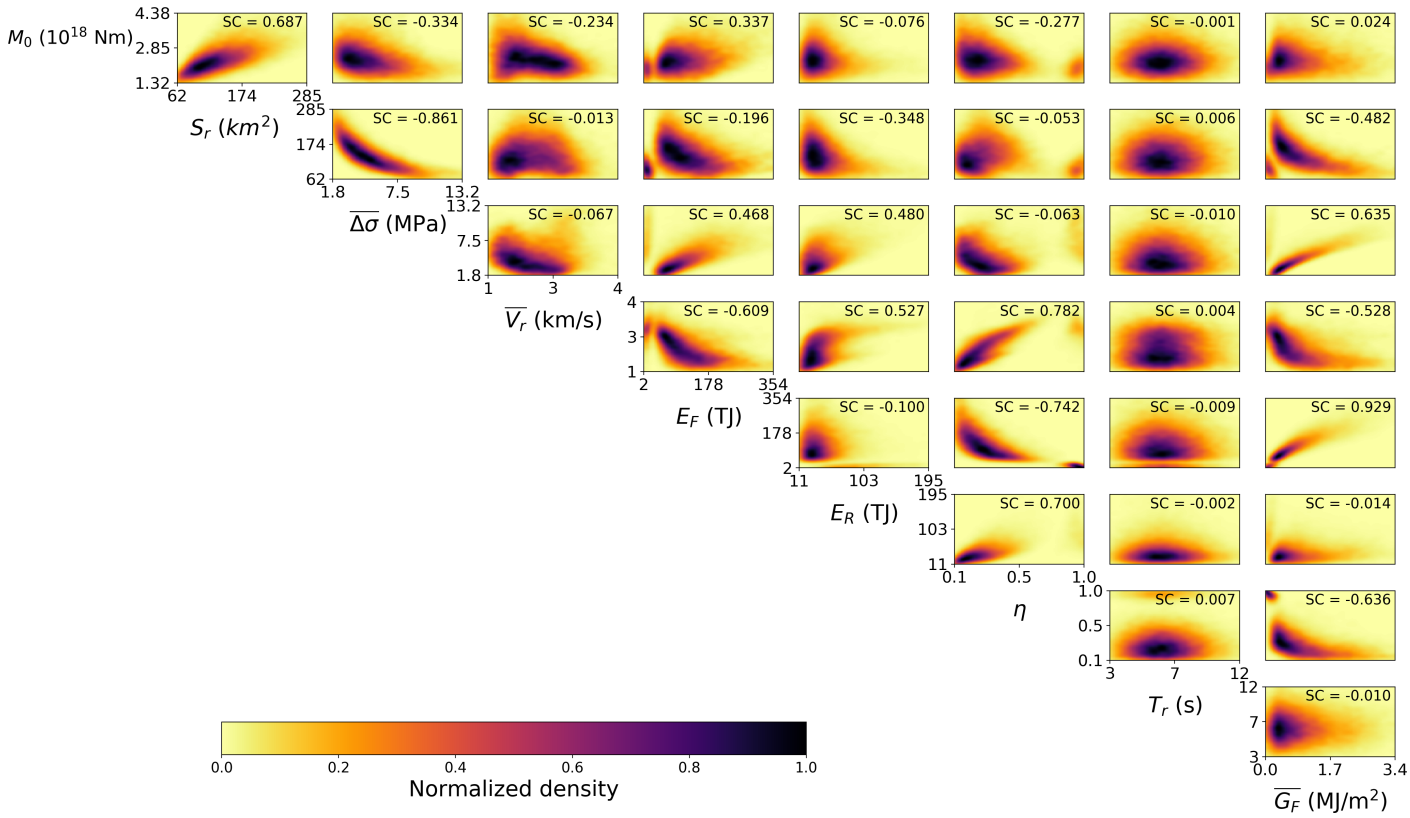

(c) ρ_2

Figure S10

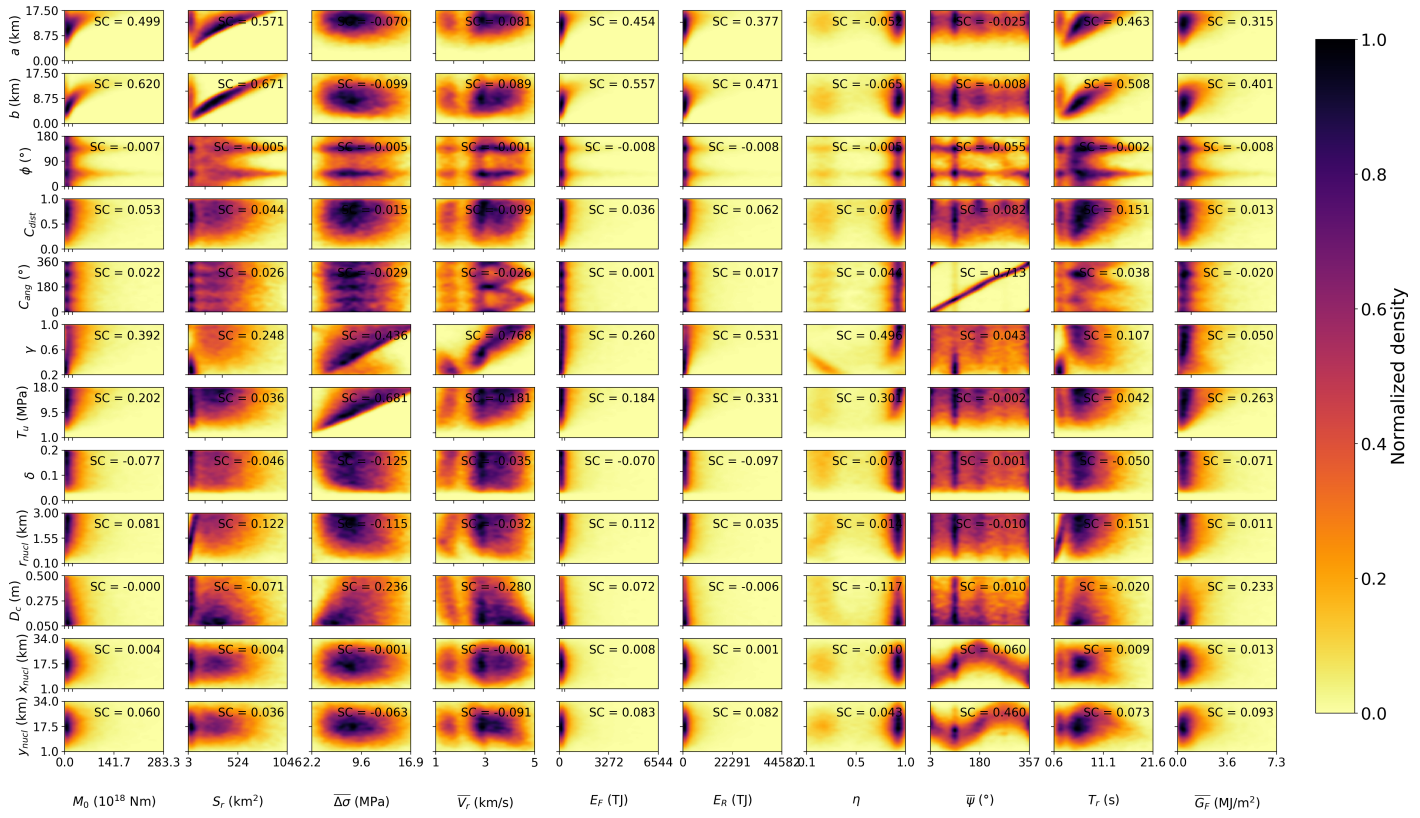

(a) ρ_0

Figure S11: KDE estimates of 2-D marginal posteriors of a) ρ_0 b) ρ_1 c) ρ_2 for pairs of model (vertical axes) and emergent (horizontal axes) quantities. The letters SC stand for Spearman's correlation coefficient. The color scale is relative to the maximum value of the distribution in each plot.

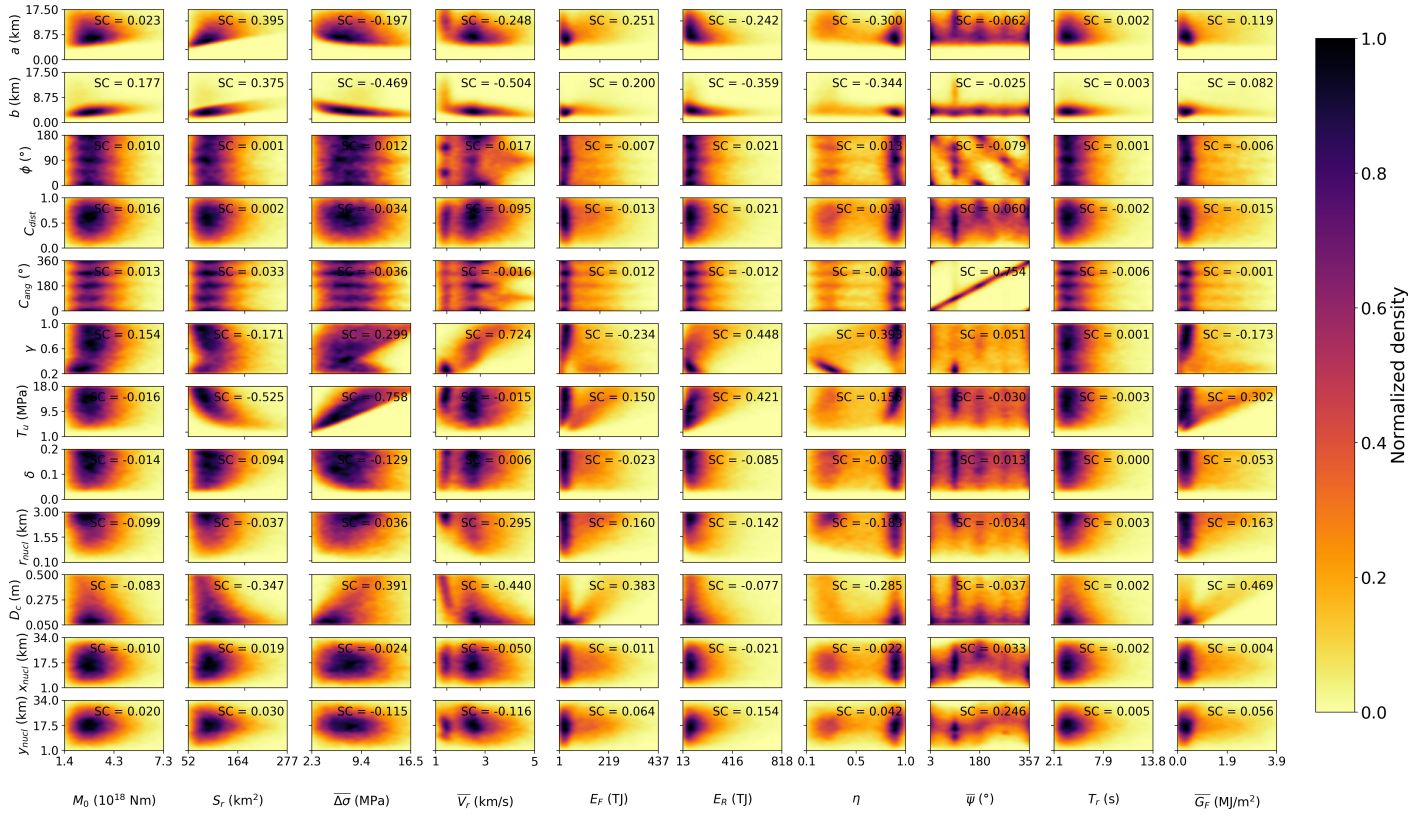

(b) ρ_1

Figure S11

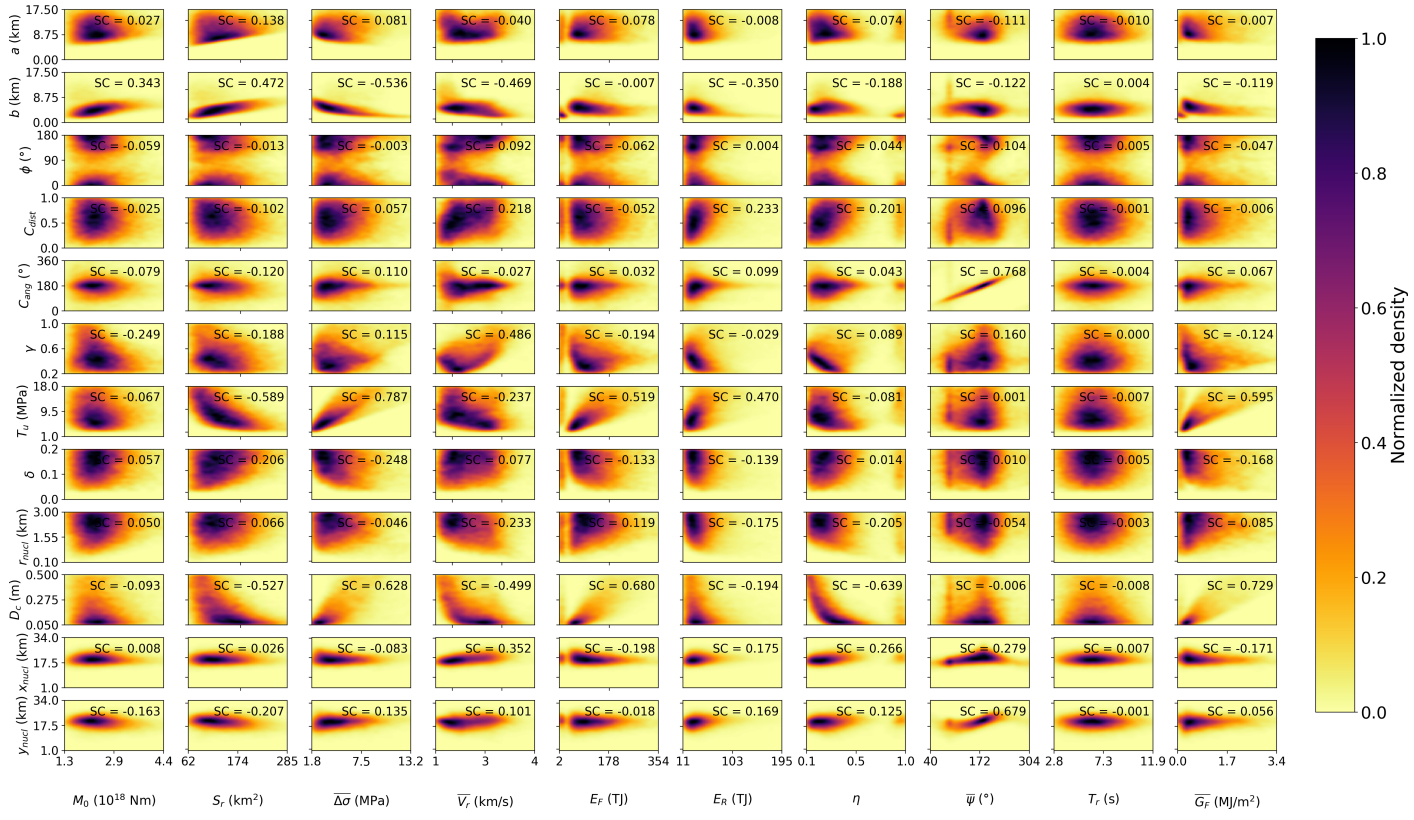

(c) ρ_2

Figure S11

Conclusions

This thesis focuses on dynamic source modeling of tectonic earthquakes. We study the problem at both short (seconds) and long (hundreds of years) time scales. We use the linear slip-weakening law for the former case and the rate-and-state friction law for the latter case.

In chapter 1 we provide a basic review of a fracture mechanical framework suitable for dynamic source modeling. In chapters 2, 3, and 4, we review basic solutions, and their features, for ideally brittle, slip-weakening, and rate-and-state models, respectively, and highlight common features and differences between these models.

In chapter 5, we focus on the influence of externally applied shear stress perturbations during simply periodic seismic cycles on the occurrence time of earthquakes. We examine this problem using the aging version of the rate-and-state law on finite strike-slip faults immersed in a 3-D homogeneous, isotropic elastic half-space, utilizing the quasi-dynamic approximation. We systematically study the dependence of the clock advance (the difference between earthquake occurrence times on the unperturbed and perturbed faults) on the application time of the stress load, its amplitude, and spatial extent, highlighting the importance of slip rate at the time and place of application.

For positive stress perturbations, the clock advance can be both positive and negative, while for negative change, it is only negative (earthquake delay). For a given amplitude and geometry of the stress perturbation, the graph of clock advance vs application time can be divided into three distinct parts (as also seen in previous studies, e.g., Perfettini et al. 2003b; Gallovič 2008; Cho et al. 2009): the static phase, the oscillatory phase, and the instantaneous triggering phase.

During the static phase, which occurs at the beginning of the seismic cycle, the graph is constant, so the clock advance does not depend on the timing of the load. In the instantaneous triggering phase, which occurs near the end of the cycle and only for positive stress perturbations, the perturbation immediately destabilizes the whole fault and triggers an earthquake. In these two phases, the earthquakes following the perturbation are always whole system events,

rupturing the whole fault.

The oscillatory phase, in which the clock advance graph is (non-periodically) increasing and decreasing, occurs in between the two phases. In the majority of the decreasing part of the oscillatory phase, whole system events are launched, as in the other two phases. But in a small portion of the decreasing part and in the increasing part, the earthquakes following the perturbation are only partial ruptures that do not completely release stress on the whole fault. The whole system earthquakes eventually get launched as well, but they are significantly delayed; the duration between large earthquakes may be prolonged by up to 80% when compared to the unperturbed cycles. This occurs even for positive perturbations, which normally tend to advance the upcoming earthquake.

We link this mechanism to the behavior observed on the Parkfield segment of the San-Andreas, California fault. This segment underwent quasi-periodic M_w 6 earthquakes with a mean recurrence time of 22 years and the next M_w 6 earthquake was expected to arrive between 1988 and 1993. Instead, it arrived in 2004, which corresponds to a significant delay. Moreover, the segment experienced a stress perturbation due to the 1983 Coalinga-Nuñez earthquakes and only smaller events (with M_w of at most 4.9) occurred on the segment in the expected period. We reproduce the mechanism described in the previous paragraph on a heterogeneous model of the Parkfield segment, adapted from Barbot et al. (2012), to demonstrate that it could have been responsible for the delay.

In chapter 6, we present a Bayesian dynamic inversion for a 12-parameter elliptic model governed by the slip-weakening law, applied to the 2017 Lesvos M_w 6.3 Earthquake. Beginning with a prior probability density function (pdf) ρ_{pr} on the 12 parameters, we obtain three posterior pdfs by updating the prior with progressively more constraints on the model. To calculate the initial posterior pdf ρ_0, we use the constraint that the model results in a rupture that breaks at least twice the area of the nucleation zone and lasts more than 1 second. This condition removes uninteresting models that produce negligible wave radiation. As ρ_0 does not yet depend on seismic data, it may be understood as a corrected prior pdf. For the second pdf ρ_1, we require that the magnitude produced by the model is close to the value obtained from a prior centroid moment inversion. For the final pdf ρ_2, we add seismic waveforms from fifteen near-regional seismic stations and require that the model produces synthetic waveforms close to the observed ones.

We evaluate correlations and trade-offs of different pairs of parameters by examining their 2-D marginal pdfs. To quantify uncertainties for each parameter, we calculate the sizes of the

highest density region (HDR) of the respective 1-D marginal pdfs. By comparing, for each quantity, the successive 1-D marginal pdfs for the chain $\rho_{pr} \rightarrow \rho_0 \rightarrow \rho_1 \rightarrow \rho_2$, we determine the step at which the quantity becomes the most resolved. We quantify this resolution by comparing the HDR sizes of successive distributions. We also evaluate the mutual dissimilarity of the pdfs by calculating the Hellinger distances between them.

We find that pdfs of some parameters either change only mildly in each update or significantly change only due to the first, minimum rupture, constraint. Therefore, neither the observed moment magnitude nor the waveforms are important for the shape of their final posterior (ρ_2) pdf. These parameters include the size of the nucleation zone, the initial stress (relative to the yield strength) inside the nucleation, the distance of the nucleation zone from the center of the patch, and the characteristic slip-weakening distance.

Pdfs of the dimensions of the patch and the total ruptured area are almost completely determined by adding the magnitude constraint — they changed only negligibly after adding the constraint on seismic waveforms.

Finally, we identify quantities strongly resolved by adding the waveform constraint. From model parameters, these include the location of the hypocenter, its orientation with respect to the center of the patch, and the ratio of the initial stress to the yield strength. From quantities that emerge as results of the simulation, the best resolved was radiated energy, but a good resolution is also seen for the radiation efficiency, the mean angle of rupture propagation, and the slip-weighted average stress drop and rupture speed.

The present study has several limitations which should be addressed in the future. For instance, Gaussian distributions for the observational and modeling observational errors were considered and their joint standard deviation was not based on a thorough analysis (Dettmer et al., 2007; Duputel et al., 2014; Minson et al., 2014; Hallo & Gallovič, 2016). Erring on the side of caution, we set it to a conservative estimate larger than the maximum seismogram amplitude, which could have diluted some of the results. Modeling uncertainties are caused by unknown elastic velocity structure, fault position and geometry, or numerical errors. Observational uncertainties include those of the centroid moment tensor inversion, as well as errors in seismograms. A crude sensitivity analysis of the effect of the standard deviations could be made by repeating the inversion with different values and comparing the results. At the moment, this is difficult for dynamic inversions due to the prohibitive computational cost of forward solvers. The standard deviations could also be incorporated in a hierarchical approach (Sambridge et al., 2013; Mustać & Tkalčić, 2015) as inverted hyper-parameters, with

the uncertainties about their values encoded in their own prior probability density functions.

Another limitation is given by the assumption of the simple elliptic patch model. Even though it probably suffices for the specific application to the Lesvos earthquake, given the utilized low-frequency range of the seismograms, relatively large station distances, and small complexity suggested by the prior moment tensor inversion, more general models should be used for modeling synthetic seismograms at higher frequencies and for more complicated earthquakes. This is not trivial, because increasing the number of free parameters may increase the non-uniqueness of the inversion (manifesting, for example, as correlations among model parameters) and also rapidly compromises our ability to properly sample the whole model space. One route is to consider Bayesian inversion methods with classes of models defined by a variable number of parameters (such as in the trans-dimensional kinematic inversion of Hallo & Gallovič, 2020), balancing the complexity of the model and its ability to fit data.

The analysis was limited to one earthquake and the results cannot naively be generalized to earthquakes with different seismogram frequency ranges and station distributions. Nevertheless, the approach of assessing the roles of various constraints by comparing progressively updated posterior pdfs can be applied to any Bayesian dynamic source inversion. In addition, the calculation of the posterior distributions ρ_0 and ρ_1 did not require seismic waveforms. We propose that similar distributions could be pre-calculated for a wide range of settings (i.e. fault geometry, moment magnitude). Such pre-calculated distributions could then be used as a basis for prior distributions in future Bayesian waveform inversions. As seen in this study, even though the posterior distributions are usually appreciably different from the prior, they are still influenced by it to a large degree. Therefore, such standardized priors would enable greater comparability between studies and better assessments of inversion results.

The rate-and-state and the slip-weakening law could be combined in future inversions. For instance, the initial stress field of a seismic event could be estimated from long-term rate-and-state modeling of the fault or even the whole fault system (Barbot et al., 2012). For example, the earthquake simulator RSQSim (Richards-Dinger & Dieterich, 2012) takes into account all known mutually interacting locked and creeping faults in California governed by the rate-and-state friction and successfully reproduces basic characteristics of the real earthquake catalog. An inversion utilizing the slip-weakening law (which is more efficient than the rate-and-state law for modeling the co-seismic phase of rupture) could then be launched with fixed initial stress given by the long-term modeling, inverting only for frictional parameters, which would allow for faster exploration of the parameter space.

One of the big goals of earthquake physics is to find a constitutive law that governs the entire rupture process, accurate at both small and large values of slip and slip-rate, and suitable for modeling both the co-seismic and the inter-seismic phases in a unified manner. No matter how brilliant the laboratory and theoretical studies proposing new constitutive laws may be, the validity of models based on these laws will ultimately have to be tested against the behavior of tectonic faults. To find parameters of such models, dynamic source inversions will be required. The inversions should utilize not only seismic waveforms from the event but also long-term seismological, geodetic, and morphological data about afterslip and other types of inter-seismic deformation. With advancements in computational capabilities, a great number of dynamic source inversions for different earthquakes could be performed automatically, with only minimal human input, yielding many competing dynamic earthquake source models. These models will in turn produce falsifiable predictions about the evolution of seismicity in the world, which can then be compared against observed data to assess the plausibility of each candidate constitutive law. This will not only advance our understanding of fundamental earthquake physics but, if done in a Bayesian framework, could be naturally incorporated in probabilistic models for seismic forecast and hazard assessment.

List of included publications

1. Kostka & Gallovič (2016): Kostka, F., and Gallovič, F. (2016), Static Coulomb stress load on a three-dimensional rate-and-state fault: Possible explanation of the anomalous delay of the 2004 Parkfield earthquake, J. Geophys. Res. Solid Earth, 121, 3517–3533, doi: 10.1002/2015JB012646.

2. Kostka et al. (2022): Kostka, F., Zahradník, J., Sokos, E. & Gallovič. F. (2022). Assessing the role of selected constraints in Bayesian dynamic source inversion: Application to the 2017 Mw 6.3 Lesvos earthquake, Geophys. J. Int., 228(1), 711–727, doi: 10.1093/gji/ggab359

Bibliography

Abercrombie, R. E. & Rice, J. R., 2005. Can observations of earthquake scaling constrain slip weakening?, *Geophysical Journal International*, **162**(2), 406–424.

Aghababaei, R. & Budzik, M. K., 2020. Fracture modes of brittle junctions under shear, *Extreme Mechanics Letters*, **35**, 100644.

Aharonov, E. & Scholz, C. H., 2018. A physics-based rock friction constitutive law: Steady state friction, *Journal of Geophysical Research: Solid Earth*, **123**(2), 1591–1614.

Aki, K. & Richards, P. G., 2002. *"Quantitative Seismology"*, University Science Books, 2nd edn.

Alava, M., Nukala, P., & Zapperi, S., 2006. Statistical models of fracture, *Advances in Physics*, **55**.

Allison, K. L. & Dunham, E. M., 2018. Earthquake cycle simulations with rate-and-state friction and power-law viscoelasticity, *Tectonophysics*, **733**, 232–256.

Altenbach, H. & Öchsner, A., 2020. *Continuum Damage Mechanics*, Springer Berlin Heidelberg, Berlin, Heidelberg.

Ampuero, J. P. & Ben-Zion, Y., 2008. Cracks, pulses and macroscopic asymmetry of dynamic rupture on a bimaterial interface with velocity-weakening friction, *Geophysical Journal International*, **173**.

Ampuero, J.-P. & Rubin, A. M., 2008. Earthquake nucleation on rate and state faults — Aging and slip laws, *Journal of Geophysical Research: Solid Earth*, **113**(B1).

Anderson, T. L., 2017. *Fracture mechanics: fundamentals and applications*, CRC Press/Taylor & Francis.

Andrews, D. J., 1976a. Rupture velocity of plane strain shear cracks, *Journal of Geophysical Research (1896-1977)*, **81**(32), 5679–5687.

Andrews, D. J., 1976b. Rupture propagation with finite stress in antiplane strain, *Journal of Geophysical Research (1896-1977)*, **81**(20), 3575–3582.

Andrews, D. J., 1985. Dynamic plane-strain shear rupture with a slip-weakening friction law calculated by a boundary integral method, *Bulletin of the Seismological Society of America*, **75**(1), 1–21.

Andrews, D. J., 1994. Dynamic growth of mixed-mode shear cracks, *Bulletin of the Seismological Society of America*, **84**(4), 1184–1198.

Aochi, H. & Matsu'ura, M., 2002. Slip- and time-dependent fault constitutive law and its significance in earthquake generation cycles, *Pure and Applied Geophysics*, **159**, 2029–2044.

Aochi, H. & Ulrich, T., 2015. A probable earthquake scenario near Istanbul determined from dynamic simulations, *Bulletin of the Seismological Society of America*, **105**(3), 1468–1475.

Badea, L., Ionescu, I. R., & Wolf, S., 2004. Domain decomposition method for dynamic faulting under slip-dependent friction, *Journal of Computational Physics*, **201**(2), 487–510.

Bakun, W. H., Aagaard, B., Dost, B., Ellsworth, W. L., Hardebeck, J. L., Harris, R. A., Ji, C., Johnston, M. J. S., Langbein, J., Lienkaemper, J. J., Michael, A. J., Murray, J. R., Nadeau, R. M., Reasenberg, P. A., Reichle, M. S., Roeloffs, E. A., Shakal, A., Simpson, R. W., & Waldhauser, F., 2005. Implications for prediction and hazard assessment from the 2004 Parkfield earthquake, *Nature*, **437**(7061), 969–974.

Barbot, S., 2019. Slow-slip, slow earthquakes, period-two cycles, full and partial ruptures, and deterministic chaos in a single asperity fault, *Tectonophysics*, **768**, 228171.

Barbot, S., Lapusta, N., & Avouac, J.-P., 2012. Under the hood of the earthquake machine: Toward predictive modeling of the seismic cycle, *Science*, **336**(6082), 707–710.

Barenblatt, G., 1959. The formation of equilibrium cracks during brittle fracture. general ideas and hypotheses. axially-symmetric cracks, *Journal of Applied Mathematics and Mechanics*, **23**(3), 622–636.

Barenblatt, G., 1962. The mathematical theory of equilibrium cracks in brittle fracture, vol. 7 of **Advances in Applied Mechanics**, pp. 55–129, eds Dryden, H., von Kármán, T., Kuerti, G., van den Dungen, F., & Howarth, L., Elsevier.

Barenblatt, G. & Cherepanov, G., 1960. On the wedging of brittle bodies, *Journal of Applied Mathematics and Mechanics*, **24**(4), 993–1015.

Barenblatt, G. I., 2003. *Scaling*, Cambridge Texts in Applied Mathematics, Cambridge University Press.

Basili, R., Kastelic, V., Demircioglu, M., B., Garcia, Moreno, D., Nemser, E., S., Petricca, P., Sboras, S., P., Besana-Ostman, G., M., Cabral, J., Camelbeeck, T., Caputo, R., Danciu, L., Domac, H., Fonseca, J., García-Mayordomo, J., Giardini, D., Glavatovic, B., Gulen, L., Ince, Y., Pavlides, S., Sesetyan, K., Tarabusi, G., Tiberti, M., M., Utkucu, M., Valensise, G., Vanneste, K., Vilanova, S., & Wössner, J., 2013. The European Database of Seismogenic Faults (EDSF) compiled in the framework of the project SHARE, *http://diss.rm.ingv.it/share-edsf/, doi: 10.6092/INGV.IT-SHARE-EDSF*.

Bedford, A., 1985. *Hamilton's Principle in Continuum Mechanics*, Chapman & Hall/CRC research notes in mathematics series, Pitman Advanced Publishing Program.

Beeler, N. M., Tullis, T. E., & Weeks, J. D., 1994. The roles of time and displacement in the evolution effect in rock friction, *Geophysical Research Letters*, **21**, 1987–1990.

Beeler, N. M., Tullis, T. E., & Goldsby, D. L., 2008. Constitutive relationships and physical basis of fault strength due to flash heating, *Journal of Geophysical Research: Solid Earth*, **113**(B1).

Beléndez, A., Pascual, C., Méndez, D., Beléndez, T., & Neipp, C., 2007. Exact solution for the nonlinear pendulum, *Revista Brasileira de Ensino de Física*, **29**(4), 645–648.

Ben-Zion, Y., Rice, J. R., & Dmowska, R., 1993. Interaction of the san andreas fault creeping segment with adjacent great rupture zones and earthquake recurrence at parkfield, *Journal of Geophysical Research: Solid Earth*, **98**(B2), 2135–2144.

Berenger, J.-P., 1994. A perfectly matched layer for the absorption of electromagnetic waves, *Journal of Computational Physics*, **114**(2), 185–200.

Bhattacharya, P., Rubin, A. M., Bayart, E., Savage, H. M., & Marone, C., 2015. Critical evaluation of state evolution laws in rate and state friction: Fitting large velocity steps in simulated fault gouge with time-, slip-, and stress-dependent constitutive laws, *Journal of Geophysical Research*, **120**, 6365–6385.

Biswas, S., Ray, P., & Chakrabarti, B., 2015. *Statistical Physics of Fracture, Breakdown, and Earthquake: Effects of Disorder and Heterogeneity*.

Bizzarri, A., 2010. How to promote earthquake ruptures: Different nucleation strategies in a dynamic model with slip-weakening friction, *Bulletin of The Seismological Society of America*, **100**.

Bizzarri, A., 2011. On the deterministic description of earthquakes, *Reviews of Geophysics*, **49**(3).

Bizzarri, A., 2012. Modeling repeated slip failures on faults governed by slip-weakening friction, *The Bulletin of the Seismological Society of America*, **102**, 812–821.

Bizzarri, A., 2014. Rake rotation introduces ambiguity in the formulation of slip-dependent constitutive models: slip modulus or slip path?, *Annals of Geophysics*, **57**, 0547.

Bizzarri, A. & Cocco, M., 2003. Slip-weakening behavior during the propagation of dynamic ruptures obeying rate- and state-dependent friction laws, *Journal of Geophysical Research*, **108**.

Bizzarri, A. & Cocco, M., 2005. 3D dynamic simulations of spontaneous rupture propagation governed by different constitutive laws with rake rotation allowed, *Annals of Geophysics*, **48**.

Bizzarri, A. & Das, S., 2012. Mechanics of 3-D shear cracks between Rayleigh and shear wave rupture speeds, *Earth and Planetary Science Letters*, **357-358**, 397–404.

Bizzarri, A., Cocco, M., Andrews, D. J., & Boschi, E., 2001. Solving the dynamic rupture problem with different numerical approaches and constitutive laws, *Geophysical Journal International*, **144**(3), 656–678.

Bohloli, B., Soldal, M., Smith, H., Skurtveit, E., Choi, J. C., & Sauvin, G., 2020. Frictional Properties and Seismogenic Potential of Caprock Shales, *Energies*, **13**(23).

Bouchard, P.-O., Bay, F., & Chastel, Y., 2003. Numerical modelling of crack propagation: Automatic remeshing and comparison of different criteria, *Computer Methods in Applied Mechanics and Engineering*, **192**, 3887–3908.

Bourdin, B., Francfort, G., & Marigo, J.-J., 2008. The variational approach to fracture, *Journal of Elasticity*, **91**, 5–148.

Brace, W. F. & Byerlee, J. D., 1966. Stick-slip as a mechanism for earthquakes, *Science*, **153**(3739), 990–992.

Broberg, K., 1960. The propagation of a brittle crack, *Arkiv Fysik*, **18**(2), 159–92.

Broberg, K. B., 1989. The near-tip field at high crack velocities, *International Journal of Fracture*, **39**(1-3), 1–13.

Broberg, K. B., 1994. Intersonic Bilateral Slip, *Geophysical Journal International*, **119**(3), 706–714.

Broberg, K. B., 1996. How fast can a crack go?, *Materials Science*, **32**(1), 80–86.

Broberg, K. B., 1998. Crack expanding with constant velocity in an anisotropic solid under anti-plane strain, *International Journal of Fracture*, **93**(1), 1–12.

Broberg, K. B., 1999. *Cracks and Fracture*, Academic Press, San Diego.

Brochard, L., Tejada, I., & Sab, K., 2016. From yield to fracture, failure initiation captured by molecular simulation, *Journal of the Mechanics and Physics of Solids*, **95**.

Burjánek, J. & Zahradník, J., 2007. Dynamic stress field of a kinematic earthquake source model with k-squared slip distribution, *Geophysical Journal International*, **171**(3), 1082–1097.

Burridge, R., 1973. Admissible Speeds for Plane-Strain Self-Similar Shear Cracks with Friction but Lacking Cohesion, *Geophysical Journal International*, **35**(4), 439–455.

Burridge, R. & Knopoff, L., 1967. Model and theoretical seismicity, *Bulletin of the Seismological Society of America*, **57**(3), 341–371.

Burridge, R. & Willis, J. R., 1969. The self-similar problem of the expanding elliptical crack in an anisotropic solid, *Mathematical Proceedings of the Cambridge Philosophical Society*, **66**(2), 443–468.

Burridge, R., Conn, G., & Freund, L. B., 1979. The stability of a rapid mode ii shear crack with finite cohesive traction, *Journal of Geophysical Research: Solid Earth*, **84**(B5), 2210–2222.

Byerlee, J. D., 1967. Theory of friction based on brittle fracture, *Journal of Applied Physics*, **38**(7), 2928–2934.

Campillo, M. & Ionescu, I. R., 1997. Initiation of antiplane shear instability under slip dependent friction, *Journal of Geophysical Research: Solid Earth*, **102**(B9), 20363–20371.

Castellaro, S. & Mulargia, F., 2001. A simple but effective cellular automaton for earthquakes, *Geophysical Journal International*, **144**(3), 609–624.

Cattania, C., 2019. Complex earthquake sequences on simple faults, *Geophysical Research Letters*, **46**(17-18), 10384–10393.

Cattania, C. & Segall, P., 2019. Crack models of repeating earthquakes predict observed moment-recurrence scaling, *Journal of Geophysical Research: Solid Earth*, **124**(1), 476–503.

Cattania, C., Hainzl, S., Wang, L., Enescu, B., & Roth, F., 2015. Aftershock triggering by postseismic stresses: A study based on coulomb rate-and-state models, *Journal of Geophysical Research: Solid Earth*, **120**(4), 2388–2407.

Chatzipetros, A., Kiratzi, A., Sboras, S., Zouros, N., & Pavlides, S., 2013. Active faulting in the north-eastern Aegean Sea Islands, *Tectonophysics*, **597-598**, 106–122.

Chen, J. & Spiers, C. J., 2016. Rate and state frictional and healing behavior of carbonate fault gouge explained using microphysical model, *Journal of Geophysical Research: Solid Earth*, **121**(12), 8642–8665.

Chen, T. & Lapusta, N., 2009. Scaling of small repeating earthquakes explained by interaction of seismic and aseismic slip in a rate and state fault model, *Journal of Geophysical Research: Solid Earth*, **114**(B1).

Chen, X. & Zhang, H., 2006. Modelling Rupture Dynamics of a Planar Fault in 3-D Half Space by Boundary Integral Equation Method: An Overview, *Pure and Applied Geophysics*, **163**(2), 267–299.

Cho, I., Tada, T., & Kuwahara, Y., 2009. Stress triggering of large earthquakes complicated by transient aseismic slip episodes, *Journal of Geophysical Research: Solid Earth*, **114**(B7).

Chousianitis, K. & Konca, A. O., 2018. Coseismic Slip Distribution of the 12 June 2017 Mw = 6.3 Lesvos Earthquake and Imparted Static Stress Changes to the Neighboring Crust, *Journal of Geophysical Research: Solid Earth*, **123**(10), 8926–8936.

Cocco, M. & Bizzarri, A., 2002. On the slip-weakening behavior of rate- and state dependent constitutive laws, *Geophysical Research Letters*, **29**(11).

Cochard, A. & Madariaga, R., 1994. Dynamic faulting under rate-dependent friction, *pure and applied geophysics*, **142**, 419–445.

Console, R., Murru, M., & Falcone, G., 2009. Perturbation of earthquake probability for interacting faults by static coulomb stress changes, *Journal of Seismology*, **14**(1).

Corish, S. M., Bradley, C. R., & Olsen, K. B., 2007. Assessment of a nonlinear dynamic rupture inversion technique applied to a synthetic earthquake, *Bulletin of the Seismological Society of America*, **97**(3), 901–914.

Cotton, F. & Coutant, O., 1997. Dynamic stress variations due to shear faults in a plane-layered medium, *Geophysical Journal International*, **128**(3), 676–688.

Craggs, J., 1960. On the propagation of a crack in an elastic-brittle material, *Journal of the Mechanics and Physics of Solids*, **8**(1), 66–75.

Dahlen, F. A., 1972. Elastic Dislocation Theory for a Self-Gravitating Elastic Configuration with an Initial Static Stress Field, *Geophysical Journal International*, **28**(4), 357–383.

Dalguer, L. A. & Day, S. M., 2007. Staggered-grid split-node method for spontaneous rupture simulation, *Journal of Geophysical Research: Solid Earth*, **112**(B2).

Das, S., 2003. Dynamic fracture mechanics in the study of the earthquake rupturing process: theory and observation, *Journal of the Mechanics and Physics of Solids*, **51**(11), 1939 –

1955, Proceedings of a Symposium on Dynamic Failure and Thin Film Mechanics, honoring Professor L.B. Freund.

Das, S. & Aki, K., 1977. A numerical study of two-dimensional rupture propagation, *Geophysical Journal of the Royal Astronomical Society*, **50**, 643 – 668.

Dascalu, C., Ionescu, I. R., & Campillo, M., 2000. Fault finiteness and initiation of dynamic shear instability, *Earth and Planetary Science Letters*, **177**(3), 163–176.

Daub, E. & Carlson, J., 2008. A constitutive model for fault gouge deformation in dynamic rupture simulations, *Journal of Geophysical Research*, **113**.

Davies, G. E., Davies, G., & Oates, J., 1994. *Colobine Monkeys: Their Ecology, Behaviour and Evolution*, Cambridge University Press.

Day, S. M., 1982. "Three-dimensional simulation of spontaneous rupture: The effect of nonuniform prestress", *Bulletin of the Seismological Society of America*, **72**(6A), 1881–1902.

Day, S. M., Dalguer, L. A., Lapusta, N., & Liu, Y., 2005. Comparison of finite difference and boundary integral solutions to three-dimensional spontaneous rupture, *Journal of Geophysical Research: Solid Earth*, **110**(B12).

De Arcangelis, L., Redner, S., & Herrmann, H., 1985. A random fuse model for breaking processes, *http://dx.doi.org/10.1051/jphyslet:019850046013058500* , **46**.

Dettmer, J., Dosso, S. E., & Holland, C. W., 2007. Uncertainty estimation in seismo-acoustic reflection travel time inversion, *The Journal of the Acoustical Society of America*, **122**(1), 161–176.

Di Carli, S., François-Holden, C., Peyrat, S., & Madariaga, R., 2010. Dynamic inversion of the 2000 tottori earthquake based on elliptical subfault approximations, *Journal of Geophysical Research: Solid Earth*, **115**(B12).

Di Toro, G., Han, R., Hirose, T., Paola, N., Nielsen, S., Mizoguchi, K., Ferri, F., Cocco, M., & Shimamoto, T., 2011. Fault lubrication during earthquakes, *Nature*, **471**, 494–498.

Dieterich, J. H., 1972. Time-dependent friction in rocks, *Journal of Geophysical Research*, **77**(20), 3690–3697.

Dieterich, J. H., 1979. Modeling of rock friction: 1. experimental results and constitutive equations, *Journal of Geophysical Research: Solid Earth*, **84**(B5), 2161–2168.

Dieterich, J. H., 1988. Probability of earthquake recurrence with nonuniform stress rates and time-dependent failure, *pure and applied geophysics*, **126**(2), 589–617.

Dieterich, J. H., 1992. Earthquake nucleation on faults with rate-and state-dependent strength, *Tectonophysics*, **211**, 0–134.

Dieterich, J. H. & Kilgore, B. D., 1994. Direct observation of frictional contacts: New insights for state-dependent properties, *Pure and Applied Geophysics PAGEOPH*, **143**(1-3), 283–302.

Dieterich, J. H. & Richards-Dinger, K. B., 2010. Earthquake recurrence in simulated fault systems, *Pure and Applied Geophysics*, **167**(8-9), 1087–1104.

Dugdale, D., 1960. Yielding of steel sheets containing slits, *Journal of the Mechanics and Physics of Solids*, **8**(2), 100 – 104.

Dunham, E., 2007. Conditions governing the occurrence of supershear rupture under slip weakening friction, *Journal of Geophysical Research*, **112**.

Dunham, E. M., Favreau, P., & Carlson, J. M., 2003. A supershear transition mechanism for cracks, *Science*, **299**(5612), 1557–1559.

Dunham, E. M., Belanger, D., Cong, L., & Kozdon, J. E., 2011. Earthquake Ruptures with Strongly Rate-Weakening Friction and Off-Fault Plasticity, Part 1: Planar Faults, *Bulletin of the Seismological Society of America*, **101**(5), 2296–2307.

Duputel, Z., Agram, P. S., Simons, M., Minson, S. E., & Beck, J. L., 2014. Accounting for prediction uncertainty when inferring subsurface fault slip, *Geophysical Journal International*, **197**(1), 464–482.

Díaz-Mojica, J., Cruz-Atienza, V. M., Madariaga, R., Singh, S. K., Tago, J., & Iglesias, A., 2014. Dynamic source inversion of the m6.5 intermediate-depth zumpango earthquake in central mexico: A parallel genetic algorithm, *Journal of Geophysical Research: Solid Earth*, **119**(10), 7768–7785.

Elmer, F.-J., 1997. Nonlinear dynamics of dry friction, **30**(17), 6057–6063.

Erdogan, F. & Sih, G., 1963. On the crack extension in plates under plane loading and transverse shear, *Journal of Basic Engineering*, **85**, 519–525.

Erickson, B., Birnir, B., & Lavallée, D., 2008. A model for aperiodicity in earthquakes, *Nonlinear Processes in Geophysics*, **15**(1), 1–12.

Erickson, B., Dunham, E., & Khosravifar, A., 2017. A finite difference method for off-fault plasticity throughout the earthquake cycle, *Journal of the Mechanics and Physics of Solids*, **109**.

Eshelby, J. D., 1957. The determination of the elastic field of an ellipsoidal inclusion, and related problems, *Proceedings of the Royal Society of London. Series A. Mathematical and Physical Sciences*, **241**(1226), 376–396.

Eshelby, J. D., 1963. The Distribution of Dislocations in an Elliptical Glide Zone, *Physica Status Solidi (b)*, **3**(11), 2057–2060.

Eshelby, J. D., 1969. The elastic field of a crack extending non-uniformly under general anti-plane loading, *Journal of Mechanics Physics of Solids*, **17**(3), 177–199.

Favreau, P., Campillo, M., & Ionescu, I. R., 1999. Initiation of in-plane shear instability under slip-dependent friction, *Bulletin of the Seismological Society of America*, **89**(5), 1280–1295.

Favreau, P., Campillo, M., & Ionescu, I. R., 2002. Initiation of shear instability in three-dimensional elastodynamics, *Journal of Geophysical Research: Solid Earth*, **107**(B7).

Festa, G. & Vilotte, J.-P., 2006. Influence of the rupture initiation on the intersonic transition: Crack-like versus pulse-like modes, *Geophysical Research Letters*, **33**(15).

Fialko, Y., 2007. Fracture and Frictional Mechanics – Theory, in *Treatise on Geophysics*, vol. 4, Elsevier.

Fossum, A. F. & Freund, L. B., 1975. Nonuniformly moving shear crack model of a shallow focus earthquake mechanism, *Journal of Geophysical Research*, **80**, 3343–3347.

Francfort, G. & Marigo, J.-J., 1998. Revisiting brittle fracture as an energy minimization problem, *Journal of The Mechanics and Physics of Solids*, **46**.

Freed, A. M., 2005. Earthquake triggering by static, dynamic, and postseismic stress transfer, *Annual Review of Earth and Planetary Sciences*, **33**(1), 335–367.

Freund, L. B., 1979. The mechanics of dynamic shear crack propagation, *Journal of Geophysical Research: Solid Earth*, **84**(B5), 2199–2209.

Freund, L. B., 1990. *Dynamic Fracture Mechanics*, Cambridge Monographs on Mechanics, Cambridge University Press.

Freund, L. B. & Clifton, R. J., 1974. On the uniqueness of plane elastodynamic solutions for running cracks, *Journal of Elasticity*, **4**(4), 293–299.

Fukuyama, E. & Mikumo, T., 1993. Dynamic rupture analysis: Inversion for the source process of the 1990 Izu-Oshima, Japan, earthquake (M = 6.5), *Journal of Geophysical Research: Solid Earth*, **98**(B4), 6529–6542.

Fukuyama, E., Xu, S., Yamashita, F., & Mizoguchi, K., 2016. Cohesive zone length of metagabbro at supershear rupture velocity, *Journal of Seismology*, **20**(4), 1207–1215.

Gabriel, A.-A., Ampuero, J.-P., Dalguer, L. A., & Mai, P. M., 2012. The transition of dynamic rupture styles in elastic media under velocity-weakening friction, *Journal of Geophysical Research: Solid Earth*, **117**(B9).

Gabriel, A.-A., Li, D., Chiocchetti, S., Tavelli, M., Peshkov, I., Romenski, E., & Dumbser, M., 2021. A unified first-order hyperbolic model for nonlinear dynamic rupture processes in diffuse fracture zones, *Philosophical Transactions of the Royal Society A: Mathematical, Physical and Engineering Sciences*, **379**(2196), 20200130.

Galis, M., Pelties, C., Kristek, J., Moczo, P., Ampuero, J.-P., & Mai, P. M., 2015. On the initiation of sustained slip-weakening ruptures by localized stresses, *Geophysical Journal International*, **200**(2), 890–909.

Galis, M., Ampuero, J.-P., Mai, P. M., & Kristek, J., 2019. Initiation and arrest of earthquake ruptures due to elongated overstressed regions, *Geophysical Journal International*, **217**(3), 1783–1797.

Gallovič, F., 2008. Heterogeneous coulomb stress perturbation during earthquake cycles in a 3d rate-and-state fault model, *Geophysical Research Letters*, **35**(21).

Gallovič, F., Valentová, L., Ampuero, J.-P., & Gabriel, A.-A., 2019a. Bayesian dynamic finite-fault inversion: 1. Method and synthetic test, *Journal of Geophysical Research: Solid Earth*, **124**(7), 6949–6969.

Gallovič, F., Valentová, L., Ampuero, J.-P., & Gabriel, A.-A., 2019b. Bayesian Dynamic Finite-Fault Inversion: 2. Application to the 2016 Mw 6.2 Amatrice, Italy, earthquake, *Journal of Geophysical Research: Solid Earth*, **124**(7), 6970–6988.

Gallovič, F., Zahradník, J., Plicka, V., Sokos, E., Evangelidis, C., Fountoulakis, I., & Turhan, F., 2020. Complex rupture dynamics on an immature fault during the 2020 Mw 6.8 Elazığ earthquake, Turkey, *Communications Earth Environment*, **1**(1), 40.

Ganas, A., Oikonomou, I., & Tsimi, C., 2013. Noafaults: a digital database for active faults in greece, *Bull. Geol. Soc. Greece*, **47**, 518–530.

Gao, H., 1988. Nearly circular shear mode cracks, *International Journal of Solids and Structures*, **24**, 177–193.

Gdoutos, E., 1990. Fracture Mechanics Criteria and Applications, Engineering Application of Fracture Mechanics, Springer, Dordrecht.

Gelman, A., Carlin, J. B., Stern, H. S., & Rubin, D. B., 2004. *Bayesian Data Analysis*, Chapman and Hall/CRC, 2nd edn.

Geubelle, P. & Kubair, D., 2001. Intersonic crack propagation in homogeneous media under shear-dominated loading: numerical analysis, *Journal of the Mechanics and Physics of Solids*, **49**(3), 571–587.

Geubelle, P. H. & Rice, J. R., 1995. A spectral method for three-dimensional elastodynamic fracture problems, *Journal of the Mechanics and Physics of Solids*, **43**(11), 1791–1824.

Gobron, S. & Chiba, N., 2001. Crack pattern simulation based on 3d surface cellular automata, *The Visual Computer*, **17**, 287–309.

Goldsby, D. L. & Tullis, T. E., 2011. Flash heating leads to low frictional strength of crustal rocks at earthquake slip rates, *Science*, **334**(6053), 216–218.

Gomberg, J., Beeler, N. M., Blanpied, M. L., & Bodin, P., 1998. Earthquake triggering by transient and static deformations, *Journal of Geophysical Research: Solid Earth*, **103**(B10), 24411–24426.

Gomberg, J., Belardinelli, M. E., Cocco, M., & Reasenberg, P., 2005. Time-dependent earthquake probabilities, *Journal of Geophysical Research B: Solid Earth*, **110**(5), 1–12.

Graves, R. W., 1996. Simulating seismic wave propagation in 3d elastic media using staggered-grid finite differences, *Bulletin of the Seismological Society of America*, **86**(4), 1091–1106.

Griffith, A. A., 1921. The phenomena of rupture and flow in solids, *Philosophical Transactions of the Royal Society of London. Series A, Containing Papers of a Mathematical or Physical Character*, **221**(582-593), 163–198.

Gross, D., 2014. Some Remarks on the History of Fracture Mechanics, in *The History of Theoretical, Material and Computational Mechanics - Mathematics Meets Mechanics and Engineering*, vol. 1, pp. 195–209, Springer.

Gu, J.-C., Rice, J. R., Ruina, A. L., & Tse, S. T., 1984. Slip motion and stability of a single degree of freedom elastic system with rate and state dependent friction, *Journal of the Mechanics and Physics of Solids*, **32**(3), 167 – 196.

Guatteri, M. & Spudich, P., 1998. Coseismic temporal changes of slip direction: The effect of absolute stress on dynamic rupture, *Bulletin of the Seismological Society of America*, **88**(3), 777–789.

Guatteri, M. & Spudich, P., 2000. What can strong-motion data tell us about slip-weakening fault-friction laws?, *Bulletin of the Seismological Society of America*, **90**(1), 98–116.

Gurtin, M. E., Mizel, V. J., & Williams, W. O., 1968. A note on cauchy's stress theorem, *Journal of Mathematical Analysis and Applications*, **22**(2), 398–401.

Hallo, M. & Gallovič, F., 2016. Fast and cheap approximation of Green function uncertainty for waveform-based earthquake source inversions, *Geophysical Journal International*, **207**(2), 1012–1029.

Hallo, M. & Gallovič, F., 2020. Bayesian Self-Adapting Fault Slip Inversion With Green's Functions Uncertainty and Application on the 2016 Mw 7.1 Kumamoto Earthquake, *Journal of Geophysical Research: Solid Earth*, **125**(3), e2019JB018703, e2019JB018703 2019JB018703.

Harris, R. A., 1998. Introduction to special section: Stress triggers, stress shadows, and implications for seismic hazard, *Journal of Geophysical Research: Solid Earth*, **103**(B10), 24347–24358.

Hartranft, R. & Sih, G., 1977. Stress singularity for a crack with an arbitrarily curved front, *Engineering Fracture Mechanics*, **9**(3), 705–718.

Hastings, W. K., 1970. Monte Carlo sampling methods using Markov chains and their applications, *Biometrika*, **57**(1), 97–109.

Herrera, C., Ruiz, S., Madariaga, R., & Poli, P., 2017. Dynamic inversion of the 2015 Jujuy earthquake and similarity with other intraslab events, *Geophysical Journal International*, **209**(2), 866–875.

Hillers, G., Ben-Zion, Y., & Mai, P. M., 2006. Seismicity on a fault controlled by rate- and state-dependent friction with spatial variations of the critical slip distance, *Journal of Geophysical Research: Solid Earth*, **111**(B1).

Hirose, T., 2005. Growth of molten zone as a mechanism of slip weakening of simulated faults in gabbro during frictional melting, *Journal of Geophysical Research*, **110**(B5).

Huang, Y. & Gao, H., 2000. Intersonic crack propagation–part i: The fundamental solution, *J. Appl. Mech*, **68**(2), 169–175.

Hyndman, R. J., 1996. Computing and graphing highest density regions, *The American Statistician*, **50**(2), 120–126.

Ida, Y., 1972. Cohesive force across the tip of a longitudinal-shear crack and griffith's specific surface energy, *Journal of Geophysical Research (1896-1977)*, **77**(20), 3796–3805.

Ida, Y., 1973. The maximum acceleration of seismic ground motion, *Bulletin of the Seismological Society of America*, **63**(3), 959–968.

Ida, Y. & Aki, K., 1972. Seismic source time function of propagating longitudinal-shear cracks, *Journal of Geophysical Research (1896-1977)*, **77**(11), 2034–2044.

Ide, S. & Aochi, H., 2005. Earthquake as multiscal dynamic ruptures with heterogeneous fracture surface energy, *Journal of Geophysical Research*, **110**.

Ide, S. & Takeo, M., 1997. Determination of constitutive relations of fault slip based on seismic wave analysis, *Journal of Geophysical Research: Solid Earth*, **102**(B12), 27379–27391.

Im, K., Marone, C., & Elsworth, D., 2019. The transition from steady frictional sliding to inertia-dominated instability with rate and state friction, *Journal of the Mechanics and Physics of Solids*, **122**, 116–125.

Irwin, G., 1948. Fracture dynamics, in *Proceedings of the ASM Symposium on Fracturing of Metals, Cleveland (Oh)*.

Irwin, G. R., 1957. Analysis of stresses and strains near the end of a crack traversing a plate, *Journal of Applied Mechanics. Vol. E24, 351-369*.

Irwin, G. R., 1958. Fracture, in *Elasticity and Plasticity / Elastizität und Plastizität*, pp. 551–590, ed. Flügge, S., Springer Berlin Heidelberg, Berlin, Heidelberg.

Johnson, T., 1981. Time-dependent friction of granite: Implications for precursory slip on faults, *Journal of Geophysical Research: Solid Earth*, **86**(B7), 6017–6028.

Kanamori, H. & Brodsky, E. E., 2004. The physics of earthquakes, *Reports on Progress in Physics*, **67**(8), 1429–1496.

Kaneko, Y. & Lapusta, N., 2010. Supershear transition due to a free surface in 3-d simulations of spontaneous dynamic rupture on vertical strike-slip faults, *Tectonophysics*, **493**(3), 272–284.

Karagianni, E., Panagiotopoulos, D., Panza, G., Suhadolc, P., Papazachos, C., Papazachos, B., Kiratzi, A., Hatzfeld, D., Makropoulos, K., Priestley, K., & Vuan, A., 2002. Rayleigh wave group velocity tomography in the aegean area, *Tectonophysics*, **358**(1), 187–209.

Kassir, M. K. & Sih, G. C., 1966. Three-Dimensional Stress Distribution Around an Elliptical Crack Under Arbitrary Loadings, *Journal of Applied Mechanics*, **33**(3), 601.

Kato, N., 2001. Simulation of seismic cycles of buried intersecting reverse faults, *Journal of Geophysical Research*, **106**(B3), 4221–4232.

Kato, N., 2003. Repeating Slip Events at a Circular Asperity: Numerical Simulation with a Rate- and State-Dependent Friction Law, *Bull. Earthq. Res. Inst.*, **78**.

Kato, N., 2004. A possible effect of an intermediate depth intraslab earthquake on seismic cycles of interplate earthquakes at a subduction zone, *Earth, Planets and Space*, **56**(6), 553–561.

Kato, N., 2014. Deterministic chaos in a simulated sequence of slip events on a single isolated asperity, *Geophysical Journal International*, **198**(2), 727–736.

Kato, N. & Hirasawa, T., 2000. Effect of a large outer rise earthquake on seismic cycles of interplate earthquakes: A model study, *Journal of Geophysical Research: Solid Earth*, **105**(B1), 653–662.

Kato, N. & Tullis, T., 2001. A composite rate- and state-dependent law for rock friction, *Geophysical Research Letters*, **28**, 1103–1106.

Kearse, J. & Kaneko, Y., 2020. On-fault geological fingerprint of earthquake rupture direction, *Journal of Geophysical Research: Solid Earth*, **125**(9).

Keilis-Borok, V., 1959. On estimation of displacement in an earthquake source and of source dimension, *Ann. Geofis.*, **12**.

King, G., Stein, R., & Lin, J., 1994. Static stress changes and the triggering of earthquakes, *Bulletin - Seismological Society of America*, **84**.

Kiratzi, A., 2018. The 12 June 2017 Mw 6.3 Lesvos Island (Aegean Sea) earthquake: Slip model and directivity estimated with finite-fault inversion, *Tectonophysics*, **724-725**, 1–10.

Knopoff, L., 1958. Energy release in earthquakes, *Geophysical Journal of the Royal Astronomical Society*, **1**(1), 44–52.

Knops, R. J. & Payne, L. E., 1971. *Uniqueness theorems in linear elasticity*, Springer tracts in natural philosophy, v. 19, Springer-Verlag, Berlin.

Konstantinou, K. I., Mouslopoulou, V., Liang, W.-T., Heidbach, O., Oncken, O., & Suppe, J., 2017. Present-day crustal stress field in Greece inferred from regional-scale damped inversion of earthquake focal mechanisms, *Journal of Geophysical Research: Solid Earth*, **122**(1), 506–523.

Kosloff, D. D. & Liu, H.-P., 1980. Reformulation and discussion of mechanical behavior of the velocity-dependent friction law proposed by Dieterich, *Geophysical Research Letters*, **7**(11), 913–916.

Kostka, F. & Gallovič, F., 2016. Static Coulomb stress load on a three-dimensional rate-and-state fault: Possible explanation of the anomalous delay of the 2004 Parkfield earthquake, *Journal of Geophysical Research (Solid Earth)*, **121**(5), 3517–3533.

Kostka, F., Zahradník, J., Sokos, E., & Gallovič, F., 2022. Assessing the role of selected constraints in Bayesian dynamic source inversion: application to the 2017 Mw 6.3 Lesvos earthquake, *Geophysical Journal International*, **228**(1), 711–727.

Kostrov, B., 1964. Selfsimilar problems of propagation of shear cracks, *Journal of Applied Mathematics and Mechanics*, **28**(5), 1077–1087.

Kostrov, B., 1966. Unsteady propagation of longitudinal shear cracks, *Journal of Applied Mathematics and Mechanics*, **30**(6), 1241 – 1248.

Kostrov, B. V., 1975. On the crack propagation with variable velocity, *International Journal of Fracture*, **11**(1), 47–56.

Kostrov, B. V. & Das, S., 1984. Evaluation of stress and displacement fields due to an elliptical plane shear crack, *Geophysical Journal International*, **78**(1), 19–33.

Kristek, J., Moczo, P., & Archuleta, R. J., 2002. Efficient methods to simulate planar free surface in the 3d 4th-order staggered-grid finite-difference schemes, *Studia Geophysica et Geodaetica*, **46**(2), 355–381.

Kuroki, H., Ito, H. M., & Yoshida, A., 2004. Effects of nearby large earthquakes on the occurrence time of the Tokai earthquake – An estimation based on a 3-D simulation of plate subduction –, *Earth, Planets and Space*, **56**(2), 169–178.

Labuz, J. F. & Zang, A., 2012. Mohr-coulomb failure criterion, *Rock Mechanics and Rock Engineering*, **45**(6), 975–979.

Lapusta, N. & Liu, Y., 2009. Three-dimensional boundary integral modeling of spontaneous earthquake sequences and aseismic slip, *Journal of Geophysical Research: Solid Earth*, **114**(B9).

Lapusta, N. & Rice, J. R., 2003. Nucleation and early seismic propagation of small and large events in a crustal earthquake model, *Journal of Geophysical Research: Solid Earth*, **108**(B4).

Lapusta, N., Rice, J. R., Ben-Zion, Y., & Zheng, G., 2000. Elastodynamic analysis for slow tectonic loading with spontaneous rupture episodes on faults with rate- and state-dependent friction, *Journal of Geophysical Research: Solid Earth*, **105**(B10), 23765–23789.

Lekkas, E., Emmanuel, A., Carydis, P., Skourtsos, E., Mavroulis, S., Antoniou, V., & Spyrou, N. I., 2017. Factors controlling the distribution of building damage in the traditional Vrissa settlement induced by the 2017 June 12, Mw 6.3 Lesvos (Northeastern Aegean Sea, Greece) earthquake.

Levander, A. R., 1988. Fourth-order finite-difference P-SV seismograms, *Geophysics*, **53**(11), 1425–1436.

Linker, M. F. & Dieterich, J. H., 1992. Effects of variable normal stress on rock friction: Observations and constitutive equations, *Journal of Geophysical Research*, **97**(B4), 4923.

Liu, C., Bizzarri, A., & Das, S., 2014. Progression of spontaneous in-plane shear faults from sub-Rayleigh to compressional wave rupture speeds, *J. Geophys. Res. Solid Earth*, **119**(11), 8331–8345.

Liu, Y. & Lapusta, N., 2008. Transition of mode II cracks from sub-Rayleigh to intersonic speeds in the presence of favorable heterogeneity, *Journal of the Mechanics and Physics of Solids*, **56**(1), 25 – 50.

Liu, Y. & Rice, J. R., 2007. Spontaneous and triggered aseismic deformation transients in a subduction fault model, *Journal of Geophysical Research: Solid Earth*, **112**(B9).

Lyakhovsky, V. & Ben-Zion, Y., 2014. A continuum damage-breakage faulting model and solid-granular transitions, *Pure and Applied Geophysics*, **171**.

Madariaga, R., 1976. Dynamics of an expanding circular fault, *Bulletin of the Seismological Society of America*, **66**(3), 639–666.

Madariaga, R., 1979. On the relation between seismic moment and stress drop in the presence of stress and strength heterogeneity, *Journal of Geophysical Research: Solid Earth*, **84**(B5), 2243–2250.

Madariaga, R. & Olsen, K. B., 2000. Criticality of rupture dynamics in 3-d, *Pure and Applied Geophysics*, **157**, 1981–2001.

Madariaga, R. & Ruiz, S., 2016. Earthquake dynamics on circular faults: a review 1970-2015, *Journal of Seismology*, **20**(4), 1235–1252.

Madariaga, R., Olsen, K., & Archuleta, R., 1998. "Modeling dynamic rupture in a 3D earthquake fault model", *Bulletin of the Seismological Society of America*, **88**(5), 1182–1197.

Malekan, M., Budzik, M. K., Jensen, H. M., & Aghababaei, R., 2021. Fracture analyses of surface asperities during sliding contact, *Tribology International*, **159**, 106939.

Marone, C., 1998a. Laboratory-derived friction laws and their application to seismic faulting, *Annual Review of Earth and Planetary Sciences*, **26**(1), 643–696.

Marone, C. & Saffer, D. M., 2015. The Mechanics of Frictional Healing and Slip Instability During the Seismic Cycle, in *Treatise on Geophysics: Earthquake Seismology*, pp. 111–138, Elsevier.

Marone, C., Raleigh, C. B., & Scholz, C. H., 1990. Frictional behavior and constitutive modeling of simulated fault gouge, *Journal of Geophysical Research*, **95**(B5), 7007.

Marone, C., Cocco, M., Richardson, E., & Tinti, E., 2009. Chapter 6: The Critical Slip Distance for Seismic and Aseismic Fault Zones of Finite Width, in *Fault-Zone Properties and Earthquake Rupture Dynamics*, vol. 94 of **International Geophysics**, pp. 135–162, Academic Press.

Marone, C. J., 1998b. The effect of loading rate on static friction and the rate of fault healing during the earthquake cycle, *Nature*, **391**(6662), 69–72.

Martinec, Z., 2019. *Principles of Continuum Mechanics: A Basic Course for Physicists*, Nečas Center Series, Springer International Publishing; Birkhäuser, 1st edn.

McClintock, F., 1960. Travelling cracks in elastic materials under longitudinal shear, *Journal of the Mechanics and Physics of Solids*, **8**(3), 187–193.

McGarr, A., 2003. Maximum slip in earthquake fault zones, apparent stress, and stick-slip friction, *Bulletin of the Seismological Society of America*, **93**(6), 2355–2362.

Melin, S., 1986. When does a crack grow under mode II conditions?, *International Journal of Fracture*, **30**(2), 103–114.

Mello, M., Bhat, H., & Rosakis, A., 2016. Spatiotemporal properties of sub-rayleigh and supershear rupture velocity fields: Theory and experiments, *Journal of the Mechanics and Physics of Solids*, **93**, 153 – 181.

Metropolis, N., Rosenbluth, A. W., Rosenbluth, M. N., Teller, A. H., & Teller, E., 1953. Equation of state calculations by fast computing machines, *The Journal of Chemical Physics*, **21**(6), 1087–1092.

Minson, S. E., Simons, M., Beck, J. L., Ortega, F., Jiang, J., Owen, S. E., Moore, A. W., Inbal, A., & Sladen, A., 2014. Bayesian inversion for finite fault earthquake source models – II: the 2011 great Tohoku-oki, Japan earthquake, *Geophysical Journal International*, **198**(2), 922–940.

Mirwald, A., Cruz-Atienza, V. M., Díaz-Mojica, J., Iglesias, A., Singh, S. K., Villafuerte, C., & Tago, J., 2019. The 19 September 2017 (Mw 7.1) Intermediate-Depth Mexican Earthquake: A Slow and Energetically Inefficient Deadly Shock, *Geophysical Research Letters*, **46**(4), 2054–2064.

Miyake, Y. & Noda, H., 2019. Fully dynamic earthquake sequence simulation of a fault in a viscoelastic medium using a spectral boundary integral equation method: does interseismic stress relaxation promote aseismic transients?, *Earth, Planets and Space*, **71**(1), 137.

Molinari, A. & Perfettini, H., 2017. A micromechanical model of rate and state friction: 2. Effect of shear and normal stress changes, *Journal of Geophysical Research: Solid Earth*, **122**(4), 2638–2652.

Monterrubio-Velasco, M., Rodriguez-Perez, Q., Zúñiga, F., Scholz, D., Aguilar-Meléndez, A., & De la Puente, J., 2019. A stochastic rupture earthquake code based on the fiber bundle model (TREMOL v0.1): Application to Mexican subduction earthquakes, *Geoscientific Model Development*, **12**, 1809–1831.

Moreno, Y., Correig, A., Gómez, J., & Pacheco, A., 2001. A model for complex aftershock sequences, *J. geophys. Res.: Solid Earth*, **106**, 6609–6619.

Murphy, S., O'Brien, G. S., McCloskey, J., Bean, C. J., & Nalbant, S., 2013. Modelling fluid induced seismicity on a nearby active fault, *Geophysical Journal International*, **194**(3), 1613–1624.

Mustać, M. & Tkalčić, H., 2015. Point source moment tensor inversion through a Bayesian hierarchical model, *Geophysical Journal International*, **204**(1), 311–323.

Nadeau, R. M. & Guilhem, A., 2009. Nonvolcanic Tremor Evolution and the San Simeon and Parkfield, California, Earthquakes, *Science*, **325**(5937), 191–193.

Nadeau, R. M. & Johnson, L. R., 1998. Seismological studies at Parkfield VI: Moment release rates and estimates of source parameters for small repeating earthquakes, *Bulletin of the Seismological Society of America*, **88**(3), 790–814.

Nadeau, R. M. & McEvilly, T. V., 1999. Fault Slip Rates at Depth from Recurrence Intervals of Repeating Microearthquakes, *Science*, **285**(5428), 718–721.

Nadeau, R. M. & McEvilly, T. V., 2004. Periodic Pulsing of Characteristic Microearthquakes on the San Andreas Fault, *Science*, **303**(5655), 220–222.

Nadeau, R. M., Foxall, W., & McEvilly, T. V., 1995. Clustering and Periodic Recurrence of Microearthquakes on the San Andreas Fault at Parkfield, California, *Science*, **267**(5197), 503–507.

Nagata, K., Nakatani, M., & Yoshida, S., 2012. A revised rate- and state-dependent friction law obtained by constraining constitutive and evolution laws separately with laboratory data, *Journal of Geophysical Research (Solid Earth)*, **117**, 2314–.

Neuber, H., 1937. *Theory of notch stresses: principles for exact calculation of strength with reference to structural form and material. (English Translation, 1958)*, no. 293p. in Translation series, USAEC Office of Technical Information, Oak Ridge, Tennessee.

Nielsen, S. & Madariaga, R., 2003. On the self-healing fracture mode, *Bulletin of the Seismological Society of America*, **93**(6), 2375–2388.

Noda, H. & Hori, T., 2014. Under what circumstances does a seismogenic patch produce aseismic transients in the later interseismic period?, *Geophysical Research Letters*, **41**(21), 7477–7484.

Northern California Earthquake Data Center, 2014. *UC Berkeley Seismological Laboratory, Dataset, doi:10.7932/NCEDC*.

Ohnaka, M., 2013. *The Physics of Rock Failure and Earthquakes*, Cambridge University Press, Cambridge.

Ohnaka, M. & Yamashita, T., 1989. A cohesive zone model for dynamic shear faulting based on experimentally inferred constitutive relation and strong motion source parameters, *Journal of Geophysical Research: Solid Earth*, **94**(B4), 4089–4104.

Okada, Y., 1992. Internal deformation due to shear and tensile faults in a half-space, *Bulletin of the Seismological Society of America*, **82**(2), 1018–1040.

Okubo, K., Rougier, E., Lei, Z., & Bhat, H., 2020. Modeling earthquakes with off-fault damage using the combined finite-discrete element method, *Computational Particle Mechanics*, **7**.

Okubo, P. G. & Dieterich, J. H., 1984. Effects of physical fault properties on frictional instabilities produced on simulated faults, *Journal of Geophysical Research: Solid Earth*, **89**(B7), 5817–5827.

Otsubo, M., Shigematsu, N., Imanishi, K., Ando, R., Takahashi, M., & Azuma, T., 2013. Temporal slip change based on curved slickenlines on fault scarps along itozawa fault caused by 2011 iwaki earthquake, northeast japan, *Tectonophysics*, **608**, 970–979.

Pace, B., Bocchini, G. M., & Boncio, P., 2014. Do static stress changes of a moderate-magnitude earthquake significantly modify the regional seismic hazard? Hints from the L'Aquila 2009 normal-faulting earthquake (Mw 6.3, central Italy), *Terra Nova*, **26**(6), 430–439.

Page, M. T., Dunham, E. M., & Carlson, J. M., 2005. Distinguishing barriers and asperities in near-source ground motion, *Journal of Geophysical Research (Solid Earth)*, **110**(B11), B11302.

Palmer, A. C. & Rice, J. R., 1973. The growth of slip surfaces in the progressive failure of over-consolidated clay, *Proceedings of the Royal Society of London. A. Mathematical and Physical Sciences*, **332**(1591), 527–548.

Pan, J., Li, H., Si, J., Pei, J., Fu, X., Chevalier, M.-L., & Liu, D., 2014. Rupture process of the Wenchuan earthquake (Mw 7.9) from surface ruptures and fault striations characteristics, *Tectonophysics*, **619**(SI), 13–28.

Pan, Z., Ma, R., Dalei, W., & Chen, A., 2017. A review of lattice type model in fracture mechanics: theory, applications, and perspectives, *Engineering Fracture Mechanics*, **190**.

Papadimitriou, P., Kassaras, I., Kaviris, G., Tselentis, G.-A., Voulgaris, N., Lekkas, E., Chouliaras, G., Evangelidis, C., Pavlou, K., Kapetanidis, V., Karakonstantis, A., Kazantzidou-Firtinidou, D., Fountoulakis, I., Millas, C., Spingos, I., Aspiotis, T., Moumoulidou, A., Skourtsos, E., Antoniou, V., Andreadakis, E., Mavroulis, S., & Kleanthi, M., 2018. The 12th June 2017 Mw=6.3 Lesvos earthquake from detailed seismological observations, *Journal of Geodynamics*, **115**, 23–42.

Payne, R. M. & Duan, B., 2015. Influence of initial stress and rupture initiation parameters on forbidden zone rupture propagation, *Geophysical Journal International*, **201**(1), 70–77.

Perfettini, H., Campillo, M., & Ionescu, I., 2003a. On the scaling of the slip weakening rate of heterogeneous faults, *Journal of Geophysical Research: Solid Earth*, **108**(B9).

Perfettini, H., Schmittbuhl, J., & Cochard, A., 2003b. Shear and normal load perturbations on a two-dimensional continuous fault: 1. Static triggering, *Journal of Geophysical Research*, **108**, 2408.

Perrin, G., Rice, J. R., & Zheng, G., 1995. Self-healing slip pulse on a frictional surface, *Journal of the Mechanics and Physics of Solids*, **43**(9), 1461 – 1495.

Peyrat, S. & Olsen, K. B., 2004. Nonlinear dynamic rupture inversion of the 2000 Western Tottori, Japan, earthquake, *Geophysical Research Letters*, **31**(5).

Peyrat, S., Olsen, K., & Madariaga, R., 2001. Dynamic modeling of the 1992 Landers earthquake, *Journal of Geophysical Research*, **106**(B11), 26,467–26,482.

Polizzotto, C., 2002. Thermodynamics and continuum fracture mechanics for nonlocal-elastic plastic materials, *European Journal of Mechanics - A/Solids*, **21**(1), 85–103.

Pollitz, F. F., Hammond, W. C., & Wicks, C. W., 2020. Rupture Process of the M 6.5 Stanley, Idaho, Earthquake Inferred from Seismic Waveform and Geodetic Data, *Seismological Research Letters*, **92**(2A), 699–709.

Premus, J., Gallovič, F., & Hanyk Ladislav. Gabriel, A. A., 2020. FD3D_TSN: A fast and simple code for dynamic rupture simulations with GPU acceleration, *Seismological Research Letters*, **91**(5), 2881–2889.

Press, W. H., Teukolsky, S. A., Vetterling, W. T., & Flannery, B. P., 1992. *Numerical Recipes in FORTRAN (2nd Ed.): The Art of Scientific Computing*, Cambridge University Press, USA.

Preuss, S., Herrendörfer, R., Gerya, T., Ampuero, J.-P., & van Dinther, Y., 2019. Seismic and aseismic fault growth lead to different fault orientations, *Journal of Geophysical Research: Solid Earth*, **124**(8), 8867–8889.

Preuss, S., Ampuero, J. P., Gerya, T., & van Dinther, Y., 2020. Characteristics of earthquake ruptures and dynamic off-fault deformation on propagating faults, *Solid Earth*, **11**(4), 1333–1360.

Pulido, N. & Irikura, K., 2000. Estimation of dynamic rupture parameters from the radiated seismic energy and apparent stress, *Geophysical Research Letters*, **27**(23), 3945–3948.

Ranjith, K. & Rice, J. R., 1999. Stability of quasi-static slip in a single degree of freedom elastic system with rate and state dependent friction, *Journal of the Mechanics and Physics of Solids*, **47**, 1207–1218.

Renard, F., Beauprêtre, S., Voisin, C., Zigone, D., Candela, T., Dysthe, D. K., & Gratier, J.-P., 2012. Strength evolution of a reactive frictional interface is controlled by the dynamics of contacts and chemical effects, *Earth and Planetary Science Letters*, **341-344**, 20–34.

Rice, J. R., 1980. The mechanics of earthquake rupture, in *Physics of the Earth's Interior, edited by A.M. Dziewonski and E. Boschi*, pp. 555–649, North-Holland Pub. Co.

Rice, J. R., 1993. Spatio-temporal complexity of slip on a fault, *Journal of Geophysical Research: Solid Earth*, **98**(B6), 9885–9907.

Rice, J. R. & Ben-Zion, Y., 1996. Slip complexity in earthquake fault models, *Proceedings of the National Academy of Sciences*, **93**, 3811–3818.

Rice, J. R. & Ruina, A. L., 1983. Stability of Steady Frictional Slipping, *Journal of Applied Mechanics*, **50**(2), 343–349.

Rice, J. R. & Tse, S. T., 1986. Dynamic motion of a single degree of freedom system following a rate and state dependent friction law, *Journal of Geophysical Research*, **91**(B1), 521.

Rice, J. R., Sammis, C. G., & Parsons, R., 2005. Off-fault secondary failure induced by a dynamic slip pulse, *Bulletin of the Seismological Society of America*, **95**(1), 109–134.

Richards, P., 1976. Dynamic motions near an earthquake fault: A three-dimensional solution, *Bull. Seismol. Soc. Am.*, **66**.

Richards, P. G., 1973. The dynamic field of a growing plane elliptical shear crack, *International Journal of Solids and Structures*, **9**(7), 843–861.

Richards-Dinger, K. & Dieterich, J. H., 2012. RSQSim earthquake simulator, *Seismological Research Letters*, **83**(6), 983–990.

Ripperger, J., Ampuero, J.-P., Mai, P. M., & Giardini, D., 2007. Earthquake source characteristics from dynamic rupture with constrained stochastic fault stress, *J. Geophys. Res.*, **112**(B4).

Rosakis, A. J., 2002. Intersonic shear cracks and fault ruptures, *Advances in Physics*, **51**(4), 1189–1257.

Rossmanith, H., 1995. Translation of K. Wieghardt's historical paper 'On splitting and cracking of elastic bodies', *Fatigue & Fracture of Engineering Materials & Structures*, **18**, 1371 – 1405.

Rossmanith, H. P., 1997. The struggle for recognition of engineering fracture mechanics, *Fracture Research in Retrospect (An Anniversary Volume in Honor of GR Irwin's 90th Birthday*.

Rountree, C., Kalia, R., Lidorikis, E., Nakano, A., Van Brutzel, L., & Vashishta, P., 2002. Atomistic aspects of crack propagation in brittle materials: Multimillion atom molecular dynamics simulations, *Annu. Rev. Mater. Res*, **12**, 377–400.

Rubin, A. M., 2008. Episodic slow slip events and rate-and-state friction, *Journal of Geophysical Research: Solid Earth*, **113**(B11).

Rubin, A. M. & Ampuero, J.-P., 2005. Earthquake nucleation on (aging) rate and state faults, *Journal of Geophysical Research: Solid Earth*, **110**(B11).

Ruina, A., 1980. *Friction Laws and Instabilities: A Quasistatic Analysis of Some Dry Frictional Behavior*, Division of Engineering, Brown University.

Ruina, A., 1983. Slip instability and state variable friction laws, *Journal of Geophysical Research: Solid Earth*, **88**(B12), 10359–10370.

Ruiz, S. & Madariaga, R., 2011. Determination of the friction law parameters of the Mw 6.7 Michilla earthquake in northern Chile by dynamic inversion, *Geophys. Res. Lett.*, **38**(9).

Ruiz, S. & Madariaga, R., 2013. Kinematic and Dynamic Inversion of the 2008 Northern Iwate Earthquake, *Bulletin of the Seismological Society of America*, **103**(2A), 694–708.

Sambridge, M., 2013. A Parallel Tempering algorithm for probabilistic sampling and multimodal optimization, *Geophysical Journal International*, **196**(1), 357–374.

Sambridge, M. & Mosegaard, K., 2002. Monte Carlo methods in geophysical inverse problems, *Rev. Geophys.*, **40**(3), 3–1–3–29.

Sambridge, M., Bodin, T., Gallagher, K., & Tkalčić, H., 2013. Transdimensional inference in the geosciences, *Philosophical transactions. Series A, Mathematical, physical, and engineering sciences*, **371**, 20110547.

Saraò, A., Cocina, O., Privitera, E., & Panza, G. F., 2010. The dynamics of the 2001 Etna eruption as seen by full moment tensor analysis, *Geophysical Journal International*, **181**(2), 951–965.

Scholtès, L. & Donzé, F.-V., 2012. Modelling progressive failure in fractured rock masses using a 3D discrete element method, *International Journal of Rock Mechanics and Mining Sciences*, **52**, 18–30.

Scholz, C., 1998. Earthquakes and friction laws, *Nature*, **391**, 37–42.

Scholz, C., 2002. *The Mechanics of Earthquake Faulting*, Cambridge University Press, Cambridge.

Scholz, C., Molnar, P., & Johnson, T., 1972. Detailed studies of frictional sliding of granite and implications for the earthquake mechanism, *Journal of Geophysical Research (1896-1977)*, **77**(32), 6392–6406.

Scholz, C. H. & Engelder, J. T., 1976. The role of asperity indentation and ploughing in rock friction — I: Asperity creep and stick-slip, *International Journal of Rock Mechanics and Mining Sciences & Geomechanics Abstracts*, **13**(5), 149–154.

Schröder, C. T. & Scott, W. R., 2001. On the complex conjugate roots of the Rayleigh equation: The leaky surface wave, *The Journal of the Acoustical Society of America*, **110**(6), 2867–2877.

Schwartz, D. & Coppersmith, K., 1984. Fault Behavior and Characteristic Earthquakes: Examples From the Wasatch and San Andreas Fault Zones, *Journal of Geophysical Research*, **89**.

Scott, D. W., 1992. *Multivariate Density Estimation: Theory, Practice, and Visualization*, John Wiley Sons, New York, Chicester, 1992.

Shemyakin, A., 2014. Hellinger Distance and Non-informative Priors, *Bayesian Analysis*, **9**(4), 923 – 938.

Shimada, T., Ouchi, K., Chihara, Y., & Kitamura, T., 2015. Breakdown of continuum fracture mechanics at the nanoscale, *Scientific reports*, **5**, 8596.

Sibson, R. H., 2003. Thickness of the Seismic Slip Zone, *Bulletin of the Seismological Society of America*, **93**(3), 1169–1178.

Sih, G., 1973. Some basic problems in fracture mechanics and new concepts, *Engineering Fracture Mechanics*, **5**(2), 365–377.

Sih, G. C. & Macdonald, B., 1974. Fracture mechanics applied to engineering problems-strain energy density fracture criterion, *Engineering Fracture Mechanics*, **6**, 361–386.

Sokos, E. & Zahradník, J., 2017. Lesvos June 12, 2017, Mw 6.3 event, a quick study of the source (https://www.emsc-csem.org/Files/news/Earthquakes_reports/Lesvos_Source_Study_Sokos_and_Zahradnik.pdf), *EMSC report*, accessed Dec, 31, 2021.

Sone, H. & Shimamoto, T., 2009. Frictional resistance of faults during accelerating and decelerating earthquake slip, *Nature Geoscience*, **2**(10), 705–708.

Spudich, P., 1992. On the inference of absolute stress levels from seismic radiation, *Tectonophysics*, **211**(1), 99–106.

Starr, A. T., 1928. Slip in a crystal and rupture in a solid due to shear, *Mathematical Proceedings of the Cambridge Philosophical Society*, **24**(4), 489–500.

Steacy, S., Gomberg, J., & Cocco, M., 2005. Introduction to special section: Stress transfer, earthquake triggering, and time-dependent seismic hazard, *Journal of Geophysical Research: Solid Earth*, **110**(B5).

Stein, R. S., Barka, A. A., & Dieterich, J. H., 1997. Progressive failure on the North Anatolian fault since 1939 by earthquake stress triggering, *Geophysical Journal International*, **128**(3), 594–604.

Stein, S. & Wysession, M., 2003. *An Introduction to Seismology, Earthquakes, and Earth Structure*, Wiley-Blackwell, 1st edn.

Stephens, R. I., Fatemi, A., Stephens, R. R., & Fuchs, H. O., 2000. *Metal Fatigue in Engineering*, John Wiley Sons, 2nd edn.

Stirling, M. W., Wesnousky, S. G., & Shimazaki, K., 1996. Fault trace complexity, cumulative slip, and the shape of the magnitude-frequency distribution for strike-slip faults: a global survey, *Geophysical Journal International*, **124**(3), 833–868.

Svetlizky, I., Bayart, E., & Fineberg, J., 2019. Brittle fracture theory describes the onset of frictional motion, *Annual Review of Condensed Matter Physics*, **10**.

Swendsen, R. H. & Wang, J.-S., 1986. Replica Monte Carlo Simulation of Spin-Glasses, *Phys. Rev. Lett.*, **57**, 2607–2609.

Tada, H., Paris, P. C., & Irwin, G. R., 2000. *The Stress Analysis of Cracks Handbook, Third Edition*, ASME Press.

Tada, T., 2009. Chapter 9: Boundary integral equation method for earthquake rupture dynamics, in *Fault-Zone Properties and Earthquake Rupture Dynamics*, vol. 94 of **International Geophysics**, pp. 217–267, Academic Press.

Tarantola, A., 2005. *Inverse Problem Theory and Methods for Model Parameter Estimation*, Society for Industrial and Applied Mathematics.

Templeton, E. & Rice, J., 2008. Off-fault plasticity and earthquake rupture dynamics: 1. Dry materials or neglect of fluid pressure changes, *Journal of Geophysical Research*, **113**.

Thomas, M. Y., Bhat, H. S., & Klinger, Y., 2017. *Fault Zone Dynamic Processes: Evolution of Fault Properties During Seismic Rupture*, chap. Effect of Brittle Off-Fault Damage on Earthquake Rupture Dynamics, pp. 255–280, American Geophysical Union (AGU).

Tinti, E., Spudich, P., & Cocco, M., 2005. Earthquake fracture energy inferred from kinematic rupture models on extended faults, *J. Geophys. Res.*, **110**(B12).

Toda, S. & Stein, R. S., 2002. Response of the San Andreas fault to the 1983 Coalinga-Nuñez earthquakes: An application of interaction-based probabilities for Parkfield, *Journal of Geophysical Research: Solid Earth*, **107**(B6).

Tse, S. T. & Rice, J. R., 1986. Crustal earthquake instability in relation to the depth variation of frictional slip properties, *Journal of Geophysical Research: Solid Earth*, **91**(B9), 9452–9472.

Turner, R. C., Shirzaei, M., Nadeau, R. M., & Bürgmann, R., 2015. Slow and Go: Pulsing slip rates on the creeping section of the San Andreas Fault, *Journal of Geophysical Research: Solid Earth*, **120**(8), 5940–5951.

Twardzik, C., Das, S., & Madariaga, R., 2014. Inversion for the physical parameters that control the source dynamics of the 2004 Parkfield earthquake, *Journal of Geophysical Research: Solid Earth*, **119**(9), 7010–7027.

Udias, A., Madariaga, R., & Buforn, E., 2013. Source mechanisms of earthquakes: Theory and practice, *Source Mechanisms of Earthquakes: Theory and Practice*, pp. 1–302.

Uenishi, K., 2009. On the mechanical destabilization of a three-dimensional displacement-softening plane of weakness, *Proceedings of the 38th Symposium on Rock Mechanics, Tokyo, Japan, 8–9 January 2009, Committee on Rock Mechanics, The Japan Society of Civil Engineers, Tokyo, Japan*, p. 332–337.

Uenishi, K., 2018. Three-dimensional fracture instability of a displacement-weakening planar interface under locally peaked nonuniform loading, *Journal of the Mechanics and Physics of Solids*, **115**, 195–207.

Uenishi, K. & Rice, J. R., 2003. Universal nucleation length for slip-weakening rupture instability under nonuniform fault loading, *Journal of Geophysical Research: Solid Earth*, **108**(B1).

Urata, Y., Yamashita, F., Fukuyama, E., Noda, H., & Mizoguchi, K., 2017. Apparent dependence of rate- and state-dependent friction parameters on loading velocity and cumulative displacement inferred from large-scale biaxial friction experiments, *Pure and Applied Geophysics*, **174**.

Vallée, M. & Douet, V., 2016. A new database of source time functions (STFs) extracted from the SCARDEC method, *Physics of the Earth and Planetary Interiors*, **257**, 149–157.

van den Ende, M. P. A., 2018. Microphysically based modelling of fault friction and earthquake rupture, *Dissertation, UU Dept. of Earth Sciences*.

van der Elst, N. J. & Savage, H. M., 2015. Frequency dependence of delayed and instantaneous triggering on laboratory and simulated faults governed by rate-state friction, *Journal of Geophysical Research: Solid Earth*, **120**(5), 3406–3429.

Vavryčuk, V., 2002. Non-double-couple earthquakes of 1997 January in West Bohemia, Czech Republic: evidence of tensile faulting, *Geophysical Journal International*, **149**(2), 364–373.

Viesca, R., Templeton, E., & Rice, J., 2008. Off-fault plasticity and earthquake rupture dynamics: 2. Effects of fluid saturation, *J. Geophys. Res*, **113**.

Viesca, R. C., 2016. Stable and unstable development of an interfacial sliding instability, *Phys. Rev. E*, **93**, 060202.

Viesca, R. C. & Garagash, D. I., 2015. Ubiquitous weakening of faults due to thermal pressurization, *Nature Geoscience*, **8**(11), 875–879.

Wasserman, L., 2004. *All of Statistics: A Concise Course in Statistical Inference*, Springer, New York.

Weng, H. & Ampuero, J.-P., 2019. The dynamics of elongated earthquake ruptures, *Journal of Geophysical Research: Solid Earth*, **124**(8), 8584–8610.

Weng, H. & Ampuero, J.-P., 2020. Continuum of earthquake rupture speeds enabled by oblique slip, *Nature Geoscience*, **13**(12), 817–821.

Weng, H., Huang, J., & Yang, H., 2015. Barrier-induced supershear ruptures on a slip-weakening fault, *Geophysical Research Letters*, **42**(12), 4824–4832.

Wesnousky, S. G., 1994. The Gutenberg-Richter or characteristic earthquake distribution, which is it?, *Bulletin of the Seismological Society of America*, **84**(6), 1940–1959.

Wieghardt, K., 1907. Über das Spalten und Zerreißen elastischer Körper, *Zeitschr. für Mathematik und Physik 55, 60–103*.

Willis, J. R., 1973. Self-similar problems in elastodynamics, *Philosophical Transactions of the Royal Society of London. Series A, Mathematical and Physical Sciences*, **274**(1240), 435–491.

Wu, J.-Y., Nguyen, V. P., Thanh Nguyen, C., Sutula, D., Bordas, S., & Sinaie, S., 2019. Phase field modelling of fracture, *Advances in Applied Mechanics*, **53**.

Wu, Y. & Chen, X., 2014. The scale-dependent slip pattern for a uniform fault model obeying the rate- and state-dependent friction law, *Journal of Geophysical Research: Solid Earth*, **119**(6), 4890–4906.

Xia, K., Rosakis, A., & Kanamori, H., 2004. Laboratory Earthquakes: The Sub-Rayleigh-to-Supershear Rupture Transition, *Science (New York, N.Y.)*, **303**, 1859–61.

Xia, K., Rosakis, A. J., & Kanamori, H., 2005. Supershear and subrayleigh to supershear transition observed in Laboratory Earthquake Experiments, *Experimental Techniques*, **29**(3), 63–66.

Xu, J., Zhang, H., & Chen, X., 2015. Rupture phase diagrams for a planar fault in 3-D full-space and half-space, *Geophysical Journal International*, **202**(3), 2194–2206.

Xu, S., Ben-Zion, Y., Ampuero, J. P., & Lyakhovsky, V., 2014. Dynamic ruptures on a frictional interface with off-fault brittle damage: Feedback mechanisms and effects on slip and near-fault motion, *Pure and Applied Geophysics*, **172**.

Yarema, S. Y., 1996. On the contribution of G. R. Irwin to fracture mechanics, *Materials Science*, **31**(5), 617–623.

Yoffe, E. H., 1951. The moving griffith crack, *The London, Edinburgh, and Dublin Philosophical Magazine and Journal of Science*, **42**(330), 739–750.

Yoshida, S., Maeda, T., & Kato, N., 2020. Earthquake triggering model based on normal-stress-dependent Nagata law: application to the 2016 Mie offshore earthquake, *Earth, Planets and Space*, **72**(1), 141.

Zahradník, J. & Sokos, E., 2018. *ISOLA Code for Multiple-Point Source Modeling—Review*, pp. 1–28, Springer International Publishing, Cham.

Zahradník, J., Gallovič, F., Sokos, E., Serpetsidaki, A., & Tselentis, A., 2008. Quick Fault-Plane Identification by a Geometrical Method: Application to the MW 6.2 Leonidio Earthquake, 6 January 2008, Greece, *Seismological Research Letters*, **79**(5), 653–662.

Zambom, A. Z. & Dias, R., 2013. A Review of Kernel Density Estimation with Applications to Econometrics, *International Econometric Review (IER)*, **5**(1), 20–42.

Zapperi, S., Nukala, P., & Simunovic, S., 2005. Crack avalanches in the three dimensional random fuse model, *Physica A: Statistical Mechanics and its Applications*, **357**.

Zelst, I., Wollherr, S., Gabriel, A., Madden, E., & Dinther, Y., 2019. Modeling megathrust earthquakes across scales: One-way coupling from geodynamics and seismic cycles to dynamic rupture, *Journal of Geophysical Research: Solid Earth*, **124**.

Šilhavý, M., 1991. Cauchy's stress theorem and tensor fields with divergences in Lp, *Archive for Rational Mechanics and Analysis*, **116**, 223–255.